Nano structures formed by molecular chlorine interaction with noble metal surfaces : Scanning Tunneling Microscopy/Spectroscopy study

Vladimir Cerchez

Nancy-Université

UNIVERSITE HENRI POINCARE – NANCY 1
ECOLE DOCTORALE EMMA – ENERGIE MECANIQUE ET MATERIAUX

Thesis

defended to obtain the grade of

Docteur de l'Université Henri Poincaré, Nancy I

In Physics

by

Vladimir CERCHEZ

Nano structures formed by molecular chlorine interaction with noble metal surfaces: Scanning Tunnelling Microscopy/Spectroscopy study

Public oral defence on July 13, 2011

Examining board:

President :	M. Michel PIECUCH	Professor, Université Henri Poincaré, Nancy I
Referees :	M. Erminald BERTEL	Dr. Professor, Universität Innsbruck
	M. Dimitri RODITCHEV	DR CNRS, INSP, Paris
Members:	M. Boris ANDRYUSHECHKIN	Senior Scientist, General Physics Institute, Moscow
	M. Laurent GUILLEMOT	DR CNRS, ISMO, Orsay
	M. Bertrand KIERREN	Professor, Université Henri Poincaré, Nancy I
	M. Peter ZEPPENFELD	Dr. Professor, Johannes Kepler Universität Linz

Table of contents

Introduction

Halogens form a particular group in the periodic table of the elements. Due to their extremely high electronegativity halogens manifest ultimately clear chemical properties and pronounced corrosive behavior. One can expect significant changes in atomic arrangement and electronic structure of surfaces when covered with halogen atoms.

The first attempts to understand halogen interaction with metals and semiconductors were related to the importance of this process in many industrial domains, first of all in heterogeneous catalysis and microelectronics [1, 2]. In heterogeneous catalysis halogens are widely used to modify properties of transition-metals catalysts. May be the most striking example is the ethylene epoxidation in the presence of silver catalyst – one of the most important industrial chemical reactions [3]. Addition of small amount of chlorine to the surface of silver catalyst significantly improves its selectivity towards ethylene epoxidation. Though this positive effect of chlorine is known for already 120 years and is widely used in industry its origin is not yet clear. Many scientists believe that the surface science studies of this catalytic reaction in well-defined UHV conditions on single-crystal surfaces could elucidate some key processes that are impossible to study “in vivo” in the conditions of a real chemical reactor [4].

As the knowledge about halogen adsorption on crystal surfaces has broadened it became clear that these systems are of interest not only concerning some practical applications but also from fundamental point of view. Halogens can be considered as ideal elements for the study of general trends in the interaction of active gases with solids [1, 2]. Comparing to another active gas – oxygen, halogens have several advantages. First, their sticking coefficient to the surface is few orders larger than the oxygen's one, and is usually close to 1 [2]. This makes halogens very handy for UHV conditions, where a low pressure of gases is required. Another point is that oxide film is usually very stable and it's hard to remove it from the surface. In contrast halogen monolayers (or thin halide films) are easily removed by heating the surface to moderate temperatures (400-700°C) [2].

Monoatomic films of halogen atoms adsorbed on metal surfaces are also very attractive for the study of structural phase transitions in two-dimensional systems [1]. These phase transitions can be observed already at room temperatures, whereas noble gas films commonly used for such studies need cryogenic temperatures (5-80K) that brings additional experimental difficulties. In addition as it was argued by E. Bertel et al. in their recent series of works on Br/Pt(110), phase transitions in halogen monolayers could be governed by electronic properties of the surface ([5] and references therein).

Particular interest is also related to the product of halogen-metal reaction. Halides of noble metals are narrow band (2 to 3.5 eV) dielectrics with specific electrical and optical properties (ion conductivity, high quantum efficiency, photo reactivity…). The growth of thin (few nanometers) halide films or halide nanoislands was found to start only after the metal surface is completely precovered with dense chemisorbed monolayer. The knowledge about halogen adsorption could be used for controlled growth of nanosize halide crystals, which can show particular electrical and optical behavior related to bulk halide properties and quantum size effects. Besides this, flat thin halide films seem to be promising as a padding that could decouple electronic states of adsorbates (e.g. molecular electronic states) from the metal conduction band. Flat thin films of noble metal halides due to their relatively narrow band gap could be considered as an alternative for wide gap dielectrics (MgO, NaCl, KCl, …) usually used for this purpose.

Compared to other elements of periodic table halogens are not so common for surface science and therefore are not yet so well studied. The main reason is the explicable but unfounded fear of researchers to introduce such corrosive substances into their UHV chambers. Most of work done in this field up to the moment concerns indirect studies of surface structures by surface electron spectroscopy, low energy electron diffraction and thermo desorption spectroscopy. In recent 15 years there appeared a number of STM investigations (most of them done at room temperature) of adsorbed halogen monolayers and halide films - for review on halogen adsorption see [1, 2]. However all these studies being very valuable are not sufficiently informative, especially they do not provide reliable atomic-scale information about all the structures (that are sometimes numerous and complex) on halogenated surface. The latter is mostly related to the fact that not all halogen surface structures are stable at room temperature and structural phase transitions

may take place in the temperature range above 300 K. A low temperature STM investigation (5 K and/or 77 K) is required for complete understanding of the metal/halogen interaction process. This LT STM study should be supported with DFT calculations that will give sufficiently reliable information about atomic-scale surface structure. Up to now there were a few halogen-metal systems studied so deep, that is off course not sufficient both for fundamental understanding of halogenation process and practical application of this knowledge.

In this work we address structural and electronic properties of halogen (chlorine) monolayers on metal surfaces in a low temperature range 5 K-120 K. From four elements of halogen group (F, Cl, Br, I) we have chosen chlorine as most used in practice, particularly in catalysis. Chlorine is also the most convenient halogen for UHV experiments. We omit to study halide film formation and considered only the formation of chemisorbed chlorine monolayer as a first and most "rich" stage of reaction, which is a precursor of the halide growth.

The thesis is organized as follows:

The next CHAPTER 1 contains a review of scientific literature devoted to the halogen adsorption on metals.

In CHAPTER 2 we briefly describe experimental and theoretical methods used in this work. We describe the design and technical details of halogen inlet system. Some attention is paid to the explication of particular LEED patterns observed in halogen/metal systems.

CHAPTER 3 and CHAPTER 4 describe our experimental and theoretical results on the atomic structure of chlorine chemisorbed monolayer on Ag(111) and Au(111) surfaces, respectively.

In CHAPTER 5 we report on low-temperature study of Cl/Cu(111) system. After that a discussion and comparison of three studied systems is presented.

CHAPTER 6 is dedicated to the spectroscopic study of particular self-organized Cl/Au(111) structure. We present STS measurements and results of theoretical modeling.

In CONCLUSION the main results of the work are summarized.

Bibliography of Introduction

[1] Robert G. Jones Halogen adsorption on solid surfaces // Progr. Surf. Sci. 27 25 (1988).

[2] E.I. Altman Halogens on metals and semiconductors // Landolt-Börnstein. New Series, v. III/42A1, p. 421 (2000).

[3] J.G. Serafin, A.C. Liu, S.R. Seyedmonir Surface science and the silver-catalyzed epoxidation of ethylene: an industrial perspective // J. Mol. Cat. A 131 157 (1998).

[4] Kurt W. Kolasinski Surface Science: Foundations of Catalysis and Nanoscience // John Wiley & Sons, Second edition (2008).

[5] M. Cordin et al. Phase transitions driven by competing interactions in low-dimensional systems // EPL 92 26004 (2010).

CHAPTER 1.
Halogen interaction with metal surfaces: bibliographic review

In this chapter we will expose the general behavior of halogen interaction with metal surfaces on the base of scientific literature. Results of atomic structures obtained by adsorption and interaction of halogens on dense packed (001) (011) and (111) surfaces will be presented. Halogen adsorption on metal surfaces has been studied for the last 40 years. A large number of halogen/metal systems have been studied during this period [1, 2]. We will limit our presentation to the studies achieved under ultra high vacuum conditions. Therefore we will omit to review here the numerous interesting studies realized in electrochemical environment and giving rise sometimes to similar processes and surface structures. For this, the reader can refer to the reviews of K. Itaya [3] and O.M. Magnussen [4].

1.1 General considerations

In the first approximation adsorption process takes the same scenario for all halogen-metal pairs and can be divided for convenience in two stages (see Figure 1.1):

1) formation of the chemisorbed monolayer;
2) formation of the reaction product i.e. metal halide.

Halogen molecules adsorb and dissociate to form a chemisorbed monolayer on the first stage of reaction (Figure 1.1). The Sticking coefficient remains rather large S = 0.2 to 1.0 during all the stage [2]. According to the literature the adsorption process remains dissociative even at low substrate temperatures down to 100 K [5,6,7,8,9,10,11,12]. There are almost no experimental studies for lower temperatures. The minimal temperature 25 K for dissociative adsorption was reported for Br/Pt(111) system [13].

Halogen atoms form chemical bond with substrate so such kind of adsorption is called chemisorption. Being adsorbed on the surface halogen atoms (at some non-zero coverage) usually forms an ordered 2D lattice. When the coverage increases halogen layer starts to compress and structural phase transitions are observed (Figure 1.1). When halogens adsorb on initially reconstructed surfaces (low-index faces of gold, platinum and

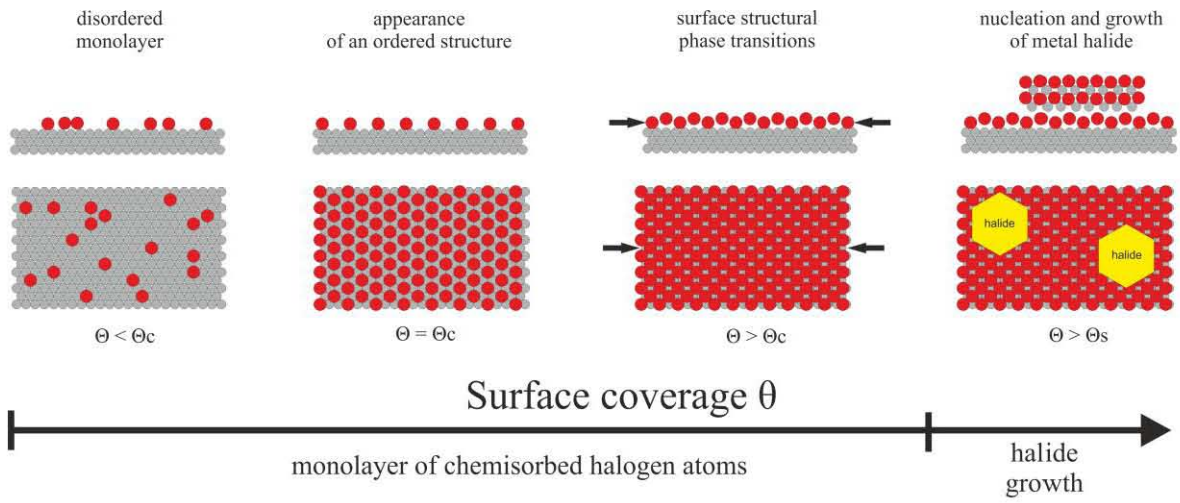

Figure 1.1 *Main steps of metal surface halogenation reaction. Substrate atoms are shown as gray circles, halogen atoms as red circles, halide islands are marked as yellow hexagons. θ_c – lowest surface coverage for ordered structure formation; θ_s – saturated surface coverage.*

iridium [14]) removal of the surface reconstruction is observed first. In most of the systems ordered structures can be observed at room temperature though in some cases low temperatures are required [7,15]. In the end of the first stage of reaction saturated halogen monolayer is formed, that mean layer of chemisorbed halogen atoms compressed as much as possible.

The second stage of reaction – nucleation and growth of metal halide – starts only after formation of saturated monolayer (Figure 1.1). If during reaction substrate has room temperature a drastic decrease (10÷1000 times) of sticking coefficient is observed [2]. Metal halide can grow either in 3D clusters [16] or as 2D flat films [17,18,19]. As it was shown in [17,18,19] halide islands grow directly on the saturated monolayer of chemisorbed halogen atoms. Chemisorbed monolayer serves as interface that reduces lattice mismatch between substrate and halide crystal.

1.2 Monolayer of chemisorbed halogen atoms

Let us discuss in more details halogenation of metal surfaces. We will restrict ourselves to the first stage of reaction as the greatest variety of surface structures and processes is observed during formation of chemisorbed monolayer. Moreover as it was already mentioned, there is significant decrease of sticking probability for halogen molecules after saturation of chemisorbed layer. That's why in many technological processes halogen interaction with metal surface will stop on the first stage of reaction. When the growth of metal halide starts structure of chemisorbed monolayer above it plays a crucial role in the growth process.

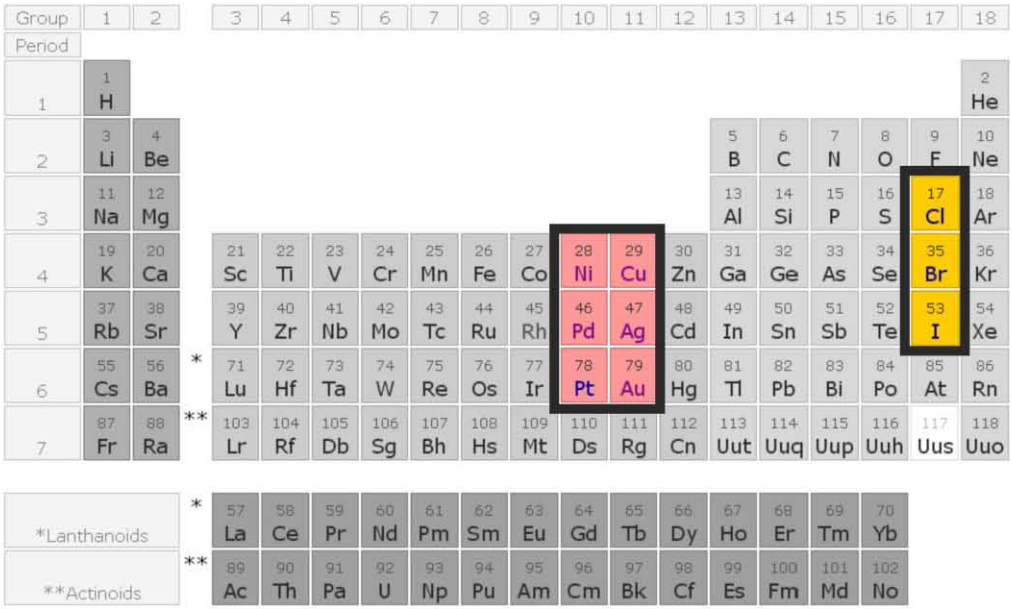

Figure 1.2. *Periodic table of elements with 10th and 11th groups of metals and 17th group of halogens highlighted.*

The most studied is halogen interaction with the10th group (Ni, Pd, Pt) and 11th group (Cu, Ag, Au) metals (see Figure 1.2). These metals are of great importance for a number of technological applications. All of them have fcc crystal structure and their physical properties are well studied. We will exclude from our review fluorine as its physic-chemical properties significantly differs from the properties of the others four halogens –

chlorine, bromine and iodine [20]. There are also significant technical problems to study fluorine adsorption in UHV conditions and only a few papers were published.

The main interest in studying chemisorbed monolayer is the ordered structures formed by halogen atoms and structural phase transitions observed on the surface during increase of halogen coverage. The diversity of phenomena observed at this stage is usually explained by the competition between lateral halogen-halogen interaction and halogen-substrate interaction. In the following two sections we will discuss these interactions.

1.2.1 Halogen-substrate interaction

Chemical bond formed by halogen atoms with 10^{th} and 11^{th} group metals is mainly covalent [21]. The degree of bond iconicity depends on the particular halogen-metal pair.

For halogens it decreases down the row of periodic table Cl-Br-I, the same as for metals from nickel and copper down to platinum and gold (except silver that forms with all halogens more ionic bond, compared to copper) [21]. The electric charge of adsorbed halogen atoms vary in the range 0 to 0.6 e^{-} [21]. The binding energy between halogen atoms and metal surface is typical for covalent bond and makes few electron-volts. It decreases down the rows of periodic table, both for halogens and metals [21].

As a rule adsorption position with maximum substrate atoms in the neighborhood is the most energetically favorable for halogen.

For instance a four-fold hollow position between 4 substrate atoms is the energetically most favorable position on the (100) face (see Figure 1.3a). That was shown for all halogens on the (100) surface of nickel, copper and silver [19,22,23,24,25,26,27,28,29]. The only exception is Au(100) surface. As it was found in [29] the preferential adsorption place for bromine atoms is a two-fold bridge position between two substrate atoms. Such unusual behavior was explained by important role of Br-Au coulomb repulsion in this system [29]. On the (111) face the three-fold hollow position is the preferential adsorption site - see Figure 1.3b for all the systems studied and where the data about atomic positions are available. [27,30,31,32,33,34,35,36,37,38].

Rather different is adsorption on (110) face. Two-fold hollow site between four substrate atoms has maximal coordination number (Figure 1.3c). However DFT calculations for Cl, Br/Cu(110) [39], Cl, Br/Pt(110) [40,41] and Cl, Br/Ag(110) [42,43] systems show that two-fold short-bridge position is energetically favorable (Figure 1.3c). Experimental evidence for halogen adsorption in short-bridge site was reported for Cl/Ni(110) [44], but more recent calculations [45] did not confirm it. There are only two systems with halogen atoms being adsorbed in high symmetry hollow site. These are I/Cu(110) [39] and I/Ag(110) [46]. Such difference for (110) face can be qualitatively explained as following. Imagine halogen atom adsorbed in two-fold hollow site and bound with substrate atoms via covalent bonds. The length of a covalent bond can be roughly estimated as the sum of halogen and metal radii [21].

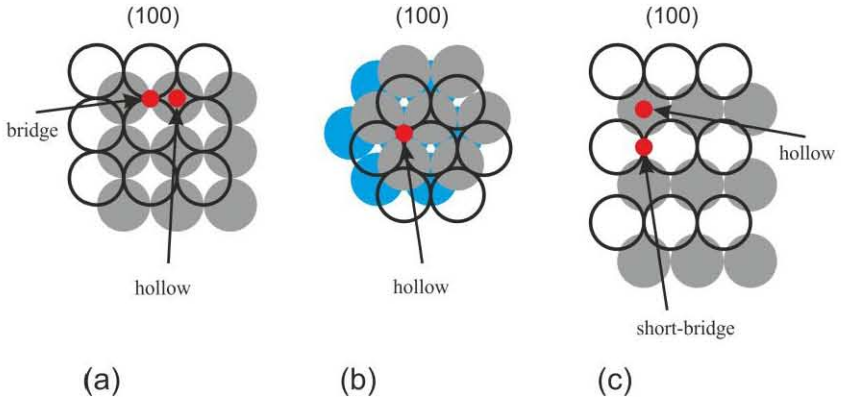

Figure 1.3 *Preferential adsorption sites for halogen atoms on low-index planes of fcc metals. Substrate atoms from the last atomic plane are shown as transparent circles, the next layer as gray circles and the third layer as blue circles.*

In the (110) face geometry the distance between atom adsorbed in hollow site and substrate atoms from the penultimate crystal plane can be smaller than the distance between adsorbate and the last plane atoms. Thus for most of halogen-metal pairs adsorption in hollow site will result in interatomic distances smaller than the length of covalent bond. For such systems short-bridge adsorption site becomes more attractive. Iodine because of it large covalent radius will be placed sufficiently far from the surface and does not interact strongly with penultimate plane even in hollow adsorption site.

We have listed in Table 1 the available data about adsorption sites for halogen atoms on metal surfaces.

The lowest binding energy for all crystal faces has on-top adsorption site. Any other site on the surface has intermediate binding energy. The difference between adsorption energy in different sites on the surface is in the range of 0.05 eV to 0.5 eV [29,46,47,48].

Metal surface represents a 2D periodic adsorption potential for halogen atoms. In the absence of other forces besides covalent bond with the substrate halogen atoms will fill preferential adsorption sites on the surface and will form lattice with the same symmetry and periodicity as substrate.

Table 1. *Preferential adsorption sites for halogens on the surface of 10th and 11th group metals: H - hollow; B – bridge; SB – short-bridge.*

	(100)			(111)			(110)		
	Cl	**Br**	**I**	**Cl**	**Br**	**I**	**Cl**	**Br**	**I**
Ni	H [22]	H [23]	H [24]	H [34]	—	—	SB(H) [44,45]	—	—
Pd	—	—	—	—	—	H [35]	—	—	—
Pt	—	—	—	—	—	H [38]	SB [40]	SB [41]	
Cu	H [25]	H [26]	H [27]	H [30]	H [30]	H [27]	SB [39]	SB [39]	H [39]
Ag	H [28]	H [29]	H [19]	H [31]	—	H [32]	SB [42]	SB [43]	H [46]
Au	—	B [29]	—	H [33]	—	—	—	—	—

1.2.2 Halogen-halogen lateral interaction

Almost nothing is known about lateral interaction between adsorbed halogen atoms - the second interaction which determines monolayer structure. In the absence of studies on the nature of halogen-halogen interaction the only source of our knowledge can be results of TDS, core-level photoelectron spectroscopy, ARPES and STM experiments.

All experimental and theoretical results indicate that halogen-halogen lateral interaction is short-range and can be observed only for interatomic distances less than 5-6 Å. In most papers the authors point out electrostatic repulsion (due to the negative charge appearing on halogen atoms after adsorption) as the main feature of this interaction. There is also experimental evidence of possible indirect interaction via substrate [49,50,51].

Along this, some of the studies have shown that halogen-halogen interaction can have also a short-range attractive contribution [13,52,53,54,55]. Possible nature of this attraction remains unclear. There is also no data concerning the effects of trio interactions on the halogen monolayer. Such effects together with attractive interatomic interaction can play crucial role for the phase diagram of chemisorbed layer [56].

As one can see, up to now there is no even qualitative interpretation of halogen-halogen interaction on metal surfaces. This makes difficult analyses of processes in chemisorbed monolayer.

Halogen atoms due to mainly repulsive interaction between them seek to increase interatomic distances in monolayer and to form lattice with hexagonal symmetry. As it was already mentioned interaction between halogen atoms is of short-range and rather week. At room temperature it can influence monolayer structure only after the density of halogen atoms reaches some level (interatomic distances have to be equal to the adsorbate-adsorbate interaction range). One can estimate such density (or absolute coverage) as $\theta > 2\text{-}3\times10^{14}$ atoms/cm^2 or, depending on the symmetry and density of crystal surface, as relative coverage $\theta > 0.2\text{-}0.4$ ML.

Interatomic repulsion limits the nearest-neighbor distances in the halogen monolayer (and, hence, its maximum density). It is useful to give some typical ~~–si~~zes" of halogen atoms and halogen-halogen distances in different compounds. That will make it possible to estimate maximal density of a halogen monolayer. Table 2 contains covalent radii, van der Waals diameters, ionic radii for halogen atoms, and interatomic distances in metal halides.

Table 2. *For each halogen the table contains values of covalent diameter d_{cov} [106], van der Waals diameter d_{VdW} [104,105] and ionic diameter d_{ionic} [107]; halogen-halogen distances in corresponding metal halides are given [60] together with smallest halogen-halogen distances in chemisorbed monolayers on corresponding metal surfaces (regardless of the surface orientation). Cl - [28,61,74]; Br - [23,50,53]; I - [19,62,64].*

	d_{cov}, Å	D_{VdW}, Å	d_{ionic}, Å	halogen-halogen distances in halide, Å						smallest halogen-halogen distances on the surface, Å					
				Ni	Pd	Pt	Cu	Ag	Au	Ni	Pd	Pt	Cu	Ag	Au
Cl	1.98	3.5	3.34	3.34	—	—	3.82	3.92	—	3.5	—	—	3.5	4.1	—
Br	2.28	3.7	3.64	3.5	—	—	4.02	4.08	—	3.5	—	—	3.62	4.1	—
I	2.66	4.05	4.12	3.67	—	—	4.27	4.56	4.1	3.5	—	—	3.62	4.1	—

The table also contains reliable experimentally measured values of minimal interatomic distances in halide layers. From this table one can see that ~~"d~~iameter" of halogen atoms on metal surfaces is always close to its van der Waals diameter. In certain systems halogen atoms can have ~~"s~~ize" smaller (approach to each other closer) than van der Waals diameter but it is always much bigger than its covalent diameter. The size of halogen atoms on the surface of a given metal always increase in the sequence chlorine-bromine-iodine.

After we have discussed properties of halogen-substrate and halogen-halogen interaction we can review structural phase transitions on metal surface during halogen adsorption on it.

1.2.3 Disordered phase: θ < 0.2 - 0.4 ML

It is impossible to observe halogen atoms on the surface at room temperature when the coverage is too low (θ < 0.2-0.4 MC) and hence interatomic distances are significantly larger than the range of adsorbate-adsorbate interaction. The main reason for this is high mobility of adsorbed atoms. We can estimate the time spent by atom in an adsorption site as [57]:

$$\frac{1}{\tau} = \nu_0 e^{-\frac{E_{act}}{kT}} \qquad (1.1)$$

In this formula ν_0 is the frequency of atomic oscillations on the surface, E_{act} – activation energy to pass potential barrier between neighboring adsorption sites, temperature T and Boltzmann constant k. The frequency ν_0 can be estimated as proper frequency of harmonic oscillator with adsorption potential being restoring force and the inertial mass being the mass of atom. Such consideration gives the value for ν_0 of an order 10^{12} to 10^{13} s^{-1} and is in a good agreement with typical value for frequency of atomic oscillations on the surface [57]. Boltzmann coefficient $e^{-\frac{E_{act}}{kT}}$ with activation energy being $E_{act} \approx 50$ to 250 meV (typical maximal difference in binding energy for different adsorption sites on the surface) has value of an order 10^{-2} to 10^{-4}. Thus the time τ spent by halogen atom in one adsorption site at room temperature is within 10^{-8} s. High mobility makes it impossible to observe adsorbed halogen atoms on the surface at room temperature and low coverage. We can suppose that at such conditions halogen monolayer is completely disordered as shown on Figure 1.4a.

The time τ can be increased by cooling down surface temperature. Lowering of temperature down to T < 100 K increases the time spent by an atom in the same adsorption site up to 10^2 s. This is sufficiently long for STM study of the surface.

From our knowledge there are only two low-temperature STM studies of low-coverage halogen layers on metals for Br/Cu(111) [55] and Br/Pt(111) [13] systems. In the former the authors observed bromine islands of (√3×√3)R30° structure at substrate temperature T = 4 K - see Figure 1.4b.

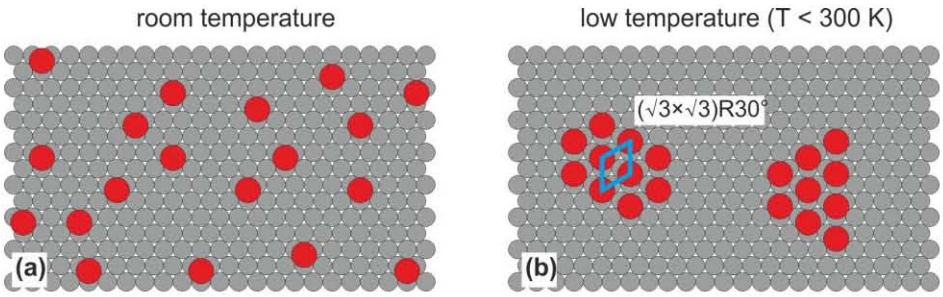

Figure 1.4 : *Schematic representation of metal surface ((111) face) covered by θ ≈ 0.05 ML of halogen:* ***(a)*** *disordered halogen layer at room temperature;* ***(b)*** *islands of (√3×√3)R30° structure formed by halogen atoms at low temperature.*

The nearest-neighbor interatomic distance in the islands was found to be 4.4 Å. The local bromine coverage in the islands is therefore estimated to θ = 0.33 ML where the average surface coverage was estimated to be θ = 0.03 ML. Such agglomeration of bromine atoms into the islands of compact structure can be the sign of attractive component in the lateral interatomic interaction. At the same time it has to be pointed out that a specific method for preparation of halogen monolayer was used in [55]. The method used icluded heating of substrate covered by bromine up to 600 K [55] and monolayer could be formed at elevated temperatures.

On the contrary, in the study of the Br/Pt(111) system [13], bromine was adsorbed on the surface at T = 25 K. At such low temperatures the mobility of bromine atoms on the surface is limited. They can diffuse only at small distances due to the energy released from the adsorption and dissociation of Br_2 molecules. The authors report on the observation of island with compact (√3×√3)R30° structure at surface coverage θ > 0.07 ML. At lower coverage dimers of bromine atoms (θ ≈ 0.01 ML) and atomic chains (θ ≈ 0.03 ML) were observed. It is clear that in these experiments the structure of bromine layer was governed by the mobility of adsorbed Br_2 molecules, probability for their dissociation in different sites on the surface and subsequent diffusion and sticking of bromine atoms rather than by adsorbate-adsorbate or adsorbate-substrate interactions [13].

As one can see up to now there is no enough information about halogen monolayer structure at low coverage. Results of Br/Cu(111) and Br/Pt(111) systems study allow us to assume the importance of lateral interaction and possible existence of islands with compact structure at this range of coverage.

1.2.4 Commensurate structures

The situation is changed when the halogen surface coverage increases. Increased atomic density allows halogen atoms to interact stronger and that limits their mobility. As a result at absolute surface coverage $\theta \approx 2\text{-}3\times10^{14}$ atoms/cm^2 (that corresponds to nearest-neighbor distances less than 5-6 Å) formation of ordered structures starts. Usually commensurate c(2×2) structure is formed on the surfaces with square (100) and rectangular (110) symmetry, and (√3×√3)R30° on the surfaces with hexagonal symmetry (111) – see Figure 1.5a. All atoms in these lattices are placed in the equivalent energetically most favorable adsorption sites. The relative surface coverage is $\theta = 0.5$ ML for c(2×2) lattice and $\theta = 0.33$ ML for (√3×√3)R30° lattice.

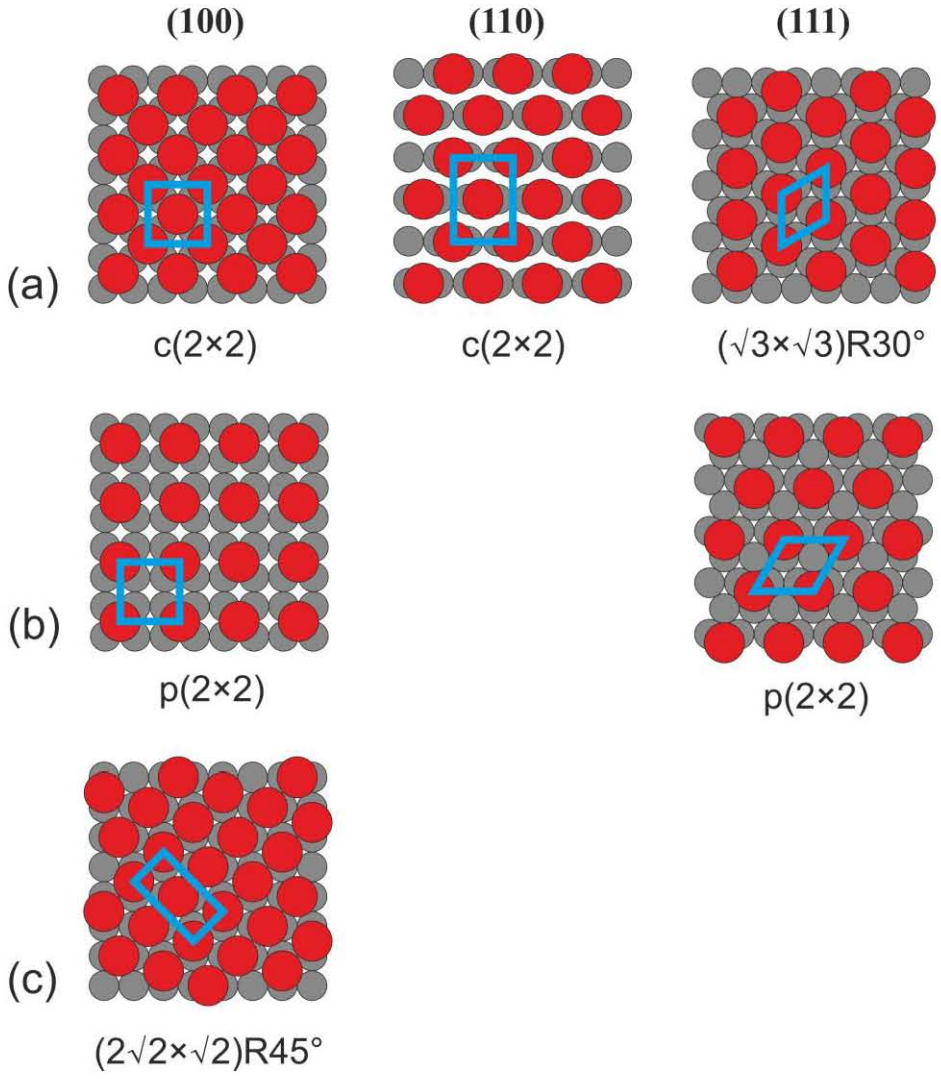

Figure 1.5. *Commensurate structures formed by halogen atoms on low-index planes of fcc metals. For each structure a unit cell is shown.*

Commensurate structures formed by halogen atoms are usually stable at room temperature. However in some systems ordered structures can be observed only at low surface temperatures. For instance, chlorine monolayer on Ag(111) [15] and Au(111) [7] surface forms $(\sqrt{3}\times\sqrt{3})R30°$ lattice at surface temperatures less than 195 K and 230 K respectively. This can be explained by smaller density of surface lattices of these metals (compared to other metals of 10^{th} and 11^{th} groups of periodic table) and hence larger interatomic distances in halogen $(\sqrt{3}\times\sqrt{3})R30°$ structure, together with relatively low adsorption energy on these metals. When iodine atoms with larger diameter are adsorbed on the same surfaces $(\sqrt{3}\times\sqrt{3})R30°$ structure becomes stable at room temperature [58,59].

Other conditions are realized on the surface of nickel and copper. These two metals in contrast to gold and silver have the densest surface lattices from all metals considered ($\theta_{Ni(111)} \approx 1.86\times10^{15}$ atoms/cm^2 and $\theta_{Ag(111)} \approx 1.38\times10^{15}$ atoms/cm^2 - $a_{Ni(111)} = 2.49$ Å and $a_{Ag(111)} = 2.89$ Å [60]). Because the small periodicity of the surface lattice for Ni and Cu the nearest-neighbor distances in c(2×2) and $(\sqrt{3}\times\sqrt{3})R30°$ structures are significantly smaller compared to other metals. As a consequence at the same absolute halogen coverage $\theta = 2\text{-}3\times10^{14}$ atoms/cm^2 formation of structures with smaller relative density of monolayer is observed on the surface of copper and nickel – see Figure 1.5b. On Ni(100) and Ni(111) surfaces chlorine forms p(2×2) lattice [61,62] with relative coverage $\theta = 0.25$ ML. These lattices are not stable at room temperature and on the Ni(111) surface only diffuse LEED spots of p(2×2) structure can be detected [62]. On (100) face of nickel the diffraction pattern appears only at temperatures below 80 K [61]. When iodine (having larger diameter) is adsorbed on the same surfaces these lattices are stable even at ambient temperature. For example in I/Ni(100) and I/Cu(100) systems commensurate p(2×3) and p(2×2) structures can be detected at room temperature [63,64].

For all systems mentioned above (Cl and I on Ni(100) and Cl/Ni(111)) besides p(2×2) or p(2×3) structures common c(2×2) (for Cl and I on Ni(100)) and $(\sqrt{3}\times\sqrt{3})R30°$ (for Cl/Ni(111)) structures are formed at larger halogen coverage [61,62,63]. A c(2×2) structure is not formed only in the I/Cu(100) system [64].

Much more intricate is the structure of first ordered structure observed on the Au(100) and Pt(100) surface [2]. All halogens form $c(2\sqrt{2}\times\sqrt{2})R45°$ commensurate structure on these surfaces for coverage $\theta = 0.5$ ML – see Figure 1.5c.

1.2.5 Partially commensurate and incommensurate structures

In most of the systems formation of commensurate structure is followed by further adsorption and compression of halogen monolayer. At this stage the 2D halogen lattice is compressed and a partially commensurate or incommensurate structure is formed. In such kind of lattice the adsorbed atoms occupy different adsorption sites on the surface and part of them are placed in energetically unfavorable sites. Compression continuously increases

with surface coverage. There are two different scenarios of compression – uniform compression and nonuniform compression.

In the former case halogen lattice is compressed uniformly as a hole. The density of adsorbed atoms on the surface remains uniform whereas the average interatomic distances decrease. Almost all halogen atoms occupy adsorption sites that are not energetically most favorable. Uniform compression can be either isotropic or uniaxial – see Figure 1.6a. For uniaxial compression a few domains with different direction of compression can be formed, depending on the symmetry of the substrate: three domains on (111) face and two domains on (100) face – see Figure 1.6b. There can be only one domain on the anisotropic (110) face. Scenario of uniform compression is realized in that system where the lateral adsorbate-adsorbate interaction is much stronger than adsorbate-substrate interaction.

A more complex scenario is realized in the systems with comparable lateral and transversal interactions. A nonuniform compression becomes energetically favorable in such case. As opposite to uniform compression a periodic system of domains with commensurate structure is formed. Neighboring domains are separated by a narrow region with increased density of halogen atoms called "heavy domain walls" – see Figure 1.7a. In the case of nonuniform compression most of adsorbed atoms remain in their energetically most favorable positions since commensurate structure is not disturbed inside domains. All compression is concentrated within domain walls where adsorbed atoms have to be arranged denser than in the commensurate structure and occupy different (and energetically less favorable) sites. The number of domain walls continuously increases (on the contrary, the width of domains decreases) with halogen coverage [65].

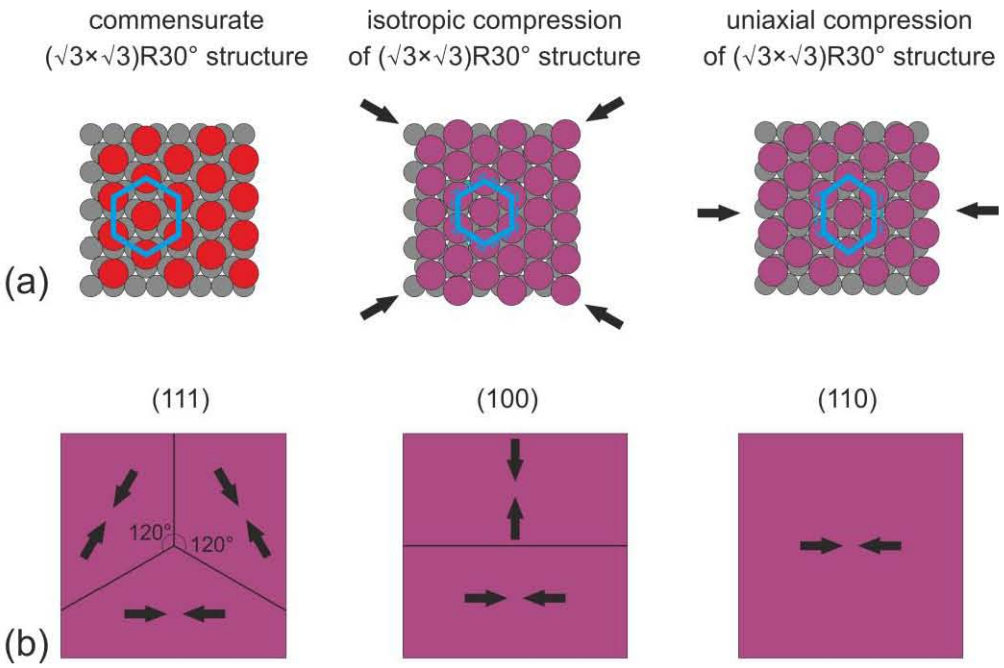

Figure 1.6. *Uniform compression of commensurate structure:* ***(a)*** *a schematic view of commensurate structure, isotropic and uniaxial compressions of commensurate structure;* ***(b)*** *formation of several domains with different direction of compression (marked with black arrows)*

Domain-wall mechanism of compression was first proposed by Frenkel and Kontorova [66], and developed later in the work of Frank and van der Merwe [67]. Adsorbate lattice with domain wall structure is compressed on the average uniaxially in the direction perpendicular to domain walls. Similar to uniaxial uniform compression we can distinguish several domains with different direction of compression - see Figure 1.7b: three domains on (111) face, two domains on (100) face and one domain on the anisotropic (110) face.

The difference between uniform and domain-wall mechanism of compression vanishes for high compression ratio when domains and domain walls have comparable width.

Similar to commensurate structures compressed halogen layer is usually ordered at room temperature. Two systems Cl/Ag(111) [15] and Br/Ag(111) [68] makes an exception. An ordered (√3×√3)R30°-Br structure is formed on Ag(111) surface at room temperature [69,70], whereas compressed monolayer is stable at temperatures T < 260 K [68]. This is not surprising since in compressed layer (independently of the exact mechanism of compression) part of adsorbed atoms occupies energetically unfavorable places and the adsorbed layer can become less stable. For Cl/Ag(111) system all ordered structures forms at temperature below T < 195 K and the reason for that was already discussed in Sec. 1.2.6.

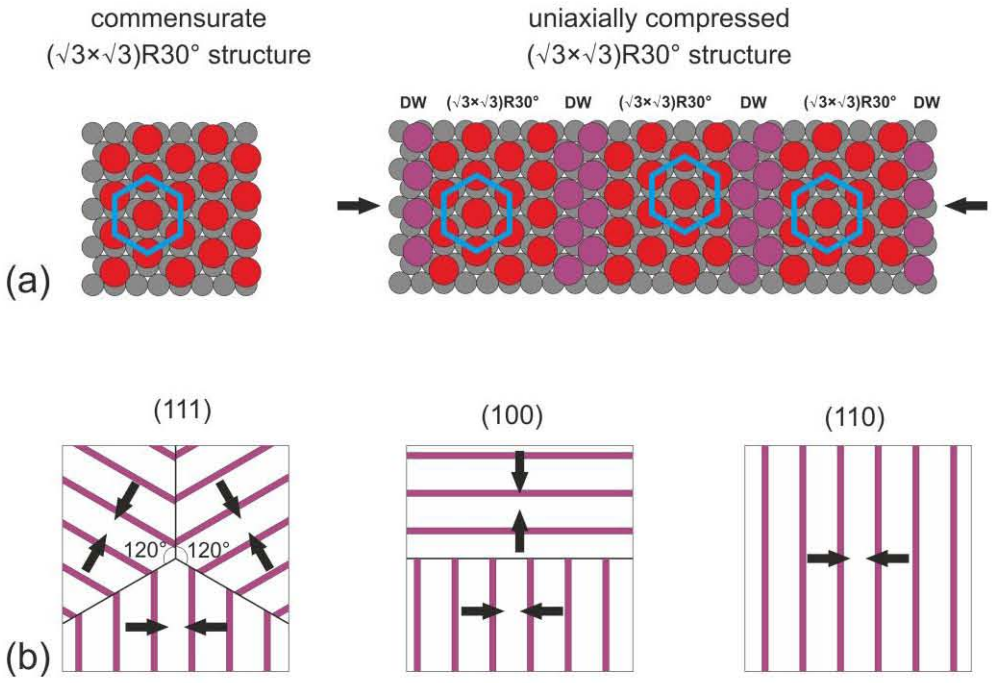

Figure 1.7. *Nonuniform compression of commensurate structure:* ***(a)*** *schematic view of commensurate structure and a nonuniform compression of it with periodic system of heavy domain walls (DW);* ***(b)*** *formation of several domains with different direction of compression (marked with black arrows). Purple lines are regions with increased density of halogen atoms - heavy domain walls.*

Spots-splitting on the LEED images is the common way to register compression of adsorbed monolayer [71,72,73,74] see Figure 1.8. Such diffraction patterns were observed for many halogen/metal systems but only in a few of them compression scenario was identified since spots position for uniform and nonuniform compressed lattice is the same [71,74]. The proof of nonuniform compression and formation of domain wall structure can be obtained by STM or EXAFS study. Such evidence was reported only for several systems: Cl/Ag(110) [75], Br/Ag(110) [76], I/Cu(110) [77], Cl, I/Cu(111) [74].

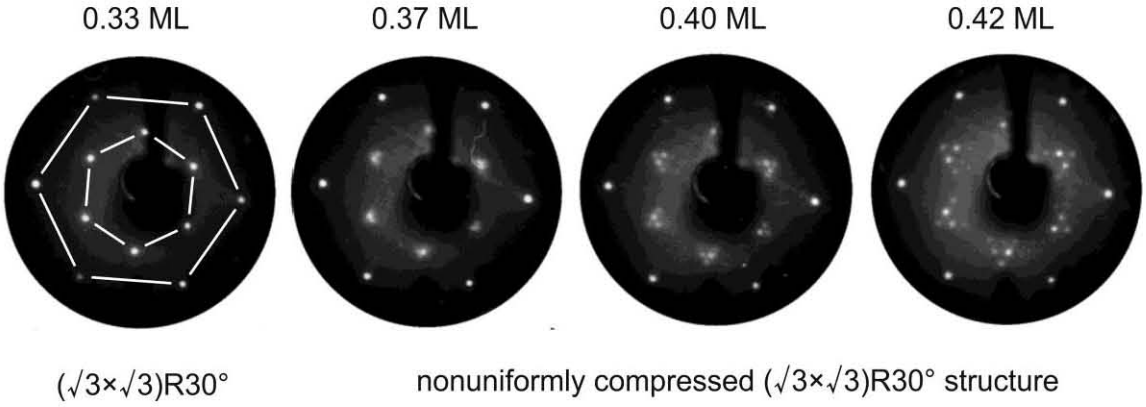

Figure 1.8. *Example of LEED pattern evolution during increase of halogen coverage and compression of (√3×√3)R30° structure in Cl/Cu(111) system [74]. A three-fold splitting of diffraction spots and formation of a triangle of 6 spots centered above (√3×√3)R30° position can be seen. Substrate diffraction spots are marked with a large hexagon on the first image; the inner small hexagon marks diffraction spots from chlorine (√3×√3)R30° structure. The splitting of diffraction spots in this system was explained as result of double diffraction from substrate and uniformly compressed chlorine layer [5] until STM study [74] has definitely showed that chlorine layer is compress nonuniformly and a domain-wall structure is formed on Cu(111) surface*

Compression of commensurate halogen monolayer is observed on (111) and (110) metal faces. On the (100) face the nearest-neighbor distances in c(2×2) structure are already small and corrugation of substrate potential is too large so no monolayer compression occurs. This is not the case for Cl, I/Ni(100) и I/Cu(100) systems where the first ordered structure is less dense p(2×2) lattice. In Cl, I/Ni(100) systems this lattice is compressed to c(2×2) [61,63]; iodine layer on Cu(100) surface is compressed to c(5×2) structure [64]. On the (100) face of gold and platinum compression of c(2√2×√2)R45° lattice leads to formation of quasihexagonal structure [2].

1.2.6 Saturated monolayer structure

Repulsive interaction between halogen atoms on the surfaces is the natural factor limiting the compression in chemisorbed monolayer. Besides this, adsorbate-substrate interaction must play an important role in formation of saturated monolayer. Compression of chemisorbed layer will increase the interaction energy between halogen atoms and substrate since part of the atoms will occupy energetically unfavorable places on the

surface. Compression may stop at that moment when gain in the energy due to the adsorption of halogen atom will no more countervail loss in adsorbate-substrate interaction energy. Most obviously it is manifested on (100) face of metals where corrugation of substrate potential is large and therefore in most of Halogen/Metal(100) systems compression of halogen monolayer is not observed [1,2].

Structure of saturated halogen monolayer on (111) face can be usually described as partially commensurate or incommensurate quasihexagonal lattice. Such lattice is formed by compression of halogen (√3×√3)R30° layer. For example it was shown for Cl and I on Cu(111) systems that saturated monolayer has domain-wall structure with (√3×√3)R30° domains being the same width as domain walls between them [74]. Due to the three-fold symmetry of substrate, there are three kinds of domains on the surface with different direction of compression. When the halogen layer is saturated the chlorine (√3×√3)R30° lattice is in average compressed by 24%, iodine lattice is compressed by 15%. Less compression of iodine monolayer compared to chlorine monolayer can be explained by larger diameter of iodine atoms (see Table 2).

Similar picture is observed for iodine monolayer on Cu(110) surface [77]. Due to two-fold symmetry of this crystal face there is only one possible direction for compression of halogen layer. Saturated iodine monolayer forms domain-wall structure with parallel linear c(2×2) domains separated by heavy domain walls of the same width [77]. In average iodine commensurate lattice is compressed by 26%.

For reliable interpretation of saturated halogen monolayer structure the use of several experimental techniques together with computer simulation is necessary. Bromine adsorption on Pt(110) surface is an example of comprehensively studied system [78]. The use of STM and IV LEED techniques together with DFT calculations allowed the authors to build a structural model for (4×1) structure of saturated monolayer. This structure consists of coupled [001] rows of bromine atoms in long-bridge adsorption sites separated by [001] rows of atoms in short-bridge positions [78].

1.2.7 Surface reconstruction

Halogen adsorption can cause metal surface to reconstruct. As it was found in the study [79] adsorption of small amount of bromine ($\theta \approx 0.3$-0.4 ML) on Cu(100) surface and subsequent annealing of the substrate up to 370 K will cause formation of chess-board pattern of reconstruction. This reconstruction consists of square islands 20×20 Å with c(2×2)-Br structure and square islands of the same size with clean surface. Similar structure is formed on the vicinal Cu(210) surface covered by bromine. Due to another surface symmetry triangular islands of reconstruction are formed [80].

Surface reconstruction was also reported for chlorine and bromine adsorption on Ni(110) surface [81,82]. In both systems formation of dimers with the length of 3.5 Å

(Cl/Ni(110)) or 5 Å (Br/Ni(110)) was observed. Such dimers became building blocks of surface structures – linear chains and c(2×4) or (3×2) lattices.

On the (110) face of platinum, chlorine adsorption leads to the formation of a long-range-ordered Cl-$PtCl_4$ adlayer [40]. Even small amount of halogen ($\theta \leq 0.1$ ML) adsorbed on metals with initially reconstructed surface (low-index faces of gold, (100) and (110) faces of platinum [14]) lifts the reconstruction and a (1×1) surface is formed. This was reported for Cl, Br, I/Au(100) [83,84,85], Cl/Pt(100) [86], Cl, Br/Pt(110) [87,88], Cl, I/Au(111) [33,89] systems.

1.3 The subject of this thesis

Chlorine adsorption on the (111) face of silver, gold and copper has been chosen as the subject of this study. Chlorine has been chosen among other halogens as the most important element for heterogeneous catalysis. Besides this chlorine is the most easy-to-use in UHV conditions halogen. Among the metals of the 10^{th} and 11^{th} row of periodic table, silver and gold have been chosen, mainly due to the importance of Cl/Ag and Cl/Au systems for heterogeneous catalysis. All experiments were carried out on the (111) face of these metals. This close-packed face is known to be thermodynamically most stable face of fcc crystal. We also included in our study chlorine adsorption on copper (111) surface. This will allow us to retrace dependence of structures formed on the parameters of surface lattice, its symmetry and presence of initial surface reconstruction for chlorine adsorption on 11^{th}-row metals.

1.3.1 Cl/Cu(111) system

From previous studies [5,69,74,102] Cl/Cu(111) is known to form ordered and stable structures at room temperature.It has been shown that it forms a (√3×√3)R30° structure on Cu(111) surface at coverage $\theta = 0.33$ ML. According to EXAFS and PED measurements chlorine occupy fcc hollow adsorption site [36,37]. This measurements were confirmed by DFT calculations [47,103]. At higher chlorine coverage $\theta > 0.33$ ML compression of (√3×√3)R30° lattice starts and a domain-wall structure is formed [5,69,74].

The structure of low-coverage chlorine layer ($\theta < 0.33$ ML) and the very first stage of (√3×√3)R30° lattice compression are unknown and still needs experimental study.

1.3.2 Cl/Ag(111) system

This system was studied for the first time by Rovida et al. in 1974 [90] using LEED measurement. Distorted (3×3) diffraction pattern was reported for saturated chlorine monolayer, explained by the authors as a corrosion layer. According to Bowker and Waugh [91] TDS spectra from chlorinated Ag(111) surface consists of two peaks. One of them (760 K) was attributed to monolayer desorption whereas another one (670 K) to silver chloride desorption.

The Ag(111) surface covered by chlorine has been studied by LEED [15,69,90,92,93,91,94], EXAFS [15,31], and room-temperature STM [95]. Besides this, DFT calculations [48,96,97,98] were used to investigate chlorine interaction with silver surface. It was found that at room-temperature adsorption of chlorine a diffuse (√3×√3)R30° LEED pattern is observed first [15,69,91], which is followed by a complex pattern described by different authors as (10×10) [15,69], (17×17) [95] or double-diffraction from epitaxial AgCl(111) layer [93,91]. In fact all the authors observed LEED patterns similar to that reported by Rovida et al. in [90]. Bowker and Waugh [91] desribe two diffraction patterns for almost saturated chlorine layer. The first one (structure ~~"C"~~) contains fractional-order spots 0.28 and 0.72 (in the units of substrate reciprocal lattice vectors) wich is in agreement with data from the study of Rovida et al. [90]. Further chlorine adsorption transform structure ~~"C"~~ to ~~"D"~~ which contains only 0.72 spots. Wu et al. [94] also reported observation of structure ~~"D"~~ for saturated chlorine monolayer. The only STM study [95] of chlorine adsorption on Ag(111) surface was done at room temperature. Poor spatial resolution due to high mobility of chlorine atoms at 300 K made it impossible to determine exact atomic structure of saturated monolayer. The authors had to use FTT transform of STM images to determine periodicity of chlorine layer.

A low-temperature LEED and EXAFS study of Cl/Ag(111) was done by Shard and coworkers [15]. A sharp (√3×√3)R30° LEED pattern was observed for surface temperatures less than 190 K and chlorine coverage $\theta = 0.33$ ML. For higher chlorine coverage splitting of diffraction spots similar to that in Cl/Cu(111) [74], I/Cu(111) [73,74], I/Ag(111) [58], I/Au(111) [89] systems is reported. For saturated monolayer the authors observed the same LEED pattern as in [90].

To conclude, in spite of rather long study of chlorine adsorption on Ag(111) surface there are still doubts about exact atomic structure of saturated chlorine layer. The structure of compressed (√3×√3)R30° lattice is not determined either. The knowledge of the exact atomic structure in the first stages of Cl adsorption could be therefore of important interest for catalysis. This was one of the motivations of our work.

1.3.3 Cl/Au(111) system

Chlorine adsorption on Au(111) surface is dissociative in the whole range of the temperatures 120-500 K studied. Two peaks are observed in TDS spectra of chlorinated gold surface [7,33,99]: high-temperature peak β_1 ($T \approx 800$ K) due to chlorine desorption [7,33] (Spencer and Lambert [99] assigned this peak to Cl and Cl_2 desorption in equal ratio), and broad low-temperature peak β_2 ($T \approx 650$ K), which appears at higher surface coverage and is due to purely Cl_2 desorption. The position of high-temperature peak β_2 shifts down the temperature which is the sign of the second-order desorption. Neither of the authors detected gold-containing fragments desorbing from the surface [7,33,99]. All the authors attribute appearance of peak β_1 with formation of a chemisorbed chlorine monolayer. At this stage of reaction surface reconstruction is removed. In [7,99] removal

of surface reconstruction was detected by disappearance of spot splitting in LEED images at some chlorine coverage (indeed due to the herringbone reconstruction diffraction spots on LEED images from clean Au(111) surface are split). STM observation of surface reconstruction removal at 120 K was done in the study [33]. However details of this process remained unstudied since chlorine does not form any ordered structures in this range of chlorine coverage and temperatures $T > 120$ K.

At chlorine coverage $\theta \approx 1/3$ ML an ordered (√3×√3)R30° structure is formed on the Au(111)-(1×1) surface [7,99]. This structure was reported to be ordered only at the temperatures below 230 K. According to LEED study [99] order-disorder phase transition observed at $T = 210$–230 K is reversible. Recent DFT calculations [33] have confirmed that the (√3×√3)R30° structure is a pure chlorine layer (no halogen-metal mixing) formed on de-reconstructed Au(111)-(1×1) surface. It has been shown that chlorine atoms occupy fcc three-fold hollow adsorption sites [33]. According to Kastanas and Koel [7] the sharpest (√3×√3)R30° LEED pattern and the appearance of the second high-temperature TDS peak β_2 are observed for the same chlorine coverage. At the same time TDS and STM study [33] clearly showed that heating Cl/Au(111) monolayer with chlorine coverage $\theta > 0.33$ ML and TDS spectra containing both β_1 and β_2, peaks up to $T_m = 750$ K ($T_{\beta_2} < T_m < T_{\beta_1}$) leads to the restoration of (√3×√3)R30° structure and disappearance of the low-temperature TDS peak β_2 (while leaving β_1 peak). These facts prove that β_1 TDS peak corresponds to the chlorine monolayer at surface coverage $\theta \leq 0.33$ ML and the low-temperature peak β_2 appears for higher chlorine coverage. In these papers any substantial change in LEED pattern are reported for chlorine coverage $\theta > 0.33$ ML and temperature range 120–500 K except the appearance of a diffuse background and broadening of substrate and (√3×√3)R30° diffraction spots [7,99].

In the STM study [33] of saturated chlorine monolayer at 120 K the honeycomb-like structure of saturated chlorine monolayer was observed for the first time. Each cell in this structure is formed by six dimers of ≈ 3.2 Å length. It was supposed that the structure can have the same nature as gold chloride. The latter DFT calculations [100] confirmed that for surface coverage $\theta > 0.33$ ML a mixed gold-chlorine layer can be formed but available experimental information was not enough to propose a structural model of honeycomb layer. It should be noticed that XPS spectra [7,33] do not show any shift of chlorine 2p core-level typical for gold chloride (typical shift is ≈ 2.5 eV) [101] in the whole studied range of coverage and temperatures. Neither UPS spectra [7] do show any significant change of 4*f* valence band of gold typical for gold chlorides [101].

On Figure 1.9 a schematic phase-diagram of Cl/Au(111) system is shown which summarize results of all previous studies [7,33,99]. The region where no ordered structures have been found is hatched on the diagram. For all chlorine coverage the temperature range below 120 K is not yet studied. This diagram clearly shows that the new data on the chlorine monolayer structure can be obtained only at temperatures T < 120 K. The structure of low-coverage chlorine layer, details of surface reconstruction removal and saturated chlorine layer structure are of main interest.

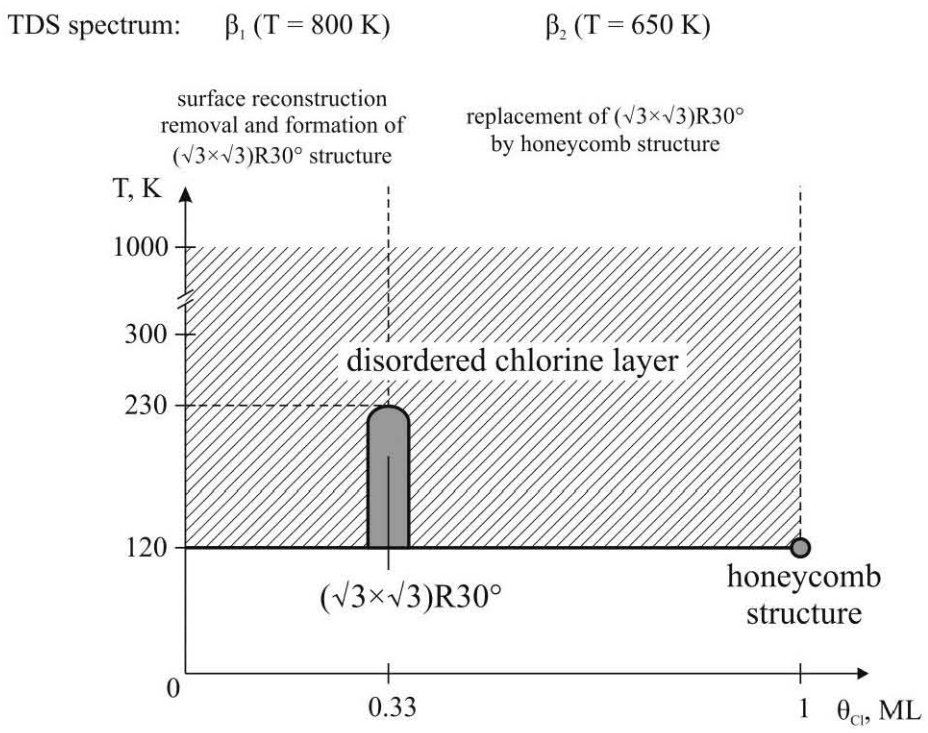

Figure 1.9. *Schematic phase-diagram of chlorine monolayer on Au(111) surface summarizing results from [7,33,99]. The region where no ordered structures have been found is hatched on the diagram; region of ordered structures existence is shown in gray. For all chlorine coverage the temperature range below 120 K is not yet studied*

1.4 Conclusion

In spite of the large number of studies, the adsorption of halogens on metal surfaces still remains poorly understood. It seems important to carry out a systematic study of halogen-metal interaction in particular at low temperature for which data are lacking. Such studies can provide us with completely new information about halogen layer structure at different surface coverage. This can be of particular relevance for the heterogeneous catalysis when a noble metal like silver is used as catalyst. One has in mind for instance the important process of ethylene epoxydation.

The objective of the theses is to study from low temperatures STM (5K to 120 K) and LEED investigations, the structural (and electronic properties) of the interfaces formed by halogen adsorption on (111) surfaces of silver, gold and copper at different surface coverage (from sub monolayer up to saturated layer coverage).

Bibliography of Chapter 1

[1] R.G. Jones. Halogen adsorption on solid surfaces // Progr. Surf. Sci. 27 25 (1988).

[2] E.I. Altman. Halogens on metals and semiconductors // Landolt-Börnstein New Series, v. III/42A1, p. 421 (2000).

[3] K. Itaya. In situ scanning tunneling microscopy in electrolyte solutions // Progr. Surf. Sci. 58 121 (1998).

[4] O.M. Magnussen. Ordered Anion Adlayers on Metal Electrode Surfaces // Chem. Rev. 102 679 (2002).

[5] W.K. Walter, D.E. Manolopoulos, R.G. Jones. Chlorine adsorption and diffusion on Cu(111) // Surf. Sci. 348 115 (1996).

[6] D.E. Taylor et al. Two-dimensional ordering of chlorine on Ag(100) // Phys. Rev. B 32 4653 (1985).

[7] G.N. Kastanas, D.E. Koel. Interaction of Cl_2 with the Au(111) surface in the temperature range of 120 to 1000 K // Appl. Surf. Sci. 64 235 (1993).

[8] A.L. Linsebigler et al. Interaction of Cl_2 with Fe(110) in the temperature range 90-1050 K // Journ. of Am. Chem. Soc. 114 465 (1992).

[9] P.A. Dowben et al. Molecular bromine adsorption and dissociation on iron and nickel surfaces // Surf. Sci. 155 567 (1985).

[10] C. Benndorf, B. Kruger. Adsorption and reaction of bromine with Ag(110) // Surf. Sci. 151 271 (1985).

[11] R.G. Jones, C.F. Mcconville, D.P. Woodruff. The formation of surface iodide on Ni(100) and adsorption of I2 at low temperatures // Surf. Sci. 127 424 (1983).

[12] D. Mueller, T.N. Rhodin. Molecular iodine adsorption on Fe(100), Fe(110) and iron iodide // Surf. Sci. 164 271 (1985).

[13] H. Xu, I. Harrison. Dissociative adsorption of Br_2 on Pt(111): hot atom dynamics // Journ. of Phys. Chem. B 103 11233 (1999).

[14] H. Ibach. The role of surface stress in reconstruction, epitaxial growth and stabilization of mesoscopic structures // Surf. Sci. Rep. 29 193 (1997).

[15] A.G. Shard, V.R. Dhanak. Chlorine adsorption on silver (111) at low temperatures // Journ. of Phys. Chem. 104 2743 (2000).

[16] B.V. Andryushechkin et al. Direct STM observation of surface modification and growth of AgCl islands on Ag(111) upon chlorination at room temperature // Surf. Sci. 431 96 (1999).

[17] B.V. Andryushechkin, K.N. Eltsov, V.M. Shevlyuga. Halide nucleation and growth on monocrystalline copper surface // Phys. of Low-Dim. Struct. 3/4 1 (2003).

[18] B.V. Andryushechkin, K.N. Eltsov, V.V. Cherkez. Epitaxial growth of semiconductor thin films on metals in the halogenation process. Atomic structure of copper iodide on the Cu(110) surface // JETP Letters 83 195 (2006).

[19] B.V. Andryushechkin et al. Local structure of the Ag(100) surface reacting with molecular iodine: experimental and theoretical study // Phys. Rev. B 80 125409 (2009).

[20] A.F. Wells Structural inorganic chemistry // Oxford University Press, v. 2, 5th. ed. (1984).

[21] A. Migani, F. Illas. A systematic study of the structure and bonding of halogens on low-index transition metal surfaces // Journ. of Phys. Chem. B 110 11894 (2006).

[22] C.W. Bauschlicher. p(2×2) and c(2×2) covarages of Cl and F on Ni(100), a comparison with O and S on Ni(100) // Chem. Phys. Lett. 118 395 (1985).

[23] B. Lairson, T.N. Rhodin, W. Ho. Adsorbate fluorescence EXAFS: determination of brominebonding structure in c(2×2)Br-Ni(001) // Solid State Communications 55 925 (1985).

[24] R.G. Jones et al. A SEXAFS study of several surface phases of iodine adsorption on Ni(100) // Surf. Sci. 179 425 (1987).

[25] P.H. Citrin et al. Geometry and electronic structure of Cl on the Cu(001) surface // Phys. Rev. Lett. 49 1712 (1982).

[26] S.D. Kenny, J.B Pethica, R.G. Edgell. A density functional study of Br on Cu(100) at low coverages // Surf. Sci. 524 141 (2003).

[27] P.H. Citrin, P. Eisenberger, R.C. Hewitt. Adsorption sites and bond lengths of iodine on Cu(111) and Cu(100) from Surface Extended X-Ray-Adsorption Fine Structure // Phys. Rev. Lett. 45 1948 (1980).

[28] G.M. Lamble et al. Structure of the c(2×2) coverage of Cl on Ag(100): a controversy resolved by surface extended x-ray-adsorption fine-structure spectroscopy // Phys. Rev. B 36 1796 (1987).

[29] S. Wang, P.A. Rikvold. Ab initio calculations for bromine adlayers on the Ag(100) and Au(100) surfaces: the c(2×2) structure // Phys. Rev. B 65 155406 (2002).

[30] M.F. Kadodwala et al. Structural determination of the Cu(111)-(√3×√3)R30°-Cl/Br surface using the normal incidence X-ray standing wave method // Surf. Sci. 324 122 (1995).

[31] G.M. Lamble et al. Surface structural determination for a weekly ordered and a disordered phase of Cl on Ag(111) // Phys. Rev. B 34 2975 (1986).

[32] P.H. Citrin, P. Eisenberger, R.C. Hewitt. Extended X-ray absorption fine structure of surface atoms on single-crystal substrates: iodine adsorbed on Ag(111). Phys. Rev. Lett. 41 309 (1978).

[33] Cynthia M. Friend et al. Chlorine adsorption on Au(111): chlorine overlayer or surface chloride? // Journ. of Am. Chem. Soc. 130 3560 (2008).

[34] L.-Q. Wang et al. Surface structure of (√3×√3)R30° Cl/Ni(111) determined using low-temperature angle-resolved photoemission extended fine structure // Phys. Rev. B 44 13711 (1991).

[35] V.R. Dhanak et al. The structure of (√3×√3)R30° iodine on Pd(111) surface studied by normal incidence X-ray standing wavefield absorption // Chem. Phys. Lett. 306 341 (1999).

[36] M.D. Crapper et al. Complete adsorption site information for Cl on Cu(111) using X-ray absorption fine structure and photoelectron diffraction // EPL 2 857 (1986).

[37] M.D. Crapper et al. Investigation of the Cu(111) (√3×√3)R30°-Cl structure using SEXAFS and photoelectron diffraction // Surf. Sci. 182 213 (1987).

[38] A. Tkatchenko et al. Charge transfer and adsorption energies in the iodine–Pt(111) interaction // Surf. Sci. 581 58 (2005).

[39] E.V. Hladchanka // unpublished results.

[40] E. Dona et al. Halogen-induced corrosion of platinum // Journ. of Am. Chem. Soc. 131 2827 (2009).

[41] V. Blum et al. Structure of the c(2×2)-Br/Pt(110) surface // Phys. Rev. B 65 165408 (2002).

[42] H. Fu et al. The first-principle study on chlorine-modified silver surfaces // Surf. Sci. 584 187 (2005).

[43] Y. Wang et al. Interaction of halogen atom with Ag(110): ab initio pseudopotential density functional study // Chem. Phys. Lett. 334 411 (2001).

[44] L. Houssiau, J.W. Rabalais. Scattering and recoiling imaging spectrometry (SARIS) study of chlorine chemisorption on Ni(110) // Nuclear Instruments and Methods in Physics Research B 157 274 (1999).

[45] J. Zhang, Z.-Y. Diao, Z.-X. Wang. Adsorption and vibrtion of Cl atoms on Ni low-index surfaces // Chemical Research in Chinese Universities 22 488 (2006).

[46] Y. Wang et al. The first-principle study of the iodine modified silver surfaces // Surf. Sci. 487 77 (2001).

[47] K. Doll, N.M. Harrison. Chlorine adsorption on the Cu(111) surface // Chem. Phys. Lett. 317 282 (2000).

[48] K. Doll, N.M. Harrison. Theoretical study of chlorine adsorption on the Ag(111) surface // Phys. Rev. B 63 165410 (2001).

[49] D.P. Woodruff. Geometrical and electronic structure of multiple surface phases: iodine on Ni(100) // Applications of Surface Science 22/23 459 (1985).

[50] K.K. Kleinherbers, E. Janssen, A. Goldmann. Submonolayer adsorption of halogens on Ag(001) and Ag(011) studied by photoemission // Surf. Sci. 215 394 (1989).

[51] K.K. Kleinherbers, A. Goldmann. Adsorbate bands of Cu(111)($\sqrt{3}\times\sqrt{3}$)R30°-Cl: an angle-resolved photoemission study // Surf. Sci. 154 489 (1985).

[52] S.B. Dicenzo, G.K. Wertheim, D.N. Buchanan. XPS studies of adatom-adatom interactions: I/Ag(111) and I/Cu(111) // Surf. Sci. 121 411 (1982).

[53] C.Y. Nakakura, E.I. Altman. Scanning tunneling microscopy study of the reaction of Br_2 with Cu(100) // Surf. Sci. 398 281 (1998).

[54] C.Y. Nakakura, G. Zheng, E.I. Altman. Atomic-scale mechanisms of the halogenation of Cu(100) // Surf. Sci. 401 173 (1998).

[55] S.U. Nanayakkara et al. Long-range electronic interactions at a high temperature: bromine adatom islands on Cu(111) // Phys. Rev. Lett. 98 206108 (2007).

[56] K. Binder, D.P. Landau. Square lattice gases with two- and three-body interactions: a model for the adsorption of hydrogen on Pd(100) // Surf. Sci. 108 503 (1981).

[57] H. Brune. Microscopic view of epitaxial metal growth: nucleation and aggregation // Surf. Sci. Rep. 31 121 (1998).

[58] U. Bardi, G. Rovida. LEED, AES and thermal desorption study of iodine chemisorption on the silver (100), (111) and (110) faces // Surf. Sci. 128 145 (1983).

[59] L. Huang et al. Determination of iodine adlayer structures on Au(111) by scanning tunneling microscopy // Journ. of Chem. Phys. 107 585 (1997).

[60] R.W.G. Wyckoff. Crystal Structures. Interscience // John Wiley & Sons v. 1 (1963).

[61] M. Kiskinova,D.W. Goodman. Modification of chemisorbed properties by electronegative adatoms: H_2 and CO on chlorided, sulfided, and phosphided Ni(100) // Surf. Sci. 108 64 (1981).

[62] W. Erley, H. Wagner. Chlorine adsorption on Ni(111) // Surf. Sci. 66 371 (1977).

[63] R.G. Jones, D.P. Woodruff. The adsorption of I_2 on Ni(100) studied by AES, LEED and thermal desorption // Vacuum 31 411 (1981).

[64] B.V. Andryushechkin et al. Structural transitions of chemisorbed iodine on Cu(100) // Surf. Sci. 497 59 (2002).

[65] A.G. Naumovets, A.G. Lyuksyutov, V. Pokrovsy. Two-dimensional crystals // Academic Press (1992).

[66] T. Kontorova, Y.I. Frenkel // Zh. Eksp. Teor. Fiz.v. 8, p. 89, 1340, 1349 (1938).

[67] F.C. Frank, J.H. Van Der Merwe. One-dimensional dislocations // Proceedings of Royal Society, London, v. 198, p. 205 (1949).

[68] D.J. Holmes, N. Panagiotides, D.A. King. Observation of a low temperature incommensurate Ag(111)(√3×√3)R30°-Br phase // Surf. Sci. 222 285 (1989).

[69] P.J. Goddard, R.M. Lambert. Adsorption-desorption properties and surface structural chemistry of chlorine on Cu(111) and Ag(111) // Surf. Sci. 67 180 (1978).

[70] O. Endo, H. Kondoh, T. Ohta. Scanning tunneling microscope study of bromine adsorbed on the Ag(111) surface // Surf. Sci. 441 L924 (1999).

[71] L.J. Clarke. Surface crystallography: an introduction to low energy electron diffraction // A Wiley-Interscience Publication (1985).

[72] P. Zeppenfeld et al. Diffraction from domain-wall system // Phys. Rev. B 38 3918 (1988).

[73] B.V. Andryushechkin, K.N. Eltsov, V.M. Shevlyuga. Atomic scale observation of iodine layer compression on Cu(111) // Surf. Sci. 472 80 (2001).

[74] B.V. Andryushechkin, V.M. Shevlyuga, K.N. Eltsov. Domain-wall mechanism of "(n√3×n√3)R30°" incommensurate structure formation in chemisorbed halogen layers on Cu(111) // Surf. Sci. 470 L63 (2000).

[75] D.J. Holmes et al. Discrimination between domain-wall and uniformly incommensurate structures by surface extended X-ray absorption fine-structure - adsorption of chlorine on Ag(110) // Journ. of Vac. Sci. & Tech. A 5 703 (1987).

[76] D.R. Batchelor et al. Fluoriscence SEXAFS study of the bromine of the silver (110) surface // Physica B 158 655 (1989).

[77] B.V. Andryushechkin, K.N. Eltsov, V.M. Shevlyuga. Atomic structure of chemisorbed iodine layer on Cu(110) // Surf. Sci. 584 278 (2005).

[78] C. Deisl et al. The phase diagram of halogens on Pt(110): structure of the (4×1)-Br/Pt(110) phase // Journ. of Phys.: Cond. Matt. 134003 (2009).

[79] T.W. Fishlock, J.B. Pethica, R.G. Egdell. Observation of a nanoscale chessboard superstructure in the Br–Cu(100) adsorbate system // Surf. Sci. 445 L47 (2000).

[80] A.T. Wee et al. Bromine etching of mesoscopic structures on Cu(210): a scanning tunneling microscopy study // Chem. Phys. Lett. 298 146 (1998).

[81] T.W. Fishlock et al. Interaction of chlorine with nickel (110) studied by scanning tunnelling microscopy // Surf. Sci. 377 629 (1997).

[82] T.W. Fishlock et al. Interaction of bromine with Ni(110) studied by scanning tunnelling microscopy // Surf. Sci. 426 212 (1999).

[83] H. Iwai et al. Chlorine-induced de-reconstruction on Au(001) and Cl-adsorbed layers // Journ. of Phys.: Cond. Matt. 7 5163 (1995).

[84] E. Bertel, F.P. Netzer. Adsorption of bromine on the reconstructered Au(100) surface: LEED, thermal desorption and work function measurements // Surf. Sci. 97 409 (1980).

[85] J. Valenzuela-Benavides, M. Herrera-Zaldivar. Structural transitions of chemisorbed iodine on Au(100): A STM and LEED study // Surf. Sci. 592 150 (2005).

[86] H. Gutleben, E. Bechtold. Adsorption of chlorine on Pt(100) face: structural aspects and desorption kinetics // Surf. Sci. 236 313 (1990).

[87] R. Schennach, E. Bechtold. Chlorine adsorption on Pt(111) and Pt(110) // Surf. Sci. 380 9 (1997).

[88] K. Swamy et al. Halogen–metal interaction: bromine on Pt(110) // Surf. Sci. 466 11 (2000).

[89] S.A. Cochran, H.H. Farrell. The chemisorption of iodine on gold // Surf. Sci. 95 359 (1980).

[90] G. Rovida et al. LEED study of chlorine chemisorption on the silver (111) surface // Japanese Journal of Applied Physics, v. 2, n. 2, p. 117 (1974).

[91] M. Bowker, K.C. Waugh. The adsorption of chlorine and chloridation of Ag(111) // Surf. Sci. 134 639 (1983).

[92] G. Rovida, F. Pratesi. Chlorine monolayers on the low-index faces of silver // Surf. Sci. 51 280 (1975).

[93] Y.Y. Tu, G.M. Blakely. Chlorine adsorption on silver surfaces // Journ. of Vac. Sci. and Tech. 15 563 (1978).

[94] K. Wu, D. Wang, J. Deng. Chlorine on Ag(111): intermediate coverage case // Surf. Sci. 264 249 (1992).

[95] B.V. Andryushechkin et al. Atomic structure of saturated chlorine monolayer on Ag(111) surface // Surf. Sci. 407 L633 (1998).

[96] N.H. De Leeuw et al. Density-functional the-ory calculations of the adsorption of Cl at perfect and defective Ag(111) surfaces // Phys. Rev. B 69 045419 (2004).

[97] A. Roland et al. The chemistry of chlorine on Ag(111) over the sub-monolayer range: a density functional theory investigation // Surf. Sci. 602 2639 (2008).

[98] P. Gava et al. Adsorption of chlorine on Ag(111): no subsurface Cl at low coverage // Phys. Rev. B 78 165419 (2008).

[99] N.D. Spencer, R.M. Lambert. Chlorine chemisorption and surface chloride formation on Au(111) // Surf. Sci. 107 237 (1981).

[100] T.A. Baker, C.M. Friend, E. Kaxiras. Effects of chlorine and oxygen coverage on the structure of the Au(111) surface // Journ. of Chem. Phys. 130 084701 (2009).

[101] K. Kishi, S. Ikeda. X-Ray Photoelectron Spectroscopic Study of the Reaction of Evaporated Metal Films with Chlorine Gas // Journ. of Phys. Chem. 78 107 (1974).

[102] K. Motai et al. STM of the Cu(111) 1×1 surface and its exposure to chlorine and sulfur // Appl. Surf. Sci. 67 246 (1993).

[103] S. Peljhan, A. Kokalj. Adsorption of chlorine on Cu(111): a density-functional theory study // Journ. of Phys. Chem. C 113 14363 (2009).

[104] A. Bondi. van der Waals volumes and radii // Journ. of Phys. Chem. 68 441 (1964).

[105] R.S. Rowland, R. Taylor. Intermolecular nonbonded contact distances in organic crystal structures: comparison with distances expected from van der Waals radii // Journ. of Phys. Chem. 100 7384 (1996).

[106] B. Cordero et al. Covalent radii revisited // Dalton Transactions 2832 (2008).

[107] R.D. Shannon. Revised effective ionic radii and systematic studies of interatomic distances in halides and chalcogenides // Acta Crystallographica A 32 751 (1976).

CHAPTER 2.
Experimental and theoretical methods used in present study

In this chapter we briefly discuss experimental and theoretical methods used in the present work. First we introduce general concepts in the study of halogen adsorption on metals. Then the experimental set-up is presented. Special attention is given to describe the design and technical details of halogen inlet system. Description of experimental procedure, preparation of the samples and chlorine adsorption is given. The rest of the chapter is concerned to the description of two main experimental techniques used: low energy electron diffraction, scanning tunneling microscopy and spectroscopy. Among other we present explication of particular diffraction patterns observed in halogen/metal systems. In the end of the chapter basics of density functional theory are introduced. Particular parameters used for density functional theory calculations of chlorine/metals systems are specified.

2.1 Introduction

From experimental point of view the first priority task in study of halogen adsorption on metals is preparation of atomically clean metal surface, controlled adsorption of halogen on it and maintenance of prepared system out of contaminations during all the measurements. That's why all experiments are carried out in ultra-high vacuum conditions with residual pressure $10^{-10} \div 10^{-12}$ Torr inside chambers. Single crystal samples with the surface cut parallel to specified crystallographic plane are used. Chemically pure gaseous Cl_2 (99.5%) is adsorbed on the surface directly in the UHV chamber. Such approach allows us to control the surface cleanness and amount of adsorbed halogen on the atomic level. Once prepared chlorine layer can be kept inside the experimental setup clean for up to several days, which is well enough for all measurements. This ensures that all results obtained are reliable and fully reproducible.

For surface study we used the following experimental techniques:

1. scanning tunneling microscopy in the temperature range 5-80 K that gave us information about surface structure at atomic scale in direct space;
2. low-energy electron diffraction that gave us information about the symmetry and periodicity of surface structures in reciprocal space;
3. surface electron properties were probed with scanning tunneling spectroscopy.

Structural models based on the experimental data were tested with DFT calculations. That ensures reliable definition of surface atomic structure.

A brief review of experimental and theoretical methods used in the thesis will be given in this chapter together with description of experimental setup, preparation of clean metal surfaces and halogen adsorption procedure.

2.2 Experimental setup

A schematic representation of experimental setup is shown on Figure 2.1. The setup consists of three large chambers (marked as *A*, *B* and *C*). A low-temperature STM (LT Omicron) is placed in chamber *A*. It can operate at temperatures 5-40 K, 55 K, 78 K, as well as at 300 K and can be used for topographic or spectroscopic measurements. Surface preparation chamber *B* is equipped a with 5 axis manipulator (*2)* with heating and cooling down options (47-1200 K). A thorium oxide coated iridium filament is placed on the back-side of the grounded sample holder and polarized to -600 V for heating the sample by electron beam. During heating of our samples the pressure inside the chamber never exceeded 10^{-9} mbar (mainly due to H_2 partial pressure). Cooling is achieved by pumping liquid nitrogen or helium through a small vessel, which is connected to a copper made sample holder. Besides it chamber *B* contains ion gun (Leybold IQE 12/38), mass-spectrometer (Balzers QMA-200), and either auger-electron spectrometer (CMA Riber OPC-105), or a low-energy electron diffraction optics (SPECTALEED Omicron). LEED unit can be placed in a small intermediate chamber *F* when AES unit is installed in chamber *B*. A high-resolution hemispherical photoelectron spectrometer (Scienta SES 200) is placed in chamber *C*, together with the ultraviolet (Specs UVS 300) and X-ray

(Specs XR 50) sources. Chlorine adsorption was done in the intermediate chamber *D*. Samples and STM tips can be uploaded into setup via a load-lock-chamber *E*. Ion (chamber *A*, *C* and *D*) or turbomolecular (chamber *B*) pumps supplied with titanium sublimation pumps are used in the setup. Residual pressure in the chambers is $10^{-10} \div 10^{-12}$Torr. The setup is equipped with linear manipulators (*1)* for sample transfer between the chambers.

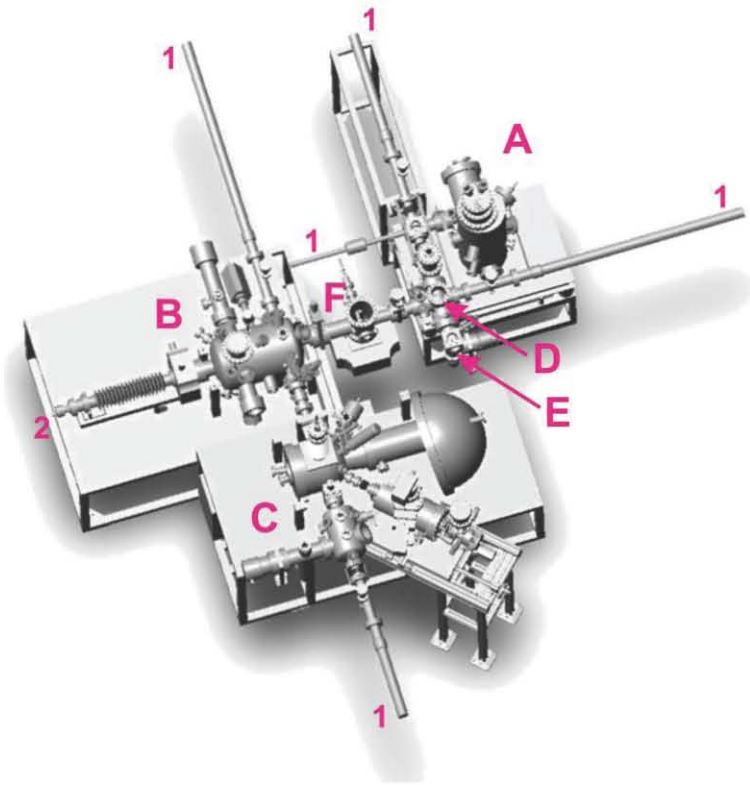

Figure 2.1. *Schematic overview of the UHV experimental setup: (**A**) LT STM chamber, (**B**) sample preparation chamber, (**C**) photo-electron spectroscopy chamber, (**D**) chlorine adsorption chamber, (**E**) lock-chamber, (**F**) LEED chamber, (1) 2 axis linear manipulator, (2) 5 axis manipulator.*

Chlorine inlet system

Basic information on technical aspects of halogen inlet into UHV can be found in the review of Jones [1].

In our setup chlorine is introduced inside the UHV chamber through a special roughing-down line (Fig. 2.2). It consists of Cl_2 pressure tank (99.5%, 5 bar), a cryo-sorption pump and pressure gauge (pirani gauge) to control chlorine pressure, connected by stainless-steel tube of 4 mm diameter. The total length of the line is about 3 meters. All the gaskets in the line are made from Teflon to avoid their corrosion due to contact with chlorine. The base pressure in the line pumped by cryo-pump is about 10^{-2} Torr. The roughing-down line is connected to UHV chamber through a piezoelectric valve *d* which is operated by a high voltage power supply. The principle of piezoelectric valve operation is essentially the same as for ordinary variable leak valve, where the fine drive screw for leak regulation is replaced by a stack of piezo-plates. To our experience the most convenient and stable material towards corrosion for gasket in piezo-valve is aluminum. Therefore

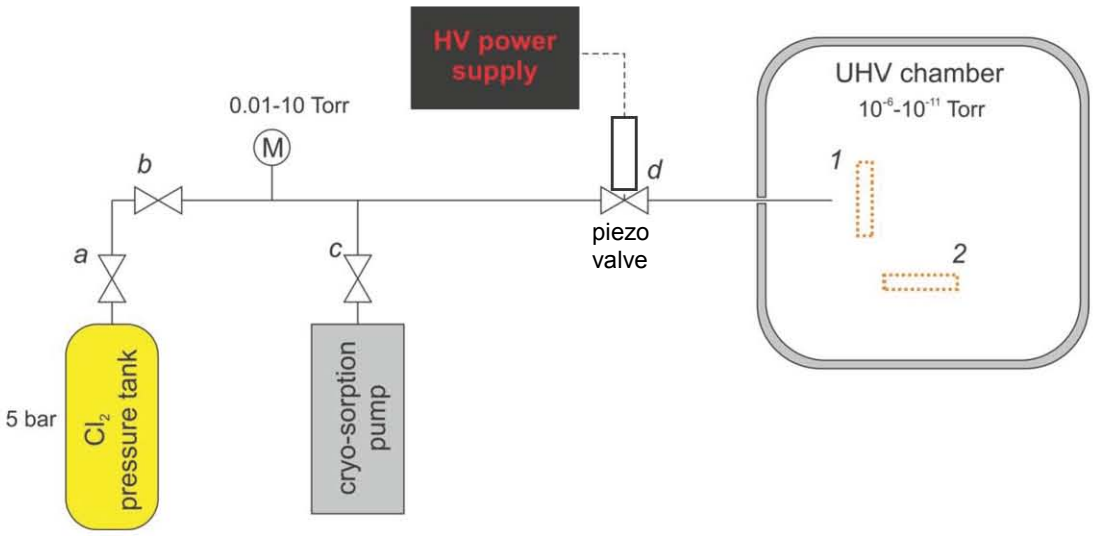

Figure 2.2. *Schematic representation of chlorine inlet system. The sample position (1) and (2) in UHV chamber correspond to the different way used for chlorination (see text)*

special gasket made from pure aluminum has been designed and placed inside the valve instead of the standard copper one. Applying the high voltage to the piezo stack one can regulate the opening of the valve and the inlet of chlorine with precision up to 1×10^{-11} Torr. At the same time the total chlorine pressure inside UHV chamber can be changed in the range $10^{-11}\div10^{-6}$ Torr. The main advantage of piezo-valve is the possibility to get reproducible leak by simply applying the same high voltage. The speed of opening and closing the valve is also rather fast. These allow one to precisely control the exposition of gas. The high voltage power supply in turns can be operated by computer or can be feedback with, for example, mass-spectrometer for high-accuracy dosage of halogen.

Special safety care must be taken for chlorine high-pressure tank. As chlorine is a high-toxic substance the high pressure tank must be placed inside a closed and permanently ventilated draft hood with the exit outside the lab-room.

Before the use the roughing-down line must be baked-out (100-150°C for about 12 hours). Before each session of adsorption the line is rinsed by chlorine (filled and then pumped) in order to remove residual water since Cl_2 forms with it HCl acid which is efficiently pumped by cryo-sorption pump. The chlorine pressure tank used in the setup was not supplied by expander. Instead it was separated from the rest of roughing-down line by two successive valves – marked as *a* and *b* on Fig. 2.2. Chlorine was first introduced into the short part of the tube between these two valves by opening valve *a*. The valve *a* on the chlorine tank was then closed and the second valve *b* opened, letting chlorine in the rest of the roughing-down line. Thus we got chlorine pressure inside the line about 20 Torr. The exact pressure depends on the relative value of the inter valve part and the whole volume of the roughing-down line.

Chlorine adsorption can be done in two ways: directly on the view of the sample surface from the stainless-steel tube (4 mm in diameter) placed in vacuum behind the inlet valve (position *1* on Fig. 2.2), or from the volume of the chamber (position *2* on Fig. 2.2). In former case the sample is placed in front of the tube at the distance of 15-20 mm and chlorine is adsorbed from the Cl_2-beam that hits the surface. For chlorine adsorption from volume the sample surface was turned away from the tube while leaving the inlet valve

opened. In case of direct adsorption in front of the tube, the chlorine Cl_2 beam is "focused" and the pressure on the sample surface is 100÷500 times larger than the Cl_2 partial pressure in the chamber (and hence, the chlorine pressure on the sample surface in the case of adsorption from volume). The structure of chlorine monolayer does not depend on the way of adsorption. The amount of adsorbed halogen can be controlled both by changing chlorine pressure in the chamber or the time of adsorption. The relative accuracy in chlorine dosage can be better than 1%.

2.3 Preparation of clean metal surfaces

In the present study we used single-crystal samples of silver Ag(111), gold Au(111) and copper Cu(111) provided by Surface Preparation Laboratory [2] with a surface miscut lower than 0.1°. For surface preparation multiple cycles of ion bombardment (Ar^+, E_{ion} = 1 keV, time = 5 to 15 min) followed by subsequent annealing (T_{anneal} = 800 K for Ag and Au) and T_{anneal} = 900 K for Cu, time = 1 to 10 min) were used. Duration of ion bombardment was selected depending on the amount of surface contaminations or thickness of adsorbate layer. We also have systematically chosen a normal incident Ar+ beam in order to minimize sputter-induced damage of the surface. The surface structure defects that appear after ion bombardment were removed by annealing the sample. Low-temperature STM was used for control of surface structure and cleanness. After chlorination the adsorbed chlorine layer (chemisorbed monolayer or chloride film) can be easily removed by heating of the sample up to 700-900 K.

2.4 Low-energy electron diffraction

Low-energy electron diffraction is an effective experimental method for analysis of surface symmetry and periodicity, and even surface structure in certain cases [3, 4].

Conditions for elastic electron diffraction on the 2D surface lattice and constructive interference can be written as following:

$$\boldsymbol{k}_{//} - \boldsymbol{k}_{//}' = n \cdot \boldsymbol{G}_{hk} \tag{2.1}$$

$$|\boldsymbol{k}| = |\boldsymbol{k}'| \tag{2.2}$$

where $\boldsymbol{k}_{//}$ and $\boldsymbol{k}_{//}'$ are the in-plane momentum components of incident and diffracted electron waves, respectively, $\boldsymbol{G}_{hk}$ is a reciprocal surface lattice vector. The first equation can be written using the Miller indexes h and k of the surface reciprocal vector $\boldsymbol{G}_{hk}$:

$$\boldsymbol{k}_{//} - \boldsymbol{k}_{//}' = h\boldsymbol{a}^* + k\boldsymbol{b}^* \tag{2.3}$$

a*, **b*** are the translation vectors of surface reciprocal lattice.

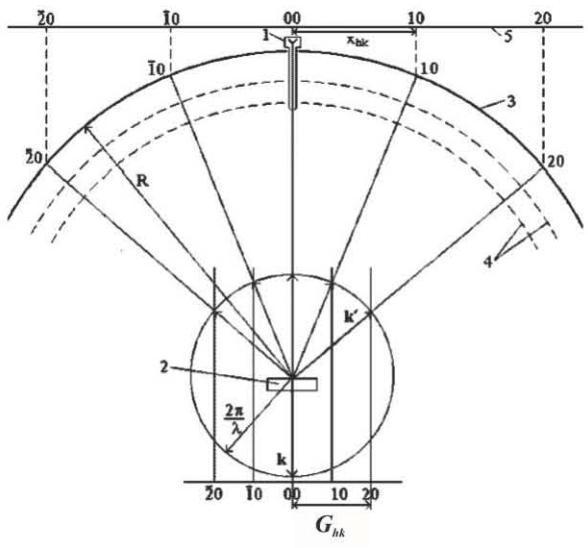

Figure 2.3. *Schematic overview of LEED unit and Ewald construction for electron diffraction on the surface lattice: 1) electron gun; 2) sample; 3) hemispherical fluorescent screen centered on the surface of the sample where electrons from the gun 1 hit the surface 2; 4) a set of grids to pick out elastically scattered electrons before they hit fluorescent screen 3; 5) the plane of view.*

Miller indexes *h* and *k* are used to identify corresponding diffraction maxima. For example, the mirror reflection beam is identified as (00). In the case of LEED experiments the Ewald construction is simplified (see Fig 2.3) as the incident beam is usually taken normal to the sample surface (hence $k_{//} = 0$)

The possibility of use LEED method for surface science study is related to the fact that typical periodicity of surface structures is 2÷50 Å and electrons with de Broglie wavelength of 1÷2 Å (i.e. kinetic energy 30÷200 eV) can be used for probing such distances. The mean free path of electrons with such energy is less than few atomic layers so the main contribution to diffraction pattern is due to the scattered near the surface.

Analysis of diffraction spots positions gives information about periodicity and symmetry of surface structure. The use of electron diffraction for surface structure determination is not as straightforward as for X ray diffraction on 3D structures (crystals) because of the periodicity breaking in the direction perpendicular to the surface and nature of electron interaction with atoms. Absence of periodicity in the third direction makes it impossible to definitely resolve the inverse diffraction problem – crystal structure determination from LEED spots position. This ambiguity can be partially solved by spots intensity analysis, which gives information about atomic arrangement inside the unit cell of the surface structure. For such analysis dependence of diffraction spots intensity on the incident electrons energy has to be taken. Similar intensity profile can be calculated for suggested structural model and then compared to experimental one. However this approach is not self-sufficient. Usually it needs additional structural information from other experimental methods.

Splitting of diffraction spots

In some cases diffraction spots on the LEED pattern are observed to be split. Such splitting is usually observed for unusual surface structures like incommensurate or compressed adsorbed layers, antiphase domains or islands, clean vicinal or reconstructed surfaces. In particular spot splitting is observed in most of halogen/metal systems when the coverage exceeds the level of commensurate structure [5].

There are two possible explanations of the splitting origin depending on the situation [3]. The first one is related to the effect of multiple diffraction process. In reality electron beam impinging the crystal surface is scattered not only by the adsorbate layer, but also by multiple substrate layers beneath. The multiple diffraction on the substrate planes will affect only the relative intensities of diffracted beams, but not their direction (position of spots on the luminescent screen), since all substrate planes have the same spatial periodicity. Thus it is sufficient to consider only two layers – adsorbate layer and the last atomic plane of the substrate. Constructive interference for electrons diffracted on such double layer can be expressed in the form

$$\boldsymbol{k}_{//} - \boldsymbol{k}_{//}' = n \cdot \boldsymbol{G}_{hk} + m \cdot \boldsymbol{g}_{hk} \tag{2.4}$$

where $\boldsymbol{G}_{hk}$ is the substrate and $\boldsymbol{g}_{hk}$ adsorbate layer reciprocal lattice vectors. If adsorbate forms commensurate lattice reciprocal vector $\boldsymbol{g}_{hk}$ is related to substrate vector $\boldsymbol{G}_{hk}$. Corresponding diffraction pattern will contain integer-order spots of the substrate and integer and half-order spots of the adsorbate layer. Position of the diffraction spots will be the same as for simple electron diffraction on adsorbate layer and given by the condition $\Delta\boldsymbol{k} = m \cdot \boldsymbol{g}_{hk}$ (though their relative intensities may change). A one-dimensional example is given on the Figure 2.4. For this simple case with a lattice constant a for the adsorbate layer having double periodicity ($a = 2b$) with respect to the substrate, the diffraction pattern simply consists of spots separated by the adsorbate reciprocal vector $a^* = 2\pi/a$.

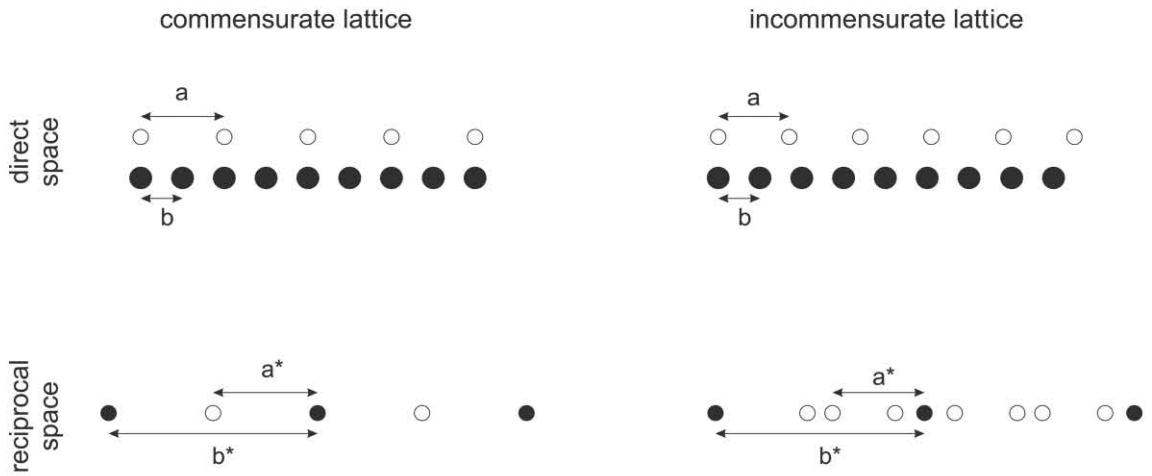

Figure 2.4. *Double-diffraction model for commensurate and incommensurate overlayers diffraction. Black and white circles show substrate and overlayer atoms, respectively, in direct space and diffraction spots coming from adsorbate layer or substrate in reciprocal space, respectively*

Let now imagine the adsorbate layer slightly compressed with periodicity decreased with respect to substrate (or adsorbate lattice has been rotated relative to the substrate). It became incommensurate to the substrate lattice and their reciprocal vectors a no more related. According to condition (4) diffraction spots will appear not only for $\Delta\boldsymbol{k} = m \cdot \boldsymbol{g}_{hk}$ but also for any linear combination of adsorbate and substrate lattice reciprocal vectors. This will give rise to characteristic spots placed around the position of commensurate lattice that looks like splitting of diffraction spots diffraction pattern. A one-dimensional example is shown on Figure 2.4. One can see that half-order spots have split into two spots. The

distance between them (splitting) is equal to *b*-2a**. The half-order spots have completely disappeared since there is no more periodicity *a = 2b* in our system. On contrary satellites appeared on each side of the integer order spots, though theses spots still are present in the diffraction pattern as the substrate periodicity has not changed.

Other considerations should be applied for explanation of the diffraction spot splitting on LEED patterns in the case of the systems made from of anti-phase domains or islands on the surface, or for vicinal surfaces [3]. In all these cases the origin of splitting is related to the phase shift between atomic arrangement in adjacent regions - domains, islands or terraces having the same surface lattice. We will consider in detail the case of anti-phase domains or islands. In kinematic approach the scattered intensity can be represented as a product of scattering factor *F* that represents the intensity scattered by a single domain and interference function *J* that represents the intensity scattered by an array of points corresponding to the whole superstructure:

$$\mathrm{I}(\Delta\mathrm{k}) = F \cdot J \tag{2.5}$$

Both functions can be expressed explicitly as:

$$F = \frac{\sin^2\left(\frac{1}{2}Na \cdot \Delta k\right)}{\sin^2\left(\frac{1}{2}a \cdot \Delta k\right)} \quad \text{and} \quad J = \frac{\sin^2\left(\frac{1}{2}Mb \cdot \Delta k\right)}{\sin^2\left(\frac{1}{2}b \cdot \Delta k\right)} \tag{2.6, 2.7}$$

Here *a* is the lattice constant inside the domain, N is number of unit cells in one domain, similarly *b* is the periodicity of the superstructure and M is number of domains covered by electrons coherence length. Figure 2.5 shows the one-dimensional example of scattered intensity function I(Δk). The scattering factor F shows maxima with periodicity given by atomic arrangement inside domains. Due to the small size of the domains (N = 5), corresponding peaks are rather broad. In contrast, the interference function *J* has much larger periodicity (and, hence, smaller periodicity in reciprocal space) and relatively narrow width of the peaks. In the case of coherent domains, F and *J* are in phase and we observe sharp spots with periodicity *a* given by the atomic arrangement inside domain. Thus the effect of boundaries between coherent domains compared to infinitely large domains is simply broadening of the diffraction spots. The same considerations are valid for coherent islands. In the case of anti-phase domains the interference function *J* appears to be out of phase relative to the scattering factor F so their product instead of single peaks shows spot splitting around position given by scattering factor F. In the case of large M (relatively large coherence length) the distance between split spots corresponds to the periodicity *b* of whole superstructure. Thus existence of some out-phasing between neighboring domains leads to the splitting of diffraction spots.

For two-dimensional lattice the phase shift between neighboring domains can be calculated explicitly as:

$$\Delta\varphi = \Delta k \cdot g = 2\pi(hl_1 + kl_2) \tag{2.8}$$

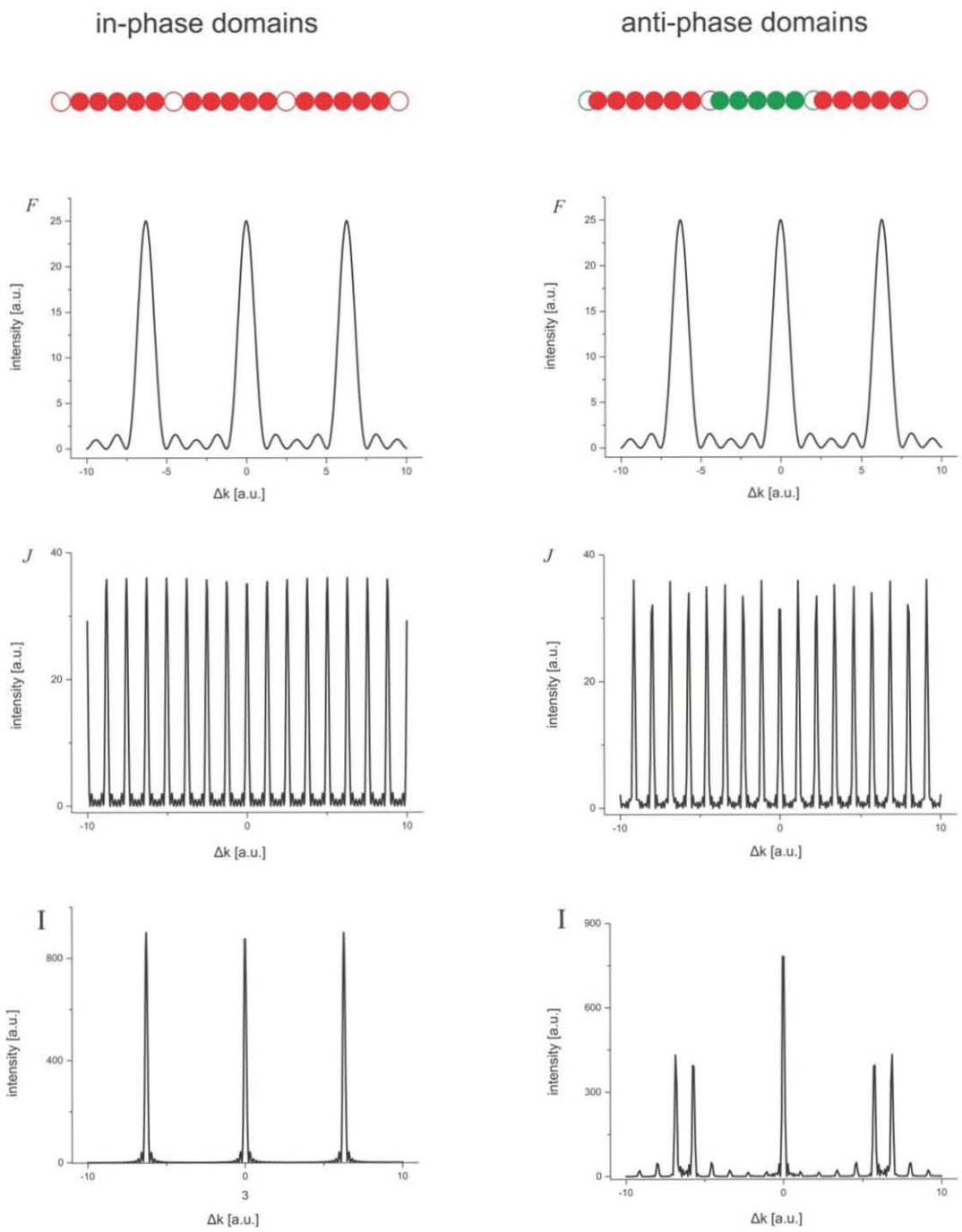

Figure 2.5. *Numerical simulation of scattering factor F, interference function J and their product intensity I as a functions of scattering vector Δk. Periodicity of atomic arrangement inside domains a = 1 u.e., number of atoms in domain N = 5, superstructure periodicity: in-phase domains b = 6; anti-phase domains b = 5.5. Coherent length M = 6*

where $\Delta\boldsymbol{k} = h\boldsymbol{a_1}^* + k\boldsymbol{a_2}^*$ is the scattering vector and $\mathbf{g} = l_1\mathbf{a_1} + l_2\mathbf{a_2}$ represents the vector connecting two equivalent atoms in neighboring anti-phase domains. The domains scatter in phase if the sum in the parentheses is integral, but out of phase if the sum is half-integral. If l_1 and l_2 are integers (**g** is a substrate vector) then the integral-order spots will be unaffected by the anti-phase domain; certain half-integral spots, on the other hand, will be broadened o split. If l_1 and l_2 are non-integers (**g** is not a substrate vector) then some of the integral-order spots may also be affected.

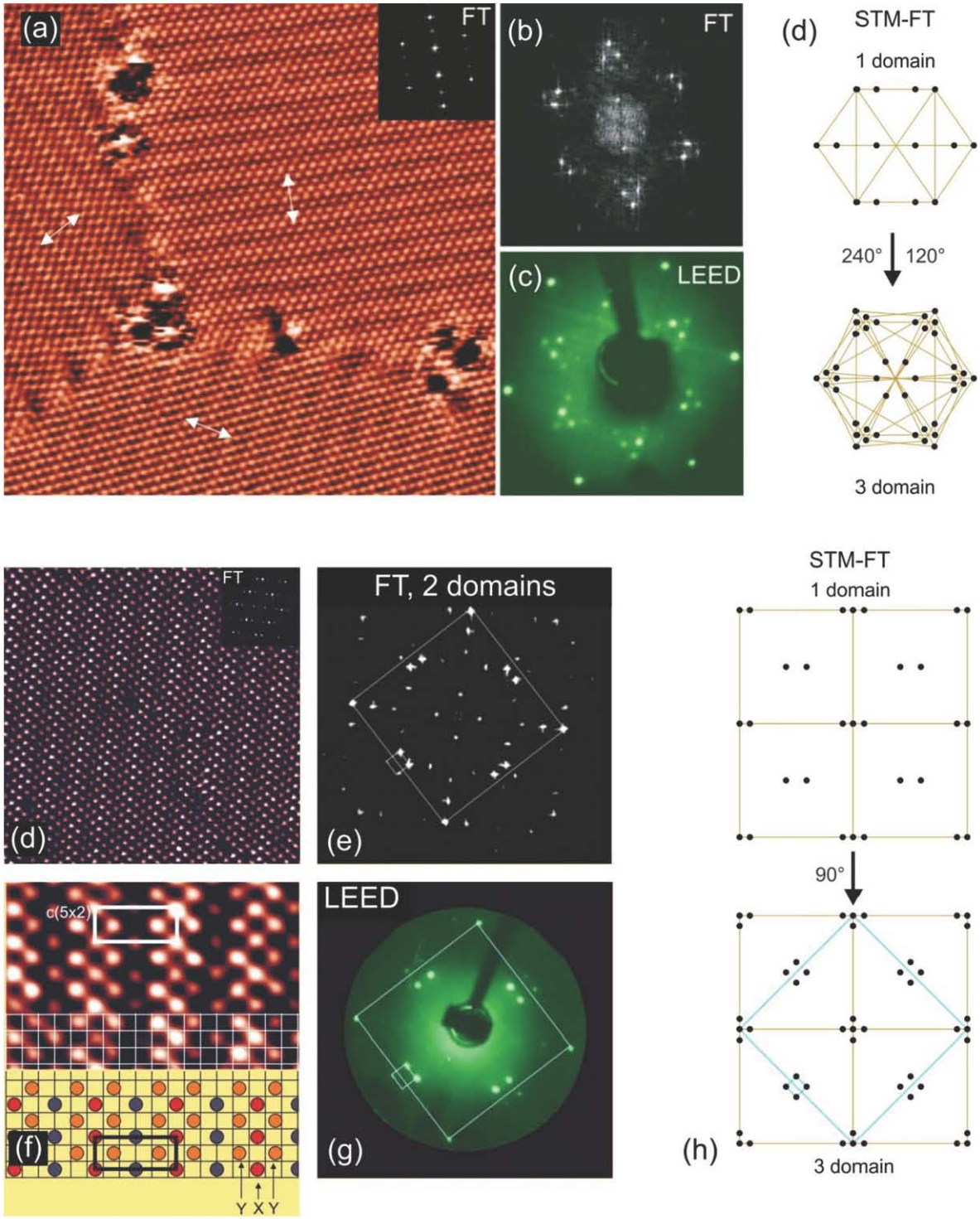

Figure 2.6. *Two examples of LEED spots splitting due to compression of commensurate halogen layer in the Cl/Cu(111) ((a)-(d)) [Andryushechkin 1] and I/Cu(100) ((d)-(h)) [Andryushechkin 2] systems.* ***(a)*** *STM image of 3 equivalent domains with compressed (√3×√3)R30°-Cl structure. On the inset - Fourier transform of STM image from single domain.* ***(b)*** *FT transform of image (a).* ***(c)*** *LEED pattern corresponding to Cl layer shown on (a).* ***(d)*** *Sketch explaining formation of FT and LEED patterns as a sum of three contributions from equivalent domains.* ***(e)*** *STM image of a single domain with compressed c(2×2)-I structure.* ***(f)*** *Atomically resolved compressed iodine monolayer from (e) with corresponding structural model of the monolayer.* ***(g)*** *FT of STM image containing to equivalent domains of compressed iodine monolayer.* ***(h)*** *LEED pattern from compressed iodine monolayer.* ***(i)*** *Sketch explaining formation of FT and LEED patterns as a sum of two contributions from equivalent domains*

On practice one has to be careful with interpretation of the origin of spot splitting in LEED patterns. Diffraction analyses alone usually can't give response on the exact origin of this effect and additional experiments, first of all STM, are required.

The one dimensional case described above gives an oversimplified explanation of the actual situation on surfaces as in some cases the distance between domains can be irregular (due to fluctuations in domain size) leading to the loose of the superstructure periodicity. This case is partly described in [3]. Finally surfaces often exhibit equivalent domains rotated by 90° or 60° depending on the surface symmetry leading to superimposed LEED patterns with same rotation. We show in Figure 2.6 example of such spilt pattern obtained for Cl adsorption on Cu(111) [5] and I on Cu(100) [6].

2.5 Scanning tunneling microscopy and spectroscopy

As mentioned above LEED analysis is very often not sufficient to resolve the surface structure and local probe in real space is needed. In this thesis most of the discovered surface structures were therefore decoded with the help of Scanning Tunneling Microscopy. Figure 2.7 shows the block diagram of a scanning tunneling microscope [4, 7, 8]. A sharp metal tip placed on the piezoelectric drive is used to probe the surface. Electrons can tunnel between the surface and STM tip when they are sufficiently close to each other (~ 10 Å). A small bias voltage (from a few millivolts to several volts) between the tip and the surface give rise to the appearance of tunnel current (up to a few nano amps). A high-resolution (up to atomic resolution) map of local electron density can be obtained when scanning the surface with the tip. This requires fulfillment of two conditions: 1) spatial position of the tip has to be controlled with precision less than 0.1 Å; 2) the tip has to be extremely sharp – ideally it should be atomically sharp. The first condition is fulfilled by the use of precise piezoelectric drivers for tip movement together with efficient vibro insulation system. Preparation of atomically-sharp tip is a difficult

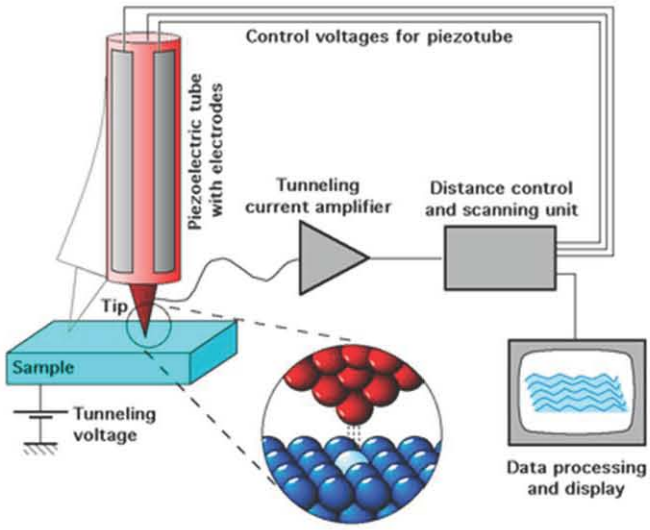

Figure 2.7. *Sketch of STM operating mode*

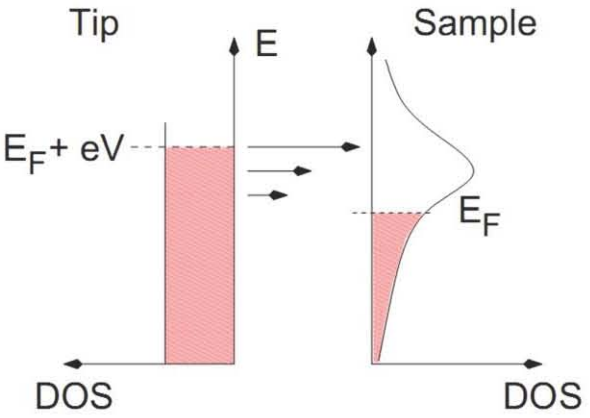

Figure 2.8. *Schematic energy diagram of tunnel junction when positive sample bias is applied. From [Kliewer]*

technical problem that was studied before [9, 10]. In our work we often saved time by using PtIr tips simply cut in air. Then the tips were prepared in situ inside STM by using voltage pulses (10 volts for few seconds) and/or gentle contact with a metallic surface (see Section 2.6). One has to note that this procedure was especially reliable for low temperature measurements as the tip apex is much more stable than at room temperature even when covered by gold cluster.

The tunneling process can be described from Figure 2.8 which illustrates the energy diagram between the tip and the surface. Electron density of states (DOS) on the tip is shown on the left of diagram. For simplicity tip DOS is supposed to be featureless. A bias voltage V is applied to the sample relative to the grounded tip (as in case of Omicron LT STM). The DOS of the sample surface is shown on the right of diagram. All the states below Fermi level are marked in red. The tunnel current is generated by electrons passing the tunnel barrier from the left to the right.

In the s-wave function approximation at T = 0 and for small bias voltage (Tersoff-Hamann approximation) the tunnel current I_t is proportional to the number of electrons tunneling through the barrier between 0 and applied voltage V:

$$I_t \propto \int_0^{eV} \rho_s(E)\rho_t(E-eV)T(E,eV,z)dE \tag{2.9}$$

where $\rho_s(E)$ is the DOS of the sample, $\rho_s(E - eV)$ the DOS of the tip at the energy eV and T(E, eV, z) the transmission probability of tunnel barrier [11, 12, 13]. The latter can be expressed as:

$$T(E,eV,z) = \exp\left[-z\sqrt{\frac{4m}{\hbar^2}(\varphi_t + \phi_s + eV - 2E)}\right] \tag{2.10}$$

From equations (2.9) and (2.10) we see that *It* decreases exponentially with the width *z* of the barrier. It also depends on the work function of the tip φ_t and the sample φ_s as well as on the applied bias voltage V and electronic state energy E.

It exist two different modes of STM operation:

1. constant-height mode: the tip moves parallel to the surface with fixed z while the $I_{tun}(x, y)$ is registered.
2. constant-current mode: I_{tun} is kept constant during the scanning by the way of a feedback loop and variation of the tip height z(x, y) is registered.

In the constant-height regime the distance between STM tip and surface relief always changes. Tunnel current increases when the tip is above the place with high electron density and it decreases above regions with low electron density. As a result a two-dimensional diagram (STM image) of tunnel current dependence with tip position (*x, y*) can be obtained. It gives an idea about surface distribution of electron density, which is related to the surface atomic structure. However a constant-current scanning regime is usually used in the practice. In this operating mode the *z* position of STM tip is adjusted to maintain tunnel current constant during scanning. STM image in such mode corresponds to a two-dimensional plot of tip *z*-coordinate versus its lateral position (*x*, *y*): when the tip is above the region with high electron density STM tip is retracted from the surface to compensate increase of tunnel current, and it is approached to the surface above regions with low electron density. In this mode the relative distance between tip and sample can be adjusted by experimentalist by changing the setpoint current or bias voltage in the feedback loop.

With STM one can obtain images of the surface with extremely high spatial resolution (up to atomic resolution or even better for "vertical" resolution). However interpretation of these images is not so straightforward. It is not known a priori how the surface electronic density is related to the surface atomic structure. In some systems (for example, clean metal surfaces) maxima in surface electron density correspond to the centers of atoms on the surface. For our knowledge in STM studies halogen atoms adsorbed on metal surfaces were always imaged as protrusions. On the contrary, oxygen atoms with similar electronegative properties are usually imaged in STM as depressions. Even more complicated situation is observed on the surface of semiconductors. Depending on the sign and magnitude of bias voltage STM image of the semiconductors surface can be change completely. For reliable interpretation of STM images additional structural information from other experimental methods is required. Comparison between experimental STM images and theoretical simulation of surface electron density is also fruitful. Density functional theory (DFT) is usually used for theoretical simulation of STM images (surface electron density).

Scanning tunneling spectroscopy

From equation (2.9) we see that differentiating the tunnel current expression with respect to the bias voltage V leads to a differential conductance:

$$\frac{dI_t}{dV} \propto \rho_s(eV) \cdot T(eV, z) \tag{2.11}$$

which is proportional to the local density of states of the sample at the energy E = eV. Here we have neglected the two terms proportional to $d\rho_t/dV$ and dT/dV. These are usually neglected provided that DOS of the tip ρ_t is constant and the transmission probability T varies smoothly in the range of applied voltages.

This is an important property of STM which is the basis of scanning tunneling spectroscopy (STS). Extremely high spatial resolution makes this method unique for investigations of the local electronic properties of the surface at the atomic scale. Also when achieved at low temperature (5K) one can obtain high energy resolution of the spectral properties at surfaces for both filled and empty states. Therefore STS is nicely complementary to ARPES.

For our investigations we have used two operating modes for tunneling spectroscopy. The first one consist to fixed the tip position (x_0,y_0,z_0) on the surface and record a differential conductance curve when sweeping bias voltage. It gives a local spectrum of the

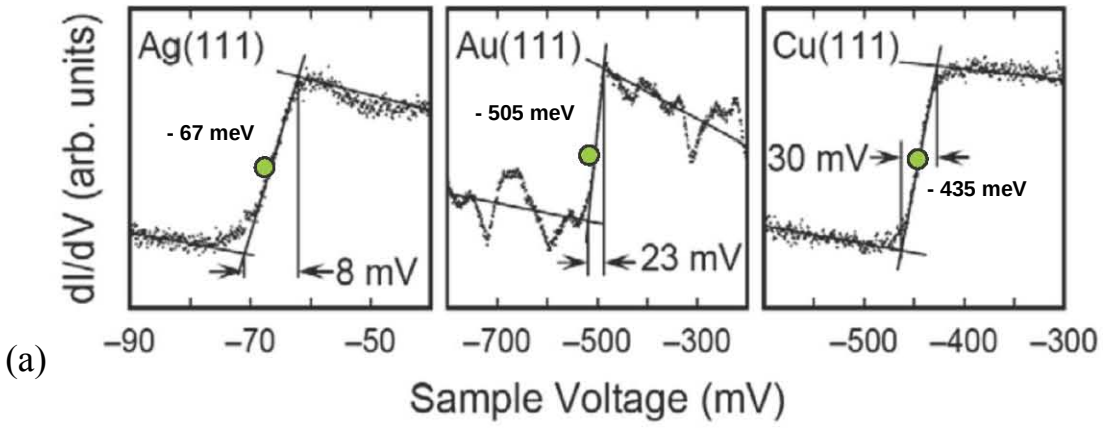

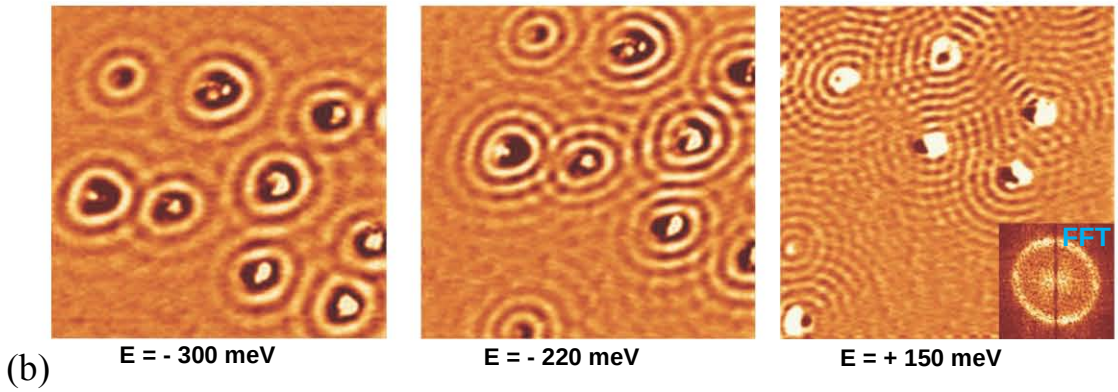

Figure 2.9: ***(a)*** *low temperature (5K) local DOS spectrum recorded with STM on a Ag(111), Au(111) and Cu(111) surfaces. From [Kliewer]* ***(b)*** *Differential conductance maps recorded in our lab on Cu(111) for three different bias voltage.*

surface DOS. We show for instance on Figure 2.9a typical DOS curves obtained on the three noble metals surfaces Ag(111) Au(111) Cu(111) [14]. We recognize the well-known step like curves corresponding to the onset of the Shockley surface state band with the three corresponding minima of the bands. The second mode gives rise to the spatial distribution of the density of states at a fixed energy. In this case *dIt/dV* signal obtained from the lock in output is recorded when scanning the surface at a fixed bias voltage. By this way one can obtained maps of the density of states at selected energy. On Figure 2.9b are presented three maps of the density of states recorded on the Cu(111) surface at E = - 300 meV, - 220 meV and E = + 150 meV. This example shows the energy dependence of the wavelength of the standing waves formed by scattering of the Shockley surface state at impurities. This type of measurement can be achieved by operating with feedback loop kept on in the same time as topography is recorded. Ideally a complete (and more accurate) experiment should be done with feedback loop off by recording a *dI/dV* spectrum on each point of the scanned area. Therefore one obtains a 3D matrix of *dI/dV* data in (x,y,E) space. A *dI/dV* map is then obtained as slice at E=const and *dI/dV* spectrum as a line at (x_0,y_0) position.

2.6 Experimental procedure

As it was already noticed sample preparation, chlorine adsorption and all measurements were done in UHV conditions. Chlorine adsorption was done on sample at 130 or 300 K. That guaranteed thermal equilibrium inside chlorine monolayer.

STM tips were prepared from W-Re (80% W, 20% Re) or Pt-Ir (80% Pt, 20% Ir) wire 0.2 mm in diameter. Tungsten-rhenium tips were prepared by constant-current electrochemical etching of wire as described in details elsewhere [10]. Residual tungsten oxide has been removed from the tip apex by ion bombardment Ar^+ (1 keV) along the axis of the tip in UHV. Platinum-iridium tips were prepared by cutting the wire. The final treatment of the tips was done directly during scanning using field emission effect. The tips were treated until atomically-resolved STM images could be obtained. We commonly used Au(111) surface to prepare the tips. This surface also served as reference for imaging. In the commercial LT- STM used, the gap voltage is applied to the sample with the tip being grounded. Lock-in technique was used for STS measurements. Modulation frequency was fixed to 700 Hz and amplitude to 5 to 30 mV peak to peak. Time constant was chosen between 1, 3 and 10 ms depending on the slope of the bias sweeping for dI/dV spectra and scan velocity during dI/dV mapping. The feedback loop of the STM was opened during spectra acquisition. Spectroscopic properties of the tip were checked before each STS experiment. The tip was considered to have proper density of states if clean and sharp step-like spectra of surface states could be measured (examples of surface state STS spectra can be found elsewhere [14]). For data treatment of STM and STS data WSxM software has been used [15].

2.7 Basics of density functional theory

On the base of experimental data structural models for the surfaces modified by chlorine action where proposed. DFT calculations were used to test them and discriminate eventually between several possible ones.

Density functional theory is one of the most powerful approaches for theoretical study of systems with large number of atoms [16, 17, 18].

The main concept of this theory consists in the following: all the properties of a many body system in a ground state are uniquely determined by the spatial distribution of its electron density [17]. This statement can be proved mathematically and is known as the first Hohenberg-Kohn theorem. In the usual quantum-mechanical description the N-particle system state is set by 3N independent variables. The Hohenberg-Kohn approach reduces the number of independent variables down to only 3 spatial coordinates of electron density function n(x,y,z).

The energy of the system (together with its other properties) is a functional of electron density n(x,y,z). The energy functional reaches its minimum for those n(x,y,z) which corresponds to the ground state of the system. This is the second Hohenberg-Kohn theorem [17].

DFT approach is usually used together with Kohn-Sham formalism. Within the framework of Kohn-Sham formalism the intractable many-body problem of interacting electrons in the external potential of atomic nuclei is reduced to a tractable problem of non-interacting electrons moving in an effective potential. This effective potential includes both static potential of atoms and interaction between all the electrons. The total energy of the system can be written as:

$$E[n] = T[n] + U[n] + V[n] \tag{2.12}$$

where T[n] is the kinetic energy of electrons, U[n] – potential energy of electrons in static potential of atomic nuclei and V[n] is the effective potential of electron-electron interaction. Here every term is the functional of electron density n(x,y,z).

Let us suppose that n(x,y,z) depends on a certain parameter a. It can be, for example, lattice parameter of a crystal or the angle between two chemical bonds in a molecule. We can minimize functional E[n] by varying parameter a and calculating each time the new value of the energy. Corresponding value $a_{\min} = a_0$ is the equilibrium lattice constant or angle between chemical bonds and $E_{\min}[n] = E_0$ is the total energy of the system in the ground state.

However in practice another approach instead of minimization the functional E[n] is used. The ground state problem of a many-body system can be reduced to the solution of a single particle Schrödinger equation [17]:

$$\left[-\frac{\hbar^2\nabla^2}{2m} + v_s(x,y,z)\right]\phi_i(x,y,z) = \epsilon_i\phi_i(x,y,z) \tag{2.13}$$

Here "wave functions" ϕ_i (these are not the wave functions in their quantum-mechanical sense) are related to the electron density

$$n(x,y,z) = \sum_i^N f_i |\phi_i(x,y,z)|^2 \quad (2.14)$$

(where f_i – occupation of *i*'th orbital) of the single "particle" in the effective potential

$$v_s(x,y,z) = v(x,y,z) + v_H(x,y,z) + v_{xc}(x,y,z) \quad (2.15)$$

Here $v(x,y,z)$ is the potential energy of electrons in the static field of atomic nuclei, $v_H(x,y,z)$ – Hartree potential which describes coulomb electron-electron interaction, and $v_{xc}(x,y,z)$ – exchange-correlation potential which describes quantum-mechanical effects in the electron-electron interaction. Equations (2.13)-(2.15) are also known as Kohn-Sham equations.

Hartree $v_H(x,y,z)$ and exchange $v_{xc}(x,y,z)$ potentials depend on the electron density n(*x*,*y*,*z*) which by-turn depends on the "wave functions" ϕ_i. These "wave functions" according to Kohn-Sham equation are related to Hartree $v_H(x,y,z)$ and exchange $v_{xc}(x,y,z)$ potentials. Thus we obtain a self-consistent system of equations (2.13)-(2.15). Solution of the system (2.13)-(2.15) starts from initial guess $n_{init}(x,y,z)$ of electron density function which in fact can be chosen arbitrary. The effective potential $v_s(x,y,z)$ is then calculated and Kohn-Shan equation (2.13) is solved for "wave functions" ϕ_i. With the use of calculated "wave functions" a new electron density n(*x*,*y*,*z*) can be found, and so on. This procedure continues until the algorithm converges.

A lot of different approaches for approximation of each term in equations (2.13)-(2.15) are developed in our days. Approximations have to be selected individually for any specific problem depending on the particular properties of the system.

2.8 DFT calculations procedure

For DFT calculations the VASP (Vienna ab initio simulation package) [19-22] software package was used.

In our particular case PAW potentials [23] and PBE exchange-correlation functions [24] were chosen. For valence-electrons description a plane-wave bases with cut-off energy 425 eV (Ag(111)-(3×3)-Cl) and 375 eV (Ag(111)-(7×7)-Ag_3Cl_7) was used. The metal surface was modeled by a slab of four (Ag(111)-(7×7)-Ag_3Cl_7) or five (Ag(111)-(3×3)-Cl) atomic layers: two (Ag(111)-(3×3)-Cl) or three (Ag(111)-(7×7)-Ag_3Cl_7) of them were fixed, while the rest layers close to the surface were free to move (relax) until the uncompensated forces acting on the atoms became less than 10^{-2} eV/Å. Conjugate gradient method was used for calculation of atomic relaxation. Vacuum gap between neighboring slabs was not less than 14-20 Å. Electron iterations were done until the change in the total energy became less than 10^{-4} eV. Monkhorst–Pack grid [25] was used for integration of Brillouin zone: a (24×24×1) grid for Ag(111)-(3×3)-Cl system and (14×14×1) for

Ag(111)-(7×7)-Ag_3Cl_7. STM images were calculated in Tersoff-Hamann approximation [26].

For DFT calculations on Cl/Au system we used PAW-PW91 pseudopotentials. Asymmetric 12 layer slab was used with 6 atomic planes allowed to relax. The vacuum gap between neighboring slabs was 20 Å. Monkhrost-Pack grid 351 was used for integration of Brillouin zone. The cut-off energy was 410 eV.

Adsorption energy has been calculated as

$$E_{ads} = \frac{1}{N_{Cl}}\left(E_{Cl/Me}^{slab} - E_{Me}^{slab} - \Delta N_{Me} E_{Me}^{bulk} - \frac{1}{2} N_{Cl} E_{Cl_2}^{total}\right) \quad (2.16)$$

where $E_{Cl/Me}^{slab}$ and E_{Me}^{slab} is the total energy of the system with chlorine adsorbed on the surface and of a clean substrate correspondingly, ΔN_{Me} – difference in the number of metal atoms in the slab between clean and adsorbate-covered surface, E_{Me}^{bulk} – energy of one metal atom in the slab, N_{Cl} – number of adsorbed Cl atoms, $E_{Cl_2}^{total}$ – energy of an isolated Cl_2 molecule.

Bibliography of Chapter 2

[1] R.G. Jones. Halogen adsorption on solid surfaces// Progr. Surf. Sci. 27 25 (1988).

[2] Surface Preparation Laboratory // http://www.surface-prep-lab.com

[3] L.J. Clarke. Surface crystallography: an introduction to low energy electron diffraction // A Wiley-Interscience Publication (1985).

[4] O. Kenjiro et al. Surface science – an introduction // Springer (2003).

[5] B. Andryushechkin et al. Domain-wall mechanism of "(n√3×n√3)R30°" incommensurate structure formation in chemisorbed halogen layers on Cu(111) // Surf. Sci. 470 L63 (2000).

[6] B. Andryushechkin et al. Structural transitions of chemisorbed iodine on Cu(100) // Surf. Sci. 497 59 (2002).

[7] G. Binning, H. Rohrer. 7×7 Reconstruction on Si(111) Resolved in Real Space // Phys. Rev. Lett. 50 120 (1983).

[8] G. Binning, H. Rohrer. Scanning tunneling microscopy// IBM Journ. Res. Develop. 30 355 (1986).

[9] T. Sakurai et al. Field ion-scanning tunneling microscopy // Progr. Surf. Sci. 33 3 (1990).

[10] K.N. Eltsov et al. // Phys. Low-Dim. Struct. 9/10 7-15 (1996).

[11] J. Tersoff, D.R. Hamann. Theory and application for the scanning tunneling microscope // Phys. Rev. Lett. 50 1998 (1983).

[12] A. Selloni et al. Voltage-dependent scanning-tunneling microscopy of a crystal surface: Graphite // Phys. Rev. B 31 2602 (1985).

[13] N.G. Lang. Spectroscopy of single atoms in the scanning-tunneling microscope // Phys. Rev. B 34 5947 (1986).

[14] J.U. Kliewer. Dynamics and Manipulation of Surface States // Thesis, Rheinisch–Westfälischen Technischen Hochschule Aachen (2000).

[15] I. Horcas et al. WSXM: A software for scanning probe microscopy and a tool for nanotechnology // Rev. Sci. Instrum. 78 013705 (2007).

[16] W. Koch, M.C. Holthausen. A Chemist's Guide to Density Functional Theory // Weinheim: Willey, 2nd edition(2002).

[17] R.M. Martin. Electronic structure. Basic theory and practical methods // Cambridge University Press (2004).

[18] D. Sholl, J.A. Steckel. Density Functional Theory: A Practical Introduction // Wiley (2009).

[19] G. Kresse, J. Hafner. *Ab initio* molecular dynamics for liquid metals // Phys. Rev. B 47 558 (1993).

[20] G. Kresse, J. Hafner. *Ab initio* molecular-dynamics simulation of the liquid-metal–amorphous-semiconductor transition in germanium // Phys. Rev. B 49 14251 (1994).

[21] G. Kresse, J. Furthmuller. Efficiency of ab-initio total energy calculations for metals and semiconductors using a plane-wave basis set // Computational material science 6 15 (1996).

[22] G. Kresse, J. Furthmuller. Efficient iterative schemes for ab initio total-energy calculations using a plane-wave basis set // Phys. Rev. B 54 11169 (1996).

[23] G. Kresse, D. Joubert. From ultrasoft pseudopotentials to the projector augmented-wave method // Phys. Rev. B 59 1758 (1999).

[24] J.P. Perdew, K. Burke, M. Ernzerhof. Generalized Gradient Approximation Made Simple // Phys. Rev. Lett. 77 3865 (1996).

[25] H.J. Monkhorst, J.D. Pack. Special points for Brillouin-zone integrations // Phys. Rev. B 13 5188 (1976).

[26] J. Tersoff, D.R. Hamann. Theory of the scanning tunneling microscope // Phys. Rev. B 31 805 (1985).

CHAPTER 3.
Ag(111) surface under molecular chlorine action

In this chapter we present our results of experimental and theoretical study of chlorine monolayer adsorbed on silver (111) surface. Low-temperature STM measurements on the initial stage of chlorine layer formation will be described first ($\theta < 0.33$ ML). Surprisingly, in this coverage range chlorine atoms were found to form linear chains of single atom width. Evolution of these structures that leads to appearance of commensurate ($\sqrt{3}\times\sqrt{3}$)R30° structure will be presented. Compression of commensurate structure will be discussed next. The first direct observation of a two-dimensional gas of interstitials on the initial stage of compression and its subsequent condensation into domain wall structure is reported. We also report on the first direct study of saturated chlorine monolayer with low-temperature scanning tunneling microscopy. Our experimental findings supported by DFT calculations clearly show that at saturation silver surface is reconstructed and a system of antiphase islands with (3×3) structure appears on the surface. We propose atomic structure model for this reconstruction. Along this reconstruction on the boundaries between adjacent anti phase (3×3) island we observed groth of nano clusters. Thanks to the combined use of LT STM measurements and DFT calculations we were able to resolve their atomic structure.

3.1 General description of the system

Figures 3.1 and 3.2 show LEED patterns from the Ag(111) surface during continuous increase of chlorine coverage. The surface was kept at the temperature 300 K and 130 K respectively. Adsorption at room temperature leads to the formation of diffuse (√3×√3)R30° pattern (Figure 3.1b), which is followed by a complex diffraction pattern when chlorine layer is saturated (Figure 3.1d). The latter one is similar to the diffraction patterns reported previously for this adsorption system [1,2,3,4,5]. When chlorine is adsorbed at lower substrate temperature a sharp (√3×√3)R30° pattern is formed first (Figure 3.2b). Subsequent halogen adsorption caused splitting of diffraction spots to triangles of six spots (Figure 3.2c). Additional spots appear in the diffraction pattern on Figure 3.2d, which are arranged similar to the spots in room-temperature complex pattern on Figure 3.1d. Finally in the saturation the same complex diffraction pattern as seen for room-temperature adsorption is formed (Figure 3.2f). The

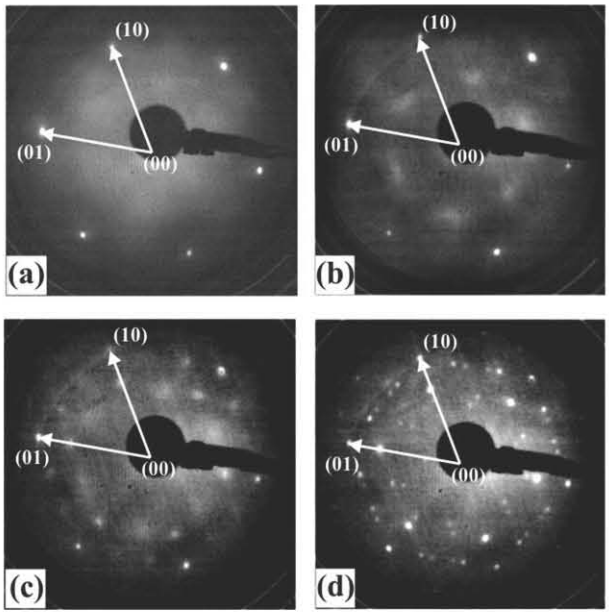

Figure 3.1. *Evolution of LEED pattern (E_0 = 90 eV) during continuous chlorine adsorption on Ag(111) surface at 300 K. The reciprocal lattice vectors of silver surface are shown*

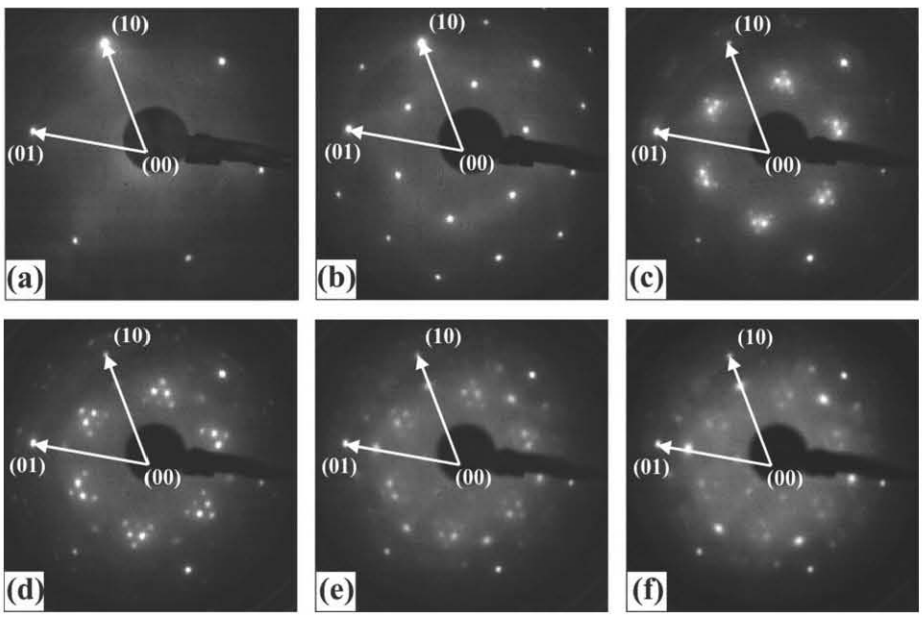

Figure 3.2. *Evolution of LEED pattern (E_0 = 90 eV) during continuous chlorine adsorption on Ag(111) surface at 130 K. The reciprocal lattice vectors of silver surface are shown*

only dtabifference between LEED patterns is the size of the spots, which are larger for chlorine layer formed at lower temperature (compare Figure 3.1d and 3.2f). After heating the surface LEED pattern at Figure 3.1d becomes more focused and coincides with the diffraction pattern on Figure 3.1d. Subsequent cool-down of the surface doesn't change sharpness of LEED pattern.

Besides this reversible structural transitions are observed in this system. In particular ($\sqrt{3}\times\sqrt{3}$)R30° pattern (Figure 3.2b) disappears when the surface is heated up to 300 K. Subsequent cool-down of the surface leads to reappearance of ($\sqrt{3}\times\sqrt{3}$)R30° pattern, which is the sign of reversible order-disorder structural phase transition on the surface. Diffuse ($\sqrt{3}\times\sqrt{3}$)R30° pattern seen at 300 K (Figure 3.1b) changes to split diffraction pattern from Figure 3.2c when the substrate is cooled-down to 130 K. This phase transition is also reversible.

Our observations conform the results of previous study by Shard et al. [6]. For coverage below saturation chlorine layer is poorly ordered at room temperature. Due to that the use of room-temperature STM is impossible. Moreover, even in saturation chlorine layer is too friable at this temperature and it is impossible to obtain high-resolution STM images [7]. That's why the use of low-temperature techniques (in particular LT STM) is crucial to obtain new information about the structure of chlorine layer. In all our experiments except mentioned above chlorine adsorption was done at room temperature of the surface but all structural measurements were carried out at low temperature. Such approach is justified by the fact that sharpest LEED pattern of saturated chlorine layer is observed after room-temperature adsorption and doesn't changes after surface cool-down whereas all other structure (like ($\sqrt{3}\times\sqrt{3}$)R30°) exists only at low temperature.

3.2 Low surface coverage (θ < 0.33 ML)

Figure 3.3 shows an STM image of Au(111) surface after adsorption of a small amount of Cl at 300 K. One can see that chlorine atoms first tend to decorate atomic steps. This observation conform results of DFT calculations by Liu et al. [8] that showed significant increase of adsorption energy for chlorine atoms on the step edge compared to flat terrace.

Along this single chlorine atoms can be seen on terrace (Figure 3.3). They are imaged in STM as protrusions. Most of adsorbed atoms are randomly distributed over the surface and are separated by large (> 7 Å) distances from each other. Few of the adsorbed atoms form pairs with smaller interatomic distance. Surprisingly even at such extra-low surface coverage formation of

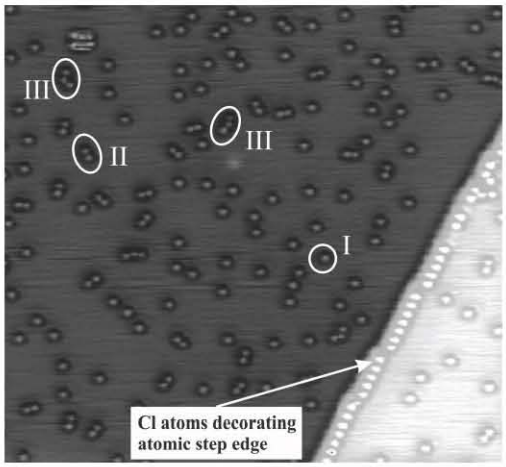

Figure 3.3. *STM image (277×275 Å^2; I_t = 1 nA; U_s = –780 mV, T = 5 K) of Ag(111) surface covered with ≈0.02 ML of chlorine. Chlorine atoms decorating atomic step can be clearly seen. (I) – single Cl atoms, (II) – dimers of Cl atoms, (III) –chains-trimers of Cl atoms*

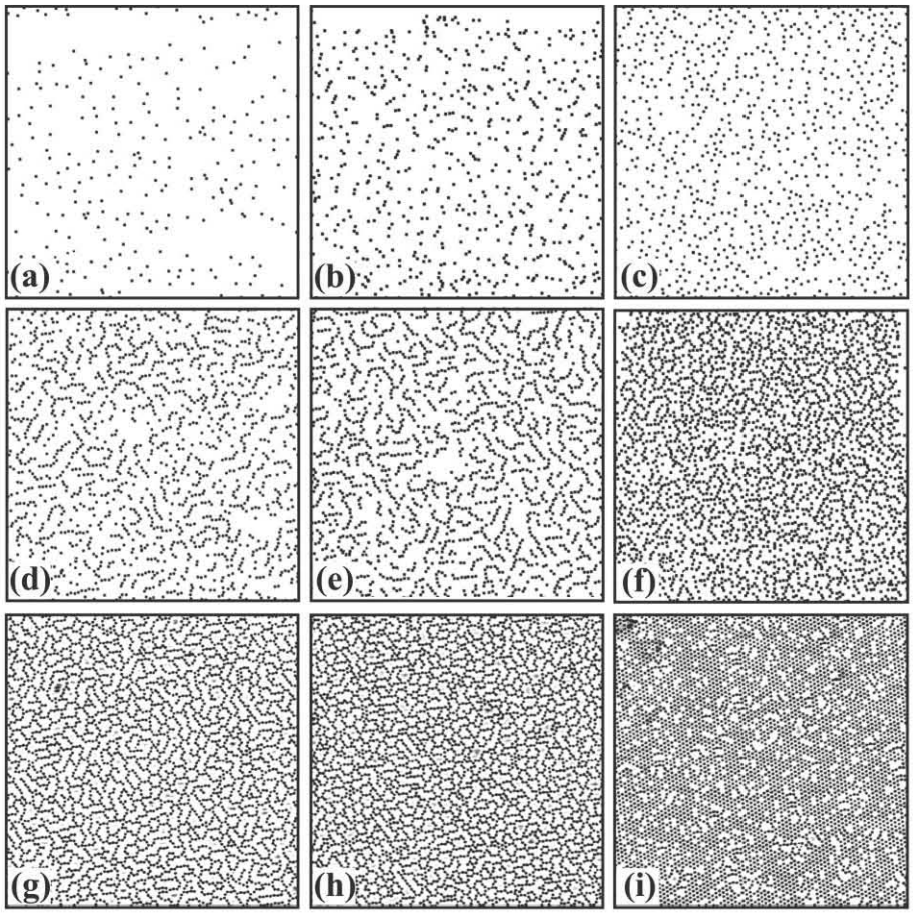

Figure 3.4. *STM images (330×330 Å^2; I_t = 1 nA; U_s = –780 mV, T = 5 K, treatment was used) demonstrating:* ***(a–f)*** *formation of chains from Cl atoms;* ***(g–i)*** *nucleation of a 2D commensurate (√3×√3)R30° structure*

atomic chains is observed. The nearest-neighbor distances in such chains are 4.4-4.5 Å. The tendency to form chains becomes more evident at higher coverage. A series of STM images of Ag(111) surface during continuous increase of surface chlorine coverage in the range 0.03-0.31 ML is shown on Figure 3.4. The images were treated to make clearer the distribution of chlorine atoms over the surface. As one can see chlorine atoms tend to form single-atom chains. The density of chains increases together with chlorine coverage but adsorbed atoms avoid formation of island with compact structure.

It can be clearly seen from Figure 3.4 that commensurate (√3×√3)R30° structure starts to form on the surface when chlorine coverage approaches 0.33 ML, which is in agreement with our LEED data and results of previous study [6]. According to [6] this structure is formed at surface temperatures less than 190 K. Table 3.1 contains results of DFT calculations of adsorption energy for chlorine atoms on Ag(111) surface. The calculations were done for surface coverage 0.33 ML, with chlorine atoms forming (√3×√3)R30° structure. An fcc three-fold hollow site is energetically most favorable, followed by hcp hollow site which has 10 meV lower adsorption energy.

Figure 3.5a shows an STM image of surface covered by 0.26 ML of chlorine. At this coverage nucleation of first (√3×√3)R30° islands starts. This image makes it possible to

Table 3.1. *Adsorption energy for Cl atoms in different sites of Ag(111) surface (the case of Ag(111)- (√3×√3)R30° -Cl structure)*

Adsorption site	Adsorption energy eV/atom
fcc hollow	–1.543
hcp hollow	–1.533
bridge	–1.457
on top	–1.082

establish adsorption sites for chlorine atoms in the chains. On Figure 3.5b a zoom-image is shown together with a hexagonal grid superimposed on it. The knots of the grid correspond to the position of substrate atoms. The grid was placed in such way that all chlorine atoms occupy energetically favorable three-fold adsorption sites and neither of them occupies on-top position. If we suppose that all chlorine atoms in (√3×√3)R30° islands a placed in fcc hollows (as the most attractive one according to our DFT calculations), than approximately the half of chlorine atoms in the chains occupy hcp hollows. The exact calculated distance between fcc and hcp adsorption sites is 4.41 Å (Ag lattice parameter being 4.0853 Å [9]) and is in good agreement with the distances measured on the STM images from Figures 3.3 and 3.4. It is surprising that interatomic distances in the chains at low chlorine coverage are less than the nearest-neighbor distances of 5 Å in the (√3×√3)R30° structure observed for higher surface coverage. This could be the sign of specific lateral interatomic interactions in chlorine layer.

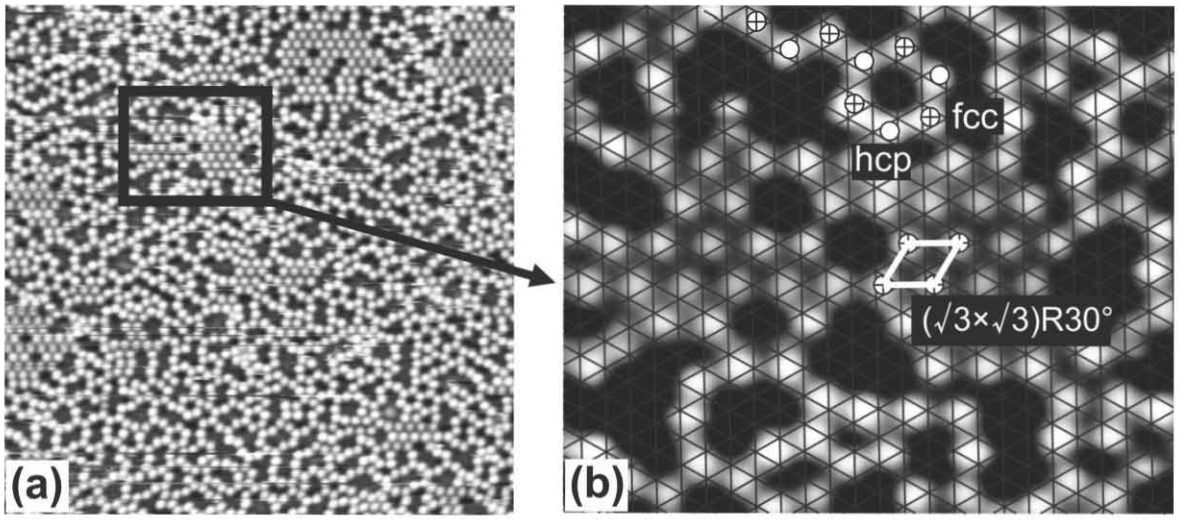

Figure 3.5. (a) *STM image (330×330 Å^2, I_t = 1 nA, U_s = –500 mV) of Ag(111) surface covered with 0.26 ML of Cl.* ***(b)*** *Zoom on a small region of image (a) superimposed with a grid. The knots of the grid corresponds to the position of substrate atoms*

3.3 Ccompression of commensurate (√3×√3)R30° structure (0.33 < θ < 0.42 ML)

As it was already mentioned in the previous section commensurate (√3×√3)R30° structure is formed at surface chlorine coverage $\theta = 0.33$ ML (Figure 3.6). The nearest-neighbor distances in this structure are 5 Å, which is larger than van der Waals diameter 3.6 Å [10,11] of chlorine atom. A corresponding LEED pattern is shown on the inset in the upper right corner of the Figure 3.6. The LEED pattern can be observed for the surface temperatures lower than 190 K [6].

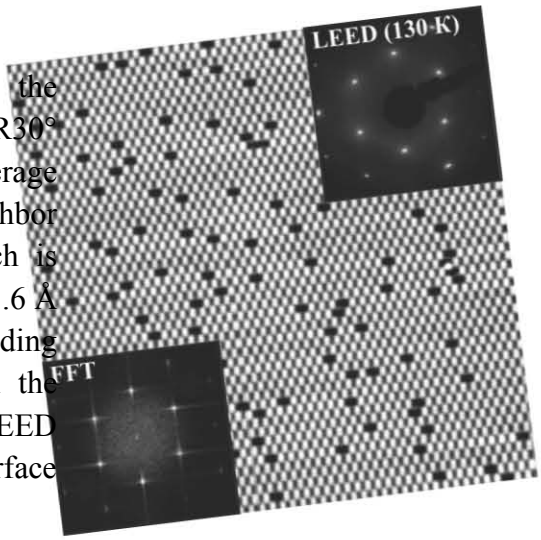

Figure 3.6. *STM image (250×250 Å^2, I_t = 1 nA, U_s = –500 mV, T = 5 K) of chlorine (√3×√3)R30° structure formed at surface coverage θ ≈ 0.33 ML. In the left bottom corner FFT of the image and in the right upper corner corresponding LEED pattern are shown*

Subsequent chlorine adsorption may cause (√3×√3)R30° structure to compress. The mechanism of commensurate lattice compression is of great interest on its own. Figure 3.7a shows an STM image of Ag(111) surface covered by 0.34 ML of Cl. New objects with the shape of three-pointed stars have appeared on the surface, although the FTT of STM image does not show any new features compared to perfect (√3×√3)R30° structure (compare inset with FTT on Figure 3.6 and 3.7a). The rows of the stars are oriented along <112> direction of the substrate. A large-scale image with single star is shown on Figure 3.7b. The star is formed due to the

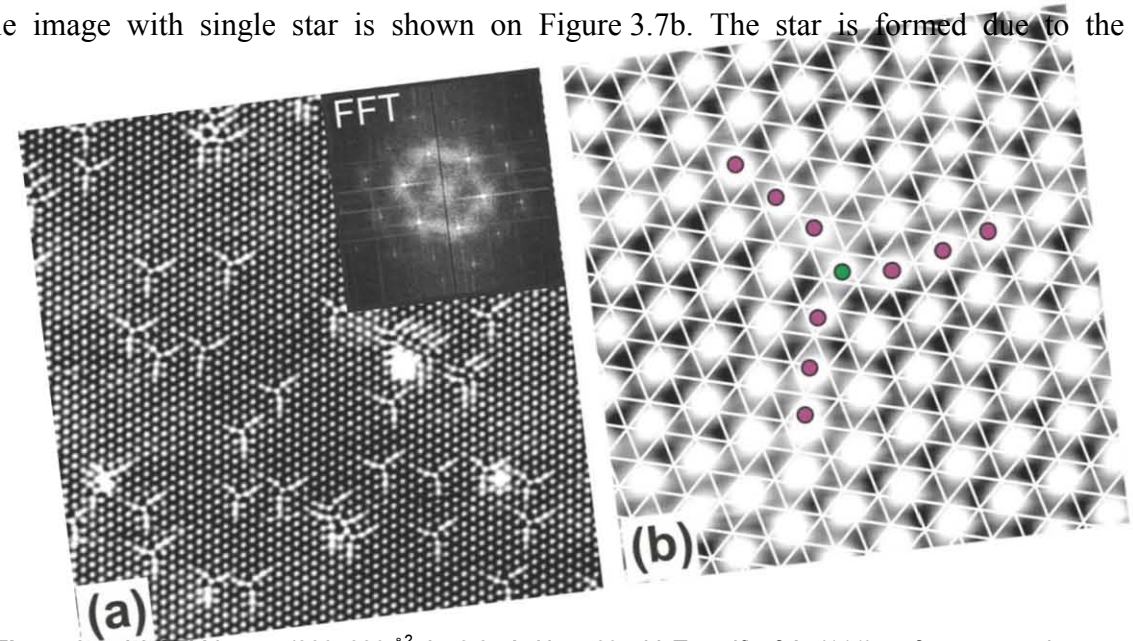

Figure 3.7. ***(a)*** *STM image (330×330 Å^2, I_t = 2.8 nA, U_s = –60 mV, T = 5 K) of Ag(111) surface covered with θ ≈ 0.34 ML of chlorine. In the upper right corner FTT of the STM image is shown.* ***(b)*** *Zoom from image (a) superimposed with a grid, the knots of the grid coincide with position of substrate atoms. An interstitial defect (additional Cl atom) in (√3×√3)R30°-Cl structure is highlighted with green circle and distorted chlorine atoms incommensurate structure with purple circles*

adsorption and penetration of additional chlorine atom into the commensurate layer, i.e. the star corresponds to an interstitial defect or a crowdion [12]. On the major part of the surface chlorine layer remains commensurate. The central atom in the crowdion occupy fcc hollow site, just as all its neighbors in the surrounding (√3×√3)R30° structure (see Figure 3.7b). However as it can be seen from the structural model of a crowdion (Figure 3.8) the central atom belongs to alternative (√3×√3)R30° sublattice marked as "2", whereas all other chlorine atoms in nonperturbed region belong to sublattice "1". Note that there exist three different (√3×√3)R30° sublattices on the (111) fcc face. That mean there can exist two different kinds of crowdions with central atoms occupying either sublattice "2" or "3". Their structural models are shown on the Figure 3.8. Chlorine atoms nearest to the center of the crowdion a placed close to hcp hollow positions, whereas the next to nearest atoms occupy bridge sites. The perturbation in atomic density is damped on the 3-4 atoms along the rows of a crowdion. This gives the diameter of a crowdion ≈ 30 Å. For our knowledge this is the first atomic-scale observation of a crowdion.

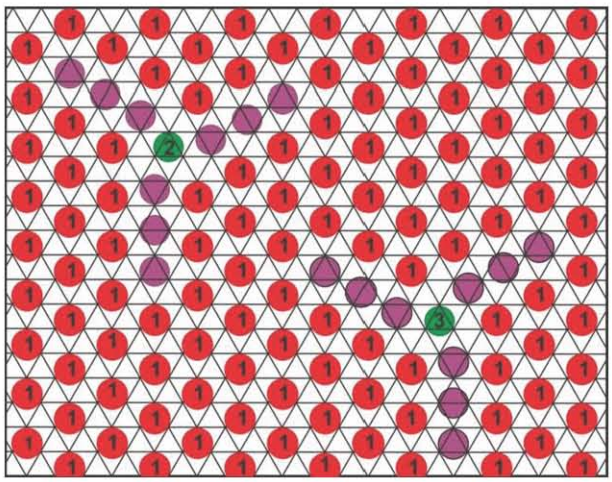

Figure 3.8. *A schematic representation of two types of crowdions (with left- and right-side chirality) in the (√3×√3)R30°-Cl structure. Chlorine atoms in different (√3×√3)R30° sublattices are marked with numbers 1, 2 and 3. Disturbed chlorine atoms forming crowdion are shown in purple. Additional chlorine atom in the center of crowdion (interstitial) is shown in green*

Further chlorine adsorption and increase of surface coverage leads to formation of spread regions of compressed halogen layer – domain walls. Figure 3.9 shows an STM

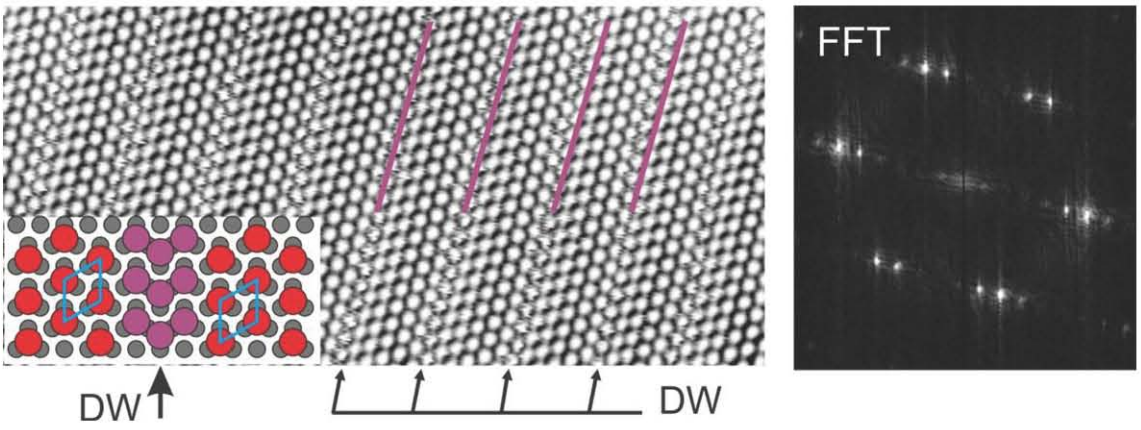

Figure 3.9. *STM image (206×97 Å^2, I_t = 1.2 nA, U_s = –100 mV, T = 5 K) of linear domain walls (DW) separating unperturbed domains of (√3×√3)R30° structure in the chlorine layer on Ag(111) surface. Chlorine atoms in DW occupy hcp hollow sites. FFT of the STM image is shown on the right. Uniaxial splitting of spots can be clearly seen*

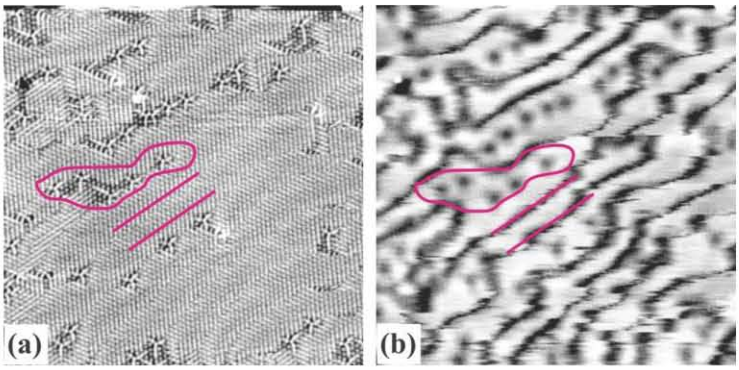

Figure 3.10. *STM images (330×330 Å^2) of the same area of Ag(111) surface covered with chlorine. The image (a) was taken with "usual" scanning parameters I_t = 2.9 nA, U_s = –48 mV, whereas image (b) was taken with elevated bias voltage: I_t = 2.9 nA, U_s = +1980 mV. Additional contrast in the areas of increased chlorine density can be clearly seen on the image (b): crowdions appear as dark spots and domain walls as dark lines*

image of silver surface cover with $\theta \approx 0.37$ ML of chlorine. On this image parallel equidistant stripes can be seen – these are $(\sqrt{3}\times\sqrt{3})$R30° linear domains separated by domain walls. The density of chlorine atoms inside the walls is increased compared to $(\sqrt{3}\times\sqrt{3})$R30° structure. The FTT of the STM image shows uniaxial splitting of the spots in the direction parallel to the axis of compression. Considering three possible directions of chlorine layer compression on (111) fcc face we can understand the origin of 6-spots triangles that appear on LEED pattern for surface coverage $\theta > 0.33$ ML (Figure 3.2d). The same diffraction pattern was observed by Shard et al. [6], though it was interpreted as diffraction from uniformly compressed chlorine layer with 13×13 periodicity. Our STM results unambiguously show that a domain wall scenario is realized in this system rather than uniform compression.

Commensurate-incommensurate phase transition via domain wall mechanism was theoretically predicted in the 1970-80 [13,14]. It was studied in details for the model systems of noble gases physisorbed on the graphite and metal surfaces [13,15]. In a recent theoretical study Lyuksyutov with colleagues have shown that during commensurate-incommensurate phase transition a 2D gas of defects can appear and it can have significant influence on the whole phase diagram of the system [16]. In particular, it was shown that for any surface temperature it exist such range of adsorbate coverage (above commensurate structure coverage) where formation of domain wall system is unfavorable and a gas of defects should exist instead. It was also shown that heating the domain wall system may lead to evaporation of heavy domain walls into the 2D gas of interstitial defects. For low density of domain walls they can be completely evaporated and the system thus will return to commensurate phase.

According to our data it is possible to observe simultaneously crowdions and domain walls in Cl/Ag(111) system. Figure 3.10a shows an STM image of silver surface covered with 0.35 ML of chlorine. It shows both crowdions and domain walls. The same surface area imaged with different scanning parameters – U_s = +2 V, I_t = 2.9 nA – is shown on the Figure 3.10b. It appears that imaging the chlorine layer with such unusual parameters add new contrast to the STM images: crowdions appears as dark spots and domain walls as

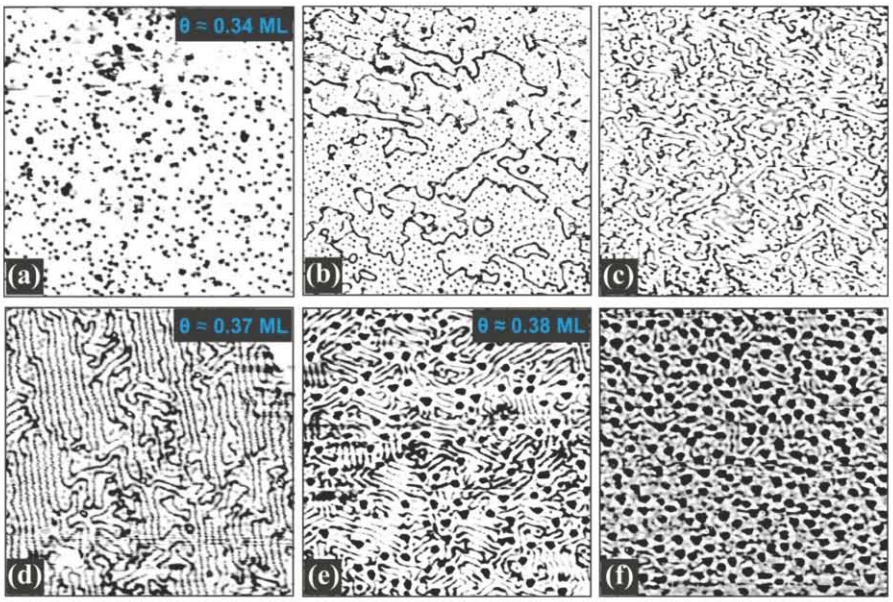

Figure 3.11. *Large-scale STM images (1000×1000 Å^2, I_t = 2.9 nA, U_s = +1980 mV, T = 5 K) of Ag(111) surface during continuous increase of surface coverage in the range 0.34 < θ < 0.40 ML. A domain walls structure with linear domains is formed at θ ≈ 0.37 ML (Figure (d)). The islands of the new (3×3) phase (small dark triangles on Figure (e)) start to nucleate after that together with continuous compression of domain wall structure (the distance between domain walls decreases)*

dark lines. Using such scanning mode we can waive atomic resolution and follow the interaction of crowdions with domain walls and the phase transitions on the surface at a larger scale, which is more informative. Figure 3.11 shows the series of such large-scale STM images (1000×1000 Å^2) of Ag(111) surface during gradual increase of chlorine coverage in the range θ > 0.33 ML.

In agreement with Lyuksyutov et al. theory [16] at low density crowdions (dark spots) are distributed randomly on the surface and looks like a frozen 2D gas of defects (Figure 11a). Starting from the coverage $\theta \approx 0.35$ ML certain domain walls (dark lines) appears on the surface (Figure 3.11b). Further chlorine adsorption leads to increase the number of domain walls and to gradual disappearance of crowdions. At surface coverage $\theta \approx 0.37$ ML the crowdions have almost disappeared and domain walls are arranged periodically at the distances about 30 Å (Figure 3.11*c–d*). This surface structure gives rise to the split LEED pattern shown on Figure 3.2c.

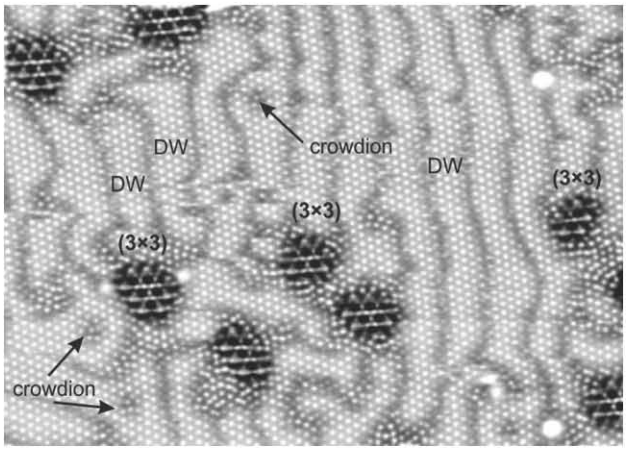

Figure 3.12. *STM image (318×225 Å^2, I_t = 2.9 nA, U_s = +1980 mV, T = 5 K) of Ag(111) surface covered with 0.38 ML of chlorine. Crowdions, domain walls and islands with (3×3) structure are clearly seen*

It should be noted that we observed transition from crowdions to

domain walls at surface temperature 5 K. According to the theory [16] the critical for this transition density of crowdions should increase with surface temperature.

After the domain wall structure has formed islands of the new surface structure starts to grow if additional chlorine is adsorbed (Figure 3.11e-f). Step by step this new phase covers the entire surface. Domain walls around the islands are bent and "stick" to them. Figure 3.12 shows an STM image of surface region with domain walls, crowdions and the islands of the new structure. The local periodicity of the surface structure inside the islands is 3×3. In the next section we will discuss in details the 3×3 phase.

3.4 The (3×3) structure

Figure 3.13a shows LEED pattern recorded at room temperature. It corresponds to the same surface coverage as STM image on the Figure 3.11f. The LEED pattern consists of many diffraction spots and is rather complex. The brightest spots have the coordinates 0.72 (in the units of reciprocal vectors) that is in good agreement with previously reported LEED data [6,1,2,3,4,5,17]. To our experience this LEED pattern does not change when the surface is cooled down to 100 K. On the atomically-resolved STM image of this surface structure recorded at 5 K (Figure 3.13b) a system of triangular islands can be seen. The average size of the islands is 15-30 Å. They are surrounded by a poorly-ordered structure that can be described as compressed chlorine (√3×√3)R30° layer. It consists of domain walls fragments. The same STM images can be observed for the surface temperature 77 K. The FFT of STM image from Figure 3.13b is very similar to the LEED pattern of saturated Cl layer (compare Figures 3.13c and 3.13a). The contribution to diffraction and FFT patterns of poorly-ordered compressed layer can be seen as increase of diffuse background intensity close to (√3×√3)R30° spots.

As it was already mentioned the islands have (3×3) local periodicity (Figure 3.13d). That corresponds to the size of the unit cell 8.67×8.67 Å. As it follows from Figure 3.13d the surface structure in neighboring islands is out of phase. Hence the new phase can be considered as the system of anti-phase domains (islands) of (3×3) structure. There are 9 possible antiphase domains of (3×3) structure on the (111) face of fcc crystal. It is well known that a system of antiphase domains will give rise to the splitting of diffraction spots in LEED [18,19,20,21]. In fact diffraction spots on the Figure 3.13a are grouped around the (3×3) positions so the LEED pattern can be considered as split (3×3) pattern.

The spot splitting on the LEED and FFT pattern is explained by the phase shift between neighboring (3×3) islands. In Chapter 2 we already discussed the influence of antiphase domains on LEED pattern, but for the case of ordered surface structures. Actually there is no need for perfect ordering of antiphase islands for spot splitting. According to MacKee et al. [19] splitting arises from the interference of electron beams diffracted by antiphase domains. Houston and Park have shown that sharp diffraction pattern with splitted spots can be observed even for the system with wide distribution of antiphase domain sizes [21]. In such case the magnitude of the splitting is given by the average size of domains. Besides the main effect – interference of electron beams

diffracted by antiphase domains – MacKee et al. studied the influence of domain arrangement and the distances between them on the final diffraction pattern [20].

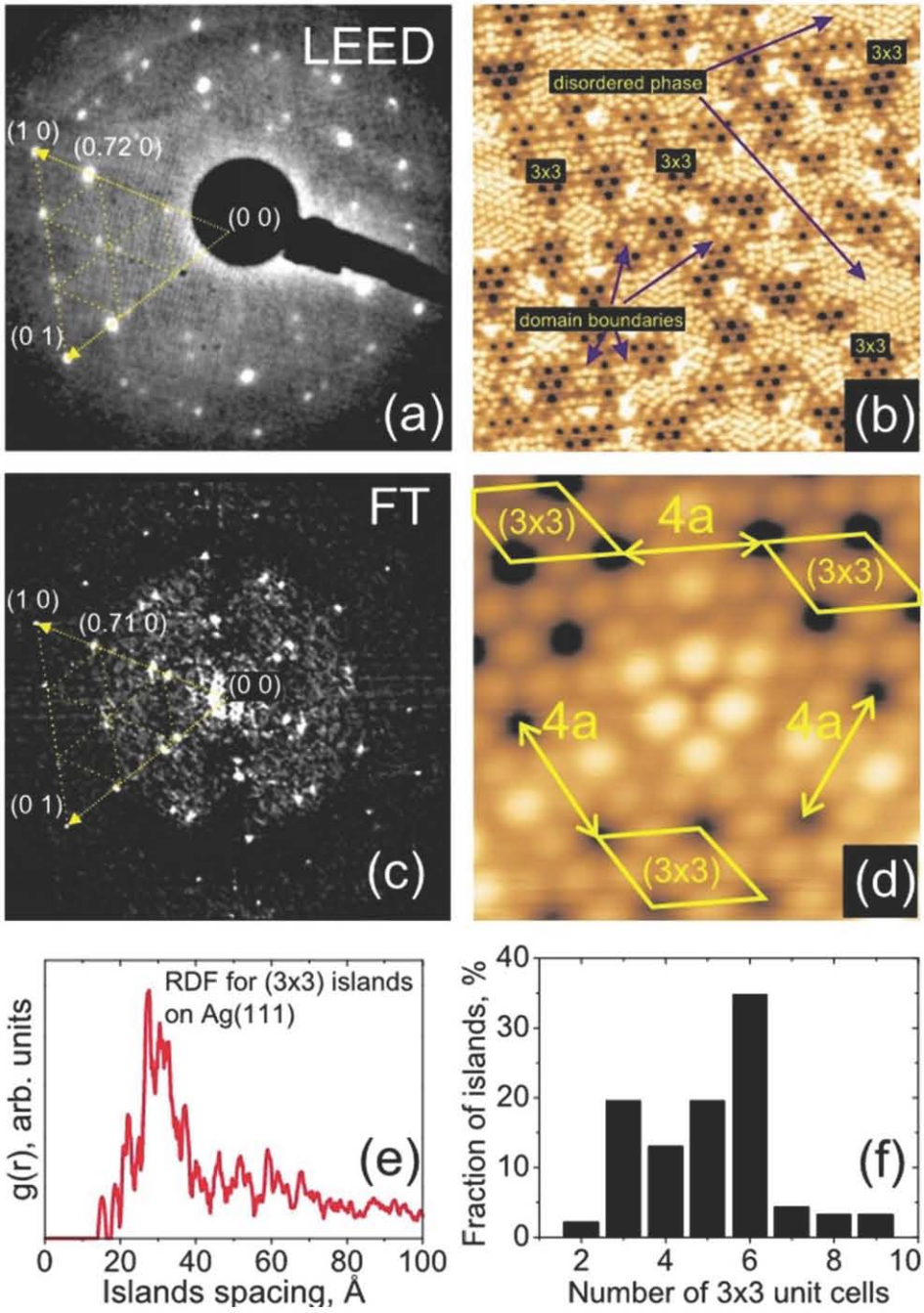

Figure 3.13. ***(a)*** *LEED pattern (E_0 = 76 eV, 300 K) obtained for Cl on Ag(111) at coverage close to saturation.* ***(b)*** *STM image (200×200 Å^2, U_s = –1.0 V, I_t = 1.6 nA, T = 5 K) taken for the same chlorine coverage as LEED pattern on (a).* ***(c)*** *FFT of STM image (b). Position of diffraction spots for ideal (3×3) structure on (a) and (c) coincides with the knots of the grid (draw with dotted line).* ***(d)*** *high resolution STM image showing coexistance of antiphase (3×3) domains.* ***(e)*** *Extracted from experimental STM images radial distribution function g(r) for 2D array of (3×3) islands.* ***(f)*** *Islands size distribution shown as a function of the number of (3×3) unit cells in the island*

According to their results the spot splitting pattern remains and it depends on the size of the domains and the distances between them. In our system the distribution of islands sizes 15–30 Å and distances between them 20–40 Å (see Figure 3.13e, f) is narrow enough so sharp spots can be observed on both LEED and FFT patterns. Thus it appears that the structure of chlorine layer at this coverage range is in average incommensurate to the substrate. In all previous studies the authors tried to describe this structure as a partially-commensurate lattice that is impossible and gave rise to numerous contradictions in the interpretation of the same experimental results.

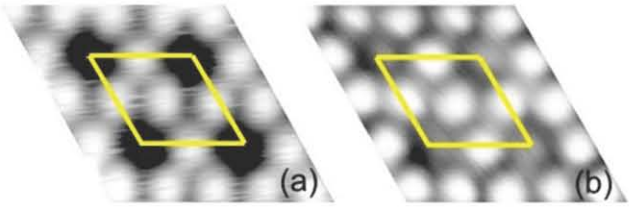

Figure 3.14. *Experimental STM images of the (3×3) island acquired at 5 K with different tunnel conditions:* ***(a)*** $U_s = -773$ *mV,* $I_t = 0.2$ *nA;* ***(b)*** $U_s = 50$ *mV,* $I_t = 2.0$ *nA*

Let us now discuss atomic structure of (3×3) phase. Figures 3.14a shows an STM image of (3×3) island in more details. Bright hexagons of atoms with dark hollow inside can be clearly seen. Each bright protrusion in the hexagon is identified with a single chlorine atom. For our knowledge halogen atoms on fcc metal surface are always imaged in STM as protrusions (for example [22,23]). We also note that for all range of bias voltage used in the present study (from –2 V to +2 V) single chlorine atoms on the Ag(111) surface (for the coverage $\theta \leq 0.37$ ML) were always imaged as protrusions. Moreover on the calculated STM images of (3×3) structure shown below chlorine atoms also appears as protrusions.

We can calculate surface coverage for all chlorine atoms visible on the Figures 3.14a. It makes $\theta = 0.33$ ML. However according to our data the nucleation of (3×3) islands starts at $\theta \approx 0.38$ ML. Hence we can assume that dark hallows inside the hexagons contains additional chlorine atoms. To check this assumption we took STM images of (3×3) structure with different scanning parameters – tunnel current and bias voltage. When the tunnel current is increased up to 2 nA and the bias voltage reduced below 100 mV additional chlorine atom inside the hallow becomes visible (Figures 3.14b). Taking into account additional chlorine atom in the hollow the surface coverage for (3×3) structure makes 0.44 ML which agrees better with our experimental data and estimation done in [6]. Note that chlorine atoms inside the hollows are shifted off-center towards one of the 6 equivalent positions near the borders of the hexagon (Figures 3.14b).

Regardless to the tunnel conditions all atoms in the (3×3) structure lies lower than chlorine atoms in neighboring compressed (√3×√3)R30° layer by 0.5 Å. The atomic corrugation inside the (3×3) structure is also rather large and is equal to 0.5 Å. This suggests possible surface reconstruction involved into formation of (3×3) phase. Existence of bright objects on the edge of islands (see Figure 3.13b) is the additional argument for surface reconstruction. Such objects could be the clusters of residual silver extruded from the substrate during reconstruction.

We based atomic structural model of (3×3) phase on the same idea as the surface reconstruction of Ag(111)-p(4×4)-O system [24,25]. According to the model 3 atoms of silver are removed within the surface (3×3) unit cell. Residual 6 silver atoms are

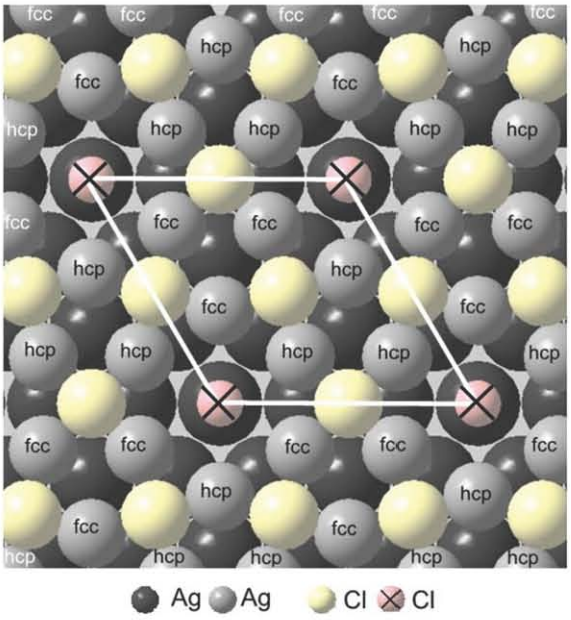

Figure 3.15. *Structural model of the (3×3) reconstruction. Within (3×3) unit-cell six Ag atoms in top layer are arranged in two triangles with atoms occupying fcc and hcp sites. Chlorine atoms may be placed between four Ag atoms and on top of the silver atom in the hole*

rearranged into two triangles of three atoms in each one. In one of the triangles atoms occupy fcc hollows and in another one hcp hollows. Chlorine atoms occupy two-fold hollows between fcc and hcp triangles (between 4 silver atoms) (Figure 3.15). Additional chlorine atoms are placed into the hollows on the corners of (3×3) unit cell. This model was used for the following DFT calculations.

Figure 3.16 shows the results of atomic coordinates' optimization and calculated STM images. Structural model as shown on Figure 3.15 but without chlorine atoms in the corners of the (3×3) unit cell was calculated first. The calculated STM image (Figure 3.16a) is in good agreement with the experimental one except the bright features inside the hexagons. These features can't be reproduced in calculations for any tunnel conditions. This proves that bright features inside the hexagons are due to additional chlorine atoms placed into the holes on the corners of (3×3) unit cell. Figure 3.16b shows results of DFT calculations for the same atomic model with chlorine atoms on the corners of (3×3) unit cell. According to our initial model (Figure 3.15) this additional atom was placed precisely above the silver atom in the hollow. It appears that for the large tip-sample distances (3-4 Å) there is no additional feature inside the hexagon. However for smaller distances (2-3 Å) calculated STM images demonstrate bright features inside the hexagons, precisely in the center. We can suppose that such on-top position for chlorine atom in the corner hall should be unstable. In order to find the stable adsorption position for this atom we modified initial model and shifted the corner chlorine atoms by 0.1 Å off-center of the hexagon. The results of calculations are shown on the Figure 3.16c. Chlorine atom in the corner hole has the minimal adsorption energy when it is shifted 0.7 Å off-center along direction of close-packed rows of the substrate (i.e. towards the borders of the hexagon). As a result chlorine atom is placed on the equal distance (about 2.7 Å) from two silver atoms in the reconstructed layer and one silver atom in the next unreconstructed layer which is in the center of the corner hole (Figure 3.16c), i.e. it occupy a three-fold adsorption site. This adsorption position is very similar to the three-fold hollow adsorption site of chlorine atoms in $(\sqrt{3}\times\sqrt{3})R30°$ structure, where the Cl-Ag distance is 2.62–2.66 Å [8]. Due to the symmetry of the system the corner chlorine atom can be shifted in any of 6 different directions. Adsorption energies for all three tested (3×3) structures together with adsorption energy for unreconstructed $(\sqrt{3}\times\sqrt{3})R30°$ layer are shown in the Table 3.2. The gain in the adsorption energy for non-symmetric position of

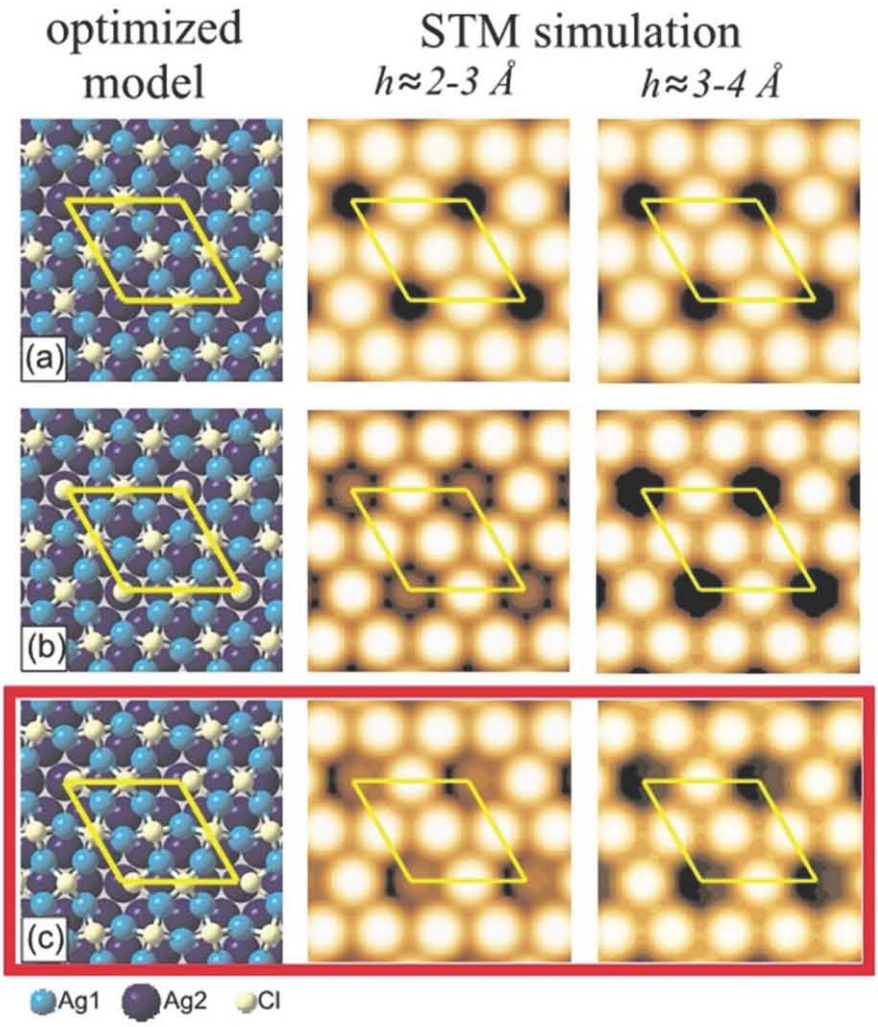

Figure 3.16. *Structural models and Tersoff-Hamann simulated STM images for the (3×3) phase calculated for two different tip heights: 2–3 Å and 3–4 Å.* ***(a)*** *The model without atoms in the holes (coverage 0.33 ML);* ***(b)*** *the model with one Cl atom per hole placed in symmetrical position (coverage 0.44 ML); and* ***(c)*** *the equilibrium structure with one Cl atom per hole shifted off-center by 0.7 Å in the direction of the close-packed atomic rows of Ag(111) surface (coverage 0.44 ML)*

corner chlorine atom (Figure 3.16b) relative to the symmetric position (Figure 3.16c) is 18 meV for each chlorine atom. Calculated STM images demonstrate the off-center feature inside the hexagons for small tip-surface distances, in good agreement with experimental observations (Figures 3.14b).

Table 3.2. *Calculated adsorption energies for different chlorine structures on Ag(111).*

Structure	θ, ML	E_{ads}, eV/atom
(√3×√3)R30° (fcc)	0.33	–1.543
(3×3) Fig. 16*a*	0.33	–1.320
(3×3) Fig. 16*b*	0.44	–1.342
(3×3) Fig. 16*c*	0.44	–1.360

To complete analysis we tested several other structural models. A structural model similar to the one discussed above but with additional silver atoms in the corner holes was tested. Calculated STM images (not shown here) demonstrate bright features

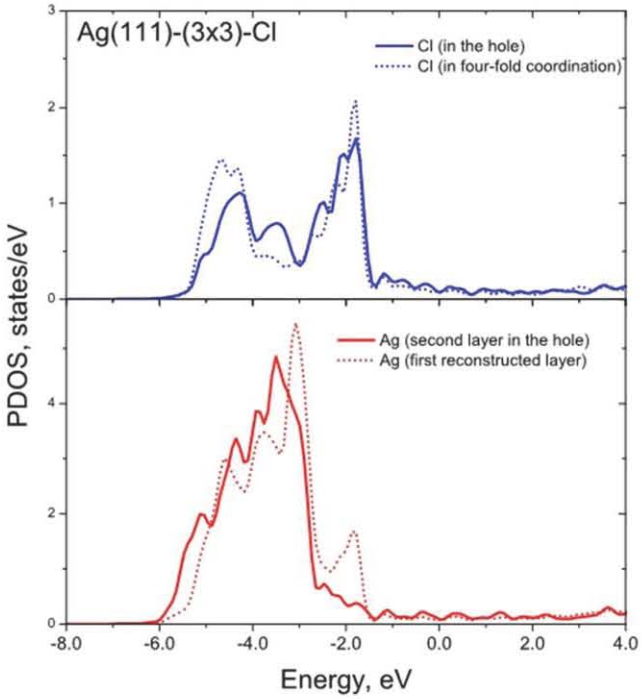

Figure 3.17. *Density of states projected on chlorine and silver atoms calculated for Ag(111)-(3×3)-Cl structure. The energies are shown with respect to Fermi level*

inside the hexagons, visible for small tip-surface distances. However we were not able to get non-symmetrical position for this additional silver atom. DFT calculations have shown that the most stable position for this atom is on-top site. This is not in line with our experimental findings. Moreover such structural model gives to low (0.33 ML) chlorine coverage. A model of a simple chlorine (3×3) overlayer together with the model of corrosion layer proposed by Rovida et al. [3] were also tested. These structures appeared to be unstable during optimization of atomic coordinates. They gave calculated STM images that significantly differ from experimental data.

Our experimental and theoretical results (Figure 3.16 and Table 3.2) can be regarded as the evidence of general trend found by Gava et al. in the DFT study of Cl/Ag(111) system [26]. The authors report on the dependence of chlorine adsorption energy on the surface coverage. According to their calculations adsorption energy decreases for chlorine coverage $\theta > 0.33$ ML. At a critical coverage $\theta = 0.5$ ML the mixed on-surface and substitution adsorption structures become competitive with the simple on-surface adsorption. In these terms, the (3×3) structure corresponding to coverage of 0.44 ML can be considered as the initial stage of the mixed layer formation since Cl atoms in the hole are only 0.5 Å higher than silver atoms from the upper silver plane.

For the final (3×3) model we also calculated PDOS for chlorine and silver atoms (see Figure 3.17). The clearly seen mixing of chlorine and silver states indicates the covalent bonding. Note that similar PDOS curves were reported in [26] for simple chlorine overlayer.

3.5 Saturated chlorine layer: Ag_3Cl_7 clusters

Further chlorine adsorption on Ag(111) leads to complete reconstruction of the surface. Figure 3.18a shows a typical LT-STM image of chlorinated Ag(111) surface corresponded to the Cl coverage slightly below the saturation level. Figure 3.18b shows the STM image of saturated coverage formed as a result of a room temperature chlorine adsorption on Ag(111). According to the STM image, regions with compressed chlorine layer adsorbed on an unreconstructed substrate disappeared, while the most part of the surface is covered with (3×3) reconstruction with characteristic dark corner holes. In addition, numerous new bright objects on the boundaries of adjacent (3×3) islands appeared, as one can see on Figure 3.18b.

The STM images acquired with higher resolution presented on Figures 3.18c,d indicates that each bright object can be considered as a cluster with a six-atom basement and bright atom (or group of atoms) in the middle. Triangles of six atoms lying in the basement of clusters are formed on the early stage of (3×3) islands growth and they play the role of domain boundaries between three adjacent (3×3) domains, as one can see on Figures 3.18c,d and Figure 3.13d.

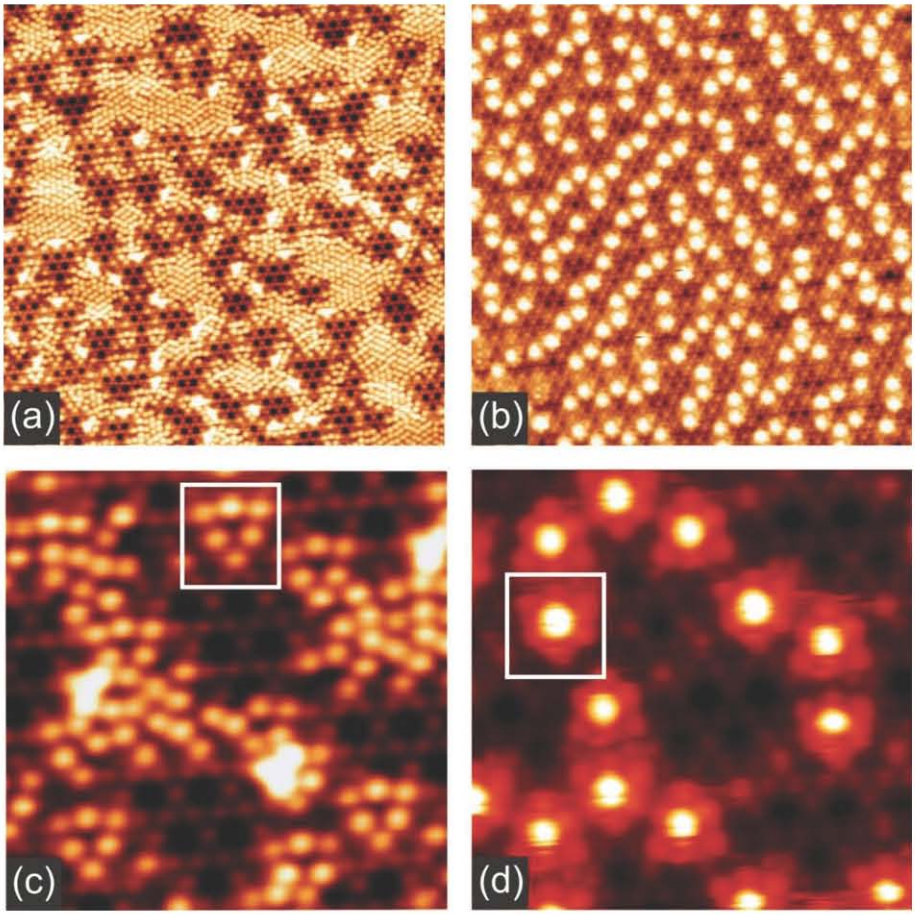

Figure 3.18. *STM images (292×292 Å^2) showing chlorinated Ag(111) surface at coverage:* ***(a)*** *slightly below the saturation level;* ***(b)*** *at full saturation. STM images (68×68 Å^2) showing:* ***(c)*** *the basement of a cluster;* ***(d)*** *complete cluster*

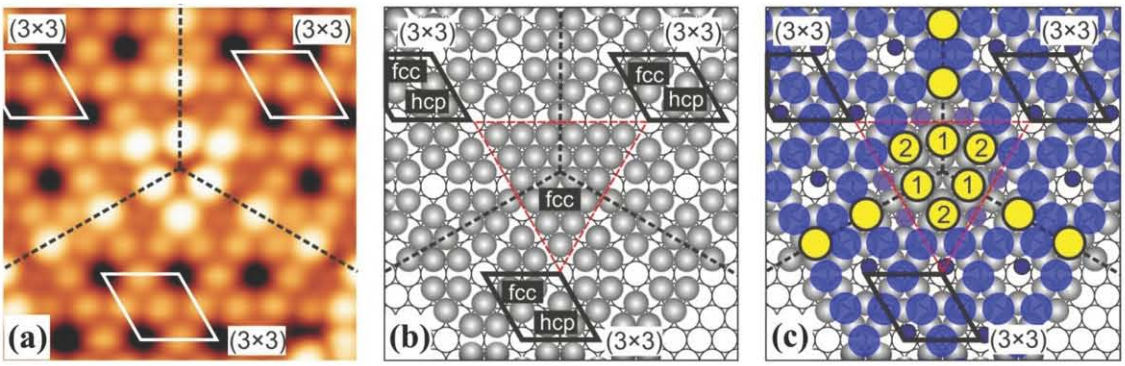

Figure 3.19. ***(a)*** *Experimental STM image of the boundary between three (3×3) islands. Domain boundaries are highlighted with dashed line* ***(b)*** *Hard ball model demonstrating arrangement of silver atoms in the upper layer in each of three (3×3) domains and under the domain boundary. Formation of the big fcc triangle (outlined in red dashed line) with 1×1 periodicity is clearly seen.* ***(c)*** *Hard ball model showing positions of chlorine atoms (in yellow) on the basement from (b)*

Figure 3.19 presents experimental STM image and corresponding model drawings showing positions of silver and chlorine atoms in area close to the domain boundary. To create these hard ball models, we used the model of the (3×3) reconstruction discussed in the previous section. According to the models presented in Figure 3.19b, in the place of the intersection of neighboring domains the triangle of 21 silver atoms packed in (1×1) lattice forms. In our model this silver triangle is covered by six chlorine atoms occupying two different three-fold positions marked in Figure 3.19c as "1" and "2" and forming characteristic bright triangle. As it follows from STM images in Figure 3.18, there are two different orientations of chlorine triangles on the surface ("corner up" and "corner down"). If we assume that silver atoms in the (1×1) triangle lying in the basement of the domain

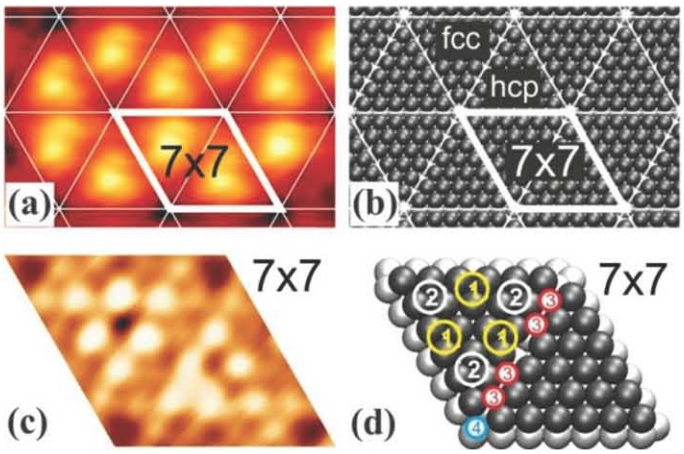

Figure 3.20. ***(a)*** *Experimental STM image demonstrating partial ordering of clusters in the (7×7) superstructure;* ***(b)*** *The arrangement of silver atoms in upper layer corresponds to the STM image from (a);* ***(c)*** *Hard ball model of the (7×7) reconstruction. Different adsorption sites for chlorine atoms are indicated. Threefold positions marked as "1" and "2" correspond to atoms in the basement of clusters. Chlorine atoms also occupy the site "3" with nearly four-fold symmetry and the corner-hole site "4" as in (3×3) reconstruction*

boundary in Figure 3.19 occupy fcc positions, then silver atoms in the basement of the domain boundary with opposite orientation should occupy hcp sites. Since fcc positions are more favorable than hcp ones, the preferable "corner down" orientation of chlorine triangles in Figure 3.18a,c is not surprising.

To determine atomic structure of clusters we used DFT calculations. In general case, clusters do not form a periodic lattice. However, in some places clusters form a new "rosette-like" superstructure described by a (7×7) unit cell as shown on Figure 3.20a. Taking into a ccount that the basement of each cluster is formed by a triangle of 21 silver atoms with (1×1) periodicity (Figure 3.19), we present on Figure 3.20b a model showing arrangement of silver atoms in the basement of the (7×7) reconstruction. Within (7×7) unit cell there are two oppositely oriented triangles of silver atoms. In the first triangle, atoms occupy fcc sites, whereas in the second one – hcp. Chlorine atoms may occupy threefold hollow adsorption sites on silver triangles marked as "1" and "2", forming a characteristic chlorine triangle, as shown on Figure 3.20c. Between silver triangles there are nearly fourfold hollow adsorption sites marked as “3” similar to the case of the original (3×3) reconstruction. Similar to the case of the (3×3) reconstruction, the holes in the corners of the (7×7) unit cell are occupied by chlorine atoms in positions “4”.

In fact, in the (7×7) structure each domain of the original (3×3) reconstruction degenerate into a single element containing one ring of chlorine atoms around a corner

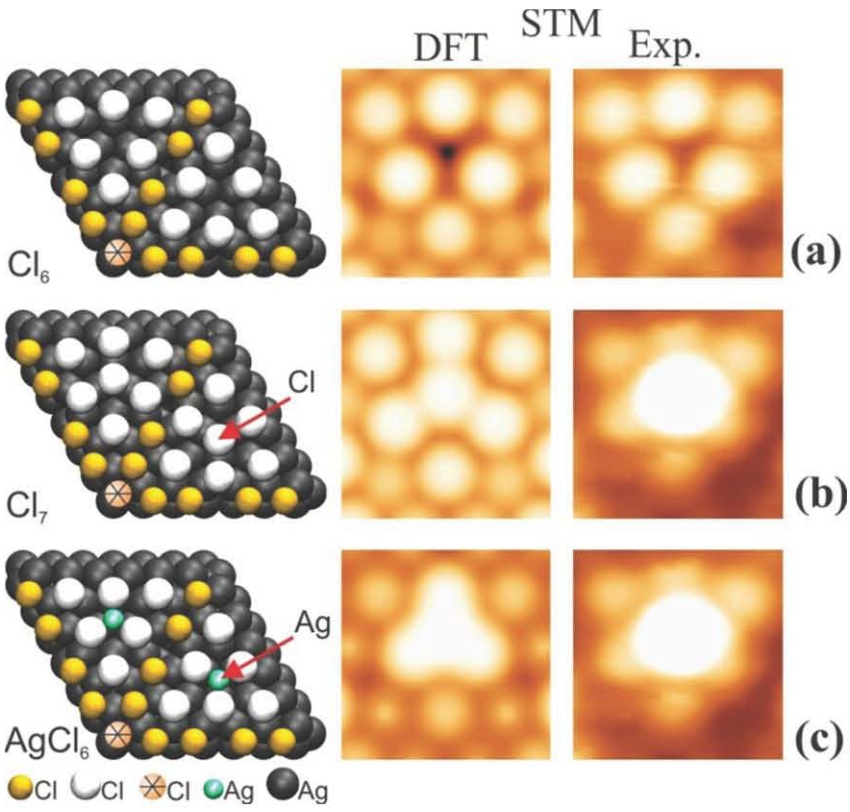

Figure 3.21. (a) *Structural model of the chlorine 6 -atom triangle and corresponding theoretical STM image shown in comparison with experimental STM image;* ***(b,c)*** *Cluster models Cl_7 and $AgCl_6$ together with theoretical STM images shown in comparison with STM image of the cluster obtained at saturation of chlorine coverage*

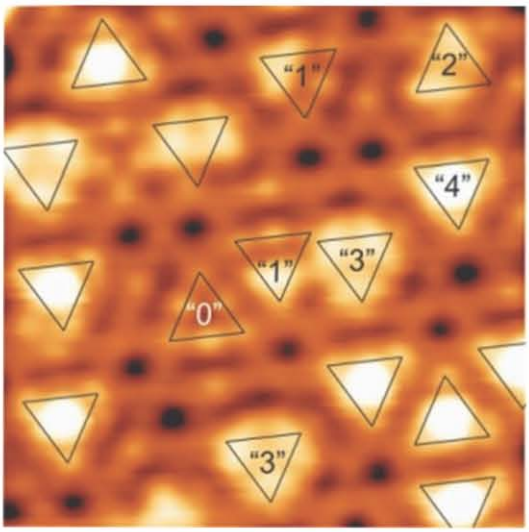

Figure 3.22. *Experimental STM image (70×70 Å^2, I_t = 1.5 nA, U_s = + 536 mV, T = 5 K) of almost saturated Cl layer on Ag(111) demonstrating different stages of clusters formation. "0" - unfilled triangles, "1" - one additional object in the corner, "2" - two objects in the corners, "3" - three objects in each corner, "4" - complete cluster*

hole. Note that a complete (7×7) reconstruction is not realized in a real experiment even at saturation coverage. However, it appears to be very convenient for DFT modeling of the clusters due to the minimal size of the unit cell. That is why all model calculations performed for clusters were made using the (7×7) unit cell.

In our DFT calculations we considered all the stages of clusters formation starting from a simple model of the six chlorine atoms triangle as shown in Figure 3.21. W e have calculated theoretical STM image for this structure using Tersoff-Hammann model [27]. The result of calculations obviously reproduces all features of the experimental STM image including a difference of the brightness between chlorine atoms in different types of the threefold positions (marked in Figure 3.20c as "1" and "2").

On the next stage, we have tested two simple structures with additional chlorine or silver atom placed in the middle of a 6-atoms chlorine triangle. The models and results of calculations are shown in Figures 3.21b,c together with an experimental STM image of the cluster. We see that the correspondence of the both theoretical images with the experiment is rather poor.

To look for a correct model, we considered an STM image corresponding to the case of incompletely formed clusters as shown in Figure 3.22. One can find five different types of objects on the surface. A simple triangle containing six chlorine atom is marked as "0". In all objects marked as "1" we detect a light spot in one of the corners of triangle. In the objects "2" already two corners are occupied, and in the objects "3" there is a light spot in each corner of triangle. Note also, the presence of the distinct minimum in the center of the object "3". Finally, we marked as "4" the complete clusters with characteristic bright spots in the center of triangle. We believe that objects "1"-"4" represent different successive stages of clusters formation. In this process the initial basement "0" accumulates step-by-step four additional atoms (chlorine and/or silver).

We assume clusters to be AgCl particles of the minimum size taking into account their formation at saturated

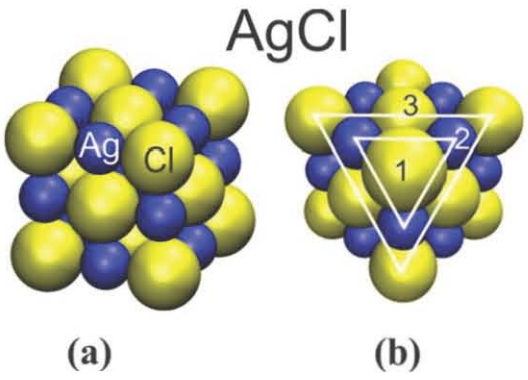

Figure 3.23. *The crystal structure of AgCl (NaCl-type).* ***(a)*** *3D view.* ***(b)*** *Orthographic projection of AgCl structure on the {111} plane. Three upper planes are indicated as "1", "2" and "3"*

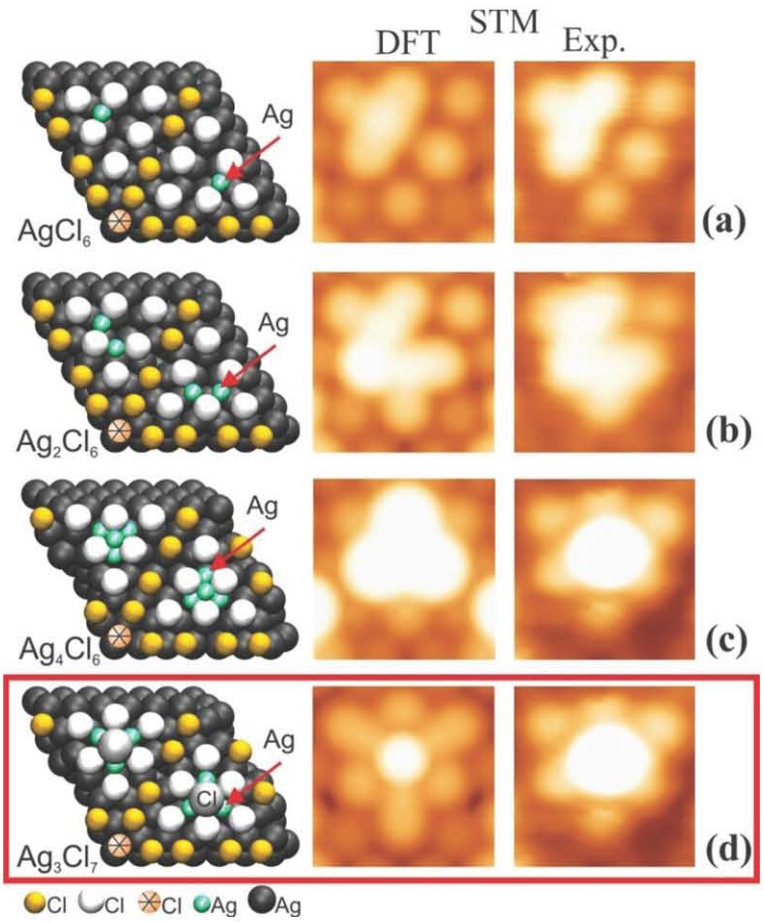

Figure 3.24. *Structural models describing the formation of clusters and corresponding theoretical STM images shown in comparison with experimental observations.* ***(a)*** *Cluster $AgCl_6$.* ***(b)*** *Cluster Ag_2Cl_6.* ***(c)*** *Cluster Ag_4Cl_6.* ***(d)*** *Cluster Ag_3Cl_7. Theoretical STM images for (a) and (b) are shown in comparison with appropriate experimental STM images acquired at intermediate coverage. For (c) and (d) comparison was made with STM image of cluster obtained at saturation*

coverage. We note that bulk crystal of silver chloride forms crystal lattice of NaCl type and consists of two fcc lattices of silver and chlorine atoms as seen on Figure 3.23a. Chlorides of fcc metals are known to grow on metal surfaces with their hexagonal plane being parallel to the substrate [28,29,30,31]. In Figure 3.23b projection of the AgCl "cube" on a {111} plane is presented. We see that the upper plane consists of a single chlorine atom in the corner of the cube. Next plane contains thre e silver atoms. Finally, in the third plane we see a triangle of six chlorine atoms, being similar to triangle in the basement of the clusters in our experiments. Thus, using an analogy with bulk silver chloride structure, we can assume that for explanation of our experimental data it is naturally to use a model of silver chloride cluster Ag_3Cl_7 (Cl-Ag3-Cl6). We also note that additional silver atoms that are necessary for Ag_3Cl_7 formation could come from the upper silver layer in the course of the (3×3) reconstruction.

Figure 3.24 presents optimized models and corresponding theoretical and experimental STM images (U_s = -500 mV) for different stages of Ag_3Cl_7 formation on the basement of a six atom triangle. According to our calculations, additional silver atom in a

corner of triangle gives rise to appearance of the lig ht feature in a good correspondence with the experimental observation (Figure 3.24a). These kind of objects (cluster $AgCl_6$) appear in the STM images rather early simultaneously with islands of the (3×3) reconstruction, as seen from Figures 3.18a and 3.13b.

Further DFT calculations were performed for cluster Ag_2Cl_6 corresponding to occupan cy of two corners of triangles with silver atoms. Excellent agreement of experimental and theoretical STM images is obvious from Figure 3.24b. A cluster Ag_3Cl_6 with three silver atoms in the corners of triangle was also considered with DFT. However, it is not shown in the Figure 3.24 since we were not able to acquire a high-resolution STM image of such objects at negative bias voltage required for the correct comparison with the theoretical images. At positive voltages (see Figure 3.22), the resolution appeared to be much worse.

On the final step of the cluster design we have tested silver (Figure 3.24c) and chlorine atoms (Figure 3.24d) placed in the middle of Ag_3Cl_6 cluster. We see that the model with four silver atoms does not correspond to the experimental observation, whereas the theoretical STM image of the Ag_3Cl_7 pyramid with chlorine atom on the top and experimental STM image of cluster observed at saturation are very similar.

Thus, we have shown that a two-dimensional array of Ag_3Cl_7 clusters is formed on the Ag(111) surface saturated with chlorine. The sequence of atomic layers in Ag_3Cl_7 corresponds to sequence of layers in silver chloride bulk crystal in the direction {111}. Optimized atomic coordinates for Ag_3Cl_7 model obtained as a result of the DFT calculations are presented in Table 3.3.

It is of interest to analyze the atomic structure of the Ag_3Cl_7 pyramid in comparison with AgCl lattice. In the case of bulk AgCl the interplane distances in a <111> direction are equal to 1.60 Å [32]. In the case of Ag_3Cl_7, the distance between upper chlorine atom and the plane consisting of three silver atoms is equal to 1.468 Å, that is in a good agreament with value for bulk crystal. In our model pairs of atoms Ag1-Ag2, Ag2-Ag3 and Ag3-Ag1 are separated by distance of 3.636 Å that is slightly less than the nearest neighbor distances in a {111} plane of bulk AgCl crystal equaled to 3.93 Å [32].

Table 3.3. *Atomic coordinates of chlorine and silver atoms in the Ag_3Cl_7 cluster*

Atom label	x_{DFT} **(Å)**	y_{DFT} **(Å)**	z_{DFT} **(Å)**
Cl0	0.000	11.928	11.218
Ag1	-1.818	12.978	9.752
Ag2	-1.818	12.978	9.752
Ag3	0.000	9.829	9.752
Cl1	-4.023	14.251	9.393
Cl2	0.000	15.198	9.334
Cl3	4.023	14.251	9.393
Cl4	2.832	10.293	9.334
Cl5	0.000	7.283	9.393
Cl6	-2.832	10.293	9.334

The distance between silver plane in Ag_3Cl_7 and an average chlorine plane lying in the basement appears to be rather short ~ 0.39 Å. Moreover, the interatomic distances in the basement chlorine plane (~ 4.3 Å) correspond to characteristic distances in chemisorbed monolayer. According to our analysis, upper chlorine atom and three silver

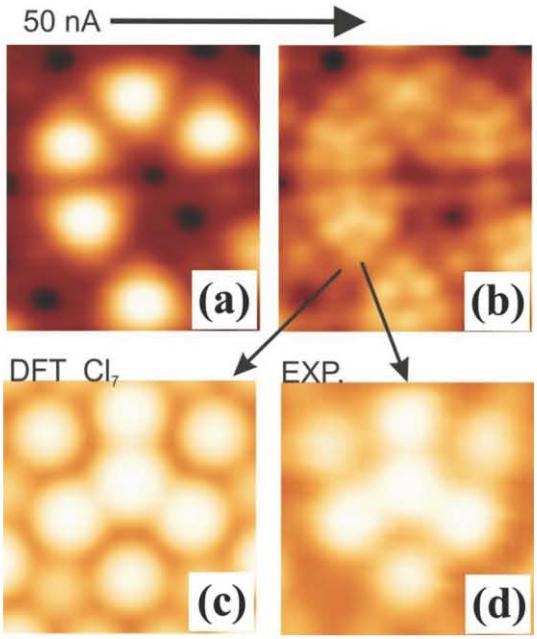

Figure 3.25. *STM images (36×40 Å^2, I_t = 1.5 nA, U_s = + 536 mV, T = 5 K):* ***(a)*** *- before and* ***(b)*** *- after scanning of selected surface area with tunnel current 50 nA.* ***(c)*** *Theoretical image of Cl_7 cluster.* ***(d)*** *High resolution STM image (I_t =1.5 nA, U_s = - 500 mV) of the cluster modified by the tip action*

atoms occupy positions in a slightly distorted AgCl lattice. The basement of the Ag_3Cl_7 cluster could be considered in some sense as an interface between Ag(111) substrate and silver chloride cluster Ag_3Cl.

It is noteworthy that Ag_3Cl_7 clusters are rigid and can be easily modified by the tip of STM even at 5 K. Indeed, we found out that scanning the surface with tunnel current increased up to 50 nA leads to the modification of the clusters, as shown in Figures 3.25a,b. We see that all the bright objects were removed from the basement. Even after action of the tip the centers of some triangles remain to be occupied. The high-resolution STM image of this new object shown in Figure 3.25c appear to be exactly the same as a theoretical STM image of the cluster Cl_7 initially presented in Figure 3.22. Artificial cluster Cl_7 was never observed after room temperature chlorine adsorption. In any case, this observation is an additional support of the structural model suggested for description of the experimentally observed clusters.

3.6 Conclusion

The structure of chlorine layer on Ag(111) surface has been studied for a wide range of surface coverage (from 0 ML up to saturation) with the use of low temperature scanning tunneling microscopy and density functional theory. A number of surface structural transitions was observed during increase of surface chlorine coverage and change of surface temperature. We can summarize our results as follows:

1. Chlorine atoms form chains at low Ag(111) surface temperature (5 K) and coverage less than 0.33 ML.
2. During compression of commensurate (√3×√3)R30°-Cl structure a two-dimensional gas of interstitial defects (crowdions) appears first, after that a system of heavy domain walls is formed.
3. It was shown that complex LEED pattern from saturated chlorine layer can be explained as diffraction from the system of small (15-30 Å) antiphase domains with (3×3) reconstruction. A structural model for (3×3) reconstruction was proposed and verified by DFT calculations.
4. Saturated chlorine layer on Ag(111) surface consists of small anti-phase domains with (3×3) reconstraction and Ag_3Cl_7 clusters on the remaining small unreconstructed areas.

Bibliography of Chapter 3

[1] P.J. Goddard, R.M. Lambert. Adsorption-desorption properties and surface structural chemistry of chlorine on Cu(111) and Ag(111) // Surf. Sci. 67 180 (1978).

[2] G. Rovida et al. LEED study of chlorine chemisorption on the silver (111) surface // Japanese Journal of Applied Physics 2, 117-120 (1974).

[3] G. Rovida, F. Pratesi. Chlorine monolayers on the low-index faces of silver // Surf. Sci. 51 280 (1975).

[4] Y.Y. Tu, G.M. Blakely. Chlorine adsorption on silver surfaces // Journ. Vac. Sci. and Techn. 15 563 (1978).

[5] M. Bowker, K.C. Waugh. The adsorption of chlorine and chloridation of Ag(111) // Surf. Sci. 134 639(1983).

[6] A. G. Shard, V. R. Dhanak. Chlorine Adsorption on Silver (111) at Low Temperatures // Journ. Phys. Chem 104 2743 (2000).

[7] B.V. Andryushechkin et al. Atomic structure of saturated chlorine monolayer on Ag(111) surface // Surf. Sci. 407 L633 (1998).

[8] N.H. De Leeuw et al. Density-functional the-ory calculations of the adsorption of Cl at perfect and defective Ag(111) surfaces // Phys. Rev. B 69 045419 (2004).

[9] L.-G. Liu, W.A. Bassett. Compression of Ag and phase transformation of NaCl // J. Appl. Phys. 44 1475 (1975).

[10] A. Bondi. van der Waals volumes and radii // J. Phys. Chem. 68 441 (1964).

[11] R.S. Rowland, R. Taylor. Intermolecular nonbonded contact distances in organic crystal structures: comparison with distances expected from van der Waals radii // J. Phys. Chem. 100 7384 (1996).

[12] O.M. Braun, Y.S. Kivshar. The Frenkel-Kontorova model: concepts, methods, and applications // Springer (2004).

[13] A.G. Naumovets, A.G. Lyuksyutov, V. Pokrovsky. Two-dimensional crystals. // Academic Press (1992).

[14] P. Bak. Commensurate phases, incommensurate phases and the devils staircase // Rep. Progr. Phys. 45 587 (1982).

[15] K. Kern, G. Comsa. Physisorbed rare gas adlayers. In: R. Vanselow, R.E. Howe. Chemistry and Physics of Solid Surfaces // Berlin: Springer-Verlag, v. VII, 65–108 (1988).

[16] I.F. Lyuksyutov, H. Pfnur, H.U. Everts. Incommensurate-commensurate transition via domain wall evaporation in an overlayer // EPL 33, 673 (1996).

[17] K. Wu, D. Wang, J. Deng. Chlorine on Ag(111): intermediate coverage case // Surf. Sci. 264 249 (1992).

[18] L.J. Clarke. Surface crystallography: an introduction to low energy electron diffraction // A Wiley-Interscience Publication (1985).

[19] C.S. Mckee, D.L. Perry, M.W. Roberts. Models for an adsorbed layer and their evaluaтion вy comparison of leed and opтical diffracтion patterns: the system W(112)-O_2 // Surf. Sci. 39 176 (1973).

[20] C.S. Mckee, M.W. Roberts, M.L. Williams. Defect surface structures studied by LEED // Advances in Colloid and Interface Science 8 29–87 (1977).

[21] J.E. Houston, R.L. Park. Low-energy electron diffraction from imperfect structures // Surf. Sci. 21 209 (1970).

[22] B.V. Andryushechkin, K.N. Eltsov, V.M. Shevlyuga. Atomic scale observation of iodine layer compression on Cu(111) // Surf. Sci. 472 80 (2001).

[23] B.V. Andryushechkin, K.N. Eltsov, V.M. Shevlyuga. Domain-wall mechanism of "(n√3×n√3)R30°" incommensurate structure formation in chemisorbed halogen layers on Cu(111) // Surf. Sci. 470 L63 (2000).

[24] J. Schnadt et al. Revisiting the structure of the p(4×4) surface oxide on Ag(111) // Phys. Rev. Lett. 96 146101 (2006).

[25] M. Schmid et al. Structure of Ag(111)-p(4×4)-O: No silver oxide // Phys. Rev. Lett. 96 146102 (2006).

[26] P. Gava et al. Adsorption of chlorine on Ag(111): no subsurface Cl at low coverage // Phys. Rev. B 78 165419 (2008).

[27] J. Tersoff, D.R. Hamann. Theory of the scanning tunneling microscope // Phys. Rev. B 31 805 (1985).

[28] M. Galeotti et al. Epitaxy and structure of the chloride phase formed by reaction of chlorine with Cu(100). A study by X-ray photoelectron diffraction // Surf. Sci. 349 L164 (1996).

[29] B.V. Andryushechkin et al. Epitaxial growth of AgCl layers on the Ag(100) surface // Surf. Sci. 421 27 (1999).

[30] B.V. Andryushechkin, K.N. Eltsov, V.M. Shevlyuga. CuI growth on copper surfaces un-der molecular iodine action: influence of the surface anisotropy in the iodine monolayer // Surf. Sci. 566 203 (2004).

[31] B.V. Andryushechkin et al. Local structure of the Ag(100) surface reacting with molecular iodine: experimental and theoretical study // Phys. Rev. B 80 125409 (2009).

[32] R.W.G. Wyckoff. Crystal Structures // Interscience, John Wiley & Sons, v. 1 (1963).

CHAPTER 4.
Au(111) surface under molecular chlorine action

In the present chapter we continue the study of chlorine interaction with metals and present results on the chlorine adsorption on gold (111) surface. In the very-low coverage regime we observe, the same as for silver (111) surface, appearance of atomic chains. Rather unusual hexagonal superstructure of nano pores spontaneously formed from these chains has been observed. We explore the evolution of these structure with chlorine coverage, that finally leads to formation of commensurate ($\sqrt{3}\times\sqrt{3}$)R30° lattice. Thermal stability of nano pores superstructure was also investigated. For high-coverage regime we report appearance of single $AuCl_2$ clusters, which can be considered as specific surface gold chloride molecules. We observed interaction of these molecules with each other and their self-arrangement into honeycomb-like superstructure in saturation.

The results of our study can be naturally divided into two parts, depending on the surface coverage. As described in the first chapter of this thesis, the chlorine layer at coverage 0.33ML adopt on Au(111) the usual (√3×√3)R30° structure, also observed on the Ag(111) and Cu(111) surface. Here, we will first consider the processes that take place on the gold surface when the coverage is less than $\theta < 0.33$ ML. In this range of coverage removal of surface reconstruction and initial stage of formation of the (√3×√3)R30° lattice are observed. This stage of reaction matches with the appearance of peak β_1 in TDS as described in the literature [1, 2, 3]. In a second part we will discuss the results which concern coverage $\theta > 0.33$ ML, when (√3×√3)R30° structure is replaced by honeycomb-like structure. This process is accompanied by appearance of peak β_2 in TDS [1, 2, 3].

All the experiments have been done with the following method: chlorine is dosed on sample at room temperature and then the surface is frozen at 5K or at temperatures ranging from 5K to 77K in the STM. All STM observations have been done at temperature between 5K and 77 K.

4.1 Low coverage (from 0 to 0.33 ML)

4.1.1 Preferential adsorption and atomic chain formation

It is well known that clean Au(111) surface reconstructs and forms a 22×√3 structure, also known as herringbone reconstruction (Fig. 4.1). During reconstruction the density of gold atoms on the surface is increased by ~4 %, which leads to the non-uniform compression of the last atomic plane of gold crystal along <110> direction (direction of close-packed rows of gold atoms) [4]. As a result a periodic system of linear domains with fcc and hcp stacking is formed on the surface: in fcc domains gold atoms in the last plane are placed in their equilibrium position for fcc crystal (as gold has fcc crystal); in hcp domain surface atoms are shifted laterally and take place as in hcp crystal. The bright stripes on the image are the boundaries between alternating fcc and hcp domains. The boundaries correspond to stacking fault regions with increased density of atoms and thus are heavy domain walls. Periodicity of the structure in <110> direction is ≈ 65 Å, with fcc domains being broader (40 Å, as measured from our data) than hcp domains (25 Å). The zig-zag form of domains is explained by another reconstruction that removes excess of elastic energy on the surface [5, 6]. The length of domains between kinks is about 220 Å. Because of the surface reconstruction, diffraction spots on LEED pattern from clean Au(111) surface are split [7].

Our results, in agreement with previously reported data [1, 2, 3], show that chlorine adsorption on Au(111) surface in the temperature range 130-300 K is dissociative. Low-T STM-images of gold surface covered by small amount of chlorine ($\theta \leq 0.01$ MC) are shown on Fig. 4.1b-4.1d. As was already mentioned in previous chapter, halogen atoms are usually imaged in STM as bright protrusions. That's why we believe that bright objects of 5 Å in diameter, which appear after chlorine deposition, can be assigned to individual chlorine atoms.

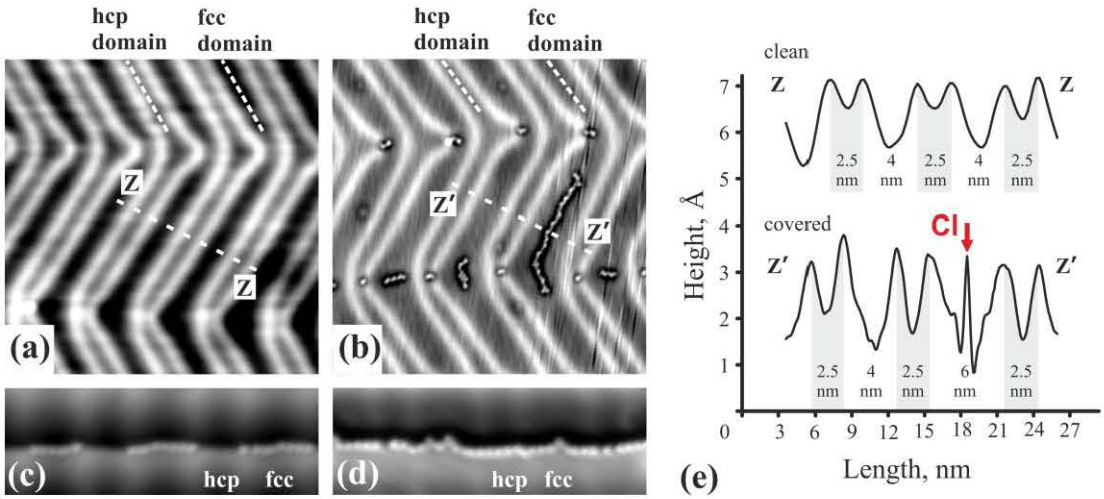

Figure 4.1. *STM image of Au(111)-22×√3.* ***(a)*** *Clean surface (360×360 Å^2, gap voltage U_s = –0.1 V, tunnel current I_t = 0.5 nA, 5 K); fcc and hcp domains are shown.* ***(b)*** *Chlorine atoms adsorbed in kinks of surface reconstruction (360×360 Å^2, U_s = 1.0 V, I_t = 1.0 nA, 5 K, $\theta \approx 0.005$ ML).* ***(c)*** *Chlorine atoms adsorbed on the atomic step edge in fcc domains (150×50 Å^2, U_s = –1.0 V, I_t = 1.5 nA, 5 K, $\theta < 0.01$ ML).* ***(d)*** *Fully decorated atomic step edge (150×50 Å^2, U_s = –0.25 V, I_t = 1 nA, 5 K, $\theta \approx 0.01$ ML).* ***(e)*** *Profiles ZZ and Z′Z′ from (a) and (b)*

From the distribution of chlorine atoms over the surface it is clear that the most attractive adsorption centers are defects – kinks of the reconstruction (Fig. 4.1b) and atomic steps (Fig. 4.1 c,d). This observation confirms results of DFT calculations published previously [8]. According to [8] adsorption energy for chlorine atom is highly increased in vicinity of vacancy, adatom or atomic step. In the latter case gain in adsorption energy is 0.38 eV. According to our observations, chlorine atoms first occupy positions on the atomic steps that are inside fcc domains. This behavior is similar for different species adsorbed on gold surfaces [9]. Only after all these positions are occupied chlorine atoms start to decorate the rest of the steps in hcp domains. Kinks of herringbone reconstruction are also known for their adsorption activity because of defects in gold atoms packing there [10]. Most of chlorine atoms are concentrated in the kinks of fcc domains. Such agglomerations contains up to 10 chlorine atoms, which leads to the local broadening of domains.

At higher coverage, when all adsorption centers close to the defects are occupied, chlorine atoms start to fill terraces but occupy only fcc domains (Fig. 4.2a). They form linear chains along the length of domains inside fcc regions of the gold surface. Along the chains, two different adsorption sites can be found, labeled A and B on Figure 4.2. For A and B arrangement, neighboring atoms are separated by distances 5.0 and 4.5 Å respectively. DFT calculations by Gao et al. [2] have predicted that the preferential adsorption site for chlorine atoms on Au(111) surface is fcc position; hcp position is found to be less favorable but the difference in adsorption energy between these two positions is only 3 meV.

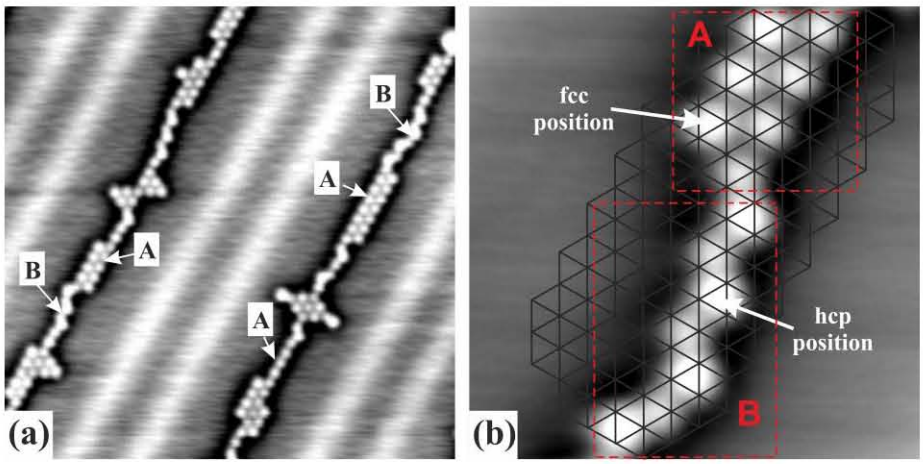

Figure 4.2. *Linear structures formed by chlorine atoms on Au(111): A regions correspond to fcc stacking of Cl atoms; B regions to alternating fcc-hcp stacking*

It should be noticed that this calculation was done for unreconstructed (1x1) surface of gold Au(111). On a reconstructed surface this calculation could be valid only for fcc domains. In hcp domains there are no fcc and hcp adsorption positions because of different arrangement for the last atomic plane on the surface. According to our results one can conclude that adsorption inside hcp domains is less favorable than adsorption inside fcc domains. Following the DFT calculations [2] we suppose that the main adsorption place for chlorine atoms in fcc domains are fcc centers. A close-up of STM image of one atomic chain is shown on the Figure 4.2b. Nodes of the grid superimposed on the image correspond to the position of gold atoms in the substrate. As one can see most of the adsorbate atoms occupy fcc positions and are situated 5 Å from each other. Chlorine atoms in such regions (labeled as A on Fig. 4.2b) form the well-known $(\sqrt{3}\times\sqrt{3})R30°$ structure. We also have found different regions with atoms wich occupy new positions. Such atoms alternate from fcc to hcp sites atoms and form zig-zag chains (labeled as B on Fig. 4.2b). The hcp sites are unambiguously identified with the help of the superimposed mesh of Fig 4.2b. The distance between atoms in fcc and hcp positions is 4.4 Å. We found also that atoms in hcp position are imaged in STM brighter than those in fcc position. The measured corrugation between hcp and fcc sites is about $\Delta z = 0.15\text{-}0.2$ Å.

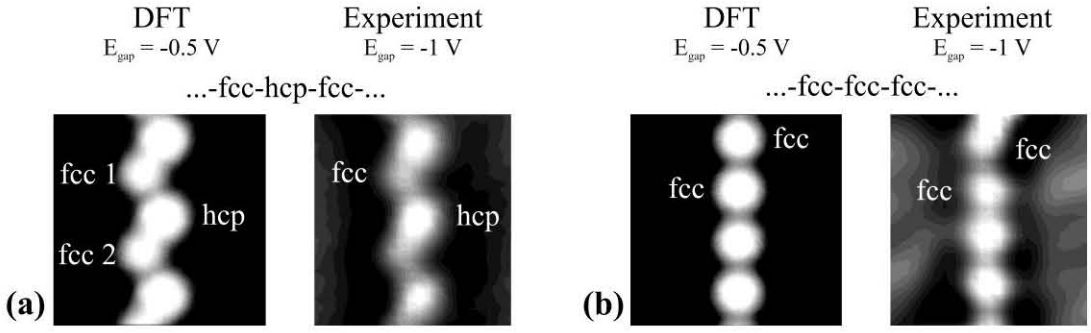

Figure 4.3. *Comparison between DFT calculation and experimental STM images for:* ***(a)*** *zigzag (fcc-hcp-fcc-hcp…) chain;* ***(b)*** *linear (fcc-fcc-fcc …) chain.*

Similar to experimental results, our DFT calculations show that for zigzag chains, atoms in hcp sites are displaced vertically by 0.16 angstroms with respect to atoms in fcc sites. DFT structure optimization also reveals a tiny lateral displacement by 0.3-0.5 Å for atoms in hcp sites leading to dimmer like pattern inside the zigzag chain (see Fig. 4.3a).

4.1.2 Removal of the reconstruction

As the Cl coverage grows, the length of the chains increases and can reach up to 200 Å being only limited by the length of fcc domains between the elbows of the herringbone reconstruction. The fcc domains with chlorine chain inside are spread more than 1.5 times and the width can reach 65-70 Å (see Fig. 4.1e). Then the chains start to bend in the surface plane and form rings. First rings usually appear in the elbows of herringbone reconstruction (Fig. 4.4a-4.4c). Initially the average size of rings is 30-50 Å. Rings are not situated on the surface randomly but rather seek to group and form a quasihexagonal structure, as one can see on the Figure 4.4c. A further spread of fcc domain is observed in the region where the rings develop. The area filled by the new structure increases with chlorine coverage. This leads to even more spread of fcc domains. As a consequence the

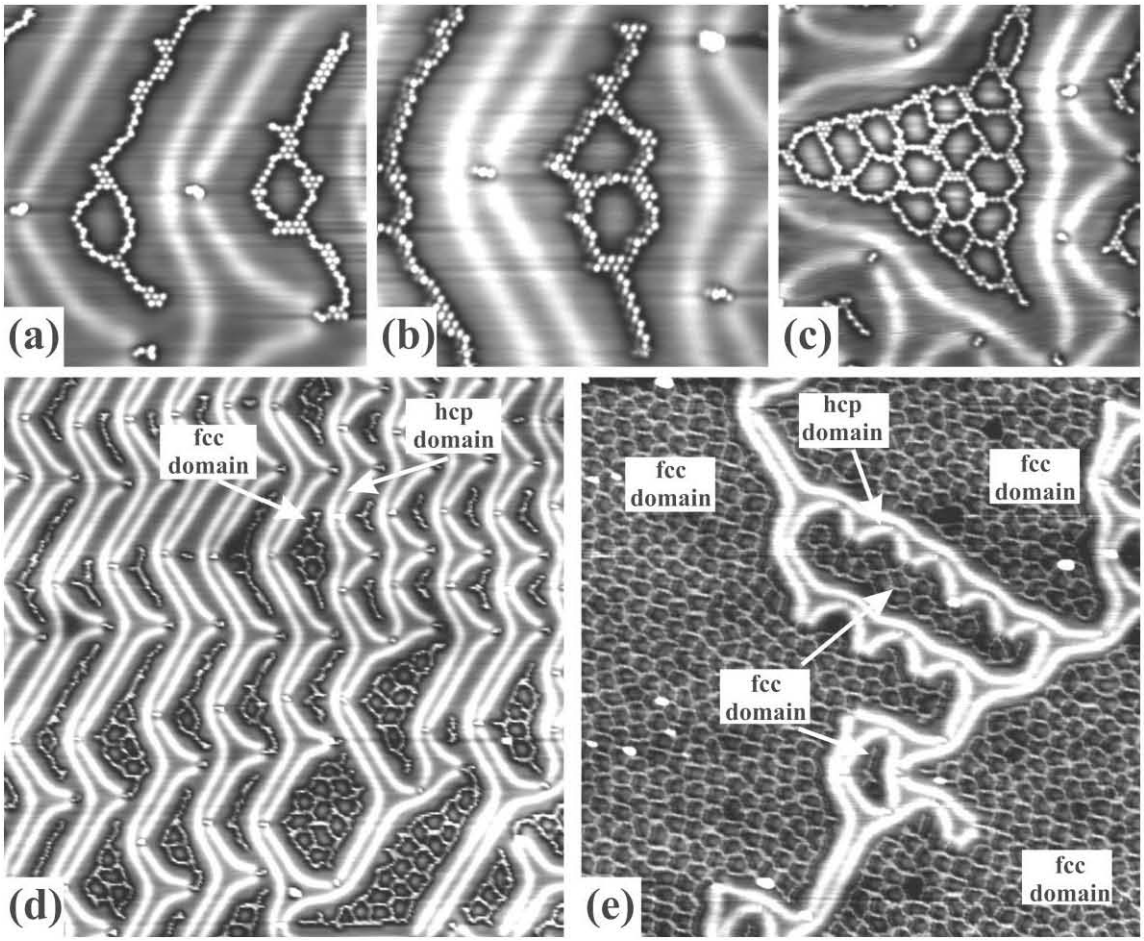

Figure 4.4 (a–c) *Appearance of nano pores (230×230 Å^2). Removal of surface reconstruction during chlorine adsorption:* ***(d)*** *1000×1000 Å^2, $\theta \approx 0.01$ M;.* ***(e)*** *1000×1000 Å^2, chlorine coverage $\theta \approx 0.08$ ML*

density of hcp domains decreases and the surface reconstruction gradually vanishes.

Figure 4.4e shows STM image of the surface with the rest of hcp domains and domain walls. It should be noticed that surface coverage is very inhomogeneous during this stage of adsorption. For example a large-scale STM image of a gold surface exposed to 0.05 ML of chlorine is shown on Figure 4.5. On this image, large regions of several thousand angstroms are filled with the ring structure and correspond to a local coverage $\theta \approx 0.1$ MC (regions labelled 1). Large regions where the rest of initial reconstruction still exists can also be seen. In the reconstructed places surface is almost clean and coverage does not exceed 0.003 ML. Only few chlorine atoms fill kinks of reconstruction or form chains and small areas with the ring structure (1-5 rings). Surface reconstruction in such regions is disturbed and domain walls have unusual form. Finally the complete removal of surface reconstruction and formation of a full nano porous 2D structure is observed at coverage $\theta_c \approx 0.12$ ML.

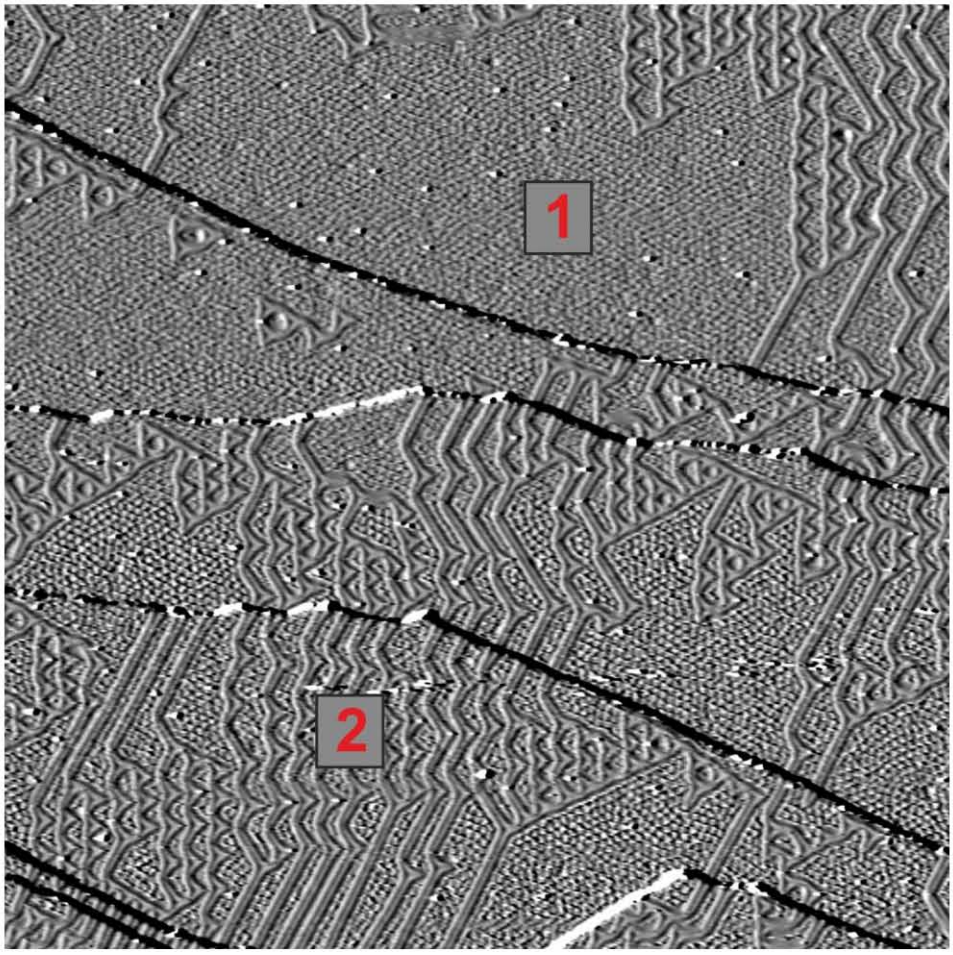

Figure 4.5. *Large-scale STM image of chlorinated Au(111) surface (3100×3100 Å^2, $U_s = -1.0$ V, $I_t = 0.5$ nA, 5 K, 0.05 ML). Regions 1 with nano porous structure (local chlorine coverage ≈ 0.09 ML) are seen together with regions 2 with surface reconstruction (local chlorine coverage ≈ 0.02 ML)*

In the literature it is reported that during chlorine adsorption on Au(111) surface at room temperature, the LEED patterns show disappearance of spot splitting [1, 3] which is the sign of surface reconstruction removal. According to our data a surface coverage of

≈0.05 ML, (approximately half of the surface still reconstructed), is well enough to observe disappearance of spot splitting at room temperature. This observation is in agreement with results published in [1]. According to [1] spot splitting disappears from LEED pattern after exposer of 0.05 L (Langmuir) at 120 K. The sharpest (√3×√3)R30° pattern being observed for exposure of 0.25 L at the same temperature, one can estimate the coverage at which removal of the reconstruction is observed by LEED . Assuming sticking coefficient for Cl_2 molecules being constant we obtain $\theta \approx 0.05$ L × 0.33 ML/0.25 L ≈ 0.06 ML.

4.1.3 Quasi hexagonal lattice of nano pores

As mentioned above, a complete nano porous 2D structure can be obtained for an average coverage of Cl $\theta_c \approx 0.12$ ML. We want to focus now on the local structure of this nano porous lattice. Figure 4.6 shows STM images of the surface for coverage increasing from 0.09ML to 0.33ML. The coverage indicated here corresponds to local coverage as estimated from STM images.

On Fig 4.6a a self-organized quasi hexagonal structure is revealed with pores of average diameter about 3nm and chlorine single wall structure. Atomic resolution is achieved and atoms inside walls can occupy fcc or hcp sites as well (like observed for single atomic chains described above).

Self ordering and hexagonal symmetry of the structure can be evidenced by the Fourier transform of the STM images presented on the right of Figure 4.6. A clear 6 fold pattern with second and third order spots is visible. From this pattern we can estimate the periodicity of the structure and find a pore to pore distance between 3.7 and 2.5 nm depending on the Cl coverage. The average diameter of pores as measured from STM image is not surprisingly found to be coverage dependent. STM images of the superstructure at surface coverage 0.12 and 0.2 ML are shown on the Figure 4.6b and 4.6c respectively. As one can see a decrease of rings diameter and thickening of their walls is observed during chlorine adsorption. In the same time the distance between pores decreases as evidenced by FFT of STM images.

The dependence of nano pores average diameter and average distance between them (super lattice period) on the coverage is shown on Figure 4.7. The lattice constant of the quasi hexagonal structure is reduced by 35 % from 0.09 ML to 0.16 ML and stabilizes at 2.5 nm. In the same time the diameter of pores gradually decreases. Further chlorine adsorption only leads to decreasing in size of the pores and loosing long range order as revealed by the smearing of 2nd and third order spots in FFT. If initially the superstructure can be formed by monoatomic chains of chlorine, we observed that the thickness of the walls increases as the surface coverage increases. One has to note that number of chlorine atoms that occupy hcp positions also decreases when the surface coverage and the thickness of ring walls grow. Finally all chlorine atoms occupy fcc positions when the ring walls become larger than two-atomic rows (see Fig. 4.6b and 4.6c). The positions of chlorine atoms inside the walls correspond to the (√3×√3)R30° structure and leads to the appearance of the corresponding spots in the Fourier transform of STM images (Fig. 4.6c). Nano porous structure completely disappears at surface coverage θ = 0.33 ML and the

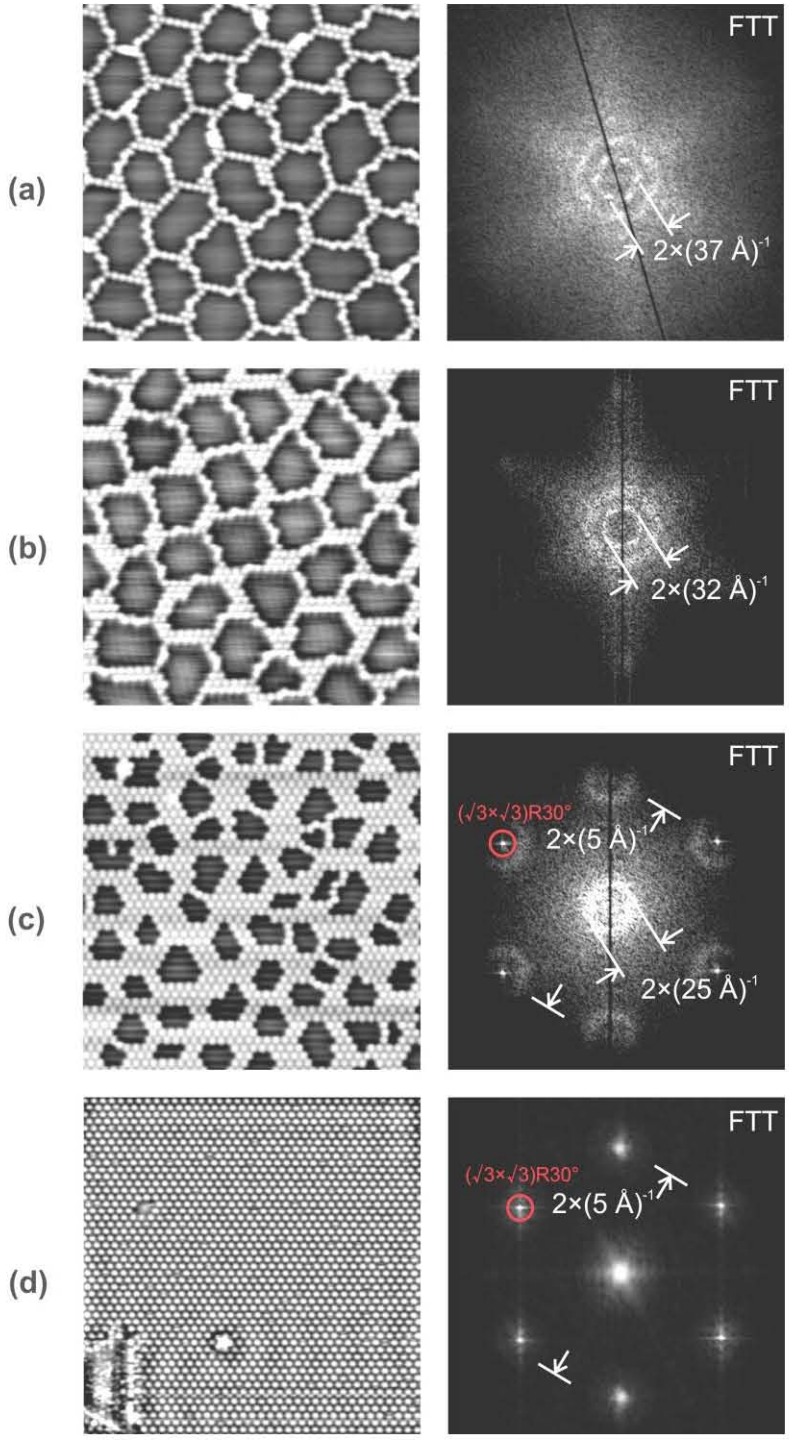

Figure. 4.6. *STM images (200×200 Å^2) and their FTT showing evolution of quasihexagonal structure with increase of chlorine coverage:* ***(a)*** *$\theta \approx 0.09$ ML;* ***(b)*** *0.12 ML;* ***(c)*** *0.2 ML;* ***(d)*** *0.33 ML - (√3×√3)R30° structure. Scanning parameters: (a) $U_s = -1.0$ V, $I_t = 0.5$ nA; (b) $U_s = -1.0$ V, $I_t = 1.0$ nA; (c) $U_s = -0.5$ V, $I_t = 1.5$ nA; (d) $U_s = -1.0$ V, $I_t = 1.0$ nA. Surface temperature T = 5 K*

well-known uniform commensurate (√3×√3)R30° structure is formed on the surface (Fig. 4.6d). Comparing the position of spots for quasi hexagonal and (√3×√3)R30° structures shows that direction of the rows formed by the pores in the superstructure fit with the <110> direction of the Au(111)-(1×1) substrate.

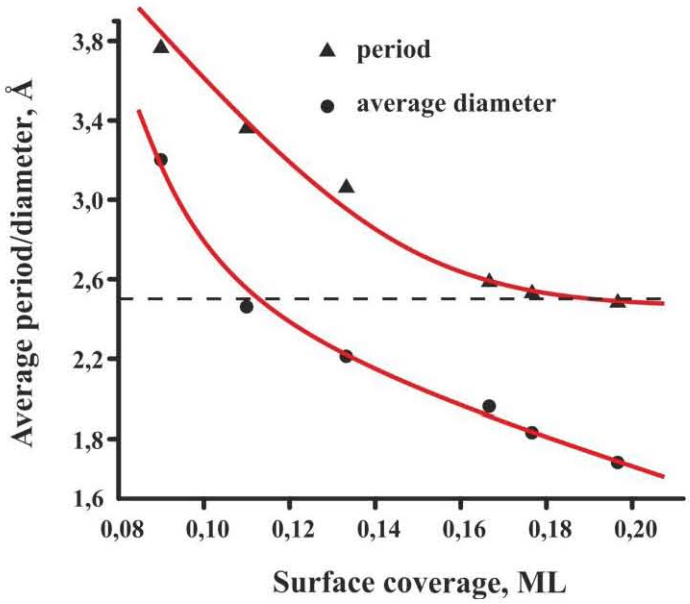

Figure 4.7. *Average period and diameter of quasi hexagonal structure vs. chlorine surface coverage.*

4.1.4 Thermal stability of nano porous lattice

It should be noticed once more that in all our experiments Cl_2 adsorption was done at 130-300 K when chlorine layer is believed to be disordered [1, 2, 3] and all STM measurements were done at T = 5 K. Therefore it was relevant to investigate the effect of temperature on the structural properties of the nano porous lattices. When the hexagonal superstructure is heated from 5 K up to room temperature, ordering seems to be lost as suggested by our LEED measurements shown of Fig 4.8.

At T = 47 K (minimal temperature available in the LEED chamber) small hexagon of spots around each reflex of the substrate is clearly visible (Fig. 4.8a). The distance between superstructure spots is roughly 13 times smaller than the distance between surface spots. This corresponds to the superstructure periodicity 37.5 Å ($13\times a_{Au(111)} = 13\times 2.88$ Å) and is in good agreement with STM measurements, 35–36 Å for $\theta \approx 0.10$–0.11 ML.

Besides these spots the LEED pattern contains additional pale and diffuse fractional-order spots. They correspond to (√3×√3)R30° structure formed by chlorine atoms in ring walls. When the temperature of the surface is increased LEED-spots from chlorine superstructure becomes more and more diffuse, so at T = 100 K one can see small circles around surface spots in the place of small hexagon (Fig. 4.8b). At even higher temperature only diffuse halo is observed around surface spots (Fig. 4.8c). We estimate from these LEED experiments the temperature of quasi hexagonal structure disordering as T ≈ 100-

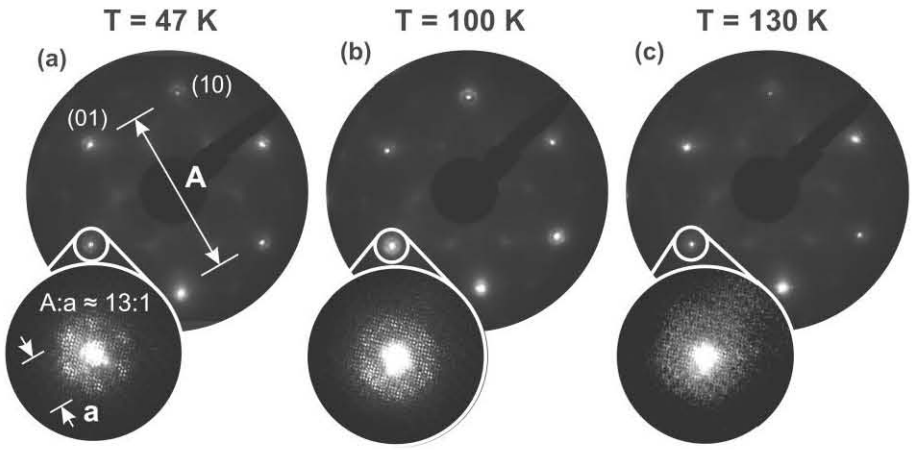

Figure 4.8. *LEED images of chlorinated Au(111) surface ($\theta \approx 0.09$ ML) at different substrate temperatures 47–130 K. Spots from substrate and ($\sqrt{3}\times\sqrt{3}$)R30°-Cl structure are clearly seen. Beside each image a zoom with spots from quasi hexagonal structure around substrate spot is shown. Electron energy was $E_0 = 145$ eV*

110 K. These results are corroborated by our STM investigations. By variable temperature measurements in STM we were able to estimate the temperature range where the hexagonal superstructure exists. The results are resented on Fig 4.9.

We see from our STM data, that the mobility of chlorine atoms in the ring walls increase very fast with the temperature. At T = 55 K (solid N_2 melting) mobility of atoms in the walls is already high and it's hard to get atomic resolution (Fig. 4.9b and 4.9e). The superstructure still exists as can be seen on the STM image and its Fourier transform on Fig. 4.9b. At even higher temperature T = 77 K (liquid N_2 boiling) we failed to get STM

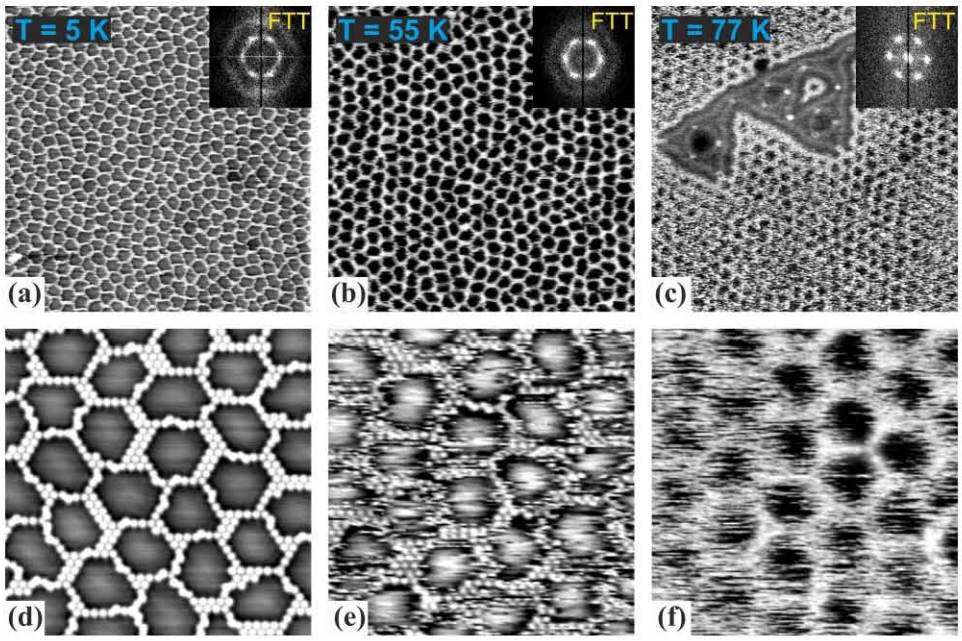

Figure 4.9. *STM images of quasi hexagonal structure on Au(111) surface ($U_s = 2.0$ V, $I_t = 0.5$ nA, $\theta \approx 0.09$ ML) at surface temperatures 5–77 K: (a–c) large images 800×800 Å^2, FTT on the inset; (d–f) corresponding high-resolution images 175×175 Å^2*

images with atomic resolution (Fig. 4.9c and f) suggesting large fluctuations in atomic position of chlorine. Nevertheless at 77K the rings and the skeleton of the nano porous structure almost survive with only small parts being destroyed. Note that atom tracking by the tip cannot be ruled out at such temperature. Loosing of the long range ordering is also reflected by disappearance of the second and third order spots in FFT at elevated temperature.

Therefore the (sub)monolayer of chlorine on Au(111) goes through an order/disorder transition in the temperature range 5-300K. From our STM and LEED experiments we found for low coverage this order-disorder transition to be around 100-110 K and reversible. Indeed by cycling the sample temperature from room temperature to 5 K we always obtained the same nano porous and ordered lattice at low temperature.

Unfortunately we have investigated the temperature of transition only for coverage $\theta \approx 0.10–0.11$ ML. We can suppose that with increase of coverage this temperature should also increase, gradually approaching to the temperature of order-disorder transition for (√3×√3)R30° structure like being measured in [1] as 230 K.

4.2 Honeycomb structure formation (θ > 0.33 ML)

4.2.1 $AuCl_2$ and $(AuCl_2)_2$ nucleation on the Au(111) surface

As presented in the first chapter of this report, in most halogen/metal systems the formation of commensurate lattice (for instance (√3×√3)R30° on (111) surfaces) is followed by compression of halogen monolayer [11]. As it was already discussed in Chapter 1, compression ratio usually can be estimated from comparison of nearest-neighbor distances in the commensurate lattice with typical size of halogen atoms (van der Waals diameter, for example). According to such geometrical considerations chlorine monolayer on Ag(111) is an analog of Cl/Au(111) system as lattice constant for (111) surface of gold and silver coincide to within 0.2 % (2.889 and 2.884 Å) [12,13]. The van der Waals diameter of chlorine atom is 3.5-3.6 Å [14] and the nearest-neighbor distance in (√3×√3)R30° structure 5 Å is much larger. Chlorine adsorption on Ag(111) surface for coverage $\theta > 0.33$ ML leads to compression of (√3×√3)R30° structure until average nearest-neighbor distances between atoms reach their diameter (see Chapter 3 and [14]).

However as we have found in our experiments there is no compression of (√3×√3)R30° structure on Au(111) surface at chlorine coverage $\theta > 0.33$ ML. The authors in [1, 2] do not report compression of commensurate structure either. Instead of this we observed appearance of the new type of objects that we will demonstrate to be $AuCl_2$ molecules.

STM image of chlorine monolayer on Au(111) surface with coverage slightly exceeding 0.33 ML is shown on the Figure 4.10. Bright linear structures (2) and point structures (1) have appeared on the terraces. Their number is increased in vicinity of atomic step 3. As one can see, such structures appear on the surface covered by chlorine monolayer with (√3×√3)R30° lattice. The structures themselves – both linear and point – are composed of identical elements, oriented towards atomic rows in (√3×√3)R30° lattice. Isolated elements are rarely found on the surface but more likely grouped to form rows –

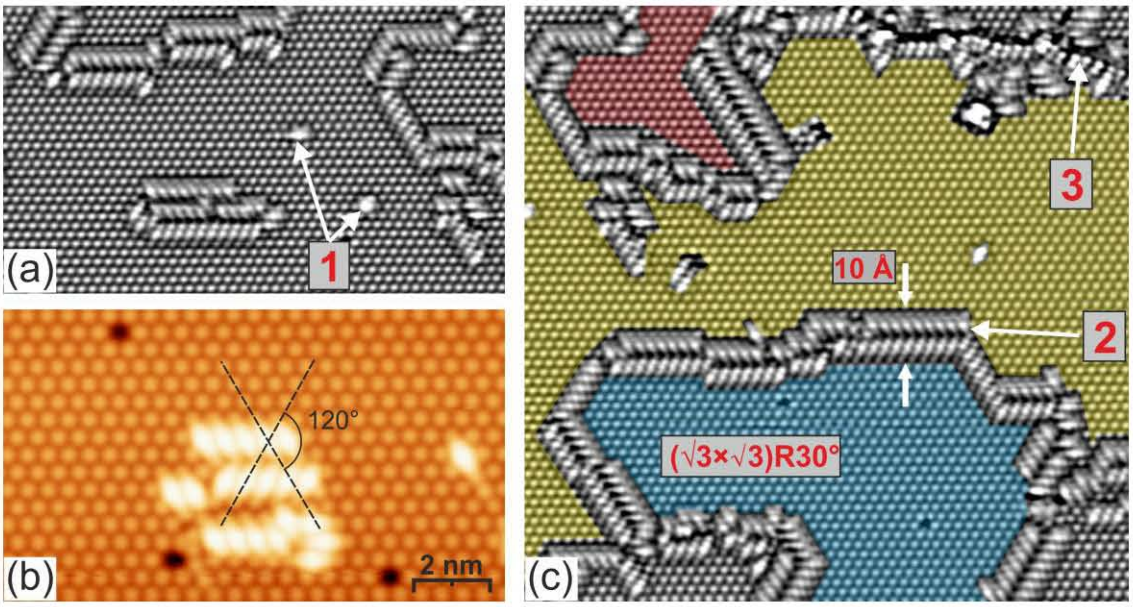

Figure 4.10. *STM images of Au(111) surface at chlorine coverage $\theta > 0.33$ ML.* ***(a)*** *Region of surface (230×120 Å^2) with point structures 1.* ***(b)*** *Linear structures 2.* ***(c)*** *Region of surface (270×250 Å^2) with linear structures 2. Number of elements is increased in the vicinity of atomic step 3. Domains with antiphase domains of (√3×√3)R30° are marked with different colors*

linear structures. The distance between centers of neighboring elements in a line is equal to 5 Å, corresponding to the nearest-neighbor distance in the (√3×√3)R30° structure.

These linear structures usually separate surface regions with anti phase (√3×√3)R30° domains marked by different colors on Figure 4.10c. The anti phase domains arise from a displacement of chlorine atoms in (√3×√3)R30° structure from one side of the isolated element, as shown on Figure 4.11a. Such shift leads to displacement of all chlorine atoms from one side of the line to the equivalent (√3×√3)R30° sub lattice when a linear structure is formed (we remind that there are three equivalent (√3×√3)R30° sub lattices on (111) face of fcc crystal). Linear structures are usually coupled and separated by distance 10 Å that is clearly seen on Figure 4.10b. The lines are oriented along atomic rows of the (√3×√3)R30° structure (<112> direction of the substrate) and each element in it is turned by 60° relative to the row axis. Elements in coupled linear structures have different orientation and are tilted by 120° relative to each other. A fragment of such a linear structure together with its structural model is shown on Figure 4.11c-d. One can see that each element in a line has the same structure as isolated elements (see Figure 4.11a and 4.11b). The length and the height of elements in a line coincide with the size of isolated element and they are similarly situated relatively the substrate

Let us now discuss the structure of a single element from Figure 4.11a,b. The length of the element is 5.5-6.0 Å, the height is equal 0.7-0.9 Å and does not depend on the gap voltage, at least in the range from -1 to +1 V. Each element consists of three protrusions, central being the brightest one. A grid with nodes corresponding to the position of substrate atoms can be superimposed on the STM image. Such superposition shows that central protrusion of element is situated above a bridge position of the substrate lattice. The two side protrusions are situated close to on top position above substrate atoms. Most of

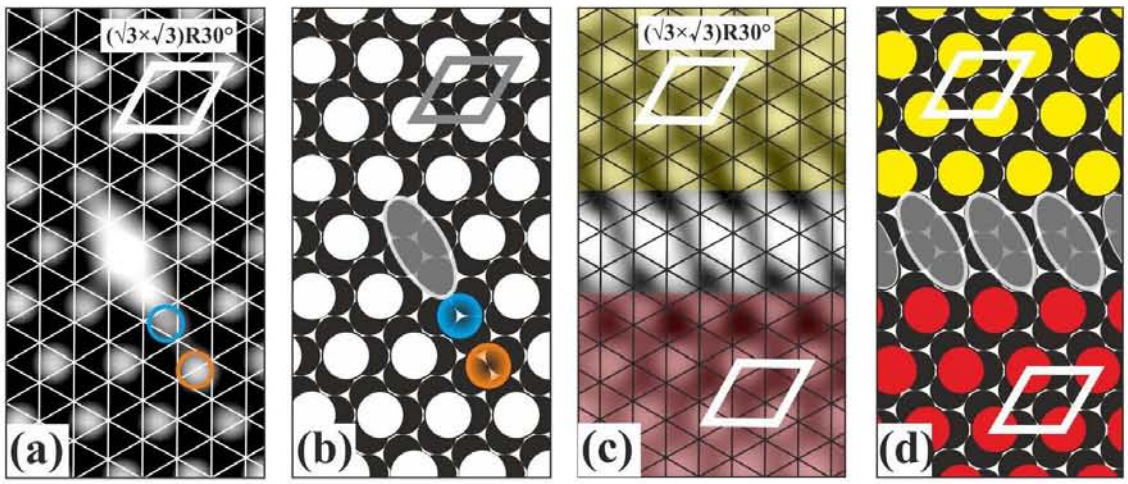

Figure 4.11: *Close up of the isolated and grouped elements formed on the saturated Cl overlayer – θ > 0.33 ML. a) and c) : STM images Us = 0.2 V and It = 0.4 nA. b) and d) : atomic model. Red and yellow colors correspond to anti phase domain with Cl atoms in fcc sites. Blue and orange colors mark hcp and bridge sites respectively*

(√3×√3)R30° structure around remains undistorted. Only two chlorine atoms from one side (down part on Fig. 4.11a) are appreciably shifted towards direction of atomic rows in chemisorbed layer. One of them (marked in blue in Figure 4.11a,b) is moved to hcp position, and the other one (marked in yellow) shifts in bridge position. This fact together with position of the central protrusion which fits with the substrate bridge symmetrical point let us suppose that these new objects are placed directly on the metal surface and not over chlorine monolayer.

We also see from Figure 4.11c that as the elements are grouped to form linear structures, the displaced atoms mentioned above are further shifted to occupy regular fcc sites but in an anti phase domain compared to the upper area.

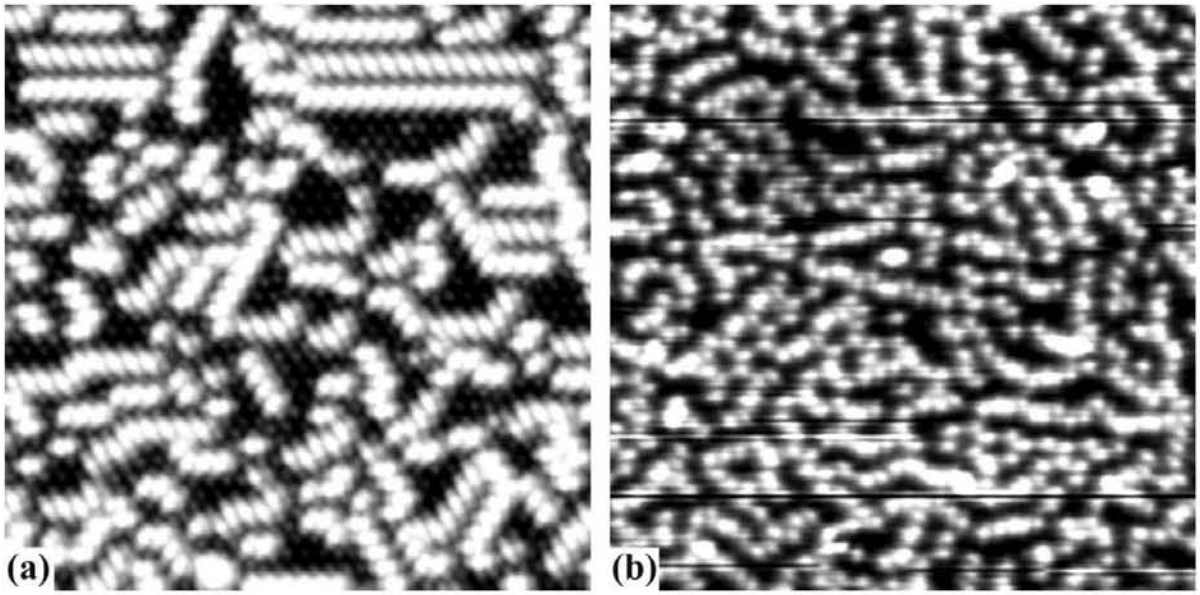

Figure 4.12. *STM images (180×180 Å^2 - 5 K) of Au(111) surface covered with two different chlorine coverage (θ > 0.33 ML):* ***(a)*** *U_s = 0.2 V, I_t = 0.4 nA;* ***(b)*** *U_s = 2.0 V, I_t = 0.5 nA*

Further chlorine adsorption increases area covered by the new linear structure and leads to gradual removal of (√3×√3)R30° structure. Figure 4.12a shows a STM image of gold surface almost fully covered by randomly distributed linear structures of different length. Small areas of (√3×√3)R30° structure still exist between them. Elements in the linear structures can be arranged in the same manner as described before and the distances between their centers are still 5 Å. Besides such arrangement of elements along atomic rows of the (√3×√3)R30° lattice, new arrangement can be found on the surface.

A close up of the new stacking and its structural model is shown on the Figure 4.13a. From our STM measurements it obvious that elementary unit can be shifted among the (√3×√3)R30° structure to form a new zig-zag dense stacking. In such kind of structure the elements are arranged across its length with period 4.3 Å which corresponds to the distance between atomic rows in (√3×√3)R30° structure, the distance between centers of elements

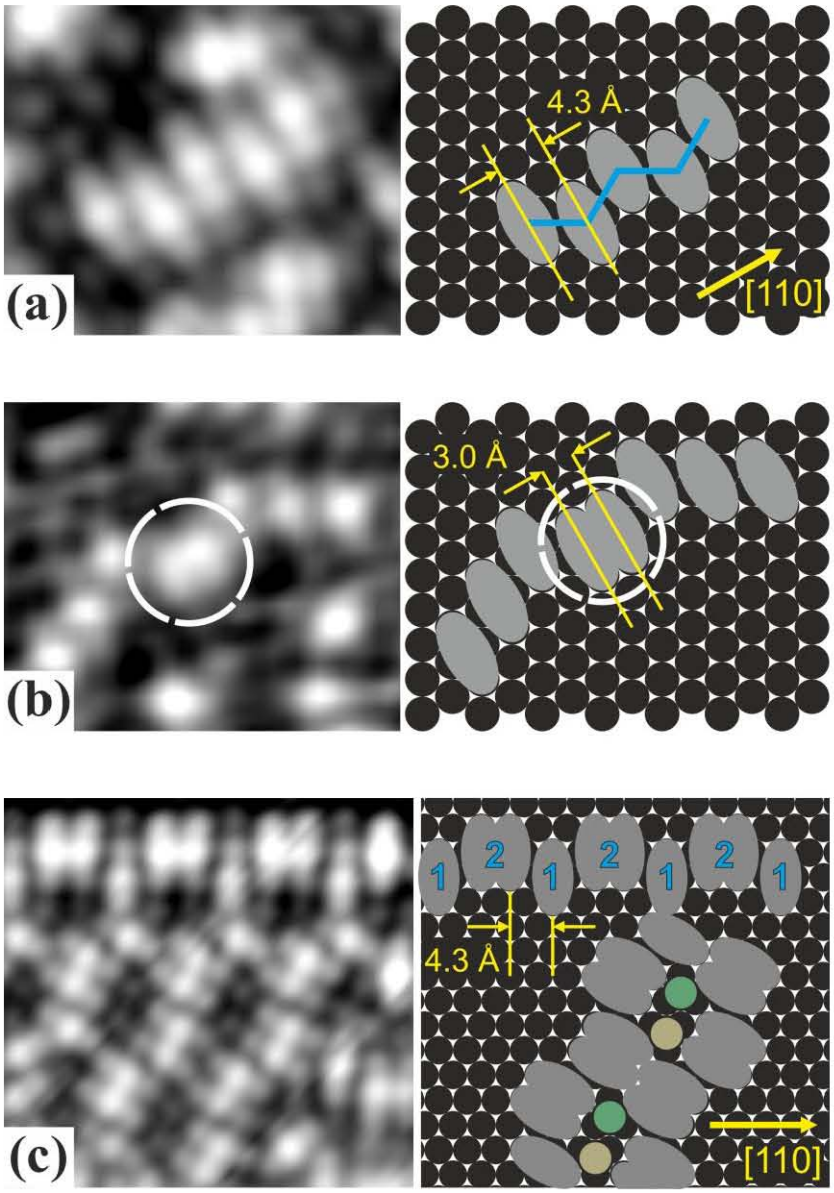

Figure 4.13. *Close up of the new stacking observed as cholrine coverage increases.* ***(a)*** *zig-zag chain* ***(b)*** *dimer formation and* ***(c)*** *arrangement in a pseudo honeycomb lattice*

being still 5 Å. Such kind of arrangement is a particular case of linear structures, shown on Figure 4.10. However subsequent compression of monolayer is related to this packing of the elements along <110> direction.

When almost all the surface is covered by linear structures, compression of the elements increases to make smaller distance between their centers and a dimerization starts. STM image of chlorine layer when part of the elements has formed dimers is shown on the Figure 4.12b. One can see that randomly distributed linear structures still exist on the surfaces and their number has increased. The elements inside them are arranged denser so it's hard to resolve with STM. Regions between linear structures are filled by chlorine monolayer with $(\sqrt{3}\times\sqrt{3})R30°$ structure. On Figure 4.13b we show STM image of typical building blocks of the new chains, consisting of dimers of elements. The corresponding structural model is given on the right part of Figure 4.13b. The distance between elements in dimer as measured from STM images is now 3.0±0.1 Å and is close to the lattice constant of Au(111) surface 2.9 Å.

It is known that gold forms with chlorine two stable compounds: AuCl and $AuCl_3$. The former is composed of …–Au–Cl–Au–Cl–… chains [19]. The latter compound is always found as $[AuCl_3]_2$ dimers, which form molecular crystal in solid state [20,21,22]. We have performed DFT calculations for molecular structures AuCl, $AuCl_2$ and $AuCl_3$ as well as for dimers $(AuCl_2)_2$ and $(AuCl_3)_2$, adsorbed on Au(111) surface. According to our results (not shown here) neither AuCl nor $AuCl_3$ and the corresponding dimers could bind on gold surface and form stable bound structure. On the contrary artificial $AuCl_2$ compound not found in the nature as stable gold chloride molecule reproduced well all features of experimental STM images – both for single molecule and dimer (Figure 4.14).

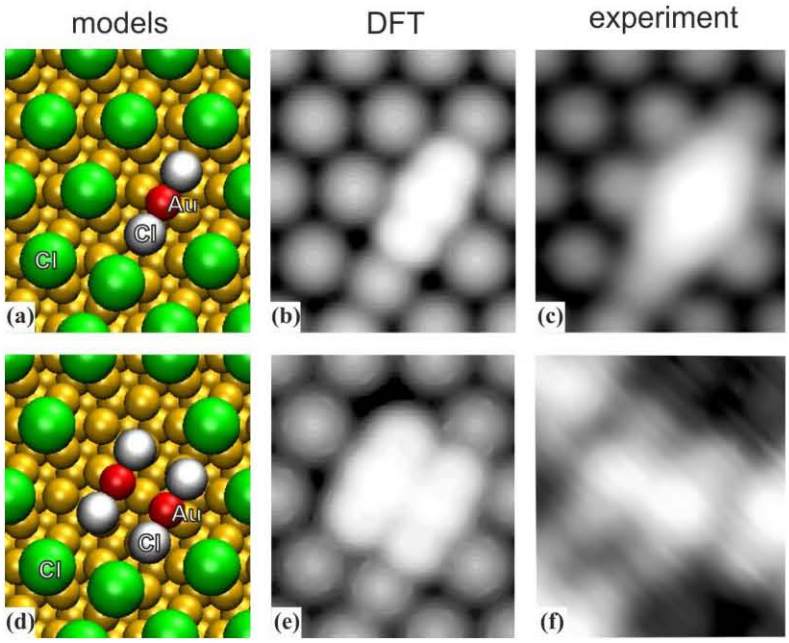

Figure 4.14: *Models of $AuCl_2$ (a) and $(AuCl_2)_2$ (d) molecules, adsorbed on Au(111) surface with $(\sqrt{3}\times\sqrt{3})R30°$ chlorine monolayer around. DFT calculated (b) and experimental (c) STM images of $AuCl_2$. Calculated (e) and experimental (f) STM images of $(AuCl_2)_2$*

Thus we consider that chlorine forms $AuCl_2$ molecules on Au(111) surface at coverage $\theta >$ 0.33 ML.

The assumption of $AuCl_2$ molecules formation is supported by TDS experiments reported in the literature. Indeed it has been shown that the low temperature peak β_2 in TDS, is shifted for more than 100 K relatively to the high temperature peak β_1 when the coverage exceeds 0.33 ML [1, 2, 3]. Such a shift is a sign of significantly different bounding of chlorine atoms in the observed objects compared to $(\sqrt{3}\times\sqrt{3})R30°$ layer. According to DFT calculations [2] the difference in chlorine adsorption energy for different adsorption sites on Au(111) surface does not exceed 0.25 eV. This is much smaller than difference in adsorption energy for chlorine atoms on Cu(111) surface 0.45 eV [15] where no second TDS peak appears after compression of $(\sqrt{3}\times\sqrt{3})R30°$ structure [16,17,18].

A qualitative explanation for existence of an artificial gold chloride molecule $AuCl_2$ on the Au(111) surface can be the necessity to use the third valence bond of Au^{3+} to stick the molecule to the surface. In this sense what we observe could be surface form of $AuCl_3$ chloride.

4.2.2 Pseudo honeycomb lattice

Surface local structure at even higher chlorine coverage is shown on Figure 4.13c with the corresponding atomic model. This high-resolution STM image was taken on the step edge of a terrace and it allows us to identify each object observed on the surface. Along the step edge a linear structure *2-1-2-1* is formed, where 2 correspond to a dimer and 1 to single element. Linear structure itself is oriented along <110> direction and the

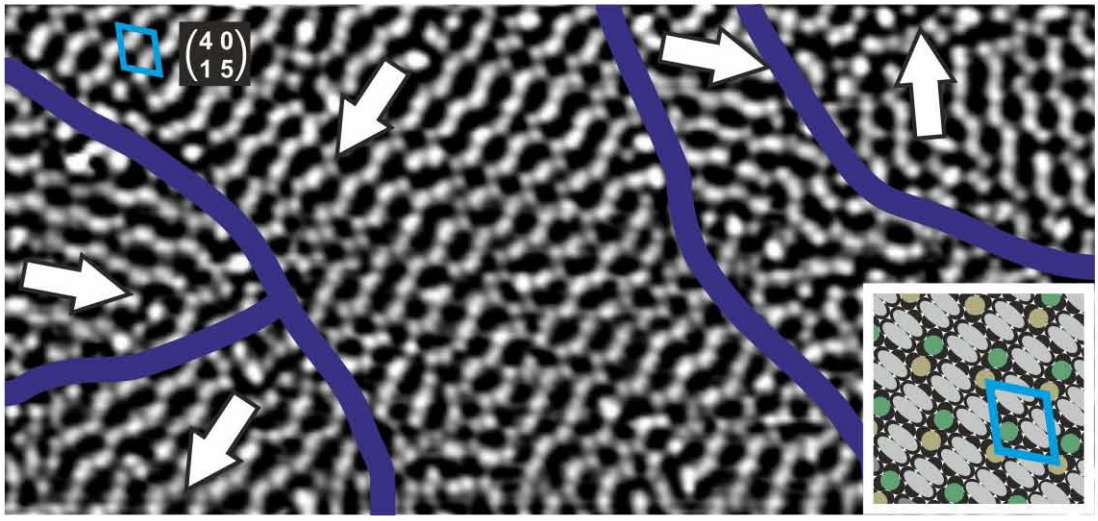

Figure 4.15. *STM image (500×310 Å^2, U_s = 1.0 V, I_t = 0.5 nA, 5 K) of saturated chlorine monolayer on Au(111) surface. Thick blue lines show boundaries between domains with different orientation (shown with arrows) of honeycomb structure. The inset shows model of honeycomb structure. Substrate atoms are marked as black circles, the elements as gray ellipses, chemisorbed chlorine atoms as green and brown circles.*

distance between 2 and 1 units is 4.3 Å. Dimers and single elements are arranged as on a chessboard.

On the terrace beside the step edge we found that dimers are arranged in an ordered 2D structure that resembles honeycomb structure. It has a quasi hexagonal unit cell formed by six dimers with two chlorine atoms in the middle. As it is shown on the model (Figure 4.13c) chlorine atoms in the middle of the cell occupy three-fold adsorption sites – one atom in fcc position and another in hcp position. This structure can be imagined being composed from <110> rows of dimers (with dimers inside it arranged as on chessboard) with period 14.7 Å (five lattice constants of Au(111) surface unit cell). Adjacent rows are shifted one relatively another by half-period. The nearest distance between dimers in two rows is 7.7 Å and the largest one is 12.6 Å.

When the surface is saturated with chlorine (Figure 4.15) almost all elements form dimers and are arranged in the pseudo honeycomb ordered structure, as depicted in Figure 4.13c. Dimers are packed in zig-zag rows along <110> direction with adjacent rows being shifted one along another by half-period. Chlorine atoms occupy free-fold positions inside the holes between adjacent rows. Several domains with different orientation of the structure can be seen on the image. Domain boundaries are marked with blue lines and domain orientation is shown with arrows. The pseudo honeycomb lattice formed can be described by a perfect structure with $\begin{pmatrix} 4 & 0 \\ 1 & 5 \end{pmatrix}$ unit cell as shown on the inset of Figure 4.15.

One has to note that similar structure was reported in [2]. The authors observed a honeycomb-like structure with a dimer of 3 Å in the corner of each cell, which is in agreement with our data. Here from STM investigation we were able to solve in detail the atomic arrangement inside this honeycomb lattice.

4.3 Conclusion

The process of chlorine adsorption on Au(111) surface was for the first time studied in detail by STM at low temperatures 5-120 K in a wide range of chlorine coverage. It was found that:

1. Chlorine atoms form closed chains (rings) that are self-organized in a quasihexagonal superstructure with period varying from 38 to 26 Å when the coverage changes in the range $\theta = 0.01–0.20$ MC.
2. For the first time we observed formation of linear structures formed by gold chloride molecules $AuCl_2$ and their self-organization to honeycomb structure at chlorine coverage $\theta > 0.33$ ML. It was found that each cell in honeycomb structure is formed of six $(AuCl_2)_2$ dimers. Two chlorine atoms are placed inside the cell and occupy fcc and hcp three-fold positions. The unite cell of the honeycomb structure is $\begin{pmatrix} 4 & 0 \\ 1 & 5 \end{pmatrix}$.
3. We investigated the proses of Au(111)-22×√3 surface reconstruction removal under adsorption of chlorine. It was found that chlorine atoms adsorbs

exclusively in fcc domains of herringbone reconstruction. Broadening of fcc domains under chlorine adsorption leads to continuous disappearance of hcp domains and reconstruction.

Bibliography of Chapter 4

[1] G.N. Kastanas, B.E. Koel. Interaction of Cl_2 with the Au(111) surface in the temperature range of 120 to 1000 K // Appl. Surf. Sci. 64 235 (1993).

[2] W. Gao et al. Chlorine Adsorption on Au(111): Chlorine Overlayer or surface chloride? // Journ. of Am. Chem. Soc. 130 3560 (2008).

[3] N.D. Spencer, R.M. Lambert. Chlorine chemisorption and surface chloride formation on Au(111) // Surf. Sci. 107 237 (1981).

[4] J.V. Barth et al. Scanning tunneling microscopy observations on the reconstructed Au(111) surface: atomic structure, long-range superstructure, rotational domains and surface defects // Phys. Rev. B 42 15 9307 (1990).

[5] S. Narasimhan, D. Vanderbilt. Elastic stress domains and the herringbone reconstruction on Au(111) // Phys. Rev. Lett. 69 10 1564 (1992).

[6] O. Schaff et al. In-situ STM studies of strain-stabilized thin-film dislocation networks under applied stress // Materials Science and Engineering A 319 914 (2001).

[7] M.A. Van Hove et al. The surface reconstructions of the (100) crystal faces of iridium, platinum and gold // Surf. Sci. 103 189 (1981).

[8] T.A. Baker, C.M. Friend, E. Kaxiras. Chlorine interaction with defects on the Au(111) surface: A first-principles theoretical investigation // Journ. of Chem. Phys. 129 104702 (2008).

[9] C. Didiot, S. Pons, B. Kierren, Y. Fagot-Revurat, D. Malterre Nanopatterning the electronic properties of gold surfaces with self-organized superlattices of metallic nanostructures // Nature Nanotechnology 2 617 (2007).

[10] J.A. Meyer et al. Preferential island nucleation at the elbows of the Au(111) herringbone reconstruction through place exchange // Surf. Sci. 365 L647 (1996).

[11] E. I. Altman. Halogens on metals and semiconductors // Landolt-Börnstein. New Series, v. III/42A1, p. 421-453 (2000).

[12] A. Maeland, T.B. Flanagan. Lattice spacings of gold–palladium alloys // Canadian Journal of Physics 42 2364 (1964).

[13] L.-G. Liu, W.A. Bassett. Compression of Ag and phase transformation of NaCl // Journ. of Appl. Phys. 44 1475 (1972).

[14] A.G. Shard, V.R. Dhanak. Chlorine Adsorption on Silver (111) at Low Temperatures // Journ. of Phys. Chem. 104 2743 (2000).

[15] K. Doll, N.M. Harrison. Chlorine adsorption on the Cu(111) surface // Chem. Phys. Lett. 317 282 (2000).

[16] P.J. Goddard, R.M. Lambert. Adsorption-desorption properties and surface structural chemistry of chlorine on Cu(111) and Ag(111) // Surf. Sci. 67 180 (1977).

[17] B.V. Andryushechkin, K.N. Eltsov, V.M. Shevlyuga. Domain-wall mechanism of "(n√3×n√3)R30°" incommensurate structure formation in chemisorbed halogen layers on Cu(111) // Surf. Sci. 470 L63 (2000).

[18] W.K. Walter, D.E. Manolopoulos, R.G. Jones. Chlorine adsorption and diffusion on Cu(111) // Surf. Sci. 348 115 (1996).

[19] R.W.G. Wyckoff. Crystal Structures // Interscience, John Wiley & Sons, v. 1 (1963).

[20] E.S. Clark, D.H. Templeton, C.H. Macgillavry. The crystal structure of gold(III) chloride // ACTA CRYSTALLOGRAPHICA, v. 11, p. 284-288 (1958).

[21] B. Reffy et al. Intriguing Gold TrifluoridesMolecular Structure of Monomers and Dimers: An Electron Diffraction and Quantum Chemical Study // Journ. of Am. Chem. Soc. 122 3127 (2000).

[22] I.J. Blackmore et al. Experimental Evidence for a Jahn-Teller Distortion in $AuCl_3$ // Angew. Chem. Int Ed. v. 44, p. 6746-6750 (2005).

CHAPTER 5.

Comparison of the structural phase transitions on (111) face of Cu, Ag and Au under chlorine action

In this chapter we want to give a comparative overview of the structural phase transitions which occur in the three systems that we have investigated. We will start this chapter with low-temperature study of surface structures formed by adsorbed chlorine atoms on Cu(111). This data will complete our observations made on silver and gold surfaces and presented in the Chapters 3 and 4 and will help us to analyze general trends in chlorine adsorption in the series of three different metals Cu-Ag-Au.

5.1 Cu(111) surface under molecular chlorine action

5.1.1 Introduction - LEED data

In the Figure 5.1 we show the LEED patterns obtained from Cu(111) surface at room temperature during continuous increasing of surface chlorine coverage. The obtained results completely agree with previously published data [1,2,3]. We can see that on the first stage, chlorine adsorbtion leads to the formation of a sharp (√3×√3)R30° pattern – see Figure 5.1b. When further chlorine is adsorbed the diffraction spots are split which is related to the inhomogeneous compression of the chlorine commensurate lattice as explained in Chapter 1. From previous studies we know that (√3×√3)R30° structure appears at chlorine surface coverage θ = 0.33 ML, whereas excess of chlorine leads to its compression. Saturated chlorine layer corresponds to surface coverage θ ≈ 0.41 ML [3].

The present study of Cl/Cu(111) system will be divided into two parts. First we will consider structures formed by chlorine atoms in the low-coverage range θ << 0.33 ML and to the formation of (√3×√3)R30°, which will be followed by the results related to the compression of this commensurate structure.

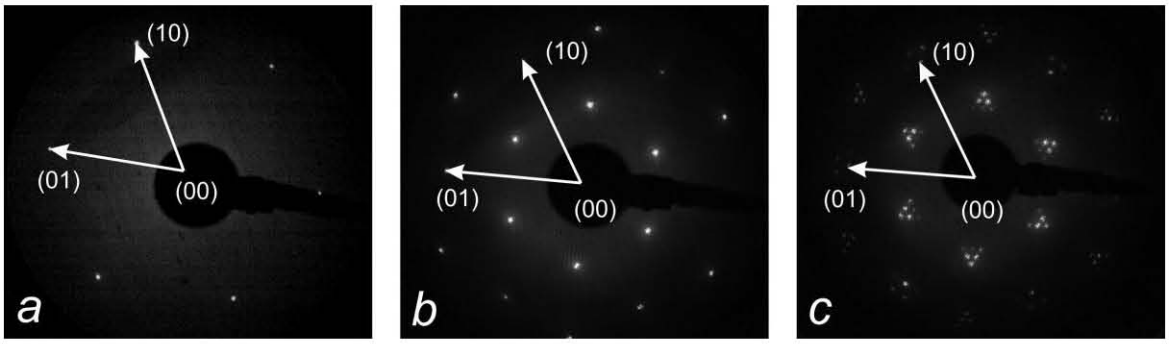

Figure 5.1. *LEED patterns obtained during continuous chlorine adsorption on Cu(111) surface at room temperature. Substrate reciprocal vectors are shown*

5.1.2 Appearance of the commensurate structure (θ <0.33 ML)

Similar to Cl/Ag(111) and Cl/Au(111) systems, chlorine adsorption on Cu(111) surface leads to the formation of linear single-atom chains – see Figure 2a. Chlorine atoms can occupy both fcc and hcp adsorption sites and are separated by the distance 3.9 Å and 4.4 Å from each other. Atoms in the hcp positions appear sligthly higher than the atoms in fcc by ≈ 0.1 Å. In most of cases atoms occupy alternately fcc and hcp sites. Number of chains and their length continuously increase with chlorine coverage - see Figure 2b. At the same time small islands of compact (√3×√3)R30° structure start to appear. In such islands all the chlorine atoms occupy equivalent fcc adsorption sites on the nearest-neighbor distance 4.4 Å. The spots of the corresponding spatial frequency appear in the FFT of STM image – see Figure 5.2c.

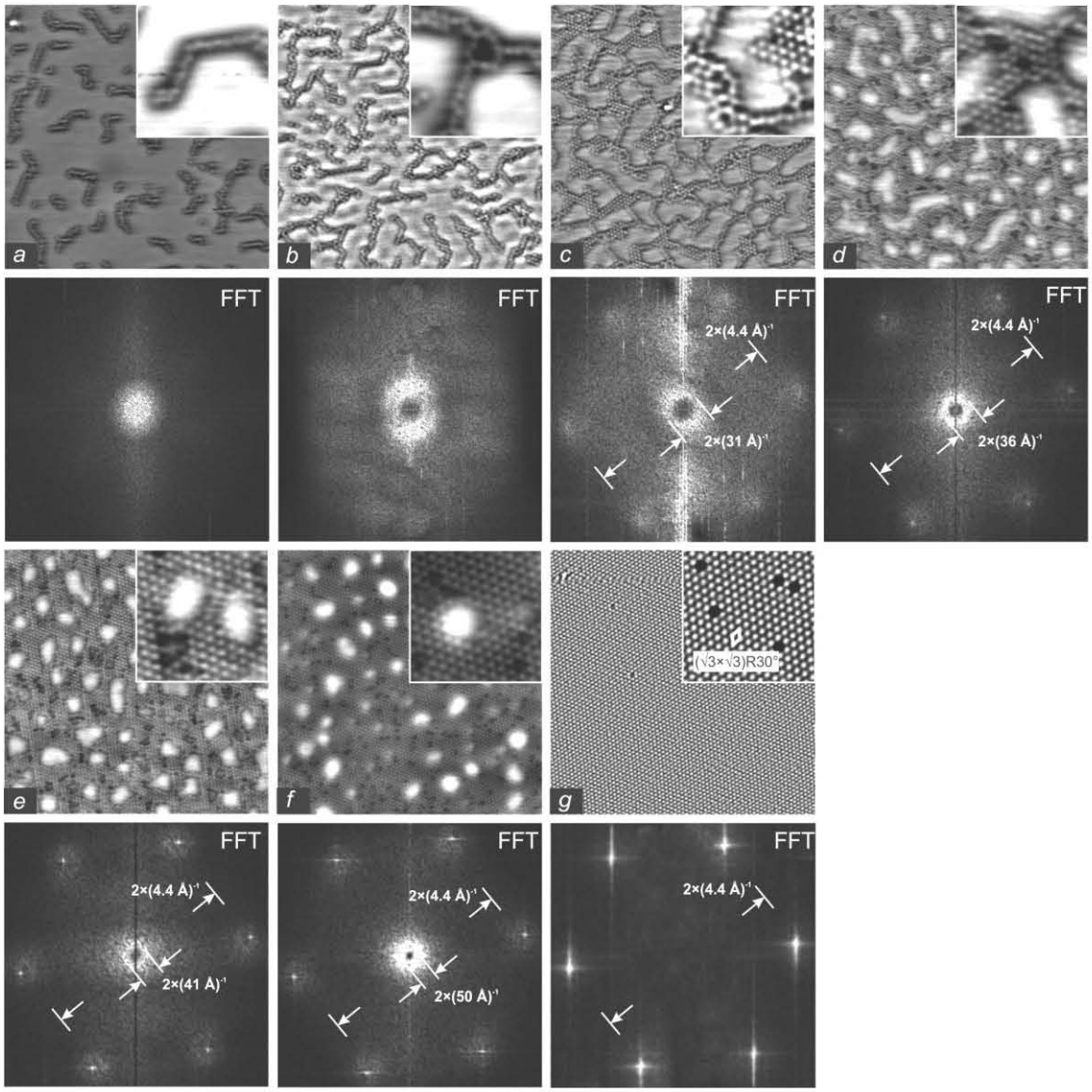

Figure 5.2. *Low-temperature STM images (310×310 Å^2, 5K) of copper surface obtained during continuous increase of chlorine surface coverage. Corresponding FFT are shown above each image. A zoom (54×54 Å^2) is shown in the corner of each STM image*

During the later increase of chlorine coverage atomic chains close up and form rings or nanopores. As opposed to the Cl/Au(111) system the size and the geometrical shape of nano pores on copper surface can greatly vary. We failed to find proper adsorption parameters to improve ordering in this system. Self ordering of nano pores seems to be restricted to Cl/Au(111) interface. Nevertheless one can see a small hexagon in the center of FFT of STM image on the Figure 5.2c which reveals a hidden quasi hexagonal long range order. The "pseudo periodicity" of this superstructure that can be measured from the size of this hexagon is about 30 Å increasing with Cl coverage (up to about 40 Å). Comparing orientation of the hexagon relative to the spots of chlorine monolayer one can see that the rows of nano pores lie parallel to the direction of atomic rows in (√3×√3)R30° structure.

Further increase of chlorine coverage leads to the decrease of the size of nano pores – see Figure 5.2d to 5.2f. We do not have sufficient experimental data to ascertain exact dependence of superstructures periodicity and nano pores size on the chlorine coverage, as we have done for Cl/Ag(111) system. We can only notice that both periodicity of the superstructure and diameter of nano pores decrease with growth of surface coverage, that one can see from STM images and their FFT on Figures 5.2c to 5.2f. This process is finished by the formation of the uniform commensurate (√3×√3)R30° lattice – see Figure 5.2g.

5.1.3 Compression of commensurate lattice (θ > 0.33 ML)

When the surface coverage exceeds θ > 0.33 ML compression of the commensurate (√3×√3)R30° structure starts. At the same time the splitting of diffraction spots in the LEED pattern is observed - Figure 5.1c, which is related to the fact that adsorbate lattice is no more commensurate with the substrate [3]. As it was reported in previous room-temperature study [3] compression of chlorine layer on Cu(111) surface is not uniform and formation of linear heavy domain walls is observed. Similarly to the case of compressed chlorine monolayer on Ag(111) surface we have found specific scanning parameters (U_{gap} ≈ + 4 V, I_t ≈ 2 nA) when heavy domain walls are imaged as dark lines. Three kinds of domains with dark lines of different orientations that correspond to three possible directions of compression are seen on the STM image on Figure 5.3a. The average period of domain wall structure is about 30 Å. We can estimate the surface coverage as $\Theta = (a+l)/3l \approx 0.36$ ML (where a is the copper lattice constant and l is the periodicity of domain-wall structure) [4]. An atomically-resolved STM image of the chlorine layer at this coverage is shown on Figure 5.3b.

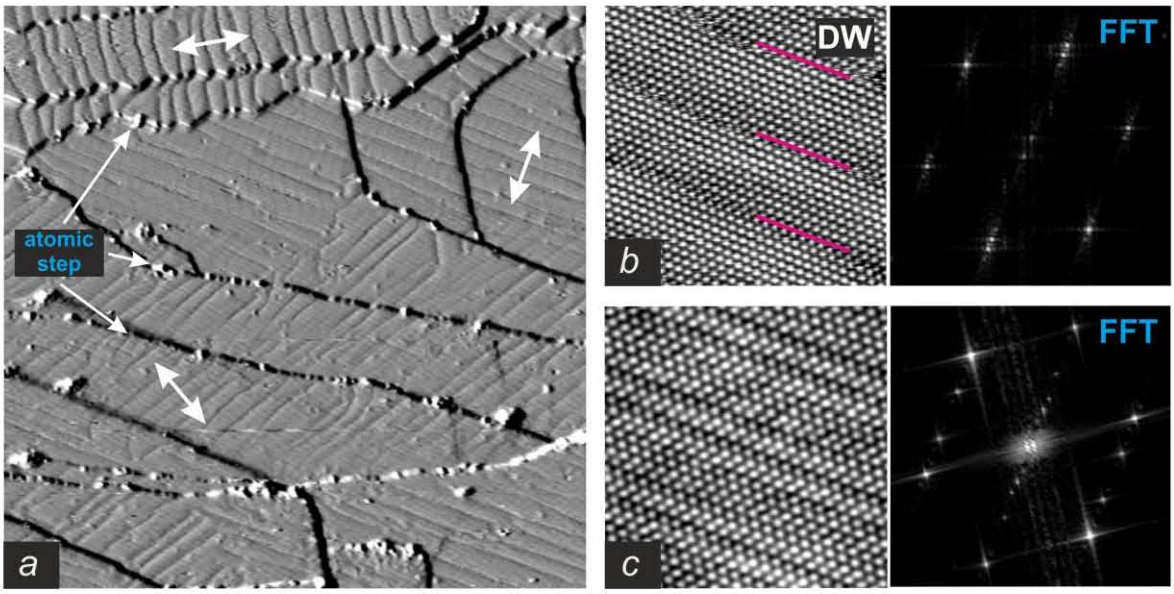

Figure 5.3. ***(a)*** *Panoramic low-temperature STM image (1000×1000 Å^2, 5K) of copper surface covered by compressed chlorine monolayer θ ≈ 0.36 ML.* ***(b)*** *Atomically resolved low-temperature STM image (10×10 Å^2, 5K) of compressed chlorine layer θ ≈ 0.36 ML.* ***(c)*** *Atomically resolved low-temperature STM image (10×10 Å^2, 5K) of saturated chlorine layer θ ≈ 0.41 ML.*

According to reference [3] the chlorine monolayer on Cu(111) surface saturates at coverage $\Theta \approx 0.41$ ML. An atomically resolved STM image of saturated chlorine layer obtained at T = 5 K is shown on Figure 5.3c. The measured periodicity of the domain-wall structure is 10-11 Å.

As it was noticed in the work [3] the width of domain walls at room temperature is rather large and is equal to approximately 3-4 atomic rows. This fact was related to the relaxation of domain walls under internal elastic tension inside them. However our low-temperature data shows that thermal energy and related to it excitations could have important role in the broadening of domain walls. In the Figure 5.4a we show STM image of the compressed chlorine layer at coverage $\theta \approx 0.36$ ML superimposed with a grid that corresponds to the position of atoms in the substrate lattice. We can see that most of chlorine atoms occupy energetically favorable fcc adsorption sites. At T = 5 K the domain walls have minimal width of 1 atom placed in hcp adsorption sites. A schematic representation of chlorine layer position relatively to substrate lattice is shown below. It should be noticed that even at so low temperature domain walls are not always imaged as lines of single atom width. For our opinion this is related to the influence of STM tip that moves less bounded atoms in the compressed region during scanning.

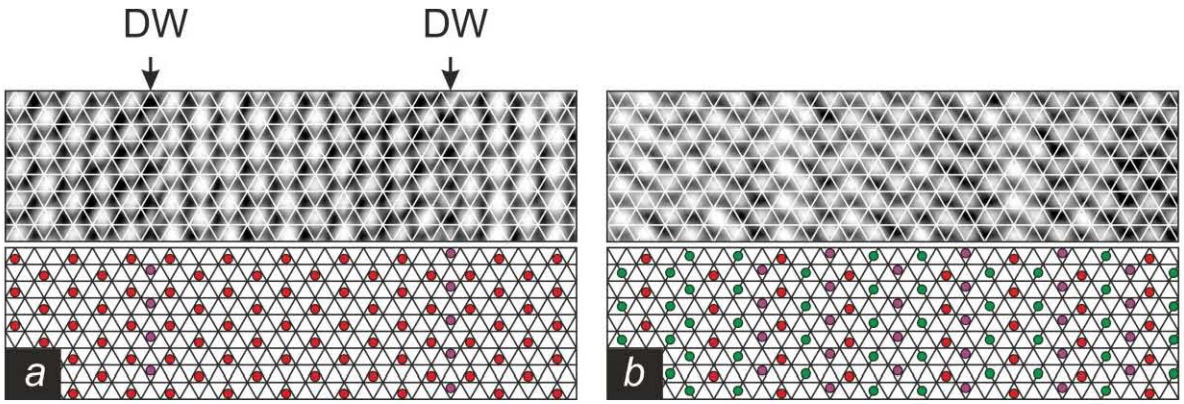

Figure 5.4. *Low-temperature STM image (76×20 Å^2, 5K) of copper surface covered with chlorine:* ***(a)*** *θ ≈ 0.36 ML;* ***(b)*** *θ ≈ 0.41 ML (saturated monolayer). Corresponding schematic view of chlorine monolayer (circles) and substrate (grid) is shown below*

The STM image of the saturated chlorine layer at surface coverage $\theta \approx 0.41$ ML is shown on Figure 5.4b. At this coverage the compression is so large that the width of domains is comparable with the width of domain walls separating them. There is no more sense to talk about domains of $(\sqrt{3}\times\sqrt{3})R30°$ structure and domain boundaries as most of atoms occupy adsorption sites different from fcc ones. It is also impossible to determine the unit cell of this structure. We can only talk about its average periodicity in the direction perpendicular to the direction of compression.

In our experiments we did not observe appearance of a gas of interstitial defects on the initial stage of the (√3×√3)R30° structure compression like for the case of Cl/Ag(111). When the surface coverage exceeded θ > 0.33 ML either unperturbed or compressed (√3×√3)R30° lattice with domain wall structure was observed. However we were able to artificially produce interstitial defects using the following procedure. During scanning of homogeneous (√3×√3)R30° structure the bias voltage was pulse-increased up to maximal value (for our Omicron LT STM this is $U_{gmax} = \pm 10$ V) for a while (~ 1s). As a result a small number of chlorine atoms was pulled out from monolayer and thrown into the neighboring unperturbed regions of (√3×√3)R30° structure. Since the surface temperature was T = 5 K in the place where such atoms touched down the surface interstitial defects similar to those observed in Cl/Ag(111) system appeared (Figure 5.5). In the same time vacancy defects appeared in the places where these atoms were pulled out - Figure 5.5a.

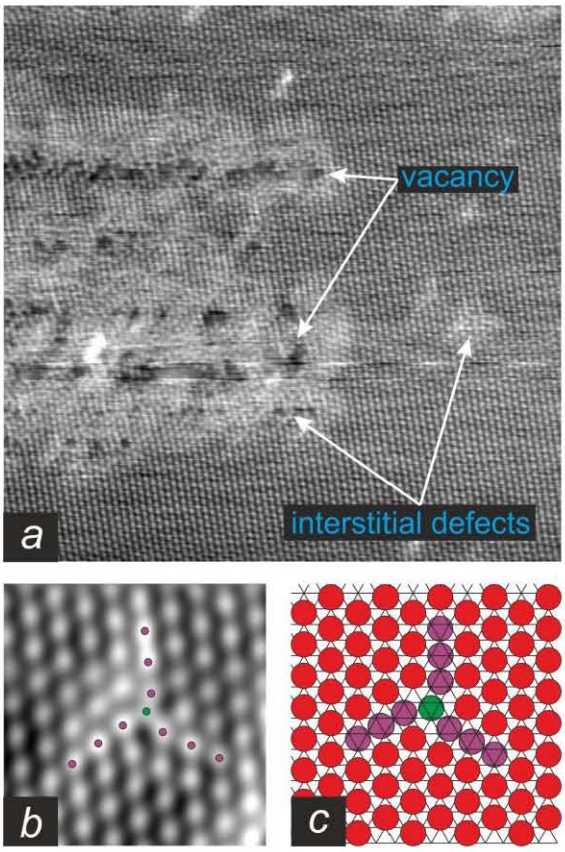

Figure 5.5 (a) *Surface region (250×250 Å^2, 5K) with chlorine (√3×√3)R30° structure at low temperature after puls-increasement of bias voltage and artificial preparation of interstitial defects (see text for details).* ***(b)*** *STM image (40×40 Å^2, 5K) of an interstitial defect.* ***(c)*** *Structural model of an interstitial defect – experiments were done at 5K*

5.2 Comparison of structural phase transitions on (111) face of Cu, Ag and Au under chlorine action

After we have discussed experimental results on the chlorine interaction with (111) face of silver, gold and copper we can make comparative analysis of the obtained data. For clarity we will summarized our and previously published results in a phase diagrams of chlorine monolayer on Cu(111), Ag(111) and Au(111) - Figure 5.7. The areas and especially the borders of each phase are drawn semi-quantitatively since we do not have enough information.

In all the three systems considered, chlorine forms a commensurate (√3×√3)R30° structure at exact surface coverage θ = 1/3 ML. This structure is always preceded by appearance of atomic chains with nearest neighbor interatomic distances equal or even less than the distances in the commensurate (√3×√3)R30° structure. Appearance of chain-like structures with so high atom density is very surprising for itself. Two main questions may arise. First, how is it possible to form one-dimensional structures on isotropic substrate with hexagonal symmetry? And why the density of atoms in the chains is larger than their

density in the two-dimensional commensurate (√3×√3)R30° lattice that appears later at much higher coverage? For our knowledge this is the first and the only observation of such surface structures.

Earlier it was already reported that chain-like structures are observed in the O/Pt(111) system [5]. The authors report on the observation of chains of two-atom width. Their formation was attributed to the low temperature of the surface 90-100 K during adsorption and hence low mobility of adsorbed oxygen atoms, together with the dependence of dissociation probability of O_2 molecules on the distribution of the adsorbed atoms on the surface. Adsorbed oxygen molecules will preferably dissociate in the vicinity and from one specific side from preadsorbed and already dissociated oxygen molecules. Due to low mobility the dissociation product – oxygen atom pairs – will stick to the surface in the same place where they appeared, thus giving rise to the two-atom chains. It is clear that such mechanism could not be responsible for the chain formation in halogen/metal systems since in our case adsorption of halogen molecules was done at room temperature when their mobility is rather high. Moreover even after heating the surface (up to 500 K) precovered with chlorine layer with $\theta << 0.33$ ML and subsequent cooling down (back to 5 K) chains of chlorine atoms still formed. As it was shown in the same work [5] adsorption of oxygen at higher or lower temperature does not give rise to chain structures.

Another example of chain formation was reported for Co atoms deposited at low temperature T < 20 K on copper (111) surface [6]. In this case low surface temperature and low mobility of cobalt atoms also played a key role. As it was shown both experimentally and theoretically the Co-Co interatomic force was largely defined by a rather week interaction through surface electron gas. This kind of indirect interaction is oscillating with the period $\lambda_F/2$, where λ_F is the surface electron Fermi wavelength [7]. For copper (111) surface $\lambda_F/2 = 15$ Å. By considering this interaction to be pairwise (which is not the case, actually) chain formation can be explained as following. Imagine that adsorbed atoms interact via nearest neighbor attractive and next-nearest-neighbor repulsive potential force as shown on the Figure 5.6 and a dimer of two atoms occupying neighboring adsorption sites has appeared occasionally on the surface.

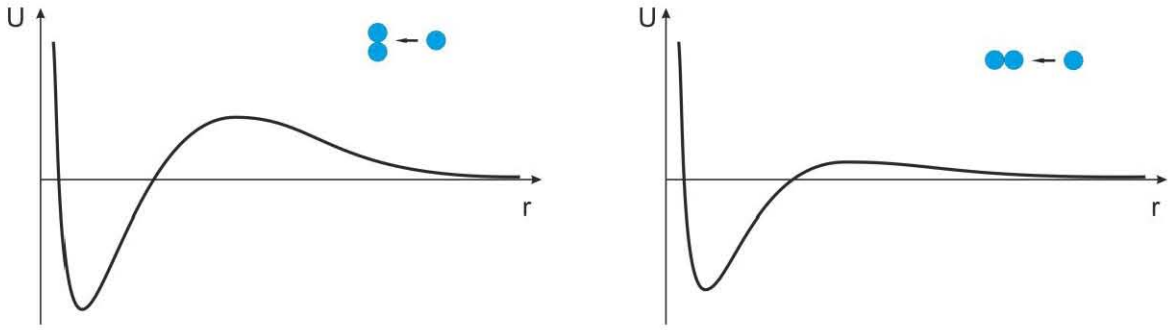

Figure 5.6. *Schematic representation of potential of a dimer for the third adsorbate atom approaching to it perpendicular (left) and along (left) the length of the dimer*

The repulsive force experienced by the third atom approaching the dimer will be larger in the direction perpendicular to the length of the dimer since it will be (nearly) the sum of the two atoms repulsive force. On the contrary it will fill smaller repulsion in the direction along the length of dimer since the repulsion of the nearest atom in dimer will be partially compensated by attraction force of the remote atom of dimer. Thus even on isotropic substrate with isotropic adsorbate-adsorbate interaction appearance of preferential direction and growth of one-dimensional structures is possible. *Ab initio* calculations that take into account non pairwise nature of interaction through surface electron gas fas confirmed this qualitative consideration [6]. The nearest-neighbor distance in the chains was imposed the distance ≈ 8 Å to the first minimum in the oscillating interatomic force.

We suppose that similar mechanism can explain appearance of chains in our experiments. Interaction through the surface electron gas seems to be too week (though in the work of Nanayakkara et al. [8] it was argued that this interaction can influence the structure of adsorbate layer even at very high temperatures T = 600 K) to compete with thermal excitations at room temperature and another more strong interaction should play dominant role – dipole-dipole or elastic interaction through the substrate. Non pairwise effects in these interactions can introduce the specific direction for growth of one-dimensional chains. The same interaction must be responsible for the high density of chlorine atoms in the chains.

Although chains are observed in all the three studied systems, their evolution with surface coverage is quite different. Atomic chains in chlorine monolayer on Ag(111) surface increase their length with the coverage but seek to avoid intersections as long as possible. Also there is no growth of (√3×√3)R30° islands up to the moment when the density of chains is so high that they start to merge. On the opposite side, areas of (√3×√3)R30° structure start to appear rather early in Cl/Au(111) and Cl/Cu(111) systems. Atomic chains can easily intersect and close-up to form nano pores. This nano pores are self-organized in the superstructure with hexagonal symmetry. On the gold surface this superstructure is particularly well ordered. Unfortunately we don't have any explanation of the driving force for this self-organization. Perhaps the answer on the question about the origin of chain formation will also elucidate the reason for self-organization of nano pores.

As it was discussed in the Chapter 1 halogen interaction with metals is usually considered in a simple geometrical approach. Based on this approach it remains unclear why there is no compression of the (√3×√3)R30° structure in the case of Cl/Au(111) system that is geometrically very similar to the system Cl/Ag(111) where we do observe compression. This fact indicates that such considerations are too simplified.

Appearance of interstitial defects (or crowdions) on the initial stage of commensurate lattice compression in Cl/Ag(111) system and their subsequent condensation into heavy domain walls are of particular interest. Previously it was reported from the indirect LEED observation a reversible "gas-of-defects/domain-walls" transition [9]. For our knowledge our LT STM results give the first direct proof of such compression mechanism existence

and they avoid possible ambiguity in the interpretation of diffraction data. Chlorine monolayer on Ag(111) surface seems to be promising for further study dynamics of two-dimensional gas-of-defects and details of commensurate lattice compression for instance in order to check the theory proposed by Lyuksyutov et al. [10]. Another theoretical approach considering point defects in commensurate structure was developed by Moderos et al. [11]. The authors have shown that existence of such defects should have crucial influence on the phase diagram of the adsorbate monolayer, notably for commensurate-incommensurate phase transitions. From experimental point of view the most interesting is the study of properties of interstitial defects, their mobility and its dependence on the surface temperature. It is also important to study the details of crowdion condensation into domain wall structure: estimation of critical value for density of interstitial when their condensation into domain walls starts, dependence of this density on the surface temperature.

It is not clear why we have not observed appearance of such interstitials during compression of commensurate chlorine lattice on Cu(111) surface. Such defects can exist in this system as we were able to produce them artificially. We can suppose that at room temperature these defects are free to move fast on the surface and they may accumulate in the vicinity of atomic steps and other surface defects. That's why when the surface is cooled down we only observe large nonperturbed regions of commensurate structure whereas all the excess of chlorine is accumulated near surface defects where it is hard to obtain atomically resolved STM images. When the surface coverage reaches some critical value formation of domain walls starts abruptly.

STM images of heavy domain walls in Cl/Ag(111) and Cl/Cu(111) systems unambiguously show that at low temperatures the width of domain wall is minimal and equal to single atomic row. This result conforms theoretical predictions and numerical simulation reported previously [12, 13]. At higher temperatures domain walls are broadened by thermal oscillations of adsorbed atoms [3].

Finally an important result concerns the proof of surface reconstruction under halogen action especially in the case of the (3x3) Cl/Ag(111). Reconstruction of surface observed for silver and gold is in line with DFT calculations [14, 15]. According to them for high coverage layer of electronegative elements it becomes energetically favorable to produce surface defects and create a mixed layer of adsorbate and metal atoms.

All the results are summarized on the phase diagram presented in Figure 5.7

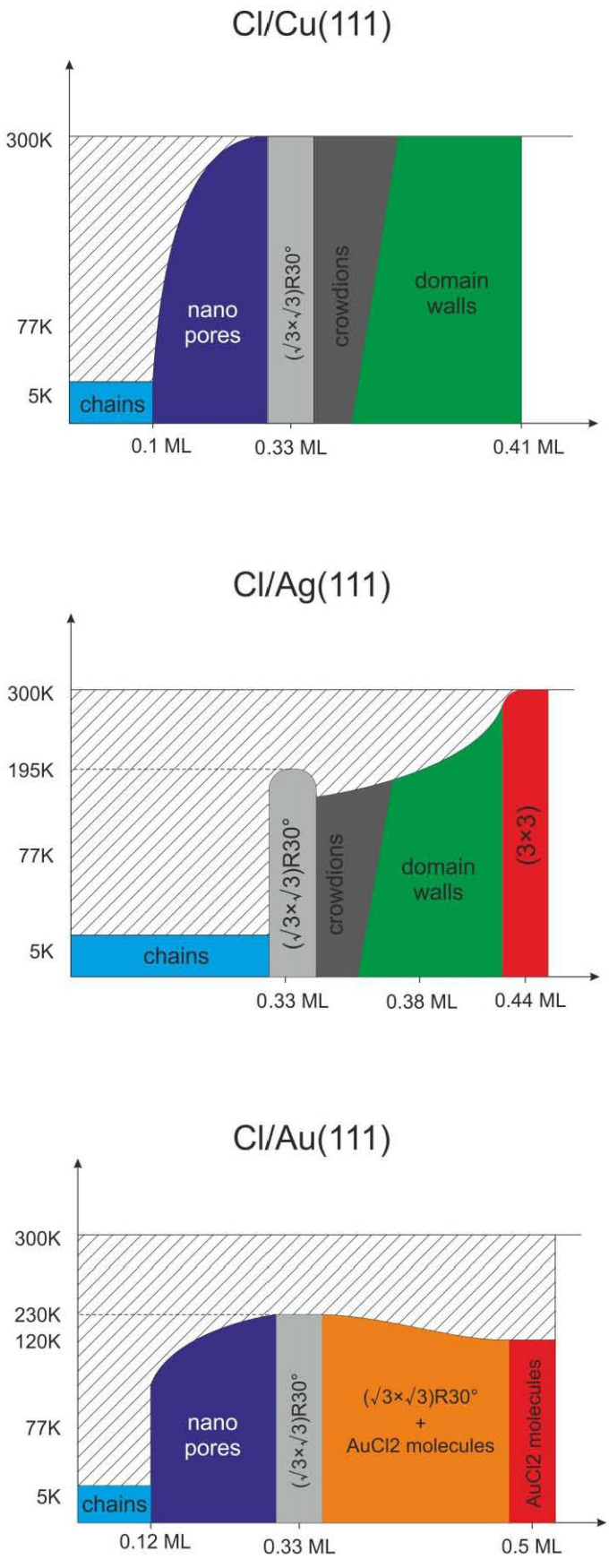

Figure 5.7. *Schematic phase diagrams for chlorine monolayer on Cu(111), Ag(111) and Au(111) surfaces The reconstructed surfaces are represented in red.*

5.3 Conclusion

1. At low coverage and low surface temperatures chlorine atoms form single-atom chains on Cu(111), Ag(111) and Au(111) surfaces. On silver surface chlorine chains avoid intersection and formation of islands with $(\sqrt{3}\times\sqrt{3})R30°$ structure, whereas on copper and gold surfaces atomic chains close-up and form nano pores which in turn are arranged in a superstructure with hexagonal symmetry.
2. On the initial stage of commensurate lattice compression appearance of the gas of interstitials is observed. Increase of the surface coverage leads to the increase of density of this gas. At some critical density interstitials start to condensate into heavy domain walls.
3. Our experimental results prove the possibility of metal surface reconstruction under chlorine action. Based on our experimental results supported with DFT calculations we propose atomic structure models for surface reconstructions on silver (111) surface and formation of halide-molecular structure on gold (111) surface.

Bibliography of Chapter 5

[1] W.K. Walter, D.E. Manolopoulos, R.G. Jones. Chlorine adsorption and diffusion on Cu(111) // Surf. Sci. 348 115 (1996).

[2] P.J. Goddard, R.M. Lambert. Adsorption-desorption properties and surface structural chemistry of chlorine on Cu(111) and Ag(111) // Surf. Sci. 67 180 (1978).

[3] B.V. Andryushechkin, V.M. Shevlyuga, K.N. Eltsov. Domain-wall mechanism of "(n√3×n√3)R30°" incommensurate structure formation in chemisorbed halogen layers on Cu(111) // Surf. Sci. 470 L63 (2000).

[4] R. Dennert, M. Sokolowski, H. Pfnur. Ordered phases and phase-diagram of sulfur adsorbed on Ru(001) // Surf. Sci. 271 1 (1992).

[5] T. Zambelli et al. Complex pathways in dissociative adsorption of oxygen on platinum // Nature 390 495 (1997).

[6] V.S. Stepanyuk et al. Quantum interference and long-range adsorbate-adsorbate interactions // Phys. Rev. B 68 205410 (2003).

[7] P. Hylgaard, M. Persson. Long-ranged adsorbate–adsorbate interactions mediated by a surface-state band // Journ. of Phys.: Cond. Matt. 12 L13 (2000).

[8] S.U. Nanayakkara et al. Long-range electronic interactions at a high temperature: bromine adatom islands on Cu(111) // Phys. Rev. Lett. 98 206108 (2007).

[9] G. Godzik, H. Pfnur, I.F. Lyuksyutov. Impurity-induced changes of overlayer symmetry and of phase transitions // EPL 56 67 (2001).

[10] I.F. Lyuksyutov, H. Pfnur, H.U. Everts. Incommensurate-commensurate transition via domain wall evaporation in an overlayer // EPL 33 673 (1996).

[11] L. Mederos, P. Tarazona, G. Navascues. Density-functional approach to phase transitions of submonolayer films. II. The role of the relaxation mechanism // Phys. Rev. B 35 3384 (1987).

[12] A.G. Naumovets, A.G. Lyuksyutov, V. Pokrovsky. Two-dimensional crystals // Academic Press (1992).

[13] O.M. Braun, Y.S. Kivshar. The Frenkel-Kontorova model: concepts, methods, and applications // Springer (2004).

[14] P. Gava et al. Adsorption of chlorine on Ag(111): no subsurface Cl at low coverage // Phys. Rev. B 78 165419 (2008).

[15] T.A. Baker, C.M. Friend, E. Kaxiras. Effects of chlorine and oxygen coverage on the structure of the Au(111) surface // Journ. of Chem. Phys. 130 084701 (2009).

CHAPTER 6.
Electron confinement in chlorine based quantum corrals

In this chapter we will focus on the influence of the nano porous lattice described in Chapter 4 on the electronic properties of the Au(111) surface. We will show that chlorine based nano pores behave like quantum corrals for electrons of the Shockley states. A detailed study of the electronic states developing inside the pores will be presented. The size and shape influence on the quantized states will be discussed together with numerical simulations within hard well model. We will show the limitation of this model to reproduce the experimental data. As an introduction to our experimental findings we will first review in this chapter the main results previously published on the surface quantum corrals.

6.1 Scientific background on surface electron confinement

6.1.1 Surface states

Surface states are specific electronic states that appear in the vicinity of crystal surface. Their appearance is a result of the breakdown of perfect crystal periodicity at the surface [1, 2]. The energy of these states can coincide with the allowed electron band in the crystal. These are so called *surface resonances*. A much more intriguing is the case of electronic states with the energy lying inside the volume band gap. Such electronic states with are also called *true surface states*. The electrons occupying these peculiar states are trapped at the surface since they cannot propagate both into the vacuum region (due to the work function of the material) from one side and into the volume of the crystal from another side since their energy is forbidden in the bulk. Therefore they are described with complex wave vector and form a two-dimensional gas on the surface. In the later discussion we will refer to the true surface states as simply surface states.

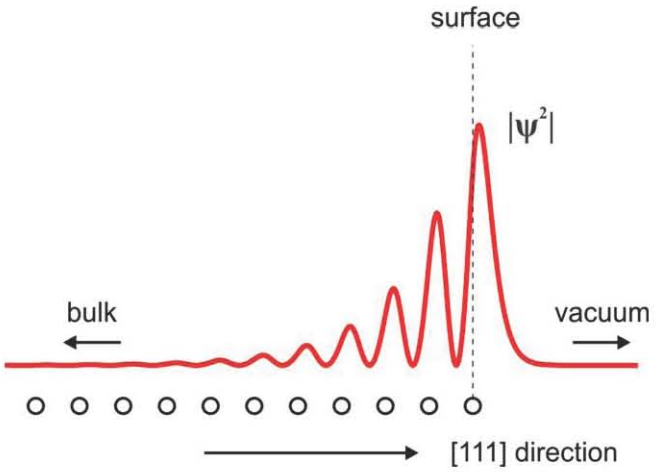

Figure 6.1. *1D diagram of the probability density of a surface –state electron*

Figure 6.1 shows the probability density of a surface state electron in the direction z perpendicular to the surface ($|\psi_z|^2$). Surface electron wave-function decays fast both into the vacuum region above the surface (typical attenuation length is 1-5 Å) and into the crystal volume below the surface (typical attenuation length up to several atomic layers). Thus surface electrons are localized near the edge of the crystal and are accessible to the local surface techniques like STM/STS and PES. Existence of the surface breaks crystals periodicity only in one z-direction, whereas in two others directions (x and y) parallel to the surface – the translation symmetry remains unchanged and surface electron wave functions are simply two-dimensional Bloch waves.

To give an example Figure 6.2 shows band structure of copper crystal projected in the (111) direction of the crystal. Here the projected bulk bands are represented as shaded gray areas. One can clearly see that several dispersive surface bands (solid red lines) appear inside bulk band gaps. There also exists surface resonance (dashed red line).

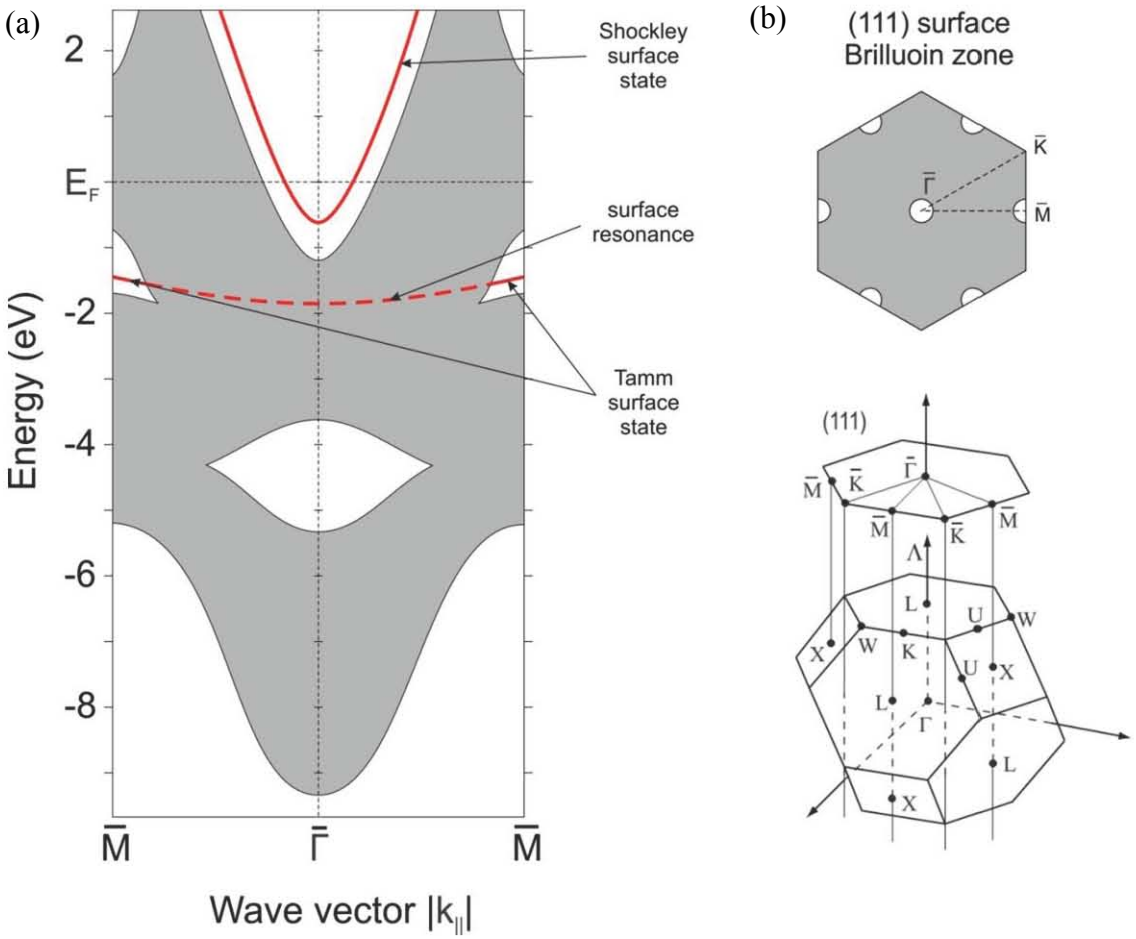

Figure 6.2 : (a) *Projected bulk band structure (shaded areas), surface states (solid red lines) and surface resonances (dashed red line) at a Cu(111) surface determined by LDA-DFT calculations Reproduced from [Zangwill] -* ***(b)*** *bulk and surface Brillouin zones are shown*

Nomenclature widely used in the literature distinguish between two types of surface states: 1) Tamm surface states refer to states that appear entirely due to the change of the potential in the last few atomic layers of the crystal and provide from rather localized and non hybridized band (for instance *d* bands) - 2) Shockley surface states appear inside inverted bulk band gaps in the crystals with relatively small interatomic distances that allow strong hybridization and band crossing [3]. Often there exist both Tamm and Shockley surface states on a given metal surface. In the case of Cu(111) surface Shockley surface state is those in the vicinity of $\bar{\Gamma}$-point inside the inverted sp-gap, whereas Tamm state appears in the bulk band d-gap around $\bar{M}$-point.

Shockley surface states on (111) faces of copper, silver and gold are of particular interest since they lie in the vicinity of surface Brillouin zone center ($\bar{\Gamma}$-point) and have simple parabolic dispersion [3] given by:

$$E_{SS} = E_{\bar{\Gamma}} + \frac{\hbar^2}{2m^*} k_{\parallel}^2 \qquad (6.1)$$

Here $E_{\bar{\Gamma}}$ is the energy of surface state bend edge, m*- surface electrons effective mass and $k_{\parallel}^2$ – surface electrons wave vector. In other words surface electrons in these metals can be considered as a two-dimensional gas of free electrons. The deviation from the parabolic dispersion that actually exists in most of cases can be disregarded being too small [4]. From ARPES measurements the band parameters (minimum of the band E_0 and effective mass m^*) can be easily determined. For instance Figure 6.3 shows the dispersive bands obtained from ARPES measurements on Ag(111), Cu(111) and Au(111) surfaces [5]. From theses curves it is clear that both E_0 and m^* are material dependant. In the case of Au(111) it is noticeable that the band is split in to sub bands due to spin-orbit interaction [6,7]. It has been shown also from many times (early in the nineties) that the onset of surface bands can be determined by STS [8,9,10]. For instance one can compare in Fig. 6.3 the energy of the onset of the step like curves measured on the noble metals and the corresponding band minima obtained from ARPES data.

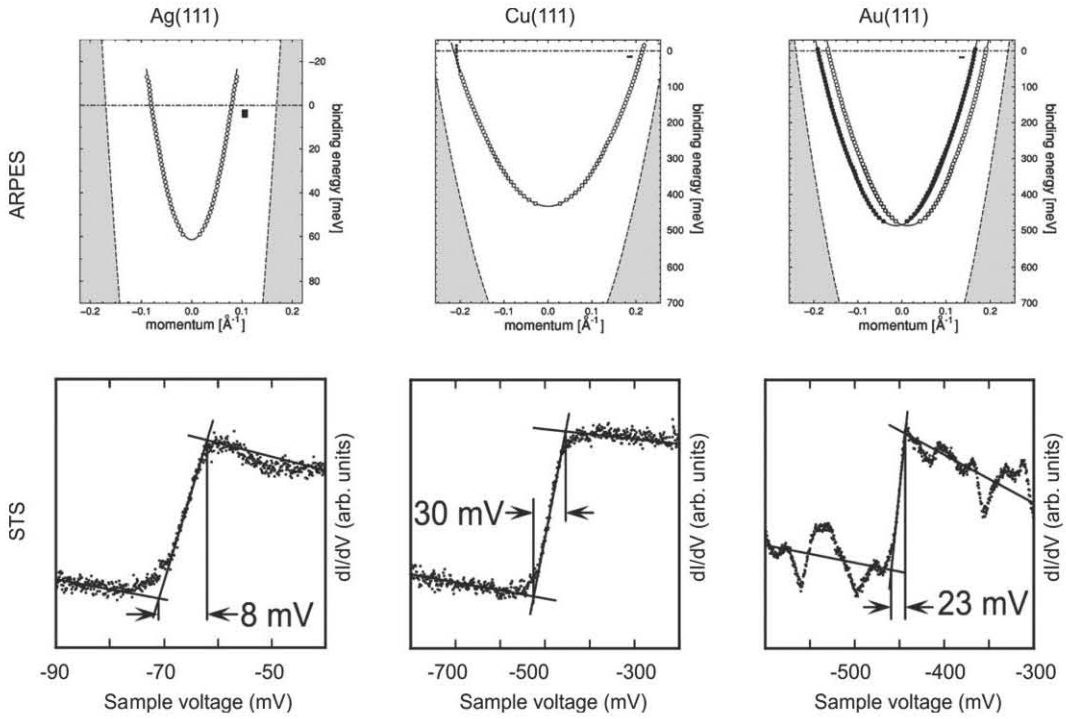

Figure 6.3 : *ARPES (upper row) and STS (bottom row) measurements of surface state on Ag(111), Cu(111) and Au(111) surface at T = 5K. ARPES data from [5], STS data from [10]*

Other fundamental properties like intrinsic life-time of surface state electrons (which is inverse proportional to their coherence length), can be measured both from ARPES and STM/STS. In the case of photo-electron spectroscopy the life time τ is related to the measured line width Γ_{SS} (FWMH) as $\Gamma_{SS} = \frac{\hbar}{\tau}$ [11]. In the case of STS the same relation is valid for width of the peaks in dI/dV spectra of quantized states in electron resonators [12]. For a non confined surface state the width of the onset in the STS step like curve can also be related to life time [10-13].

6.1.2 Scattering of surface states by impurities and surface defects

The surface state wave-function is naturally extremely sensitive to any changes in the potential at the surface (in the few last atomic planes of the crystal) induced by structural or chemical modifications. As a consequence surface electrons can be effectively scattered by any imperfections on the surface like atomic steps or adsorbed atoms. Such scattering events will lead to the modification of the constant 2D surface LDOS and can be probed by STM. This, as well as 2D nature and simple parabolic dispersion of surface electrons on copper, silver and gold surfaces, opens attractive possibility of direct studying electron-scattering and confinement phenomena [8,14,15].

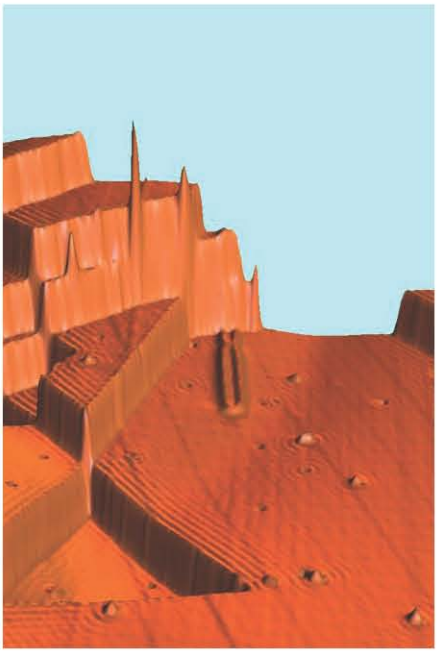

Figure 6.4 : *Surface electrons scattered by defects on Cu(111) surface - from [15])*

Figure 6.4 shows one of the very early example [15]. The Cu(111) surface imaged in STM was obtained in topographic mode with very low bias voltage, when tunnel current integrates electrons in a narrow energy window close to the Fermi level. Oscillations in surface electron density are clearly seen, both parallel to the atomic steps edges and around point imperfections on the terraces. In the above case only electrons with roughly Fermi energy contribute to the ripple pattern and the period of oscillations is about 15 Å. Spatial distribution of electrons density around the defect in the crystal at Fermi energy is known as Friedel oscillations, whose period is equal to the half Fermi wave-length $\lambda_F/2$ [16]. Taking the Fermi momentum $k_F = 0.215$ Å^{-1} for Cu(111) surface state [5] we find $\lambda_F/2 = 14.6$ Å in very good agreement with observed period.

The observed standing wave pattern can be naturally explained as interference of incoming and partially reflected by the defect surface electron waves. The main physical quantity that governs this process is the reflecting property of the defect. For point defects this property can be described as a complex phase shift in electronic amplitude acquired when an electron scatters off a defect [17,18]. In the case of linear step, that is a continuous defect, the scattering properties are more conveniently characterized by a complex reflecting coefficient [8,14,19,20].

In the latter case the standing-wave pattern can be relatively simply analyzed analytically, as was done by Bürgi [20]. The scattering properties of atomic step can be characterized by a complex reflecting coefficient $\boldsymbol{r}_{k_x} = |r_{k_x}|e^{i\phi_{k_x}}$ that depends on the electrons kinetic energy in the x-direction perpendicular to the step [8,19,4]. Here reflecting amplitude $|r_{k_x}|$ has values between 0 and 1, and ϕ_{k_x} is the phase shift in electronic amplitude acquired when an electron scatters off a step. Along reflection (with probability $r_{k_x}^2$) some electron density can be transmitted to the other side of the step (with

probability $t_{k_x}^2$) or absorbed (with adsorption probability $a_{k_x}^2$). Particle conservation implies that $r_{k_x}^2 + t_{k_x}^2 + a_{k_x}^2 = 1$. The physical meaning of adsorption is scattering of surface electrons into bulk electron states [17,18]. On the flat defect-free surface bulk and "true" surface electron states are orthogonal. Appearance of the defect breaks system symmetry and introduces coupling between surface and bulk electrons [17,21]. Taking into account all these processes (reflection, transmission and adsorption) the local density of surface electrons with energy E at a given point (x, y) can be expressed in the form (for details see [20])

$$\rho_{step}(E,x) = \frac{2}{\pi}\rho_0 \int_0^{k_E} dk_x \frac{1 + |r(k_x)| \cos\left(2k_x x + \varphi(k_x)\right)}{\sqrt{k_E^2 - k_x^2}} \qquad (6.2)$$

Here ρ_0 is the non-perturbed surface electron density and $k_E = \sqrt{2m^*(E - E_{\bar{\Gamma}})/\hbar^2}$. Coordinate x denotes the distance to the step edge in the direction perpendicular to the step.

The phase shift acquired by electron wave scattered on the step was found to be close to $-\pi$ on Ag(111) [4] and Au(111) [14] surface. Moreover, numerical solution of this equation showed that arbitrary ϕ_{k_x} value only merely changes the standing-wave pattern [20]. Under these conditions and reasonable k_x dependence of $|r(k_x)|$ one finds simplified expression for surface electron density near the step edge [20]

$$\rho_{step}(E,x) \approx \rho_0[1 - |r(k_x)| \cdot J_o(2k_E x)] \qquad (6.3)$$

where J_0 is the Bessel function of zero order. The oscillatory behavior of surface electronic LDOS is described by term $J_0(2k_E x)$. These oscillations have intrinsic $1/\sqrt{x}$ decay related to the fact that all electrons with x-component of wave vector from 0 to k_E contribute to the LDOS at fixed energy E [20]. Note that in this model all inelastic processes (such as electron-electron or electron-phonon scattering) are neglected. This simplification is valid for the case of low-temperature measurements, when the coherence length associated with inelastic processes is much larger than intrinsic $1/\sqrt{x}$ decay. Further extension of this model is possible, that allows one to study surface electron inelastic scattering [20].

This expression can be used to analyze experimental spectroscopic and topographic data to establish values of $|r_{k_x}|$ and ϕ_{k_x} [20]. Figure 6.5 shows example of such treatment for Ag(111) step [Bürgi2] (more precisely, in this example further extension of above model for calculation of constant-current tip-sample distance was used, that does not change the basic idea of this approach). The image presents an STM line scan perpendicular to the step edge, taken at bias voltage +10 meV. By choosing reflecting amplitude the authors were able to perfectly reproduce observed ripple pattern from both sides of the step. Corresponding values of reflecting amplitudes are $|r_{desc}| = 0.56$ and $|r_{asc}| = 0.37$. These r-values represent the reflection amplitude at the Fermi energy since the line scan has been taken at low bias voltage. Note that atomic step has different reflecting

coefficients depending on the side from which electrons arrive on it: it is almost 2 times larger for electrons that arrive from upper terrace. This can be understood from simple geometrical considerations: surface electrons that arrive from the lower terrace "see" the bulk crystal from the other side of the step and can easier continue their motion into bulk states, whereas electrons that arrive from the upper terrace run into the crystal edge and "see" vacuum region [22].

Scattering of electrons on point defects can be modeled in multiple scattering theory [18]. Here the possibility of scattering of surface electrons into bulk states has also to be taken into account.

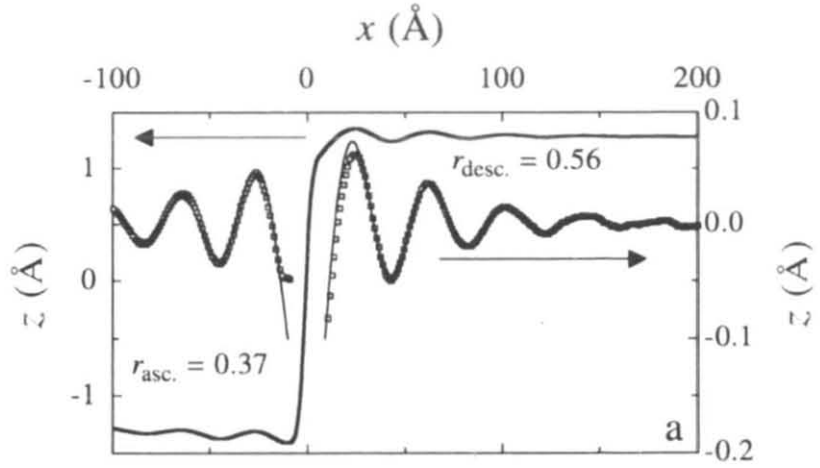

Figure 6.5. *Constant-current linescan taken across a Ag(111) step at U_{bias} = +10 meV and T = 77.3 K. The solid lines are fits of experimental data (small circles) using the model proposed by Bürgi. Reproduced from [20]*

6.1.3 Quantum corrals

Electron-scattering can be used to pattern surface LDOS in controlled manner by manipulating defects. In the limit, surface electrons can be confined inside artificially build structures – so called quantum corrals or resonators (Figure 6.6). The standing-wave pattern that appears inside the corral is the result of interference of electron waves scattered by its boundaries. Evidently, to observe interference pattern the size of the quantum corral must be at least of the same order as coherence length of surface electrons.

i) Fabrication of quantum corrals

There exist several approaches in building quantum corrals, notably using either atomic steps or adsorbed atoms as scatters forming the border of the corral. These defects have to be arranged in proper way to form bounded surface area.

Steps are natural and continuous scattering boundaries existing on the surface. Two parallel atomic steps is the simplest case of a one dimensional electron resonator (see

Figure 6.6a [20, 22] and can be described as an electronic Pérot-Fabry interferometer [20]. Such perfect parallel step arrangement can be created in the vicinity of the place where STM-tip has been (gently) crashed into the flat surface and produced a series of dislocations in the crystal. Two steps can be either both ascending/descending or one being ascending and another descending (see topographic profiles under Figure 6.6a). By this way, resonators of different widths can be created on the surface. Parallel step arrangement is naturally observed on vicinal surfaces. In this case instead of single resonator one has a series of parallel-arranged resonators of the same width (Figure 6.6b) [23]. One can also vary the width of these resonators by changing the orientation of the vicinal surface against basis low-index plane (i.e. changing the miscut angle).

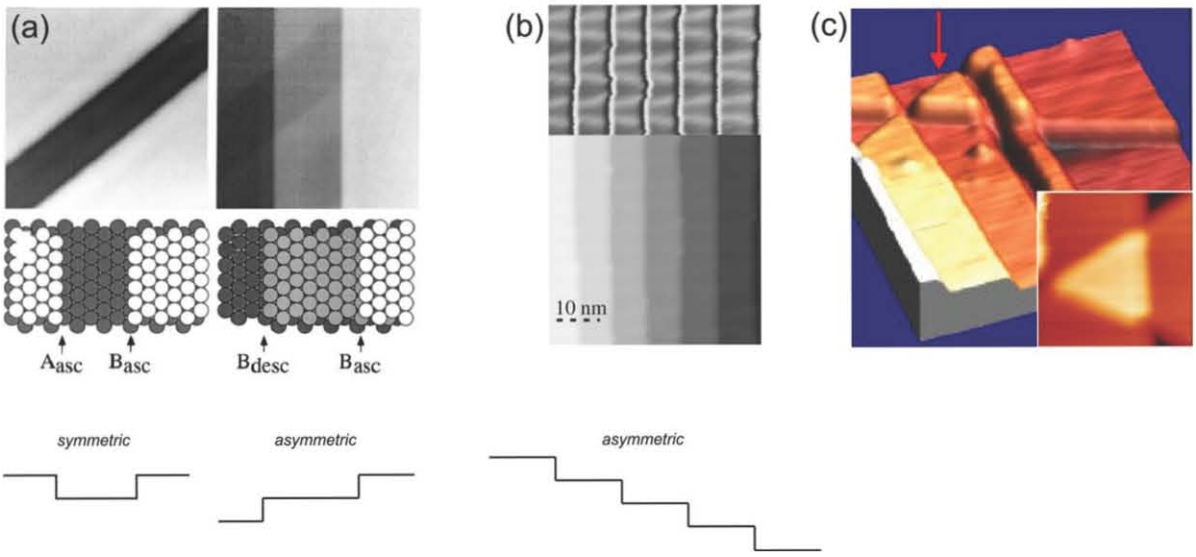

Figure 6.6 : (a) *Surface quantum resonator formed by two parallel ascending (left, 5.6 nm wide) or ascending and descending (right, 10.4 nm wide) steps [20]. (b) Vicinal surface Au(23 23 21) [24]. The width of the terraces is 5.7 nm.* ***(c)*** *Triangular island (6 nm) formed between three steps of different orientation on the Cu(111) surface [25]*

Besides linear resonators giving rise to one-dimensional electron confinement, crashing the STM-tip into the surface can also produces two-dimensional triangular resonators at the crossing of three steps of different orientations (reflecting substrate hexagonal symmetry there are three possible step directions on (111) surface of fcc metals) (Figure 6.6c) [25].

An alternative approach for fabrication of corrals with stepped boundaries is transient sputtering of a surface by ion beam which produces a set of vacancy and adatom islands on the surface – see Figure 6.7a and 6.7b [12, 22, 26]. Such islands can have almost perfect hexagonal shape (due to the hexagonal symmetry of (111) face of fcc crystal) with boundaries formed by descending (adatom islands) or ascending (vacancy islands) steps. Similar set of adatom islands can be obtained by evaporating on the surface of a small amount of metal – typically much less than 1 ML – that is known to grow in Stranski-Krastanov mode on this substrate [11, 22]. In the latter case chemical nature of atoms in the islands can differ from those of the substrate. By choosing the parameters of ion sputtering/metal evaporation one can change the size-distribution of the islands and get

access to quantum corrals of different size. One has to note this approach does not usually permit to produce a sharp size distribution.

Recently epitaxial growth of thick metal films can be used to produce nanopyramids that can be understood as a stack of monoatomic islands of decreasing size - see Figure 6.7c [27,28]. On the top of the pyramid a single hexagonal island of monoatomic height exists. This top island shows the similar electronic properties as monoatomic islands on flat surface.

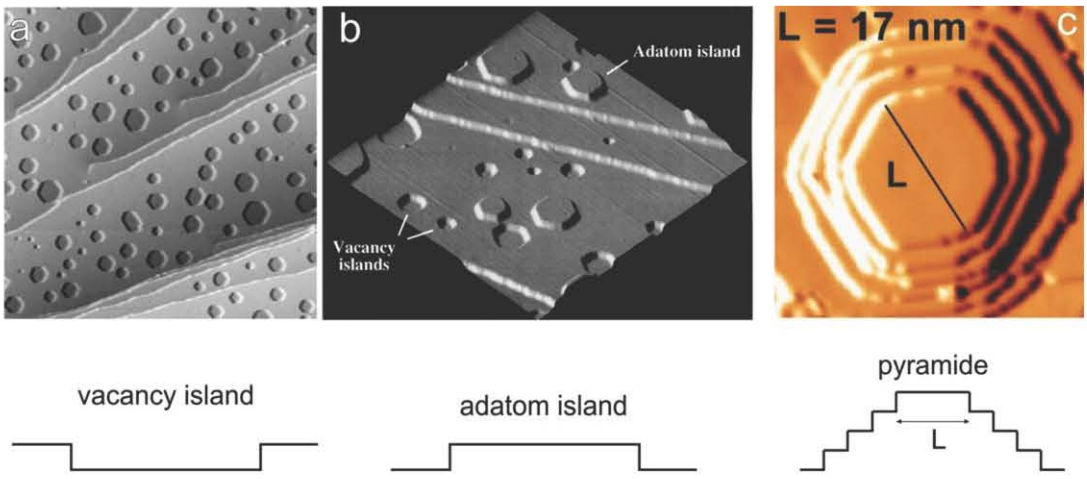

Figure 6.7 : (a) *Formation of vacancy islands on Ag(111) surface after transient Ar^+ sputtering (320×320 nm^2) [26].* ***(b)*** *A set of vacancy and adatom islands on Ag(111) surface, prepared by transient ion sputtering and subsequent Ag epitaxy (160×160 nm^2) [11].* ***(c)*** *Epitaxially grown Ag pyramids on Cu(111) surface [27]*

Another approach in quantum corral fabrication is related to manipulation with STM-tip of surface adatoms [17, 29]. Reducing the distance between adatoms down below typical wavelength of surface state electrons causes adatoms to behave like a continuous scattering boundary. Extending a boundary of tightly spaced adatoms it is possible to create a closed scattering border of any given shape [17]. Figure 6.8 shows examples of quantum corrals of different shape, created by atomic manipulation. Adatoms in the corral boundary could be in principle any chemical elements, but almost all experimental work in this area was done for quantum corrals build from metal atoms. Taking the experimentally measured values of Fermi wave-vectors k_F for noble metals [5] we can estimate the maximal distance between atoms in the border of quantum corral as

$$d = \lambda_F = \frac{2\pi}{k_F} = 3 - 8nm$$

Usually 30-100 atoms are used to build a single quantum corral of 5 to 25 nm in diameter with the nearest-neighbor distance between atoms in the border of quantum corral 9-15Å [17, 29]. The typical size of resonators built from atomic steps lie in the same range 4-15 nm [11, 13, 25]. Thus these two methods produce surface nano structures for electron confinement of approximately the same size. The obvious difference between them is the physical properties of their borders, especially their reflecting quality. The shape and the size of corrals build from atomic steps are imposed by the symmetry of substrate and can't

be changed, whereas atomic manipulation gives access to eventually any geometrical shape and size. However, the ability of STM-tip to change atomic position turns out to disadvantage since it limits the energy band that can be explored with STS without destruction of the corral [17, 11, 30]. Moreover this method is very time consuming and only few corrals can be created on the surface making investigations with spatially averaging methods (like ARPES) impossible.

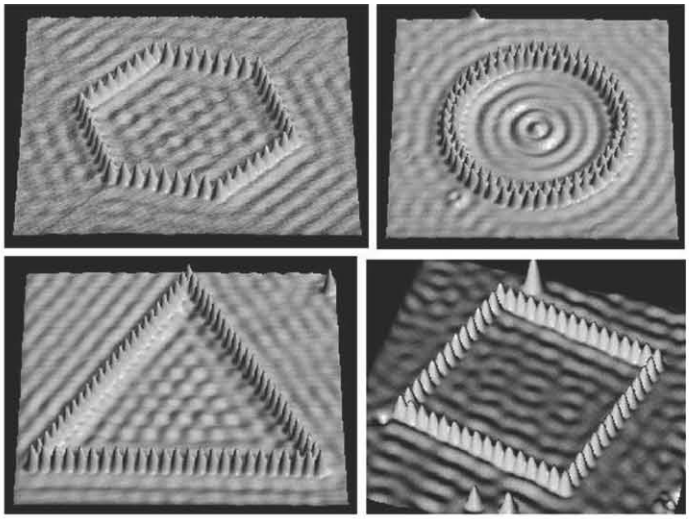

Figure 6.8 : *Quantum corrals of different shapes built by STM tip atomic manipulation from iron atoms on Cu(111) surface. Reproduced from [30]*

ii) Understanding the standing-wave pattern

Surface electron waves being reflected by the borders of quantum corral form a standing wave pattern inside it. Qualitatively all the quantum corrals of different types manifest the same electronic properties. Figure 6.9 shows example of spectroscopic data obtained on the top of one Ag nano pyramid on Cu(111) [27,28]. As it can be clearly seen from dI/dV maps – see Fig. 6.9b - the standing-wave patterns formed by confined electrons strongly depend on the energy. Local tunneling spectra taken at different points show pronounced peaks at certain energies (see spectra #1 and #2 in Fig. 6.9c). The intensity of the peaks strongly depends on the position where these spectra have been recorded. Taking STS spectra at any point along a given direction (shown on the *topo* image as the black solid line with arrows), one can get a complete section of the surface LDOS along this direction in the whole energy range from -80 meV to +90 meV. The result is presented in the middle panel of Fig.6.9c. Such representation is very convenient since it immediately shows the number of nodes in surface LDOS (marked by green points) increases with energy, starting from single maxima in the center of the corral without nodes at energy ~ -40 meV, to two maxima with one node in the center for energy ~ -30 meV, three maxima and two nodes for energy ~ 0 meV and so on.

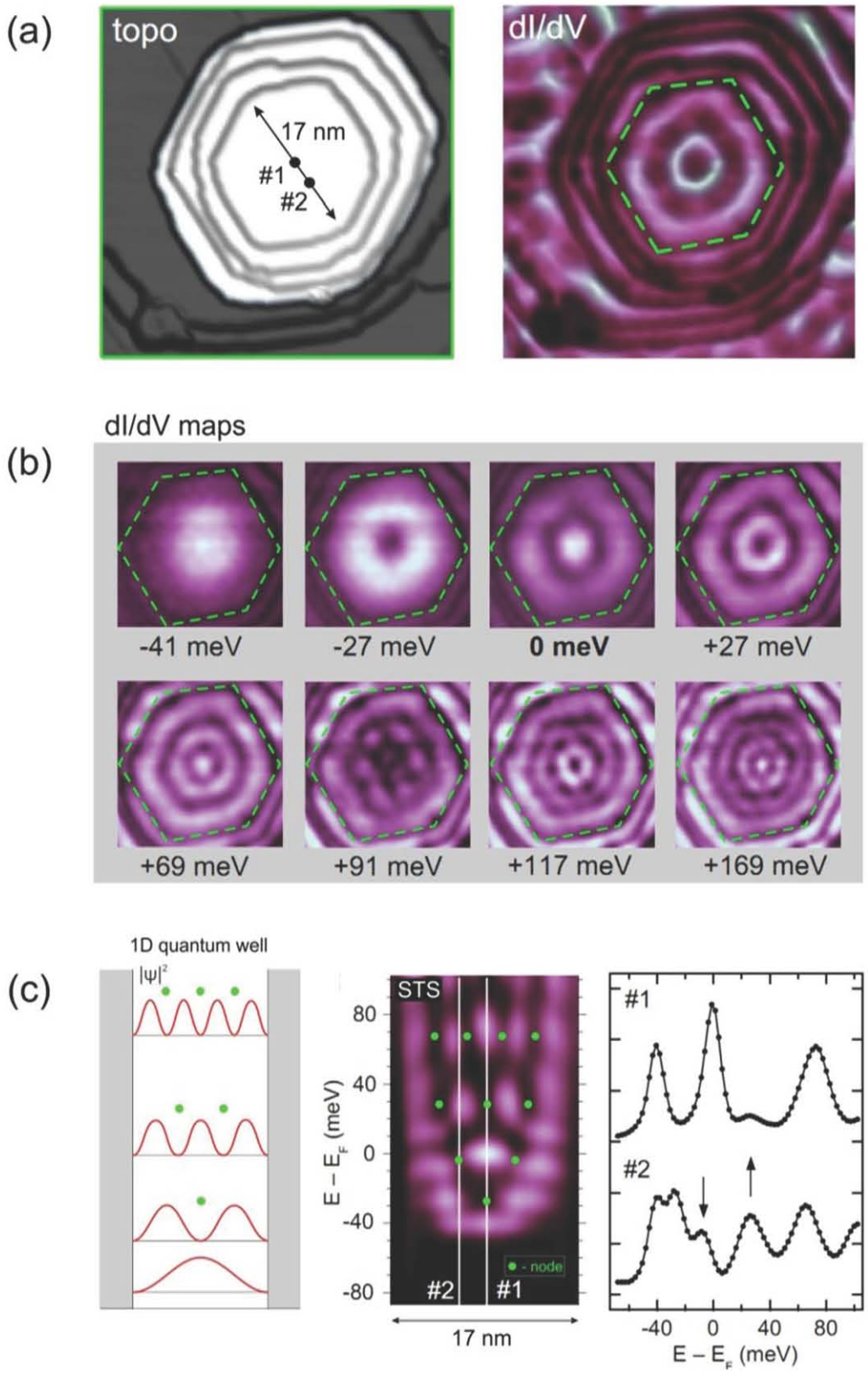

Figure 6.9 : (a) *Topographic view of Ag nanopyramyde on Cu(111) surface along with its dI/dV map -* ***(b)*** *dI/dV maps of nanopyramide taken at different bias voltage.* ***(c)*** *From left to right: electron density in a 1D quantum well - profile of surface LDOS along direction shown on Fig.6.9 (a) - single STS spectra (the points where they have been taken are shown on topo image on Fig. 6.9 (a) -. from [27]*

This resembles the nodal structure of electron density ($|\psi|^2$) inside quantum well (Figure 6.9c). Indeed, scattering potential barrier on the border of the corral prevents electrons to leave the corral and thus trap them. From this point of view we can consider quantum corrals as 2D quantum wells.

The electronic behavior of quantum corrals can be explained in a simple "particle in a box" model [17, 11, 25, 27,28]. In this approach quantum corrals are considered as a two-dimensional quantum wells with infinitely high potential barrier at the boundaries. Ripples in the surface electron density inside corral reflect electron eigenstates (more exactly $|\psi|^2$) of the quantum well probed by STM. The only physical parameters that play the role in this model are geometrical size and shape of the corral, together with dispersion relation of the free surface electrons (effective mass and minimum of the band). The eigenfunctions and energy levels, corresponding to the eigenstates of the resonator, can be directly found by solving a 2D Schrödinger equation for electrons in potential defined by the geometry of the corral. Eigenenergy E_n of the n-th electron states in quantum well can be expressed in the form [11,31]:

$$E_n = E_0 + \frac{\lambda_n}{m^* \Omega} \qquad (6.4)$$

where E_0 is the constant energy inside the well, m* the dimensionless effective mass of the surface electrons and Ω the area of the quantum well. Geometry of the resonator is included in the term λ_n. This term depends on the exact shape of the resonator. In general case the two-dimensional Schrödinger equation has no analytical solutions and eigenfunctions and geometrical factors λ_n have to be found numerically. However for few particular geometries – notably, circular, rectangular and triangular – that allow separation of spatial variables, one can find solution explicitly [15, 25].

Theoretically calculated LDOS ($|\psi|^2$) for first 12^{th} eigenstates of a hexagonal hard-wall resonator are shown on the Figure 610a [27]. Comparison with the experimentally measured dI/dV maps from Figure 6.9b immediately shows coincidence of spatial distribution of electron density for first two modes with eigenenergies -41 meV and -27 meV. It is less evident to compare directly higher order modes. Because of the finite energy width of each resonance several neighboring states can contribute to surface LDOS at given bias voltage [25,27,31]. This effect becomes more pronounced for higher order modes since the energy of neighboring eigenstates lies sequentially closer and closer at higher energy, as well as energy width of each mode increases. Figure 6.10b demonstrates results of the merge of a number of calculated modes that allow to reproduce very well experimental dI/dV maps.

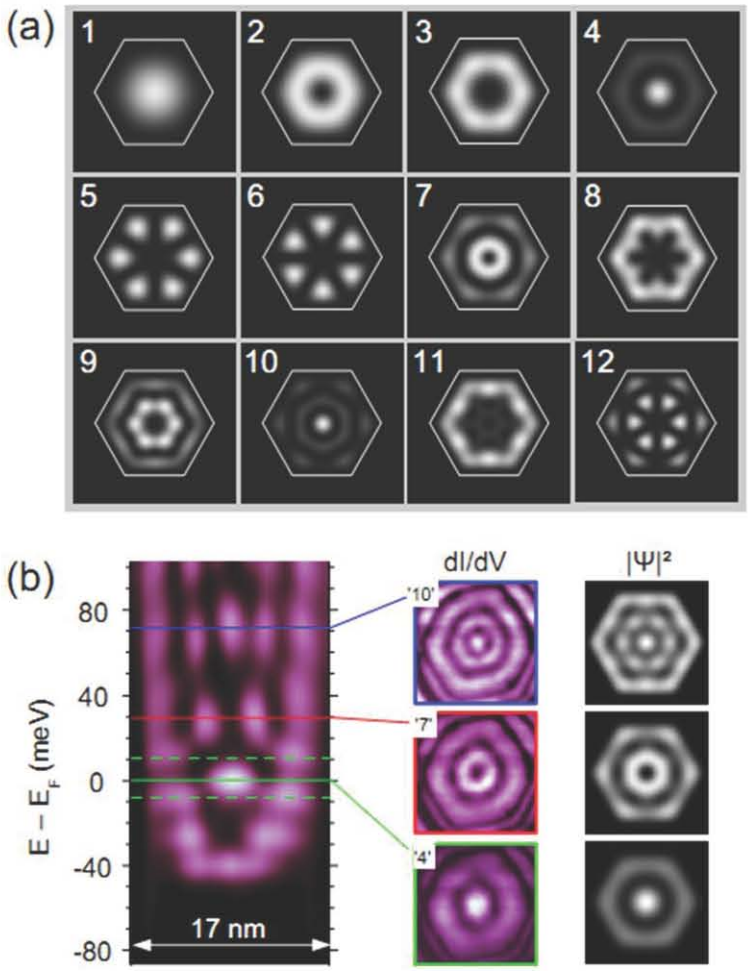

Figure 6.10 : (a) *Calculated electron LDOS ($|\psi|^2$) for hexagonal hard-wall potential well.* ***(b)*** *Comparison between experimental dI/dV maps and calculated LDOS for the 4th, 7th and 10th eigenstates. The energy of neighboring egenstates is close enough for overlapping of LDOS from different states at given energy. Calculated LDOS for the 4-7 and 10th eigenstates was convoluted with upper and lower energy eigenstates (see text for details). From [28]*

For example, careful inspection of standing-wave pattern at Fermi level (marked as „4") shows that it is formed essentially by 4th eigenstate of hexagonal well with small contribution from 3rd, 5th and 6th eigenstates: $|\psi_{0eV}|^2 = |\psi_4|^2 + 0.15\cdot(|\psi_3|^2 + |\psi_5|^2 + |\psi_6|^2)$. Similarly for the wave patterns „7" and „10", those are observed for electrons energy +27 meV and +69 meV respectively, we have $|\psi_{+27eV}|^2 = |\psi_7|^2 + 0.2\cdot(|\psi_5|^2 + |\psi_6|^2 + |\psi_8|^2)$ and $|\psi_{+69eV}|^2 = |\psi_{10}|^2 + 0.6\cdot(|\psi_9|^2 + |\psi_{11}|^2)$ [28].

Comparison of experimentally measured and calculated in "particle in a box" model eigenenergies for nano pyramids of three different sizes – 120 Å, 177 Å and 259 Å – is shown on Figure 6.11. The coincidence is remarkable in all three cases for at least first 20th eigenstates. The main source of inaccuracy comes from deviation from the perfect hexagonal shape,(small) ambiguity in corral size and value of effective mass of surface electrons confined in nano pyramids [28].

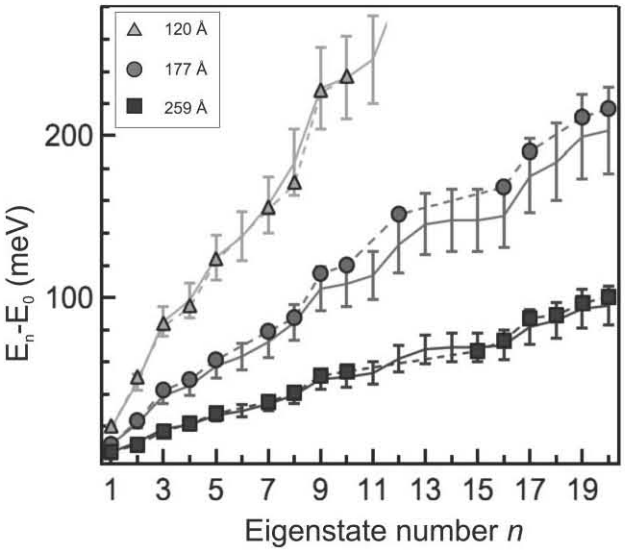

Figure 6.11. *Experimentally measured energy (relative to minimum of the surface state band E_0) for the first 20 eigenstates in nanopyramides of three different sizes. Dashed line serves to guide the eye. Solid line represents results of calculation in "particle in a box" approximation. Error bars shows inaccuracy that comes from measurements of the size of the pyramids and effective mass of electrons. Reproduced from [27]*

Such a "particle in a box" approach has been successfully applied before for prediction of eigenenergies in many types of quantum corrals of different shapes and sizes [17,25,31,32]. However such simplified picture can't explain all the observed spectral features. The first thing is the linewidth of resonances in STS spectra, which is related to the lifetime of electron states in the corral. The "particle in a box" model imply an infinitely long lifetime of eigenstates in the well, i.e. δ-peak features in the spectra, which is evidently not the case in reality. The three inevitable sources of peak broadening are thermal and instrumental effects, together with intrinsic linewidth of surface states at given energy [33]. However, in most of cases (low-temperature experiments and low modulation voltage in STS) their contribution appears to be much less than the observed peak width [33]. That mean there should exist additional broadening source. This discrepancy is eseally explained by the fact that the borders of surface resonators are not perfect reflectors, as it was already mentioned in connection with electron scattering on surface defects. It means that a quantum corral is in fact a leaky box for electrons.

To analyze electronic properties of leaky corral a multiple scattering theory has been widely applied [17,21,29,31]. As it was already discussed, a point scatterer can be characterized by a complex phase shift in amplitude of scattered electron wave. The imaginary part of the phase shift describes adsorption of surface electrons into bulk states. Multiple scattering theory takes into account the multiple reflections of an electron in the presence of many scatterers and treats the motion of an electron both outside and inside the quantum corral. The surface LDOS is calculated as a sum of all electron waves scattered in all possible scattering paths.

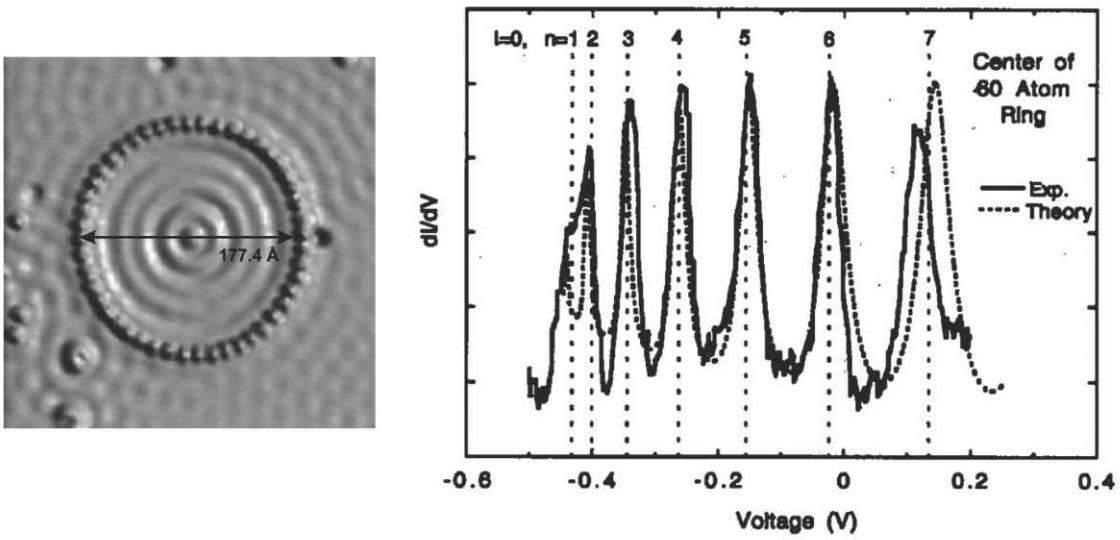

Figure 6.12. *(Solid curve): dI/dV spectrum taken above the center of 177.4 Å Fe ring. The experimental curve has had a smooth background removed. (Broken curve): results of multiple-scattering calculations performed in the "black-dot" limit. (Vertical lines): theoretical eigenenergies for l=0 states of a round, 2D hard-wall box having the same dimensions as the 177.4 Å Fe ring. From [34]*

The only adjustable parameter in these calculations is the phase shift that cannot be easily related to electronic properties of the scatterer [18]. The best match between calculated and experimentally measured LDOS is obtained in so called "black-dot limit" when the imaginary part of the phase shift is infinitely large. This is equivalent to an effective reflecting amplitude of the corrals border $|r| = 0.5$ and reflecting phase shift equal to $\varphi = -\pi$ [34]. Figure 6.12 shows example of experimental dI/dV spectra taken in the center of circular Fe corral on Cu(111) surface together with the calculated spectrum in the "black-dot limit" [34]. Calculated LDOS reproduces very well both position and width of peaks. The multiple scattering calculations in "black-dot limit" imply that 50% of electron amplitude scattered by corrals border is absorbed into bulk states, whereas only 25% of electrons are reflected back. Since each single atom effectively redirects surface electrons into bulk states greater electron confinement will not be achieved by simply packing atoms more densely along the borders of the quantum corral. Greater confinement will likely come only from surface state/adsorbate systems that do not couple surface state electrons so strongly to the bulk [34].

The latter statement explains the success of simple "particle in a box" model for Ag nano pyramids on Cu(111) discussed above. The authors suppose that bulk states can be partially quantified inside the nano pyramid. This situation is different from the usual single layer islands grown on semi-infinite substrate. Consequently the scattering of surface states into bulk states is claimed to be strongly reduced [27]. In addition surface states cannot be so simply transmitted through the borders of the island on the top of the pyramid since it is separated from the surface of the crystal by many single-atom steps. These all together make reflecting amplitude $|r|$ being very close to maximum value theoretically expected and very narrow peaks in dI/dV spectra. The residual peak width is determined by intrinsic surface electron lifetime and makes this kind of quantum corrals suitable for study of electron-electron and electron phonon coupling [27,28].

The Ag nano pyramids described above are unique example of surface quantum corrals perfectly described by simple "particle in a box" model. All the other corrals have to be treated in multiple-scattering approach, which is not so handy and clear. To get some simple explanation of the leaky borders effects we can turn to very helpful work of Bürgi et al [4, 20]. The authors have investigated – both experimentally and theoretically – the case of a one-dimensional resonator formed by two parallel atomic steps. Such resonator has a well-known analogy in optics: Fabry–Pérot interferometer. An electron wave that enters is serially reflected from one edge to another and a standing wave pattern is formed. To analyze this pattern L. Bürgi et al. applied the same model as for surface electron scattering by single atomic step discussed above but taken into account multiple reflections inside the resonator. Therefore the surface LDOS inside it is the sum over all reflected waves, which gives the following result [4]

$$\rho_{FP}(E,x) = \frac{\rho_0}{\pi}\int_0^{k_E} dk_x \frac{1}{\sqrt{k_E^2 - k_x^2}} \cdot \frac{1}{1 + r_l^2 r_r^2 - 2r_l r_r \cos(2k_x a + \phi_l + \phi_r)} \cdot \{(1 - r_l^2)[1 + r_r^2 + 2r_r \cos(2k_x(x-a) - \phi_r)] + (1 - r_r^2)[1 + r_l^2 + 2r_l \cos(2k_x x + \phi_l)]\} \quad (6.5)$$

Here r_l, φ_l and r_r, φ_r are reflecting amplitude and phase shift for atomic steps on the correspondingly left and ride sides of the resonator, and a being the width of resonator.

In the limit of vanishing reflection coefficients, $|r_{l,r}| \to 0$, the above expression reduces to the constant unperturbed surface state LDOS ρ_0. The opposite, hard-wall limit, $|r_{l,r}| \to 1$ and $\varphi_{l,r} \to -\pi$, surface electron LDOS coincides with density of states of a one-dimensional electron gas - see Figure 6.13) [4]. All the intermediate cases can be studied numerically. Figures 13a,b show results of numerical simulation of surface LDOS inside a symmetric resonator ($|r_l| = |r_r|$ and $\varphi_l = \varphi_r$) of a = 100 Å width [20]. From these graphs we immediately see that reflecting amplitude $|r|$ strongly affects peak width and intensity, whereas merely change their position. In contrast, phase shift φ strongly influences only peak position. More clearly these effects can be seen from Figures 13c,d where the energy – see Figure 13c, and peak width – see Figure 13d - of n = 5 mode of a 100 Å symmetric resonator is shown as a function of reflecting amplitude and phase shift of its borders [20].

We conclude that finite reflecting amplitude $|r|$ of a quantum corral will mainly influence the energy width of the peaks in dI/dV spectra, whereas peak position is mainly determined by phase shift φ. As it was found the reflecting phase shift φ is always very close to hard-wall value $-\pi$, that"s why the simplified "particle in a box" model can predicts very precise energy of leaky corrals eigenstates.

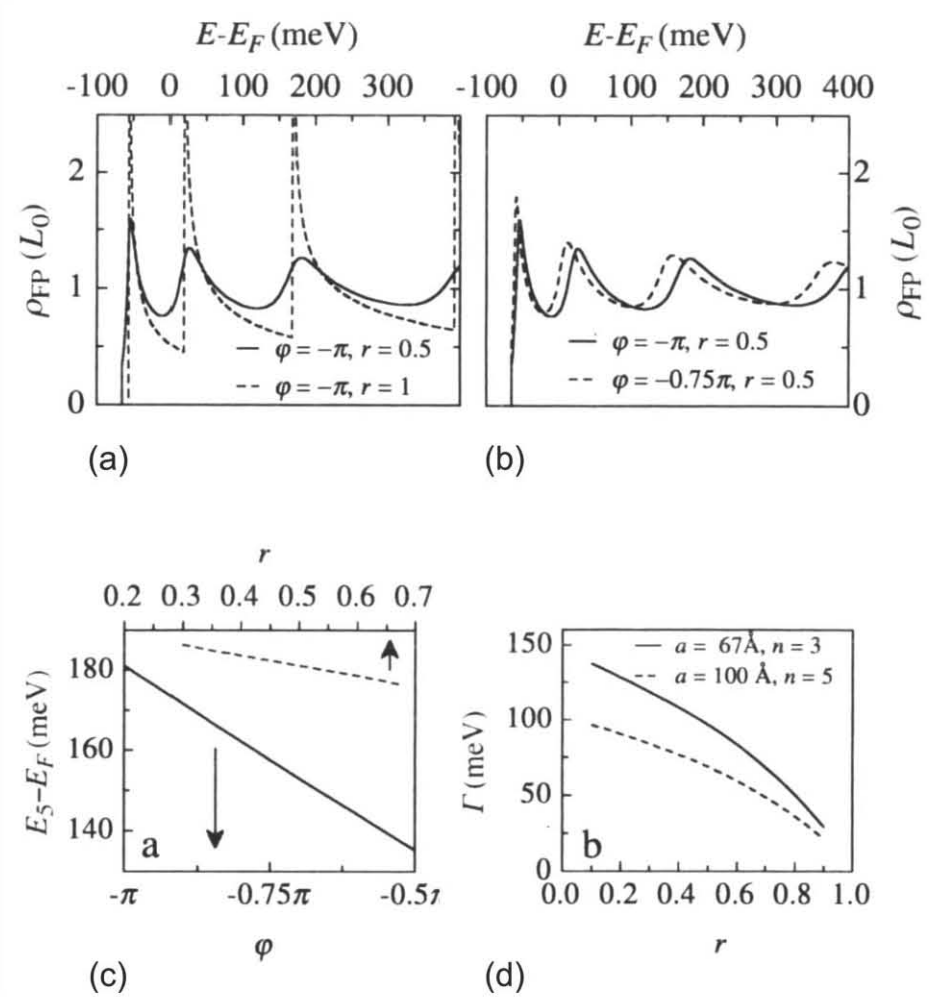

Figure 6.13 : (a) *and* ***(b)*** ρ_{FP} *from Eq. (1.5) for a 100Å width resonator. The peak width depends strongly on reflecting amplitude |r| (a), whereas phase shift influences the eigenenergy of resonator eigenstates (b).* ***(c)*** $E_{n=5}$ *of* ρ_{FP} *from Eq. (1.5) for a 100Å width resonator as a function of reflection phase shift φ (solid line, |r| = 0.5) and reflecting amplitude |r| (dashed line, φ = –π).* ***(d)*** *Linewidth of n = 3 and n = 5 peak for resonator of 67Å and 100Å width, respectively, as a function of step reflection amplitude |r| (φ = –π). Reproduced from [20]*

Numerical fit with Eq. (6.5) of experimental spectroscopic data allows one to determine the value of reflecting amplitude as a function of electron energy. The resulting data is shown on the Figure 6.14 [4] for ascending and descending steps. One sees from this curve that increasing energy from the band minima (here E_0 = -63 meV) gives rise to a fast reduction of the reflection coefficient $|r|$. The figure also shows that the reflection coefficients in the case of single step edges (ascending or descending) are much smaller than the "ideal" one corresponding to the dashed line (with maximum value equal to unity at the minimum of the band). From experiments we know that geometrical shape of quantum corral plays little role on the linewidth of resonances in the LDOS [12].

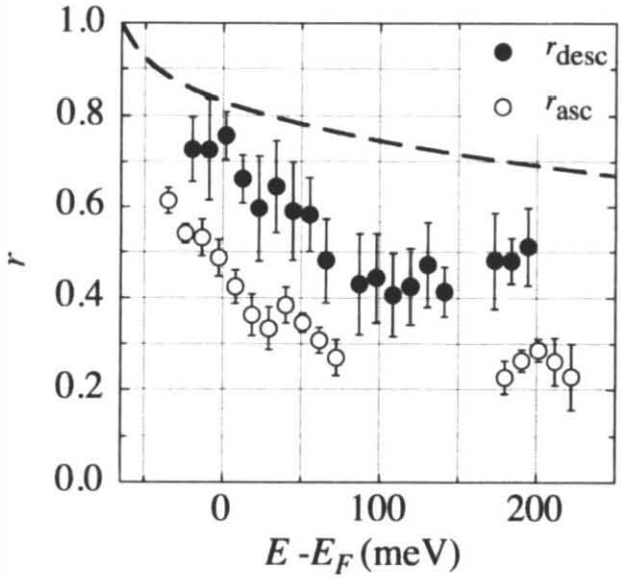

Figure 6.14 : *Experimentally measured energy dependent reflection amplitudes for descending and ascending step edges on Ag(111). Reproduced from [20]*

Therefore a phenomenological expression can be given for the contribution of a less than unity reflection coefficient to the linewidth in quantum corrals. For simplicity one can consider circular quantum corral and deduce the analytical expression of the linewidth as a function of the resonance energy E_n, reflection coefficient of the corral border $|r|$ and the area of the corrals Ω [12,13]

$$\Gamma_{r,n} \approx -\frac{\hbar^2}{m^*}\sqrt{\frac{2m^*(E_n - E_0)}{\hbar^2}}\cdot\frac{ln|r|}{\Omega} \qquad (6.6)$$

From this expression we find that the width of peaks in dI/dV spectra should exhibit a monotonic increase with the energy of eigenstate. It is also noticeable that the smaller is the diameter of the corral the larger the linewidth is. This property will make difficult fine analysis of very small quantum corral when significant losses occur at the boundaries.

In conclusion, we have seen that electronic properties of quantum corrals can be essentially caught within the simple "particle in a box" model or more accurately with multiple-scattering theory. The former approach being very simple gives rather precise values for eigenenergies of quantum corral, whereas multiple-scattering approach allows one to reproduce not only energy of eigenstates but also their finite lifetime.

In the end we would like to point out two special cases when these common approaches may fail. As it was mentioned before, epitaxial single-atom height islands may consist of chemical material *A* that is different from the material of the substrate *B*. For certain pairs *A*/*B* this epitaxial island will correspond to an attractive potential for surface electrons see Figure 6.15a. Similar behavior can be found for vacancy islands in an

epitaxial layer corresponding to repulsive potential for surface electrons. It can be shown that such attractive potential in 2D will always support at least one confined electronic state (i.e at least one bounded state should exist) [35]. In a recent paper Diaz-Tendero and coworkers have explored theoretically the consequences of this effect on the spectral properties of a quantum corral [36]. Considering the Ar/Cu(100) example they have shown that argon monolayer has repulsive energy for electrons of surface state in comparison to clean copper surface. In this case the confinement of the electrons inside Ar island is precisely described by "particle in a box model" - blue and green curves on Fig. 6.15b with a quantization energy fitting quiet well with $1/R^2$ (R being the radius of Ar island). In contrast the condition to keep at least one bound state in the attractive region of a vacancy island formed in Ar layer, independently on the size of the vacancy island leads to significant decrease of the ground state energy relatively to the "particle in a box" predictions - black and red curves on Fig. 15b. Consequently a large deviation on the $1/R^2$ law for the quantization energy is observed.

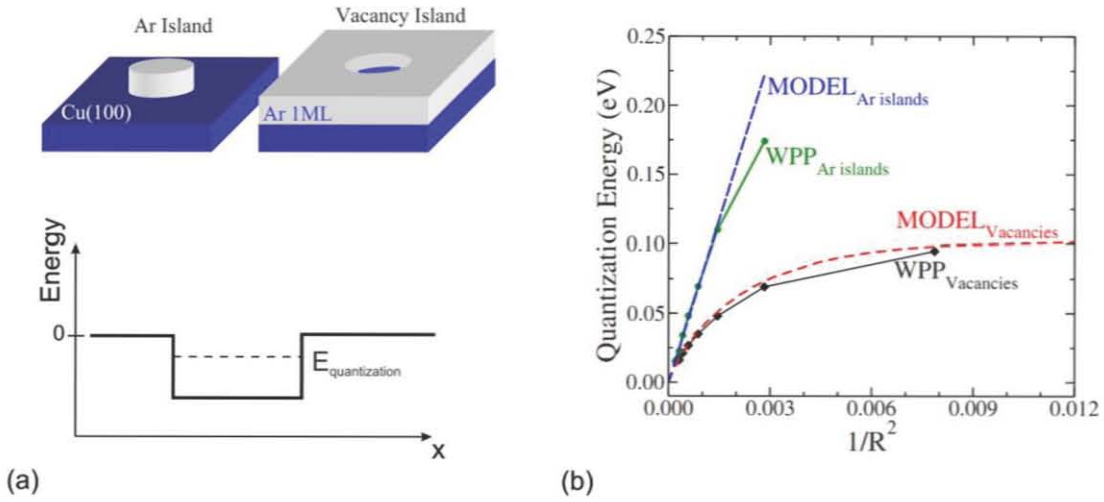

Figure 6.15 : (a) *Schematic representation of adatom and vacancy islands. On the bottom – energy profile of attractive potential in the region of adatom or vacancy islands.* ***(b)*** *Energy of ground state in Ar island (repulsive potential region) and Ar vacancy island (attractive potential region) as a function of island radius. Reproduced from [36]*

The second unusuall case was also first theoretically considered by S. Diaz-Tendero and coworkers [37]. They have taken into account that a sp-type electron state may develop on the atomic chain that forms the boundary of quantum corral build from individual atoms. Numerical simulation has shown that coupling of quantum corral eigenstates with this border state (also quantized due to finite size of the chain) will significantly perturb electronic spectra of the corral. In particular, the authors explored the case of quantum corrals of different sizes build from single copper atoms on Cu(111) substrate. Cu atoms in the border were placed at the Cu(111) surface nearest-neighbor distance (about 2.5 Å), that allows overlap of single atoms orbitals. Formation of a 1D state localized on the border of the corrals was observed with eigenergy about -3.9 eV relatively to vacuum level [38]. This border state coupled with internal quantum corrals eigenstates

that have approximately the same eigenenergies. As a consequence the energy of all the overlying eigenstates appears to differ from "particle in a box" predictions like reported in Figure 16a. Moreover the linewidth of the new sates shows an unusual behavior with a non monotonic increase with energy – see Figure 16b. A singular decrease of the linewidth is indeed observed for resonances with energy close to the quantified border state energy. Such effects of border state may also develop in epitaxial islands [37].

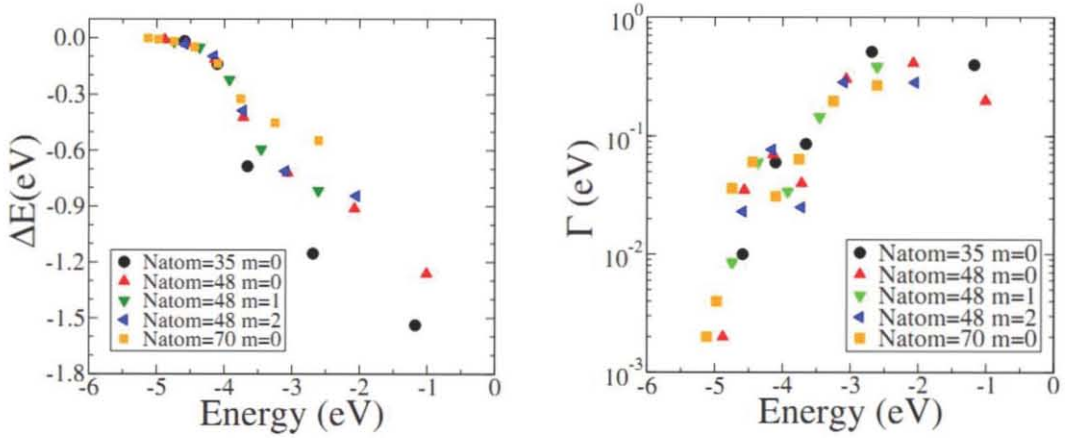

***Figure 6.16**. **(a)** Difference between the energies of the corral states obtained by the wave packet propagation method and in "particle in a box" approximation. **(b)** Width of all the confined surface states that have been studied as a function of their energy with respect to vacuum level. Reproduced from [37]*

6.1.4 Scattering of bulk electrons by the surface structures

It should be noted that bulk electrons off course are also scattered (may be less effectively) by any defects on the surface (as well as in the bulk). Since projected bulk band structure shows continuum of states for any given value of momentum $k_{||}$ (see Figure 6.2) no standing wave pattern should be observed on the surface. In reality a standing-wave pattern formed by bulk electrons can be detected in STM. It was demonstrated that standing waves around impurities on Cu(111) and Au(111) result from both surface and bulk states whereas bulk electrons do not contribute to the screening of step edges. Moreover, these bulk states imaged by STM come from the edge of the bulk Fermi-surface neck close to the L point of the Brillouin zone [39]. Oscillations of the charge density were also observed on a terrace of the Ag(110) in an energy range without any surface states [40]. The authors showed that these oscillations arise from scattering of. The predominant role of these particular states was attributed to a van Hove-like enhancement due to the bulk band curvature. Finally we have recently shown that the states at the edge of the surface-projected bulkband may be confined in surface nano corrals and show band folding due to surface reconstruction on Au(23 23 21) surface [41]. Obviously the influence of scattered bulk electrons on surface LDOS modulation is much smaller compared to surface state effects and can be observed only for electron energies lower than surface state band onset.

6.2 Spectral properties of Cl based quantum corrals

Nano porous lattices have been prepared by the way described in chapter 4, i.e. by sub monolayer (0.05 to 0.25 ML) chlorine adsorption at room temperature and cooling down to 5K. In some cases a post deposition thermal treatment has been achieved. Indeed cycling from 5 K to room temperature or slightly over (100 °C) we were able to prepare lattices with more than 90% of the nano pores single wall barrier. This procedure allowed us to optimize the shape of the quantum wells close to hexagonal one. Electron confinement has been studied in nano pores with typical diameter 2.5 to 3.5 nm.

6.2.1 Evidence of electron confinement

At a glance, the confinement of the surface electrons in chlorine based nano pores can be simply detected by STM topography recorded with different bias voltage. Indeed a giant effect has been observed on the image when the surface is covered by chlorine, forming closed nanostructures of typical diameter 2-3 nm. It is obvious for very low coverage when single atomic well nano pores are present on the surface as well for bigger dose of chlorine when the $(\sqrt{3}\times\sqrt{3})R30°$ monolayer is not yet completely formed and leaves vacancy islands of the bare Au(111) substrate.

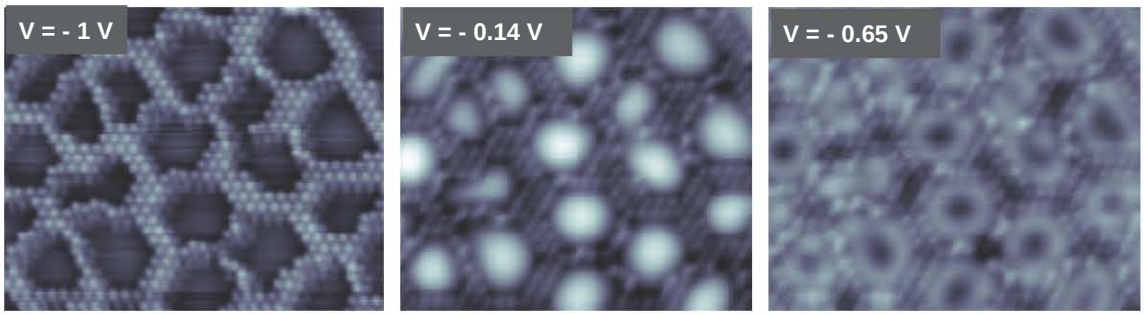

Figure 6.17 *: STM images obtained for a Au(111) surface covered by sub monolayer of chlorine. The same region has been recorded with three different bias voltage. It =0.4 nA* T_{STM} *= 5K*

Typical voltage dependence of STM images is presented in Figure 6.17. As we can see for images recorded at – 1V atomic resolution is achieved on the chlorine skeleton and the pores appear as featureless vacancies. On the opposite for voltages V = - 0.14 V and V = + 0.65 V, the atoms of chlorine are less resolved and bright features appear with shape depending on the gap voltage. Inside each pore, one broad and bright protrusion is observed at V = -0.14 V whereas an annular feature is evidenced at V = +0.65 V. One has to notice that this effect is also tip apex dependent.

The same kind of behavior has also been observed for the Cu(111) surface covered by sub monolayer of chlorine. It is shown on Figure 6.2 for two different coverage θ = 0.06 ML and θ = 0.28 ML. In the case of Cl/Cu(111) interface, at very low coverage (θ = 0.06 ML)

the chlorine atoms organize as linear features (chains) separated by typical distance of 3 nm whereas for coverage close to 0.3 ML a (√3x√3)R30° layer is formed with some vacancy islands remaining (see Figure 6.18a and 6.18c). STM images recorded for opposite voltage V = - 1 V and V = + 1 V look very different.

In both case Cl/Au(111) and Cl/Cu(111) one can explain this voltage (and/or) tip dependence of STM topography by the confinement of the Au(111) Shockley surface state inside the nano pores, giving rise to a large spatial modulation of the electron density.

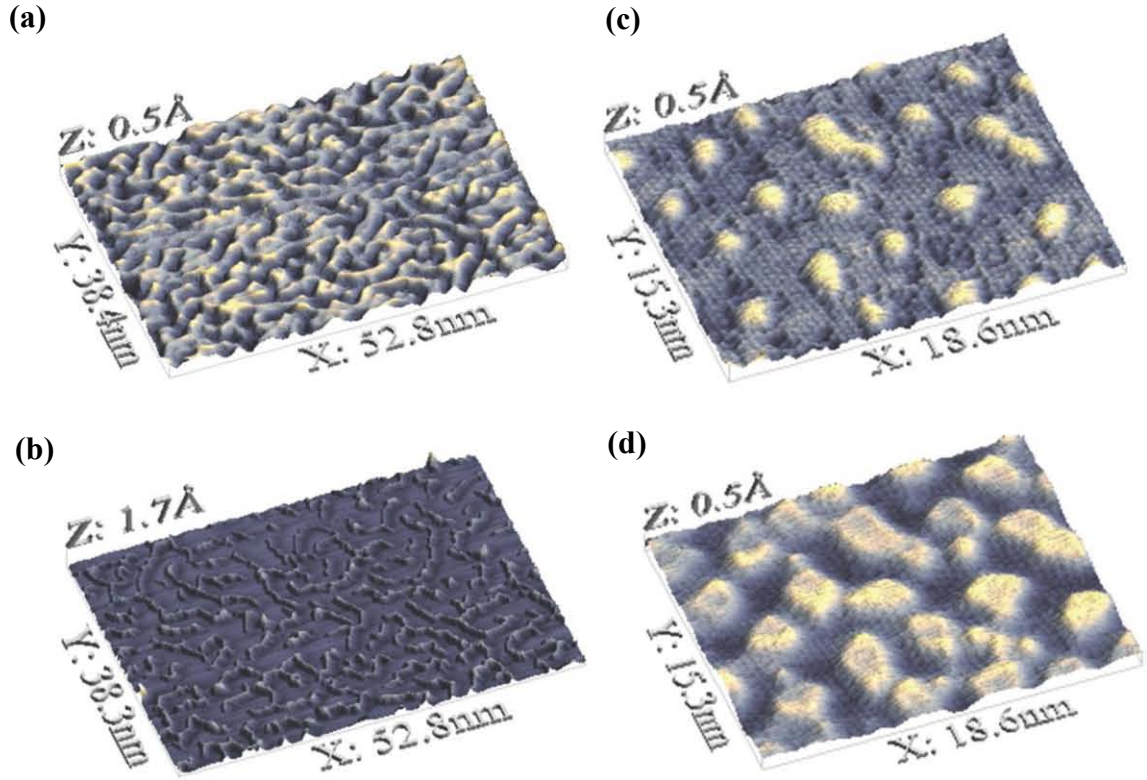

Figure 6.18 *: 3D view of STM images obtained for a Cu(111) surface covered by sub monolayer of chlorine. The same regions have been recorded with different bias voltages ; V = - 1V (a) and (c) and V = + 1 V (b and d). The coverage are 0.06 ML (a and b) and 0.28 ML (c and d).*

In order to investigate in detail the electron confinement in chlorine based nano pores we have performed local spectroscopy with STM at 5 K.

6.2.2 Local spectroscopy on quantum corrals

A. measurement of quantized states in Cl nano pores

We show in the Figure 6.19a the typical curves of the differential tunnel conductance as obtained under open feedback loop conditions and over few cells of a Cl based nano porous lattice. All the data presented in this section have been obtained at 5K with a lock in detection using a bias modulation of 20 mV peak to peak and frequency fixed to 700 Hz. The lock-in time constant was 3 or 10 ms with a 18 dB roll of. The curves are selected from a full set of data consisting in a matrix with one dI/dV spectrum per point of the scanned area. The set point before opening the backloop was fixed to + 2V in order to stabilize the tip/sample distance with a tunneling current summing over numerous electronic states. By this way we minimize the influence of the spatial distribution of the electron density.

The dI/dV curves labeled A to D in Figure 6.19a have been recorded in the corresponding positions marked A to D in the conductance map of Figure 6.19b.

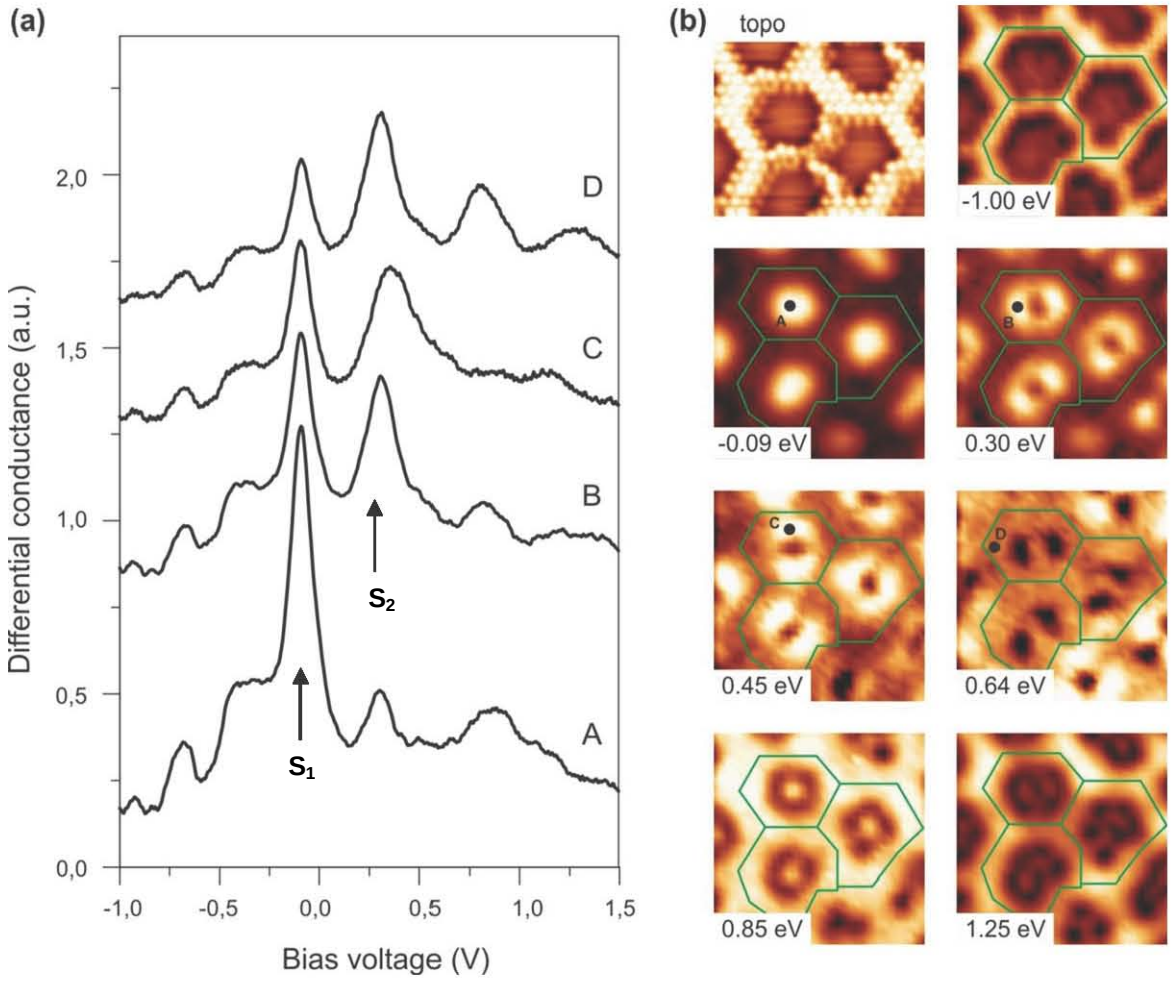

Figure 6.19. *(a): Differential conductance spectra taken at different points inside the Cl nano pores. The corresponding points A, B, C and D are marked in (b) -* ***(b)*** *Differential conductance maps recorded over the nano pores for different bias voltages.*

It is clear from our results that the local density of states inside the Cl nano pores shows sharp resonances that correspond to quantized states arising from the Shockley surface state of the Au(111) surface. Conductance maps presented Figure 6.19b are in accordance with the existence of quantized states as it shows well defined standing wave patterns inside the pores. It is noticeable that the shape of these patterns evolves with bias voltage and becomes more and more complex. Depending on the position of the nodes and maxima in the corresponding wave patterns, the intensity of the peaks in dI/dV curves varies and some resonances only appear for specific positions. For instance the curve labeled *A* in Figure 6.19 has been recorded in the center of a pore - see Fig. 6.19b. This curve essentially shows a sharp resonance (S_1) at a bias voltage V_1 = - 0.09 V and a faint peak (S_2) at V_2 = + 0.29 eV. The spatial distribution of the mode corresponding to the S_1 peak is obtained from the dI/dV map realized at the same voltage V_1 = - 0.09 V. We see that this mode corresponding to the lowest energy resonance is made from a single maximum centered in the pore. By contrast the curve labeled *B* in Figure 6.19a has been obtained by moving from the center to one side of a pore, approximately 0.5 nm off center. The S_1 peak is strongly decreased whereas S_2 increased. This tendency can be easily explained from the spatial distribution of the S_2 resonance. The dI/dV map obtained at a bias + 0.3 V shows now a new shape of the LDOS inside the pores with two maxima and a node in the middle. This explains why the S_2 peak appears essentially on the side of the pore rather in the middle. The small contribution S_2 observed on the curve recorded in the middle of the pore is explained by the finite radius of the tip which gives some spatial integration of the tunneling current and allows the electrons tunneling off center of the pore to contribute to the dI/dV curve. By moving the tip over the pores one can reveal new resonances at higher energies – see curves *C* and *D*. It is worth noting that all the curves exhibit the S_1 peak due to its rather broad spatial distribution. We want to point out that unfortunately in our experiments we were able to perform LDOS measurements for bias voltage only up +2 V. At larger bias the Cl nano porous lattice was frequently destroyed due to Cl atom picking by the tip apex. Therefore only the few first electronic states where probed by STS due to rather small size of the nano pores - the maximal average diameter investigated was about 3.5 nm.

B: Size and shape effects on quantized states inside the pores

As described before the growth mechanism of the nano porous lattice of Cl on Au(111) does not allow to get perfect hexagonal shape and sharp size distribution of the pores. Therefore we have analyzed the consequence of small deviation in size and shape on the spectral properties of the nano pores. Actual nano pores have the form close to a distorted hexagon. Undoubtedly such distortion will affect the electronic confinement inside the nano pores compared to regular hexagon box. However we can expect that for the lowest states this effect will be sufficiently small since the corresponding stationnary states are built from quantum interferences of electron waves with large wavelength.The energy of few first eigenstates could be simply determined by the area (the width and the length) of the two-dimensional quantum well (QW). Indeed this was already demonstrated

experimentally for the case of monoatomic Ag islands epitaxially grown on Ag(111) surface [11,31] and gold clusters on HOPG [32] that slightly distorted hexagonal quantum corrals can be successfully described by the model calculations with equation (1.4) for regular shape. The only parameter to be extracted from the experimental data is the box area Ω.

To perform this analysis we have chosen two nano pores which have the shape close to hexagonal with minimal distortion. Their areas are respectively $\Omega_1 = 8.8$ nm^2 (Fig. 6.20) and $\Omega_2 = 11.2$ nm^2 (Fig. 6.21).

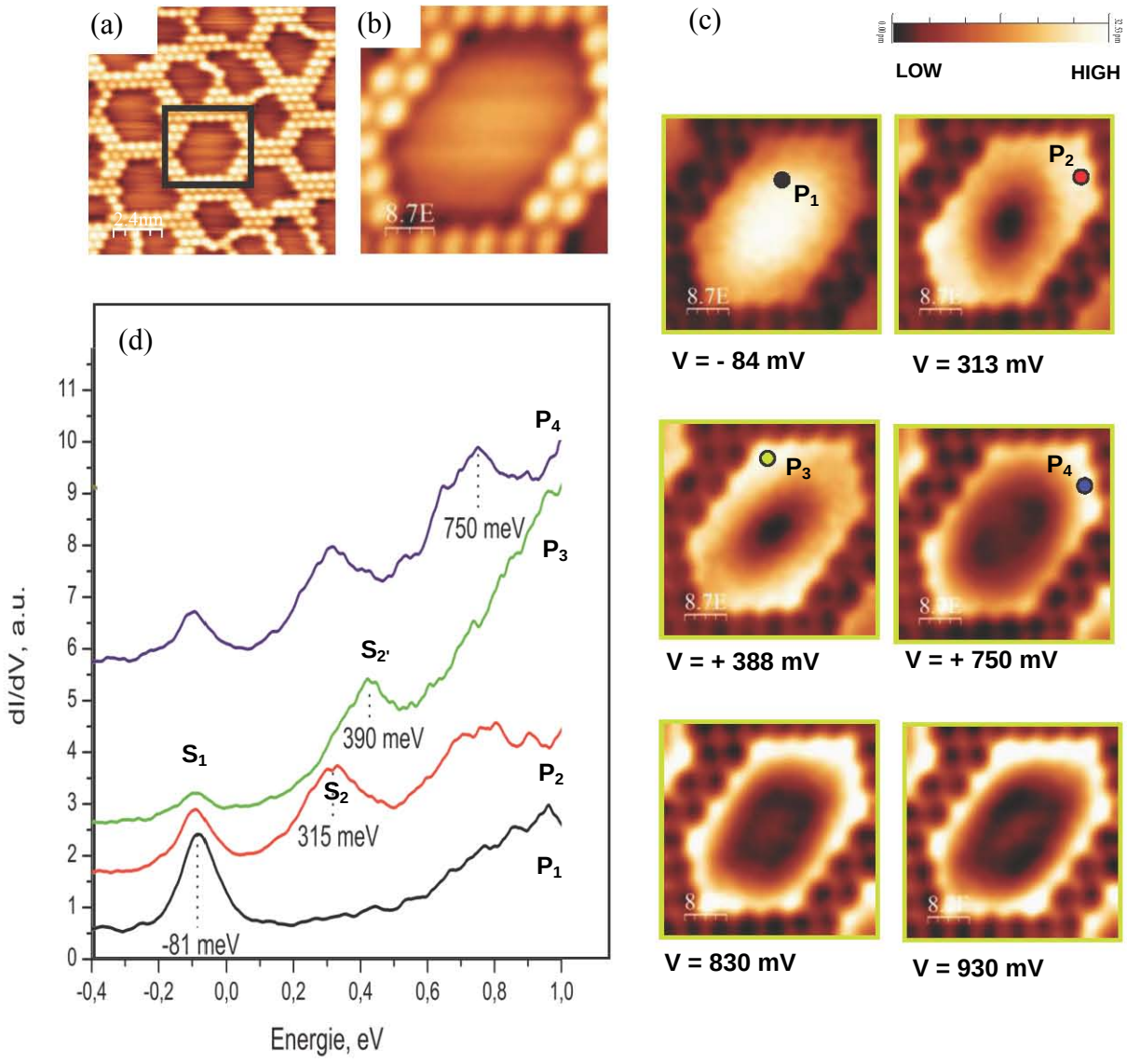

Figure 6.20 *: **(a)** and **(b)** Topographic STM images of the nano pore with selected size $\Omega_1 = 8.8$ nm^2.(It = 1 nA and Ugap= - 1V) - **(c)** Differential conductance maps of the selected nano pore recorded at different bias voltages. **(d)** dI/dV curves taken at different positions marked by the labels P_1,P_2, … on (c).*

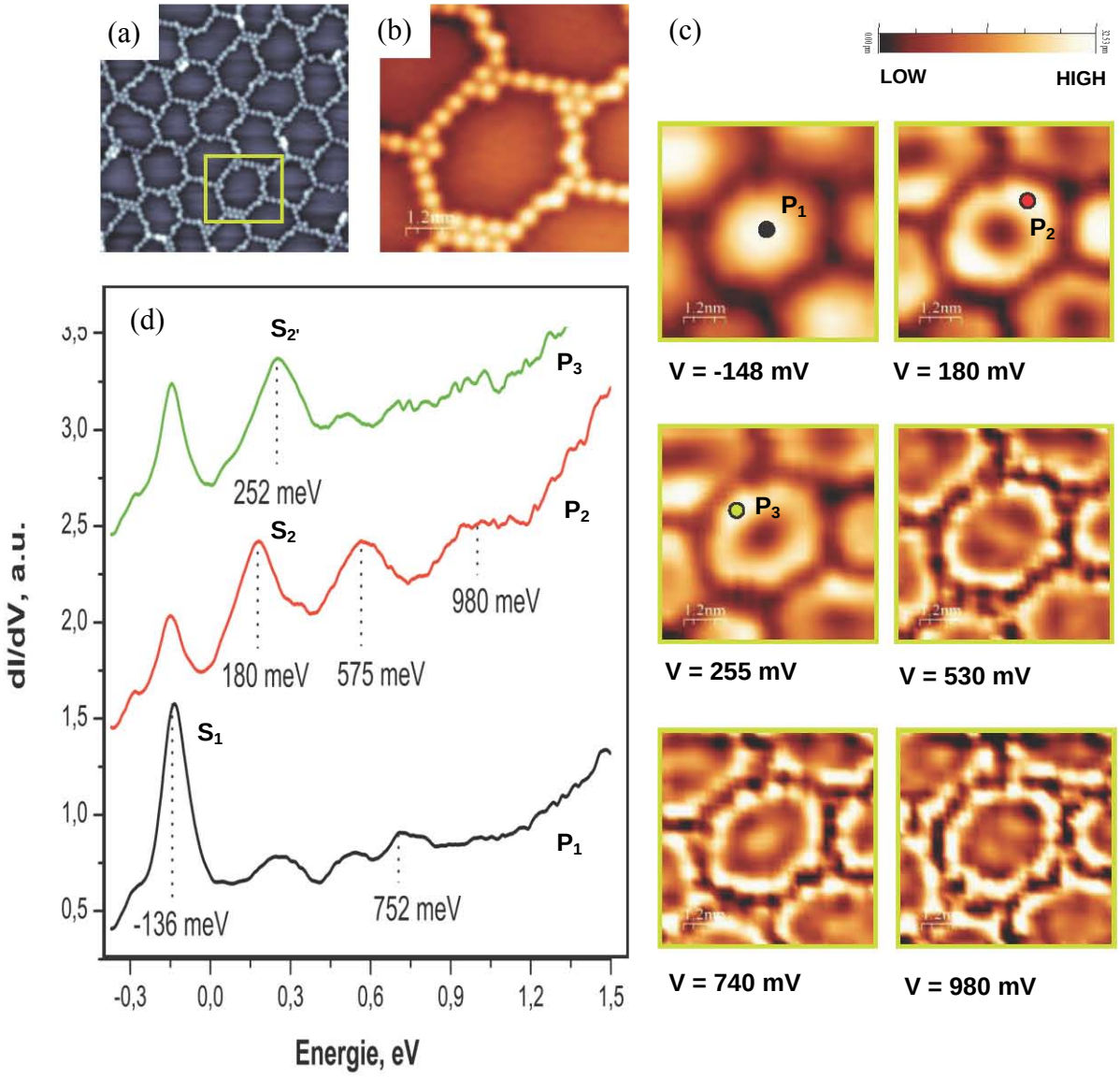

Figure 6.21 *: **(a)** and **(b)** Topographic STM images of the nano pore with selected size Ω_1 = 11.2 nm^2.(It = 1 nA and Ugap= - 1V) - **(c)** Differential conductance maps of the selected nano pore recorded at different bias voltages. **(d)** dI/dV curves taken at different positions marked by the labels P_1,P_2, … on (C).*

Differential conductance maps - Fig. 6.20c and 6.21c - recorded inside the selected nano pores at different bias voltages are shown together with the local conductance - Fig. 6.20 and 6.21d - recorded at different positions. They roughly correspond to the few first eigenmodes of the nano pores. The positions for STS are marked on the Figure 6.21d by the circles labeled P_1,P_2, …From a simple comparison of the sets of STS curves recorded for both selected nano pores it is clear that the sequence of quantum resonances is almost the same but appears with different energies of the modes. For instance the lowest energy state appear at E_1 = - 81 meV for the pore of Ω_1 area whereas it is measured to E_1 = - 136 meV for the pore of size Ω_2 .This is the obvious size effect taken into account that $\Omega_2 > \Omega_1$. Also the S_2 and $S_{2'}$ features appear at higher energy in the case of the smallest nano pore.

In order to analyze the spectral properties of the Cl nano pores we have performed theoretical calculations within the simple "particle in a box" model. As a first approximation we calculated the energy of quantized states for a two-dimensional QW of regular geometrical shape i.e. perfect hexagon of the same area as the selected pore. As presented before the eigenenergies inside a hexagonal QW with infinite barrier at boundaries is given by the relation (6.4) where the constant reference energy E_0 inside the well is taken as the minimum of the Au(111) surface state band i.e. – 505 meV (obtained from 5K-STS measurements on clean Au(111) surface). As there is no analytical solution of Schrödinger equation for hexagonal quantum well we have used numerically found values of the geometrical factors λ_n reported previously [32]. The eight first values are listed in the following table:

n	1	2	3	4	5	6	7	8
λ_n	0.708	1.795	3.213	3.712	4.716	5.211	5.951	6.945

Table: calculated value of the geometrical factor used in calculation of the eigen energies of a hexagonal quantum well [32]

The dimensionless effective mass has been fixed to 0.255 as obtained from our own ARPES measurements. The calculated values $\Delta E_n = E_n - E_0$ expressed relatively to the reference energy E_0 are plotted on Figures 6.22a and c together with experimental data.

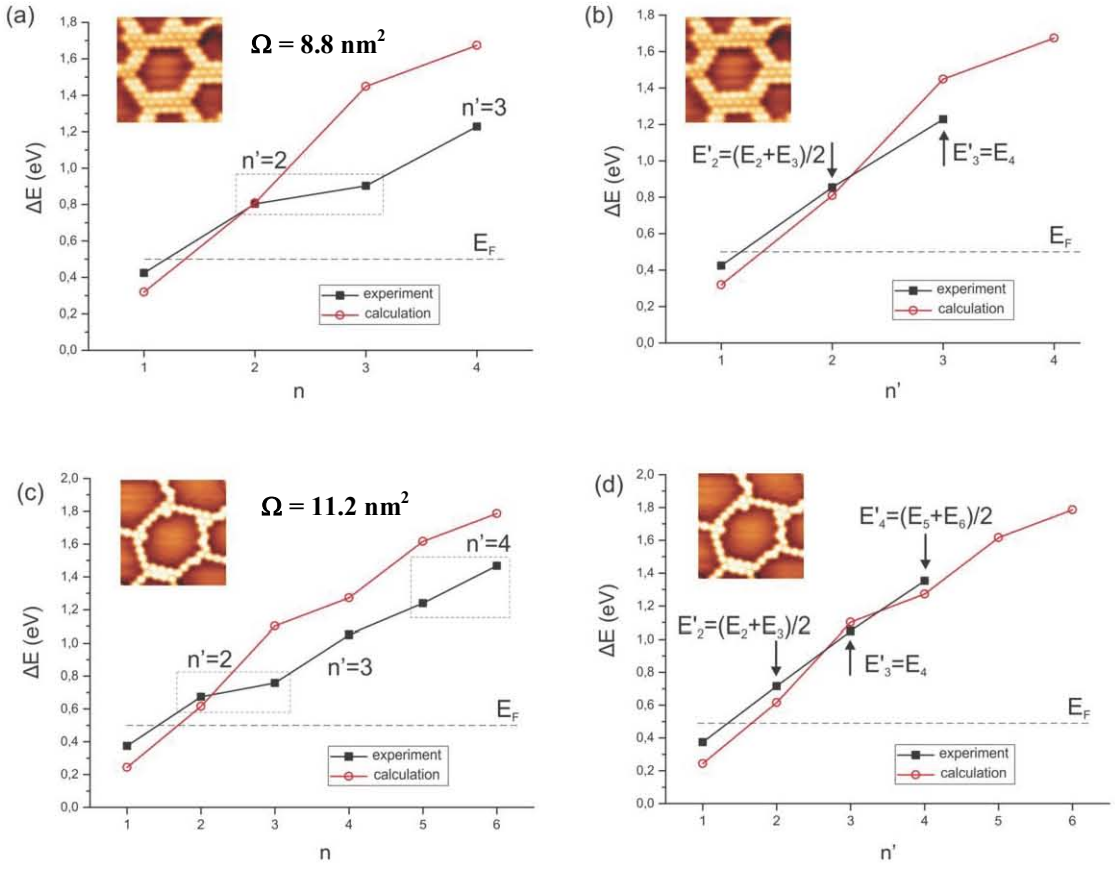

Figure 6.22 : (a) *and* ***(c)*** *Plot of the measured eigenenergies (in black) and calculated ones (in red) within the "particle in a box" model for regular hexagonal well of the same area. The energies are given relative to E_0 -* ***(b)*** *and* ***(d)*** *:the same plot as in (a) and (c) but with a corrected distortion effect (see text for details)*

At a first glance agreement between experimental energies and calculated ones is rather poor excepted for the two first eigenmodes. Moreover the spatial distribution of the calculated electron density for a perfect hexagon has almost nothing in common with the measured conductance maps. The perfect hexagonal well shows eigenstates with hexagonal symmetry of spatial distribution of electron density (Figure 6.10), whereas the nano pores demonstrate a lower symmetry of the electron density (Figures 6.20 and 6.21). Inspecting more carefully the Cl nano pores we can notice that both are slightly compressed in one direction and have elongated shape. In fact counting the number of Cl atoms in the boundaries of the pores we can see for instance for the 8.8 nm^2 pore that two sides count 4 atoms instead of 5 making the other sides. We should expect that this reduced symmetry has to remove the degeneracy of some eigenstates leading to a (small) splitting in the corresponding energy levels and a change in the spatial distribution of the LDOS. This is exactly the case for our two selected pores for the resonances S_2 and $S_{2'}$ which arise from the degeneracy of the n = 2 level in a perfect hexagon. Indeed a careful inspection of the STS curves shows that S_2 and $S_{2'}$ features are only separated by about 75 meV which is much smaller than the expected energy separation between 2nd and 3rd eigen mode in perfect hexagon of similar size. Moreover we clearly see in the conductance maps of Figures 6.20 and 6.21 that the standing wave patterns corresponding to S_2 and $S_{2'}$ resonances have both two maxima but rotated by 90 ° first appearing along the long length of the deformed hexagon and then along the shortest one.

This situation resembles the removal of degeneracy in a 2D quantum well of square shape when it is slightly compressed to a rectangular one. In this case analytical solutions exist and the electron density and energy levels can be simply expressed. The eigenstates and eigenenergies are given by:

$$\psi_{n_x n_y}(x,y) = \frac{2}{\sqrt{L_x L_y}} \sin\left(\frac{n_x \pi x}{L_x}\right) \sin\left(\frac{n_y \pi y}{L_y}\right) \tag{6.7}$$

$$E_{n_x n_y} = E_0 + \frac{1}{m^*}\frac{1}{\Omega}\lambda_{n_x n_y} = E_0 + \frac{1}{m^*}\frac{1}{L_x L_y}\frac{\hbar^2 \pi^2}{2}\left[\frac{L_y}{L_x} n_x^2 + \frac{L_x}{L_y} n_y^2\right] \tag{6.8}$$

We can notice here that the geometrical factor λ_n can be analytically determined. In the case of a perfect square QW with Lx = Ly and the n = 2 mode is two fold degenerate and has two mirror plane symmetry rotated by 90°. When the QW is distorted and compressed this degenerate state is split into two non-degenerate states with lower π symmetry leaving only one mirror plane - see Figure 6.23a and 6.23b. If the area is preserved during compression the two fold degenerate energy level $E_2 = E_{1,2} = E_{2,1}$ is split symmetrically into two new energy levels E'_{12} and E'_{21} with $E'_{12} < E_2$ and $E'_{21} > E_2$ (if $L_x > L_y$). One has to note that for small distortions of the square QW the average energy $E'_2 = (E'_{1,2} + E'_{2,1})/2$ is almost identical to the non degenerate level E_2 (see Figure 6.23c). The next one *n = 3* state with proper energy E_{22} has no degeneracy and will be almost unaffected by the distortion (its energy will only slightly increase due to the distortion).

The forth QW state $n = 4$ ($E_4 = E_{13} = E_{31}$) which is doubly degenerate will be split into two states in the same manner as $n = 2$ state.

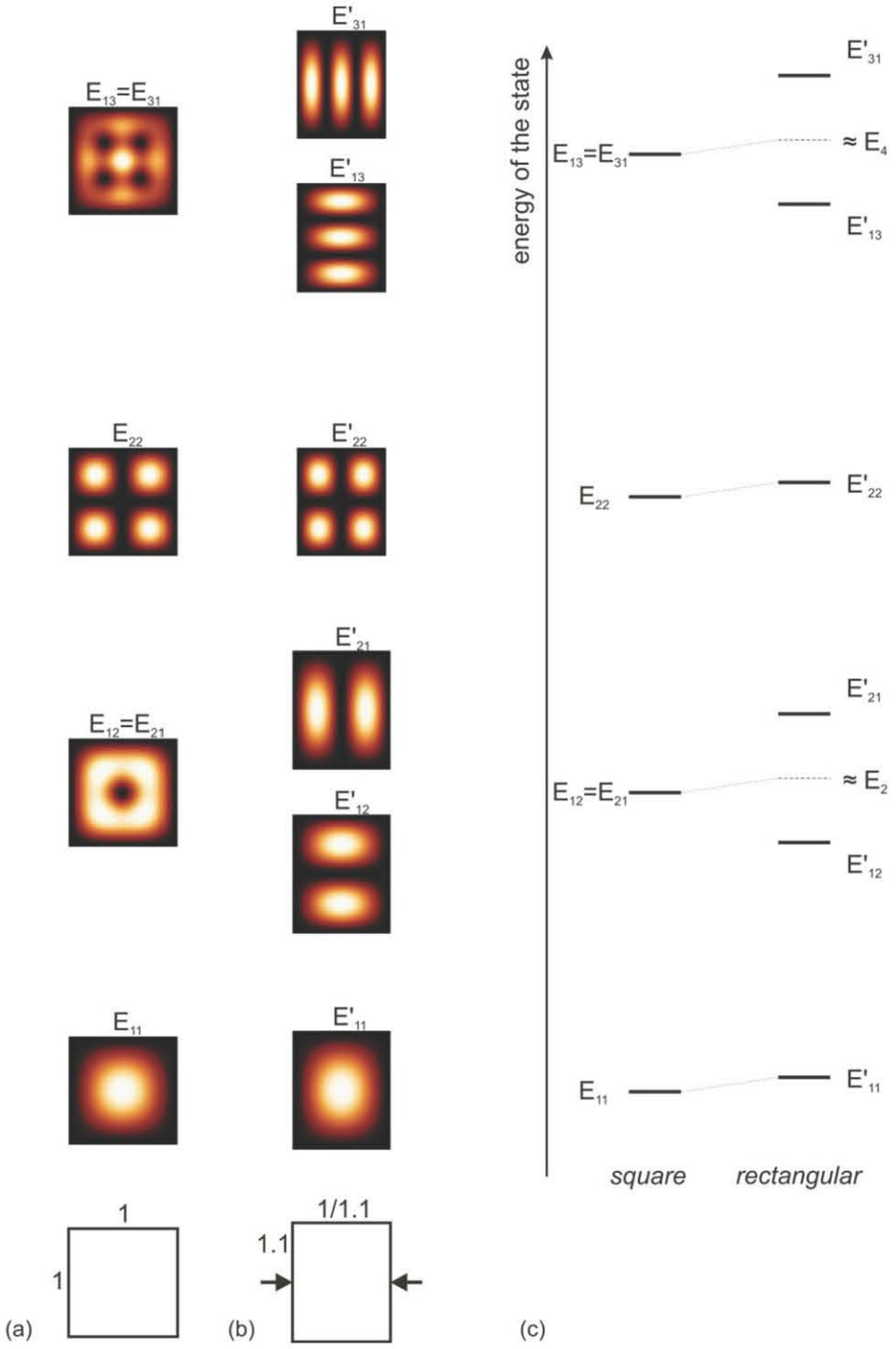

Figure 6.23. (a)-(b) *Few first eigenstates of square (a) and rectangular (b) quantum wells of the same area. Arrows shows direction of compression of the well.* ***(c)*** *Schematic energy diagram showing removing of square well eigenstates degeneracy during its distortion*

The same consideration can be applied to the quasi hexagonal Cl nano pores. We note that for both nano pores of area Ω_1 and Ω_2 the average energy $E'_2 = (E_2 + E_3)/2$ (corresponding to the mean value between the S_2 and $S_{2'}$ energies) is very close to the calculated eigenenregy E_2 of a perfect hexagon of the same size. Pushing further the analogy with square and rectangular wells we conclude that the n = 4 state in the nano pore corresponds to the n' = 3 state of hexagonal well, and so on (Figure 6.22c). By doing so, we see now from Figure 6.22b and 6.22d that the calculated energies are in better agreement with the experimental ones. This analysis shows that Cl nano pores can‟t be described by regular hexagon boxes since their distortion is too important and the area relatively small (note that according to eq. (6.4) the energy of eigenstates is inverse proportional to the QW area), so distortion effects are more important than in the case of quantum corrals usually discussed in the literature.

To go further we have solved by numerical method the 2D Schrödinger equation taken into account the exact shape (and size) of the distored hexagons formed by the Cl nano pores. The calculation procedure was performed as follows. We were able to reproduce all geometrical features of nano pores since atomically resolved STM images gave us the exact spatial position of each chlorine atom in the nano pore boundary (see Figure 6.24). Then one has associated to each Cl atom with coordinates (x_i, y_i) a phenomenological potential of Gaussian shape given by:

$$V_i(x) = V_0 e^{-\frac{(x-x_i)^2+(y-y_i)^2}{2R^2}} \qquad (6.9)$$

The Schrödinger equation was solved using the code developed by C. Chatelain (Statistical Physics group at IJL) and based on the projective method. This method leads to very fast convergence which allows parameter adjustment from many calculations. The first step was to determine the amplitude V_0 and radius R of the Gaussian potential. The amplitude of potential must be sufficiently high for the nano pore to be considered as an infinite quantum well and prevent any electron leakage. For our experience the value $V_0 = 10$ eV is sufficient for calculation of few first eigenstates. To find appropriate value of potentials radius we performed a number of calculations of the first eigenstate energy as a function of R and compared it with experimentally measured one. The best match for all nano pores that we considered was found to be R = 1.9 Å, which is physically reasonable. The mass of electrons was taken to be equal to the effective mass of Au(111) surface state electrons as in previous calculations.

In addition to the nano pores discussed above we introduced into our analysis two other nano pores of different size. Results of calculations of first six eigenenergies for the four different nano pores together with experimental results are shown on Figure 6.24.

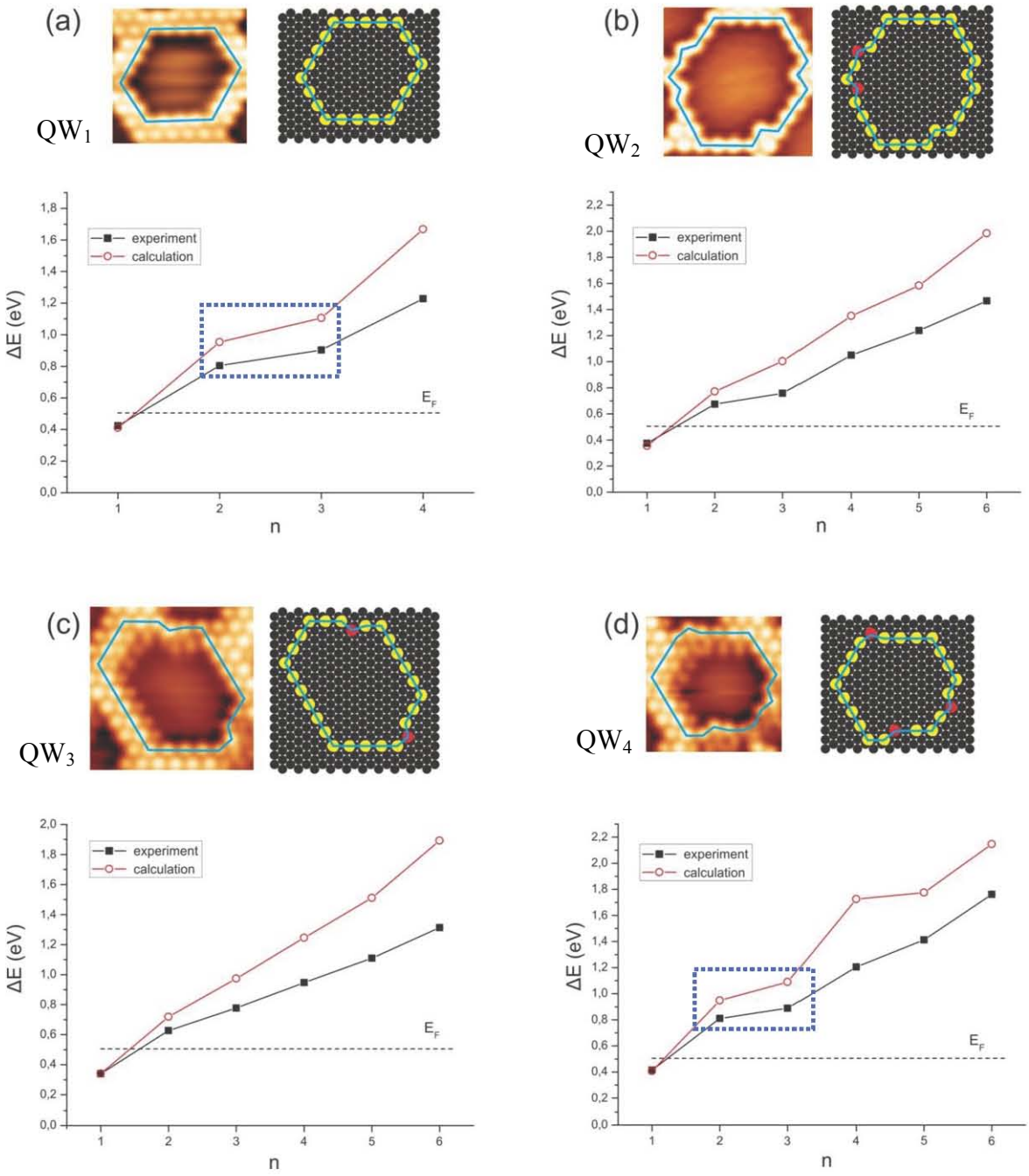

Figure 6.24 : *Results of "particle in a box" calculations with real geometrical shape for four different nano pores . The exact positions of Cl atoms are represented in yellow (fcc sites) and pink (hcp sites) on the sketch of the QW's.*

We see from Figure 6.24 that our calculations rather well reproduce the energy of the n=1 eigenstate (the absolute error is less than 10 meV) and the general tendency in the energy of eigenstates as a function of the number of the state, which is determined by the geometrical factor λ_n. For instance it is possible to catch the degeneracy splitting of the n=2 level - see dashed box in Fig. 6.24a and 6.24d - due to the deviation from the hexagonal shape. Nevertheless it is clear that these calculations systematically overestimate the eigenenergies with respect to those determined experimentally.

Besides the eigenenergy we have calculated the spatial distribution of the LDOS for each eigenstate of the nano pores. We present in Figure 6.25 the results for two nano pores (QW_3 and QW_4) together with experimentally measured dI/dV maps.

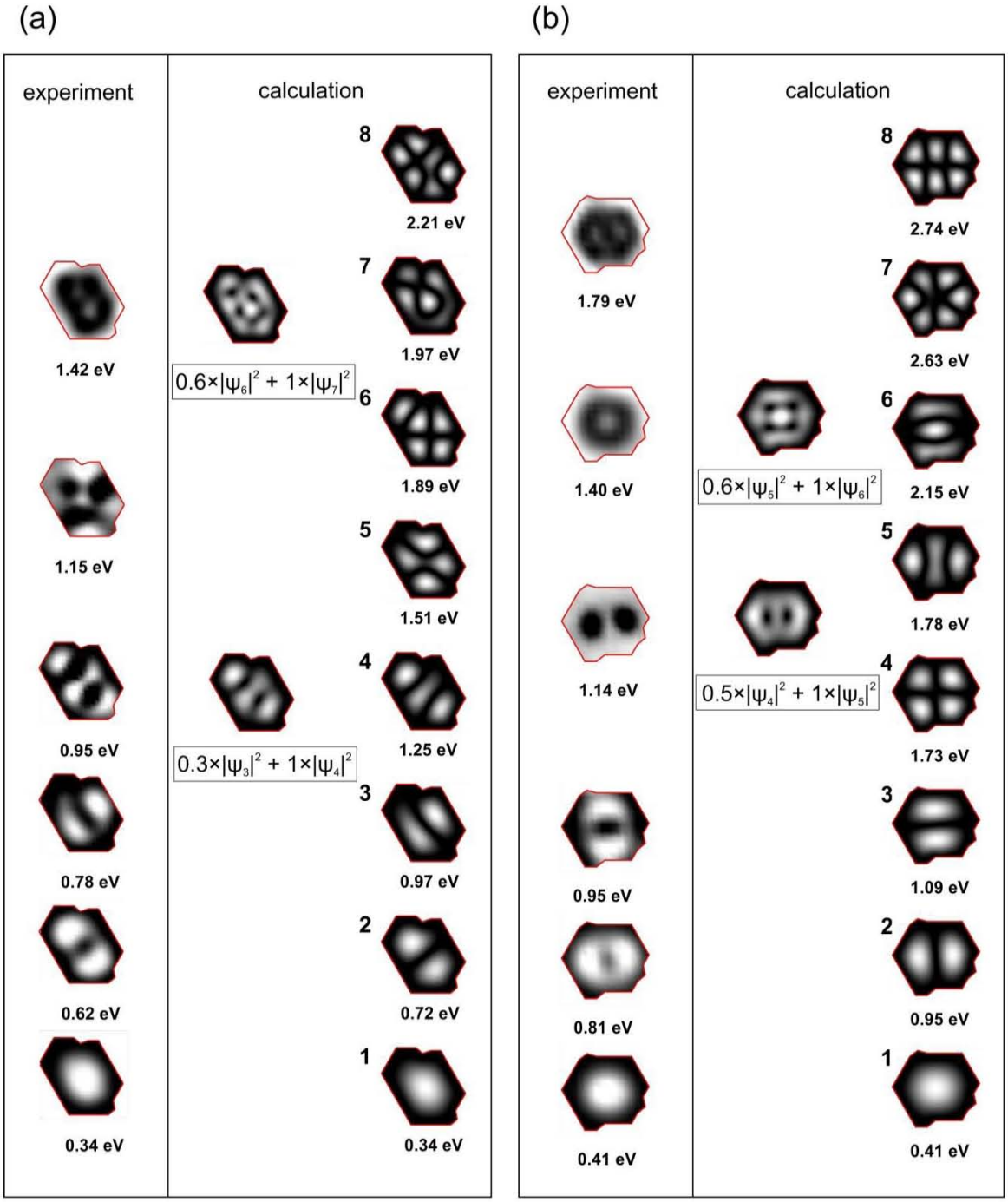

Figure 6.25 : *Comparison of experimental differential conductance maps and results of "particle in a box" calculations with real geometrical shape for nano pores QW_3 and QW_4 from Figure 6.24*

In both cases we see a very nice agreement between calculated LDOS and measured differential conductance maps for the first three eigenstates, though as it was mentioned the calculated energy is always higher. Starting from the forth state a direct comparison between the eigenmodes and the measured LDOS is not so evident. The reason is the

naturally increased linewidth of the eigenstates and their reduced separation. As it was discussed in the beginning of this chapter the width of the quantum corral states growths with the energy. As a consequence the peaks in STS spectra start to overlap. On the dI/dV maps this broadening of the states leads to the mixing of the LDOS patterns from adjacent states since at a given bias voltage several broad overlapping states can contribute to the differential conductance map. For instance the differential conductance map measured in the QW_3 at energy 0.95 eV - Fig. 6.25a is the sum of contribution from 3rd and 4th eigenstates $|\Psi|^2 = 0.3.|\Psi_3|^2 + 1.|\Psi_4|^2$. The same considerations can be applied for other high-energy dI/dV maps, though it is not trivial to find the proper composition to reproduce measurements. We were not able to find the proper composition of calculated LDOS for some of the measured dI/dV maps, while for the others the correspondence is not very good.

C : Failure of the "particule in a box model"

As mentioned above, our calculations made from the "particule in a box model" always overestimate the energy of eigenstates even by taken into account the real shape and size of the QW. Another important feature of experimental dI/dV maps not reproduced by these calculations is the high intensity of electron density close to the borders of the nano pore for high-energy modes. In contrast calculated electron density is always equal to zero on the borders of the pore and is very small in its vicinity, which corresponds to the perfect confinement inside an infinite well. Several assumptions can be proposed.

The first assumption is related to the possible modification of the surface state band – the onset of the band E_0 and surface electron effective mass m*. Expecting dependence of the quantum corrals eigenenergies from the parameters of surface electron band given by eq. (1.4) one can notice that the change of effective mass would simply rescale all the eigenenergies but will not change their relative values. The change of the surface state band minimum E_0 can neither explain such deviation since it would rigid shift all the eigenenergies by the same value.

Another explanation is related to possible finite height of the barrier of the nano pores. It is well known that the energy of eigenstates of a finite 1D QW is always lower than for a infinite potential well of the same size. The downshift of eigenenergy increases with the ordinal number of the state, just in line with our results. Apart from the eigenenergy there is also difference in the electron probability distribution inside finite and infinite wells. Boundary conditions in the infinite well impose the wavefunctions to be zero on the borders of the QW. Hence, the electron density of electrons has to vanish in region close to the border. In contrast, in finite quantum well it is known that wavefunctions can extand outside the borders, with exponentially decaying part - see Figure 6.26b. This effect becomes more pronounced for high-energy states.

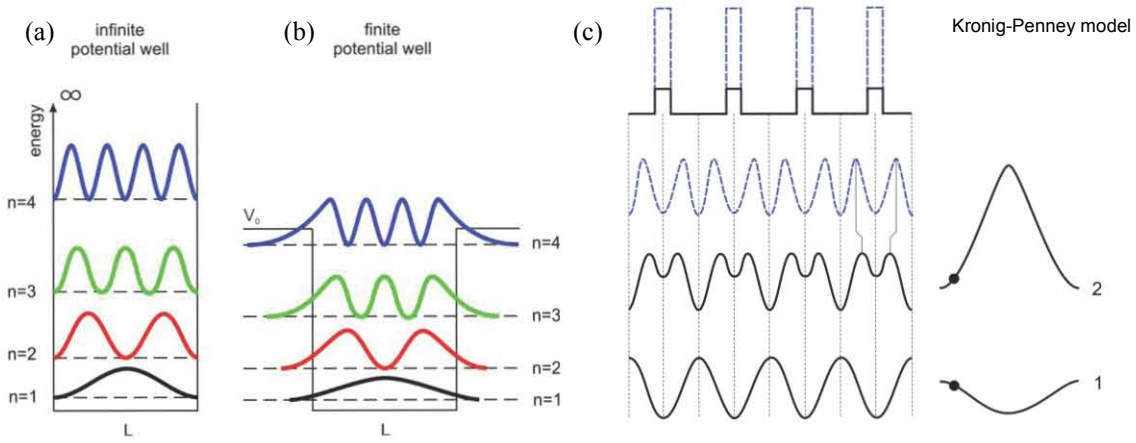

Fig. 6.26 : *Comparison of one-dimensional QW eigenenergies and electron distribution probabilities for infinite barrier* ***(a)****, finite barrier* ***(b)*** *and Kronig-Penney model* ***(c)*** *. The KP model lectron densities and bands are obtained from the applet written by P. Falstad [42].*

Additionally the spread of the wave functions outside the QW can lead, in principle, to electron coupling through the overlap of the eigenstates. In the case of a periodic distribution of quantum wells in the space it leads to the well know Kronig-Penney (KP) model and band forming by electrons propagating through the lattice of QW's. In a simplified 1D KP model the electron density can be drawn for the two first bands and energies near the band extrema. One clearly sees that whereas for states with energy in the first band the electron density is centered inside the finite well, there is a significant displacement of the LDOS maxima toward the barrier for states with energy in the second band compared to the position of maxima of the n = 2 state of (quasi) infinite well (see blue dashed lines in Figure 6.26c. This oversimplified model cannot be directly applied to our system since we have studied a 2D assembly of QW's with significant disorder.

Nevertheless the electron distribution together with the reduced energy spacing for the Cl nano pores eigenstates showing the failure of the "particle in a box model" lead us to claim that there could be electronic coupling between the QW's formed by the Cl nano pores. Such electronic coupling has been evidenced recently in two perfectly ordered systems made from molecular self-assembly of noble metal surfaces. The first example concerns a network of dehydro-DPDI on Cu(111) where band mapping has been achieved with ARPES [43] and the second case is NC-Ph6-CN- Co on Ag(111) surface investigated by STS and theoretical simulations [44].

In order to try to get additional experimental evidences of the electronic coupling between Cl nano pores we have tried to simplified our studied systems by investigation of limited number of QW's arranged in simple manner. By controlling the dose of Cl we were able to create chains of QW's containing from 2 up to 5 nano corrals. In this situation instead of bands we could expect discrete energy levels modified by the coupling. In the case of two identical QW's with fundamental level E_1 the degeneracy is lifted by the coupling and two new levels (bonding and antibonding) appear with energy separation proportional to the coupling strength - see Figure 6.26a. In the case of QW's of different sizes the original levels E_1 and E_2 are different and the coupling is less obviously evidenced by an increase in energy separation: $E_{antibonding} - E_{bonding} > E_1 - E_2$ (Fig 6.26b).

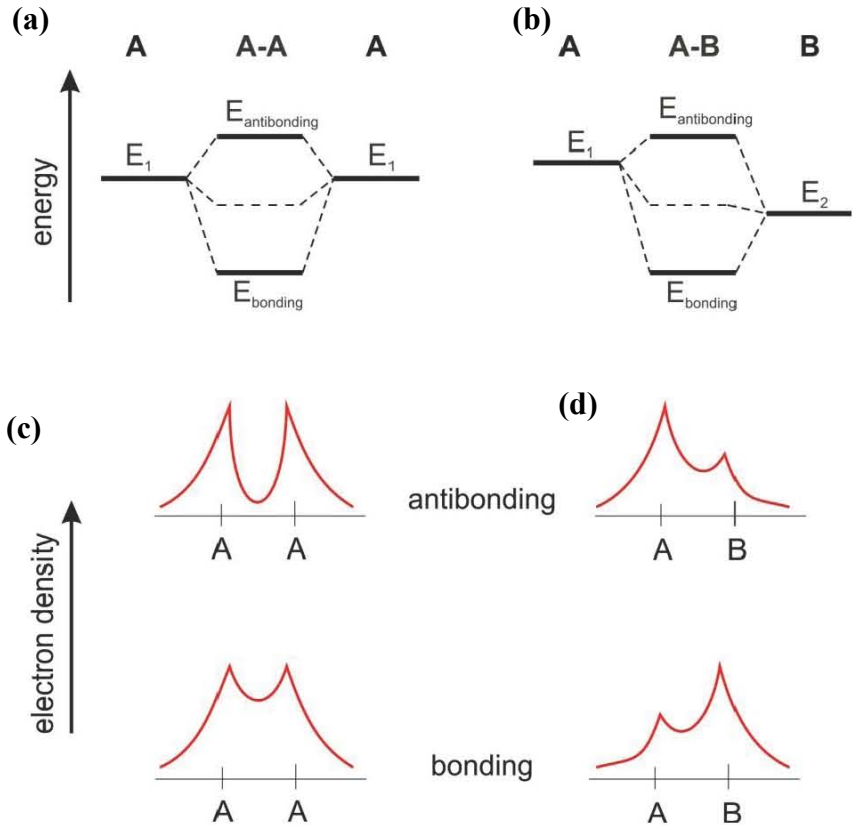

Fig. 6.27 : *sketch of the influence of the electronic coupling between QW's in te case of identical QW's (a) and (c) and in the case of different size QW's (b) and (d)*

Following this idea we have analyzed the energy of the lowest eigenmodes in sets of 2, 3 and 5 QW's arranged in linear chains (see Fig. 6.28a). The spatial distribution inside the pores together with the local DOS spectra is displayed in Figure 6.28b. For all the chains of QW's investigated we were not able to evidence the expected split of the energy levels. Unfortunately only size fluctuations dominate the spectral properties of coupled QW's. Indeed it is clear from the spectra presented in Figure 6.28c that small deviation in size between adjacent QW's induces a shift of the lowest energy resonance. If any a faint split of the eigenmodes is certainly hidden by the rather large spectral width of the measured resonances which remains here of the same order of magnitude than in the 2D lattices of QW's. Therefore a clear evidence of electronic coupling in the lattices of Cl nano pores we have studied is still challenging

Finally other possible source of the failure of the "particle in a box" model can be found in the papers of Diaz-Tendero discussed above. The spectral properties of the Cl based QW's could be influenced by the presence of a quantized 1D state on the Cl border of the pores. DFT calculation should be helpful to investigate the electronic properties of Cl atomic chains on Au(111) and probe the possible existence of a1D state with proper symmetry to couple with the quantized states inside the pores. Then we could expect to apply the WPP model of Diaz-Tendero to simulate more accurately the spectral properties of the pores.

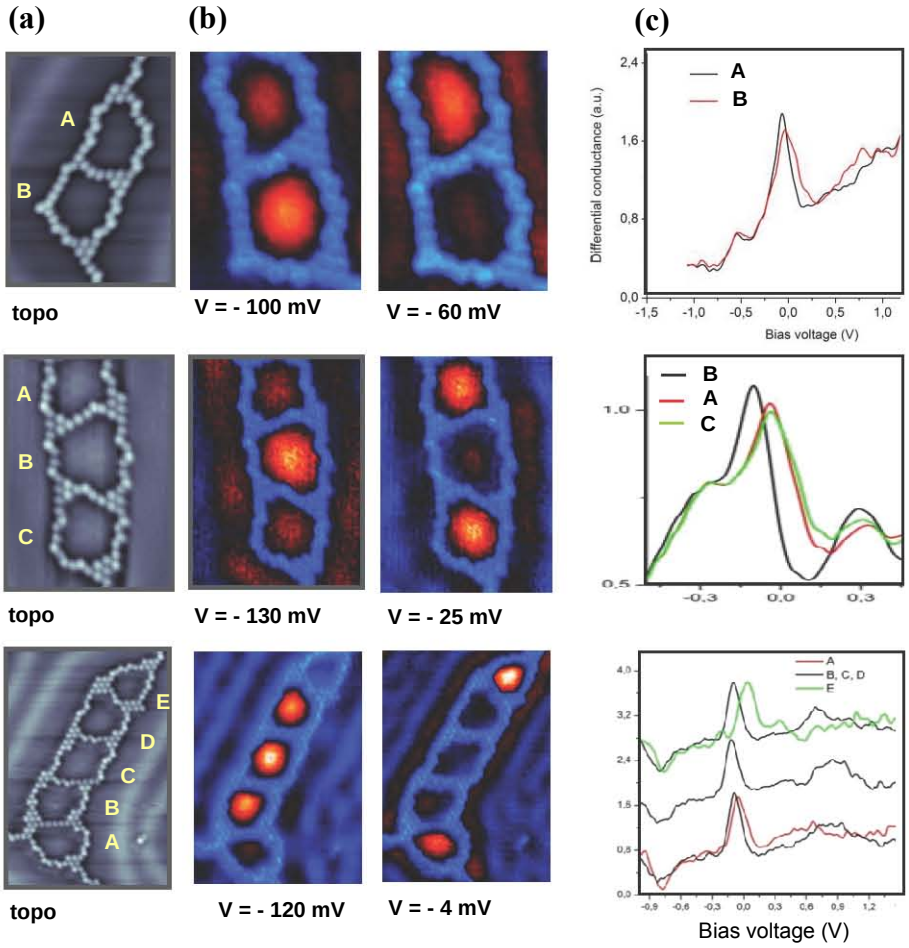

Fig. 6.28 : (a) *STM images on a set of connected QW's;* ***(b)*** *conductance maps recorded across the two lowest energy levels;* ***(c)*** *local DOS spectra recorded inside the different QW's*

6.3 Conclusion

In this chapter we have studied the spectral properties of quantum corrals made from Cl nano pores self-assembled in a quasi-hexagonal lattice. We have studied the influence of the size and shape of the pores on the energy of eigenmodes and tried to reproduce the experimental results by numerical simulations within the "particle in a box model". We have shown that this simple model fails to give the proper energies. A finite barrier height and the possible electronic coupling between neighboring pores have been evoked to explain this failure. A possible influence of the electronic structure of the chorine chains forming the corrals borders on the spectral properties of the pores cannot be ruled out.

Finally the very small diameter (3 nm) of the quantum wells made from the Cl nano pores could also explain the failure of the "particle in a box" model. Indeed in this case the fine atomic structure of the border could prevent to model it as a "simple" mirror with average reflecting coefficient. The actual electronic structure of border and the deriving scattering potential could be needed to give a proper description of the scattering process at the border and quantum interferences inside the quantum corral.

Bibliography of Chapter 6

[1] I. Tamm. Uber eine mögliche art der elektronenbindung an kristalloberflächen // Z Sowjetunion 1 733 (1932).

[2] W. Shockley. On the surface states associated with a periodic potential // Phys. Rev. 6 317 (1939).

[3] A. Zangwill. Physics at surface // Cambridge University Press (1988).

[4] L. Bürgi et al. Confinement of Surface State Electrons in Fabry-Pérot Resonators // Phys. Rev. Lett. 81 5370 (1998).

[5] F. Reinert et. al. Direct measurements of the L-gap surface states on the (111) face of noble metals by photoelectron spectroscopy // Phys. Rev. B 63 115415 (2001)

[6] E.I. Rashba et al. // Sov. Phys. Solid State **2** 1109 (1960).

[7] L. Petersen, P. Hedegard. A simple tight-binding model of spin–orbit splitting of sp-derived surface states // Surf. Sci. 459 49 (2000).

[8] L.C. Davis, M.P. Everson, R.C. Jaklevic. Theory of the local density of surface states on a metal: comparison with scanning tunneling microscopy of a Au(111) surface // Phys. Rev. B 43 3821 (1991).

[9] Ph. Avouris, I.-W. Lyo. Observation of Quantum-Size Effects at Room Temperature on Metal Surfaces With STM // Science 264 942 (1994).

[10] J. Kliewer et al. Dimensionality effects in the lifetime of surface states // Science 288 1399 (2000).

[11] J. Li et al. Electron Confinement to Nanoscale Ag Islands on Ag(111) // Phys. Rev. Lett. 80 3332 (1998).

[12] J. Kröger et al. Surface state electron dynamics of clean and adsorbate-covered metal surfaces studied with the scanning tunnelling microscope // Progr. Surf. Sci. 80 26 (2005).

[13] H. Jensen, J. Kröger, R. Berndt, S. Crampin. Electron dynamics in vacancy islands: Scanning tunneling spectroscopy on Ag(111) // Phys. Rev. B 71 155417 (2005).

[14] Y. Hasegawa, Ph. Avouris. Direct observation of standing wave formation at surface steps using scanning tunneling spectroscopy // Phys. Rev. Lett. 71 1071 (1993).

[15] M.F. Crommie, C.P. Lutz, D.M. Eigler. Imaging standing waves in a two-dimensional electron gas // Nature 363 524 (1993).

[16] J. Friedel // Nuovo Cimento Suppl. 2 287 (1958).

[17] E.J. Heller, M.F. Crommie, C.P. Lutz. D.M. Eigler. Scattering and absorption of surface electron waves in quantum corrals // Nature 369 464 (1994).

[18] S. Crampin. Surface states as probes of buried impurities // J. Phys.: Cond. Matt. 6 L613 (1994).

[19] G. Hörmandinger, J.B. Pendry. Interaction of surface states with rows of adsorbed atoms and other one-dimensional scatterers // Phys. Rev. B 50 18607 (1994).

[20] L. Bürgi. Scanning tunneling microscopy as local probe of electron density, dynamics, and transport at metal surfaces // Thesis, École Polytechnique Fédérale de Lausanne (1999).

[21] S. Crampin, M.H. Boon, J.E. Inglesfield. Influence of bulk states on laterally confined surface state electrons // Phys. Rev. Lett. 73 1015 (1994).

[22] Ph. Avouris, I.-W. Lyo. Observation of Quantum Size Effects at Room Temperature at Metal Surfaces with the STM // Science 264 942 (1994).

[23] O. Sanchez et al. Lateral confinement of surface state on stepped Cu(111) // Phys. Rev. B 52 7894 (1995).

[24] D. Malterre et al. ARPES and STS investigation of Shockley states in thin metallic films and periodic nanostructures // NJP 9 391 (2007).

[25] S. Pons. Propriétés électroniques locales de nanostructures métalliques : Etats de surface et effets de confinement // Thesis, Grenoble (2002).

[26] Kroger et al. Surface state electron dynamics of clean and adsorbat-covered metal surfaces studied with the scanning tunnelling microscope // Progr. in Surf. Sci. 80 26 (2005).

[27] C. Tournier-Colletta et al. Phonon contribution to the Lifetime of Surface State Quasiparticles Confined in Nanopyramides // Phys. Rev. Lett. 104 016802 (2010).

[28] C. Tournier-Colletta // Theses, Universite Henri Poincare, Nancy (prepared for defense).

[29] J. Kliewer, R. Berndt, S. Crampin. Scanning tunneling spectroscopy of electron resonators // NJP 3, 22.1 (2001).

[30] M.F. Crommie, C.P. Lutz, D.M. Eigler, E.J. Heller. Waves on a metal surface and quantum corrals // Surface Review and Letters 2 127 (1995).

[31] J. Li, W.D. Schneider, S. Crampin, R. Berndt. Tunnelling spectroscopy of surface state scattering and confinement // Surf Sci 422 95 (1999).

[32] H. Hövel, I. Barke Morphology and electronic structure of gold clusters on graphite: Scanning-tunneling techniques and photoemission // Progr. Surf. Sci. 81 53 (2006).

[33] S. Crampin et al. Resonator design for use in scanning tunneling spectroscopy studies of surface electron lifetimes // Phys. Rev. B 72 035443 (2005).

[34] M.F. Crommie et al. Quantum interference in 2D atomic-scale structures // Surf. Sci. 361 864 (1996).

[35] B. Simon. The bound state of weakly coupled Schrödinger operators in one and two dimensions // Ann. Phys (N.Y.) 97 279 (1976).

[36] S. Diaz-Tendero, A.G. Borisov, J.P. Gauyacq. Different quantization behavior of electrons confined in nanostructures at surface // Phys. Rev. B 76 155428 (2007).

[37] S. Diaz-Tendero, A.G. Borisov, J.P. Gauyacq. Theoretical study of electron confinement in Cu corrals on a Cu(111) surface // Phys. Rev. B 77 205403 (2008).

[38] S. Fölsch, P. Hyldgaard, R. Koch, K. H. Ploog. Quantum Confinement in Monatomic Cu Chains on Cu(111) //Phys. Rev. Lett. 92 056803 (2004).

[39] L. Petersen, P. Laitenberger, E. Lægsgaard, F. Besenbacher. Screening waves from steps and defects on Cu(111) and Au(111) imaged with STM: Contribution from bulk electrons // Phys. Rev. B 58 7361 (1998).

[40] J. I. Pascual, A. Dick, M. Hansmann, H.-P. Rust, J. Neugebauer, K. Horn. Bulk Electronic Structure of Metals Resolved with Scanning Tunneling Microscopy // Phys. Rev. Lett. 96 046801 (2006).

[41] C. Didiot, V. Cherkez, B. Kierren Y. Fagot-Revurat, D. Malterre. Bulk state confinement and band folding in nanostructured surfaces // Phys. Rev. B 81 075421 (2010).

[42] http://www.falstad.com/qm1dcrystal/

[43] J. Lobo-Checa et al. Band formation from coupled quantum dots formed by nanoporous network on a copper surface // Nature 325 300 (2009).

[44] F. Klappenberger et al. Tunable Quantum dot array formed from self-assembled metal-organic networks // Phys. Rev. Lett. 106 026802 (2011).

Conclusion

In the present thesis we reported and discussed on the results of the study of surface structures formed by molecular chlorine adsorbed on (111) faces of silver, gold and copper. The use of low-temperature scanning tunneling microscopy allowed us to investigate the details of halogenation of noble-metals that remained almost unstudied up to now, notably surface structures formed by the adsorbed halogen atoms in low-coverage range and the initial stage of commensurate structure compression.

We have found that at low temperatures and small surface coverage ($\theta << 0.33$ ML) adsorbed chlorine atoms form linear chains of one atom width. Such unexpected behavior was observed on (111) faces of all three studied metals. We suppose that a specific non monotonic interaction between adsorbed chlorine atoms can be responsible for this self-organization. Additional support for this assumption derives from the observation that nearest-neighbor distances in the chains are even smaller than in the commensurate structure formed at higher halogen coverage. Further STM measurements and DFT calculations could be helpful to reveal the shape and the physical origin of chlorine-chlorine interaction.

An important result of our work concerns the initial stage of commensurate chlorine lattice compression. For the first time we proved with LT STM the existence of a two-dimensional gas of interstitial defects in the commensurate halogen lattice that are mobile at high temperature. These interstitial defects that appear in the chlorine layer at surface coverage larger than 0.33 ML can be considered as point defects theoretically predicted and described for Pt(100) surface (crowdions). The increase of chlorine coverage leads to

the increase of the density of interstitials and subsequent their condensation into heavy domain walls. We hope that this discovery will contribute to the understanding of structural phase transitions and order-disorder phase transitions in two-dimensional systems. Our results qualitatively agree with theoretical predictions discussed above, however further experimental and theoretical study (notably on the dynamics of interstitials as a function of surface temperature) is required to get full and quantitative description of uniaxial compression. The Cl/Ag(111) system seems to be the most adapted for such study.

Based on our LT STM data supported by DFT calculations we propose atomic-structure models for saturated chlorine layer on Ag(111) and Au(111) surfaces, which were the subject of considerable discussion in the literature. This result is of great importance for the following study of the role of chlorine in the modification of noble-metals-based catalysts.

Finally a Cl nano porous superstructure has been found to form on Au(111) and is of particular interest. Our spectroscopic measurements and theoretical simulations show that confinement of surface electrons in the nano pores exists but can't be explained within the simple "particle in a box" model. That could be the sign of existence of the electronic coupling between neighboring pores. In such case the nano pores superstructure could be considered as a two-dimensional array of coupled quantum dots and development of a two-dimensional electron band structure could be expected. The possible development of a one-dimensional electronic state on the border of nano pores that could amplify electronic coupling can't be excluded either. To give reliable answer on this question additional angle resolved photoelectron spectroscopy study is required together with theoretical simulation of electron confinement in nano pores based on realistic scattering potential of the adsorbed Cl atoms.

To conclude, this work shows the richness of halogen/metal systems, notably as model systems for phase-transitions in two-dimensional systems and order-disorder phase transitions. Our study has clarified on the atomic level several complex issues on the halogen-metal interaction.

APPENDIX

Terminology and the list of abbreviations

This section contains definitions for some notions and abbreviations used in the thesis.

Sticking coefficient S :
It characterizes amount of adsorbed atoms from the whole number of particles interacting (colliding) with the surface. It has value inthe range 0÷1.

Surface coverage θ :
It can be defined in three different ways:

(1) Number of adsorbed species (atoms or molecules) on the unit of surface area. Defined so it can be also named as *absolute surface coverage* and is measured in [number_of_species/cm^2].

(2) Ratio of number of adsorbed objects to the number of substrate atoms for the same area, i.e.

$$\theta = \frac{number\_of\_adsorbed\_objects\_for\_unit\_of\_area}{number\_of\_substrate\_atoms\_for\_unit\_of\_area}$$

We will call it *relative surface coverage* and measure in monolayers [ML]. Surface coverage defined so usually has magnitude less than 1 but for some adsorbed atoms like hydrogen it can be larger than 1.

(3) Quantity reduced to the maximum monoatomic coverage for this adsorbate:

$$\theta = \frac{current\_coverage}{maximal\_coverage}$$

In this case $0 \le \theta \le 1$ for the first adsorbed layer and $\theta \ge 1$ for multilayer coverage. Only definition (1) and (2) will be used in this work. In each case corresponding unit will be used so it will be clear which definition is used.

Monolayer :
The monolayer is referred to the first adsorbed layer of single atomic plane thickness *regardless* of surface coverage.

Low-index faces

Three main low index faces of fcc crystal are shown on the Figure 1a: (100), (110) and (111). Miller indexes of crystallographic plane parallel to the surface are used for crystal face notation. On Figure 1b atomic arrangement and unit cell (defined by vectors $\mathbf{a_1}$ and $\mathbf{a_2}$) for low-index crystal face is shown. For notation of different directions on the surface corresponding Miller indexes are used.

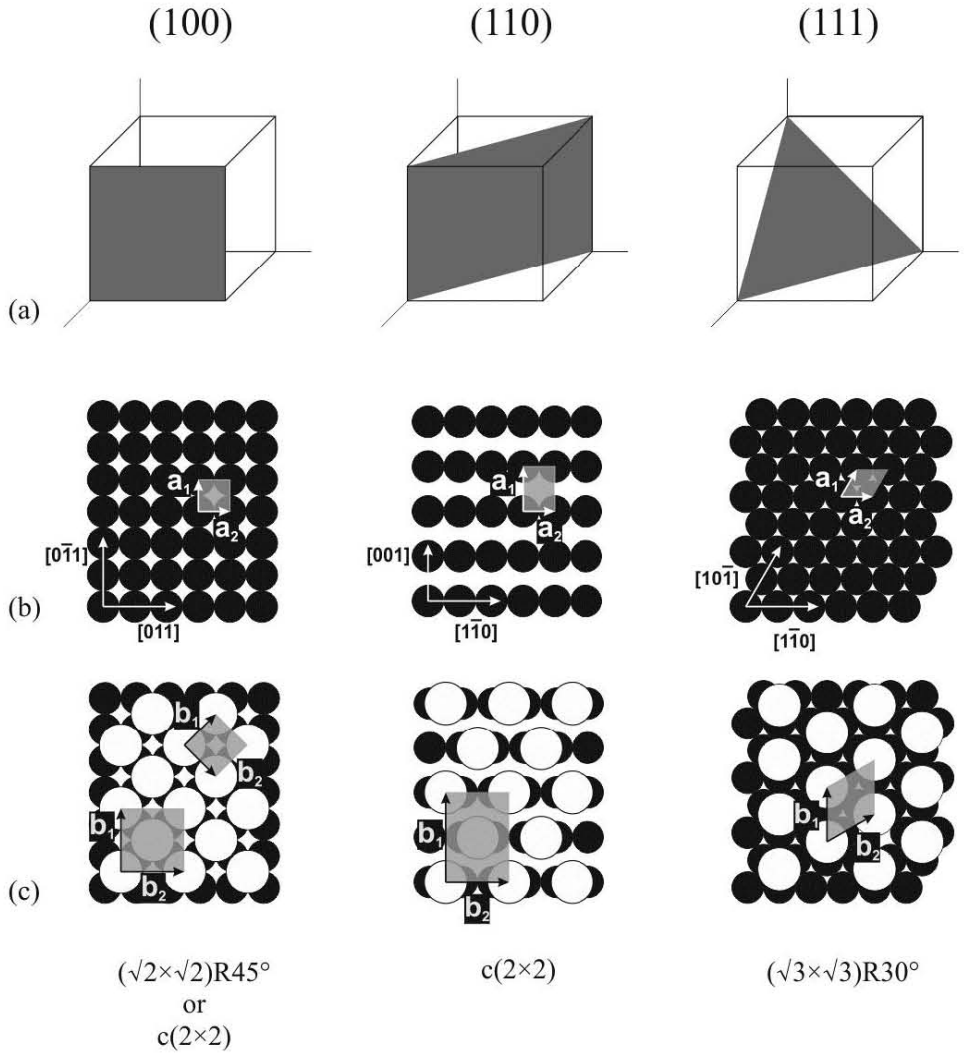

Figure 1. (a) *Orientation of three low-index planes in fcc crystal relative to the crystallographic directions.* ***(b)*** *Atomic structure of low-index planes in fcc crystal. Unit cell and surface lattice vectors, together with main crystallographic directions are shown for each plane.* ***(c)*** *Common surface commensurate structures formed by adsorbed halogen atoms. Unit cell and lattice unit vectors are shown for each structure*.

Commensurate and incommensurate structures:

Tto identify different ordered structures formed by adsorbed atoms on the surface one has to specify relationship between vectors of adsorbate and substrate lattices. There are two ways for that commonly used in the literature. The most general is Park and Madden [1] notation. For adsorbate ($\mathbf{b_1}$, $\mathbf{b_2}$) and substrate ($\mathbf{a_1}$, $\mathbf{a_2}$) lattice vectors we can always write

$$\mathbf{b_1} = G_{11}\mathbf{a_1} + G_{12}\mathbf{a_2}$$
$$\mathbf{b_2} = G_{21}\mathbf{a_1} + G_{22}\mathbf{a_2}$$

Adsorbate structure can then be identified by matrix

$$G = \begin{pmatrix} G_{11} & G_{12} \\ G_{21} & G_{22} \end{pmatrix}$$

The area of the lattice unit cell is $|\mathbf{a_1} \times \mathbf{a_2}|$. Then det G gives us the ratio of areas of adsorbate and substrate lattice unit cells. Det G can be used also for classification of surface structures:

1) det G *and all matrix coefficients are integers*

the two unit cells are unambiguously related and adsorbate unit cell has the same translation symmetry as substrate. This is called **commensurate** adsorbate lattice.

2) *det G is a rational fraction (or det G is integer and some of the matrix coefficients are rational fractions)*

the two unit cells are relatively related. In this case the adsorbate structure is still commensurate but the surface unit cell is larger than the adsorbate lattice mesh. The size of such surface mesh is determined by the period of coincidence for adsorbate and substrate lattices. This is **partially commensurate** lattices. Translation vectors for partially commensurate lattices are related to lattice vectors of adsorbate and substrate lattices by matrixes P and Q:

$$\begin{pmatrix} c_1 \\ c_2 \end{pmatrix} = P \cdot \begin{pmatrix} a_1 \\ a_2 \end{pmatrix} = Q \cdot \begin{pmatrix} b_1 \\ b_2 \end{pmatrix}$$

Matrixes P and Q are chosen in such way that det P and det Q are the least integers possible and are related as following:

$$\det G = \frac{\det P}{\det Q}$$

3) *det G is an irrational number*

The two unit cells are completely **incommensurate** and the real surface cell does not exist. In such a case the substrate simply plays the role of support for the two dimensional adsorbate lattice.

A more convenient but less general notation was proposed by Wood [2]. In this approach for adsorbate **A** which forms lattice on the *(hkl)* face of material **X** the surface structure can be identified as

$$\boldsymbol{X}(hkl)\text{-}(p\times q)\text{-R}\varphi^{\circ}\text{-}\mathbf{A}$$

where p and q gives relation between adsorbate lattice vectors length and substrate vectors length

$$\begin{aligned} |\mathbf{b_1}| &= p\ |\mathbf{a_1}|, \\ |\mathbf{b_2}| &= q\ |\mathbf{a_2}| \end{aligned}$$

and φ is the angle of rotation for adsorbate lattice.

Note that Wood notation can be used only in that case when for both adsorbate lattice vectors angle of rotation φ is the same, i.e. adsorbate should form the same Brave lattice as substrate has (or adsorbate and substrate lattices must have rectangular or square unit cells). In general, Wood notation is not suitable for surface structures with different symmetry. To give an example the most common halogen commensurate structures are shown on Figure 1c. For (√2×√2)R45° structure c(2×2) notation is usually used.

Abbreviations:

The following abbreviations will be used in the thesis:

AES – Auger Electron Spectroscopy;
ARPES – Angle-resolved Photoelectron Spectroscopy;
DFT – Density Functional Theory.
EXAFS – Extended X-ray Absorption Fine Structure;
KP – Kronig-Penney
LEED – Low Energy Electron Diffraction;
PED – Photoelectron diffraction
QW – Quantum Well
UHV – Ultra High Vacuum;
UPS – Ultraviolet Photoelectron Spectroscopy;
STM – Scanning Tunneling Microscopy;
STS – Scanning Tunneling Spectroscopy;
TDS – Thermal Desorption Spectroscopy;
XPS – X-ray Photoelectron Spectroscopy;

Bibliography of Appendix

[1] R.L. Park, H.H. Madden. Annealing changes on the (100) surface of palladium and their effect on CO adsorption // Surf. Sci. 11 188 (1968).

[2] E.A. Wood. Vocabulary of surface crystallography // Journ. of Appl. Phys. 35 1306 (1964).

Acknowledgements

This thesis would not have been possible unless the assistance of many people from Jean Lamour Institute (IJL) in Nancy and General Physics Institute (GPI) in Moscow.

I have been indebted in the preparation of this thesis to my supervisor, Prof. Bertrand Kierren from University of Nancy, whose patience and kindness, as well as his academic experience, have been invaluable to me. I am also extremely grateful to Dr Boris Andryushechkin from General Physics Institute in Moscow, whose energy and scientific ideas were the driving force of the study and who was the supervisor of the work from Russian side. I am very much obliged to Dr Konstantin Eltsov, the head of Surface Phenomena Laboratory at the GPI, and Prof. Daniel Malterre, the head of Surfaces and Spectroscopies Group at the IJL, without whom this collaboration and my thesis would have never begun.

I am deeply grateful to the referees of my thesis – Prof. Erminald Bertel and Dr Dimitri Roditchev – who graciously agreed to read the manuscript and gave their remarks. It was a pleasure for me that Prof. Michel Piecuch, Prof. Peter Zeppenfeld and Dr Laurent Guillemot could come to participate in the defense jury.

I would like to thank Evgeny Gladchenko from GPI, who performed most of DFT calculations for this work. I also want to thank Dr Emilie Gaudry who supported this work with DFT calculations too. I am grateful to Dr Christophe Chatelain who provided us with his code for numerical solution of two-dimensional Schrödinger equation and who was very enthusiastic about our study.

The help of our technical engineer Luc Moreau was invaluable during all experimental series.

I would like to thank my colleagues in the lab, in particular Dr Yannick Fagot-Revurat, Cédric Tournier-Colletta and Luis Cardenas for their friendliness and willingness to assist.

My parents have been a constant source of support – both emotional and moral.

Lastly, and most importantly, I wish to thank my wife Xenia – my greatest inspiration and joy.